
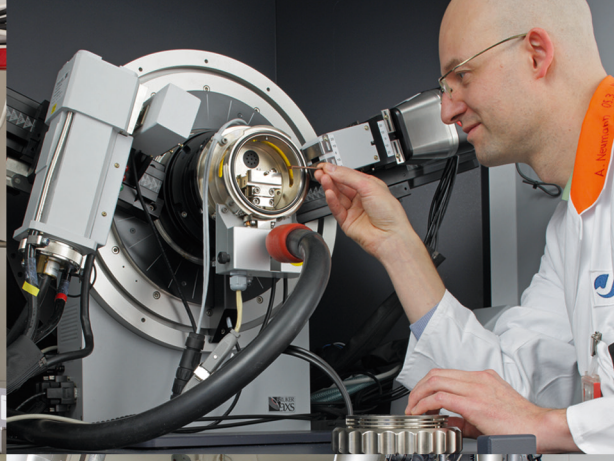


Institute of Energy and Climate Research
IEK-6: Nuclear Waste Management & Reactor Safety
Report 2009/2010

Material Science for Nuclear Waste Management

M. Klinkenberg, S. Neumeier, D. Bosbach (Editors)

JÜLICH
FORSCHUNGSZENTRUM

Mitglied der Helmholtz-Gemeinschaft

Schriften des Forschungszentrums Jülich
Reihe Energie & Umwelt / Energy & Environment Band / Volume 119

Forschungszentrum Jülich GmbH
Institute of Energy and Climate Research (IEK)
Nuclear Waste Management and Reactor Safety (IEK-6)

Institute of Energy and Climate Research
IEK-6: Nuclear Waste Management & Reactor Safety
Report 2009/2010
Material Science for Nuclear Waste Management

M. Klinkenberg, S. Neumeier, D. Bosbach (Editors)

Schriften des Forschungszentrums Jülich
Reihe Energie & Umwelt / Energy & Environment Band / Volume 119

ISSN 1866-1793 ISBN 978-3-89336-735-1

Bibliographic information published by the Deutsche Nationalbibliothek.
The Deutsche Nationalbibliothek lists this publication in the Deutsche Nationalbibliografie; detailed bibliographic data are available in the Internet at http://dnb.d-nb.de.

Publisher and Distributor:	Forschungszentrum Jülich GmbH Zentralbibliothek 52425 Jülich Phone +49 (0) 24 61 61-53 68 · Fax +49 (0) 24 61 61-61 03 e-mail: zb-publikation@fz-juelich.de Internet: http://www.fz-juelich.de/zb
Cover Design:	Grafische Medien, Forschungszentrum Jülich GmbH
Printer:	Grafische Medien, Forschungszentrum Jülich GmbH
Copyright:	Forschungszentrum Jülich 2011

Schriften des Forschungszentrums Jülich
Reihe Energie & Umwelt / Energy & Environment Band / Volume 119

ISSN 1866-1793
ISBN 978-3-89336-735-1

The complete volume ist freely available on the Internet on the Jülicher Open Access Server (JUWEL) at http://www.fz-juelich.de/zb/juwel

TABLE OF CONTENTS

1 Preface

This is the first issue of a new series of bi-annual reports intended to provide an overview of research activities for the safe management of nuclear waste in the Institute of Energy and Climate Research (IEK-6), Nuclear Waste Management and Reactor Safety devision in Jülich. The report gives a thematic overview of the research in 2009 and 2010 by short papers of five to eight pages. Some papers are discussing the work within different projects with intensive overlap, such as the work on irradiated (reactor) graphite. Other projects are represented by several papers, such as the work on ceramic waste forms. Furthermore, some background information about the IEK-6 completes the picture of the activities of the Institute. In summary, a hopefully comprehensive overview of the current research at IEK-6 will be provided.

During the years 2009 and 2010 a number of substantial changes took place within IEK-6. In April 2009 Dirk Bosbach succeeded Reinhard Odoj as head of the nuclear waste management part of the Institute. Bruno Thomauske joined the Institute in August 2009 as head of the nuclear fuel cycle part. Therefore, the continuation of the nuclear waste management research activities in Jülich is ensured.

New research topics, such as ceramic waste forms and more basic science oriented research on materials containing actinides for the safe management and disposal of nuclear waste, were started at IEK-6. Also, new research groups on "Structure Research" and "Nuclear Safeguards" were established. The structure research group covers a broad spectrum from material synthesis to (micro)structural characterisation including computational approaches and thermodynamics as a cross cutting topic, in order to support the Institute's research programme on the long-term safety of nuclear waste disposal and innovative waste management strategies. The nuclear safeguards group, included in IEK-6 since May 2009, coordinates the joint safeguards R&D programme between the International Atomic Energy Agency (IAEA) ant the Federal Ministry of Economics and Technology (BMWi).

By installing a number of new instruments, IEK-6 was able to enhance significantly the Institute's analytical capabilities: A Zeiss NVision 40 Cross beam workstation with a SIINT zeta FIB column was made available in particular for preparing radioactive samples for subsequent TEM studies. Also, the FEI Quanta 200 F ESEM was upgraded by a EDAX TEXS LambdaSpec WDX detector. A Horiba LabRAM HR Vis Raman microscope is expected to advance research on ceramic waste forms and in particular on secondary phase formation upon spent fuel corrosion by in-situ measurements. With regard to powder x-ray diffraction measurements, a new Bruker D4 diffractometer was set up in addition to the existing Bruker D8 instrument. Furthermore, Parr hydrothermal reactors and a vacuum hot press (FCT Systeme) have extended the possibilities to synthesise new materials for the safe management of nuclear waste.

A number of new research projects were started in 2009/2010: "New materials for nuclear waste management" is funded by the Ministry of Innovation, Science and Research of the

state of NRW. The collaborative project VESPA, funded by the Federal Ministry of Economics and Technology, focuses on the geochemical behaviour of mobile fission und activation products. In SKIN, European collaborative project, slow kinetic processes relevant for the long term safety of nuclear waste disposal are being investigated. CARBODISP develops disposal concepts of irradiated (reactor) graphite with respect to the German Konrad repository for radioactive waste with negligible heat generation and is funded by the Federal Ministry of Education and Research.

However, also unpleasant developments occurred, first and foremost the shut-down of the IEK-6 hot cell facility by the end of 2009 and the resulting loss of a substantial part of the Institute's radiochemistry laboratories. Fortunately, many people in Forschungszentrum Jülich supported IEK-6 in providing additional laboratory capacities in other buildings. In particular, access to the GHZ central hot cell facility in Forschungszentrum Jülich has ensured to continue the well-established research on spent fuel corrosion under repository conditions in the future. Without any doubt, the fact that IEK-6 laboratories are spread over the campus in Jülich implicates demanding working conditions, however, the Institute has successfully met the challenge - last but not least due to the motivation of the IEK-6 staff.

Various fascinating research results could be achieved in 2009/2010. Four real highlights should be mentioned here: (1) The separation of Am(III) from Cm(III) on the basis of the LUCA process; (2) the identification of the uptake mechanism for Zr and Se by LDH secondary phases, which form during the corrosion of research reactor spent fuel; (3) the optimisation of the preparation of CeO_2 - 8 YSZ ceramic waste forms and (4) the improvement of the segmented gamma scanning for the non-destructive characterisation of low-level radioactive waste drums. In addition to the scientific results, 4 patents were applied.

Within a collaborative effort by the Forschungszentrum Jülich (Institute IEK-6, Nuclear Physics Institute, Centre for Technology), Siemens AG, and the Frankfurt Institute for Advanced Studies coordinated by Prof. Thomauske, RWTH-Aachen/Forschungszentrum Jülich, the AGATE report - concept of a gas cooled, accelerator driven transmutation facility - has been completed on behalf of the Ministry of Innovation, Science and Research of the state of NRW. This study was performed to explore the feasibility of transmutation for nuclear waste created by German power plants. The Advanced Gas-cooled Accelerator-driven Transmutation Experiment - AGATE has been conceptually proposed as an alternative to currently pursued Pb/Bi cooled ADS systems.

The quality control group (PKS) at IEK-6 qualifies heat-generating vitrified waste from reprocessing in France, the United Kingdom and the Vitrification Plant Karlsruhe (VEK) as well as nuclear waste with negligible heat generation in Germany on behalf of the Federal Office for Radiation protection (BfS). The group has seen a significant fluctuation in staff during the last two years but has now actually reached a peak number in staff. IEK-6 is committed to further strengthen the group and thus ensure an important contribution to the safe management of nuclear waste in Germany.

These successes are the result of competent and highly motivated people including graduate students, an excellent laboratory infrastructure and a productive working environment.

The link to Jülich´s partner university RWTH Aachen was strengthened due to the fact that Dirk Bosbach holds the chair for the disposal of nuclear waste and Bruno Thomauske the chair for nuclear fuel cycle. Further, a new accredited Master Curriculum "Nuclear Safety Engineering" was established at RWTH Aachen University in 2010. 13 students started this 2 years programme. A new practical course on nuclear measuring techniques in the radiochemistry laboratories of IEK-6 as well as the lecture "Introduction to Nuclear Chemistry" was launched in 2010 and has attracted almost 50 students from nuclear safety engineering, chemistry, computational engineering science and nuclear technology at RWTH Aachen. 14 PhD students are currently (May 2011) working on research projects related to the safe management of nuclear waste in Jülich. 6 PhD candidates successfully defended their theses during the last 2 years, one with summa cum laude at RWTH Aachen University. IEK-6 is committed to support the education in Aachen and beyond on nuclear/radio-chemistry with respect to the safety of nuclear waste management. IEK-6 also participates in the new graduate school Energy a nd Climate HITEC, which was founded 2011 in Jülich.

Last but not least, as a rather recent change, the **Institute of Energy- and Climate Research (IEK)** was founded by combining the former Institute of Energy Research (IEF) and parts of the former Institute of the Chemistry of the Geosphere (ICG) in 2010. Furthermore, in early 2011 the nuclear safety research part was renamed to "**Nuclear Waste Management and Reactor Safety**" (IEK-6).

Jülich, July 2011

2 Institute's Profile

Due to the use of nuclear energy about 17.000 t (27.000 m^3) of high level waste and about 300.000 m^3 of low- and intermediated level waste will have accumulated in Germany until 2022. Research in the Institute of Energy and Climate Research (IEK-6), Nuclear Waste Management and Reactor Safety devision focuses on fundamental and applied aspects of the safe management of nuclear waste - in particular the nuclear aspects. In principle, our research in Forschungszentrum Jülich is looking at the material science / solid state aspects of nuclear waste management. It is organized in several research areas:

The **long-term safety of nuclear waste disposal** is a key issue when it comes to the final disposal of high level nuclear waste in a deep geological formation. We are contributing to the scientific basis for the safety case of a nuclear waste repository in Germany. In Jülich we are focusing on a fundamental understanding of near field processes within a waste repository system. The main research topics are spent fuel corrosion and the retention of radionuclides by secondary phases. In addition, **innovative waste management strategies** are investigated to facilitate a qualified decision on the best strategy for Germany. New ceramic waste forms for disposal in a deep geological formation are studied as well as the partitioning of long-lived actinides. These research areas are supported by our **structure research group**, which is using experimental and computational approaches to examine actinide containing compounds.

Complementary to these basic science oriented activities, IEK-6 also works on rather applied aspects. The development of non-destructive methods for the **characterisation of nuclear waste** packages has a long tradition in Jülich. Current activities focus on improving the segmented gamma scanning technique and the prompt gamma neutron activation analysis.
Furthermore, the **waste treatment group** is developing concepts for the safe management of nuclear graphite.

Within the **product quality control group (PKS)** 16 scientists and engineers are currently working on the qualification of radioactive waste on behalf of the Federal Office for Radiation Protection (BfS).
The **nuclear safeguards** group is coordinating the joint safeguards R&D programme between IAEA and BMWi.

Research and development activities are integrated into national and international research programms and cooperations. They represent a substantial part of the Helmholtz Research programme "Nuclear Safety Research".

Material science for nuclear waste management is the research subject of IEK-6, Nuclear Waste Management part.

2.1. Staff

77 staff members (July 2011)

33 scientists	16 PhD students	4 graduands
11 engineers & technicians	7 laboratory assistants	6 administration

Fig. 1: Staff of IEK-6 – Nuclear Waste Management (October 2009).

2.2. Organization chart

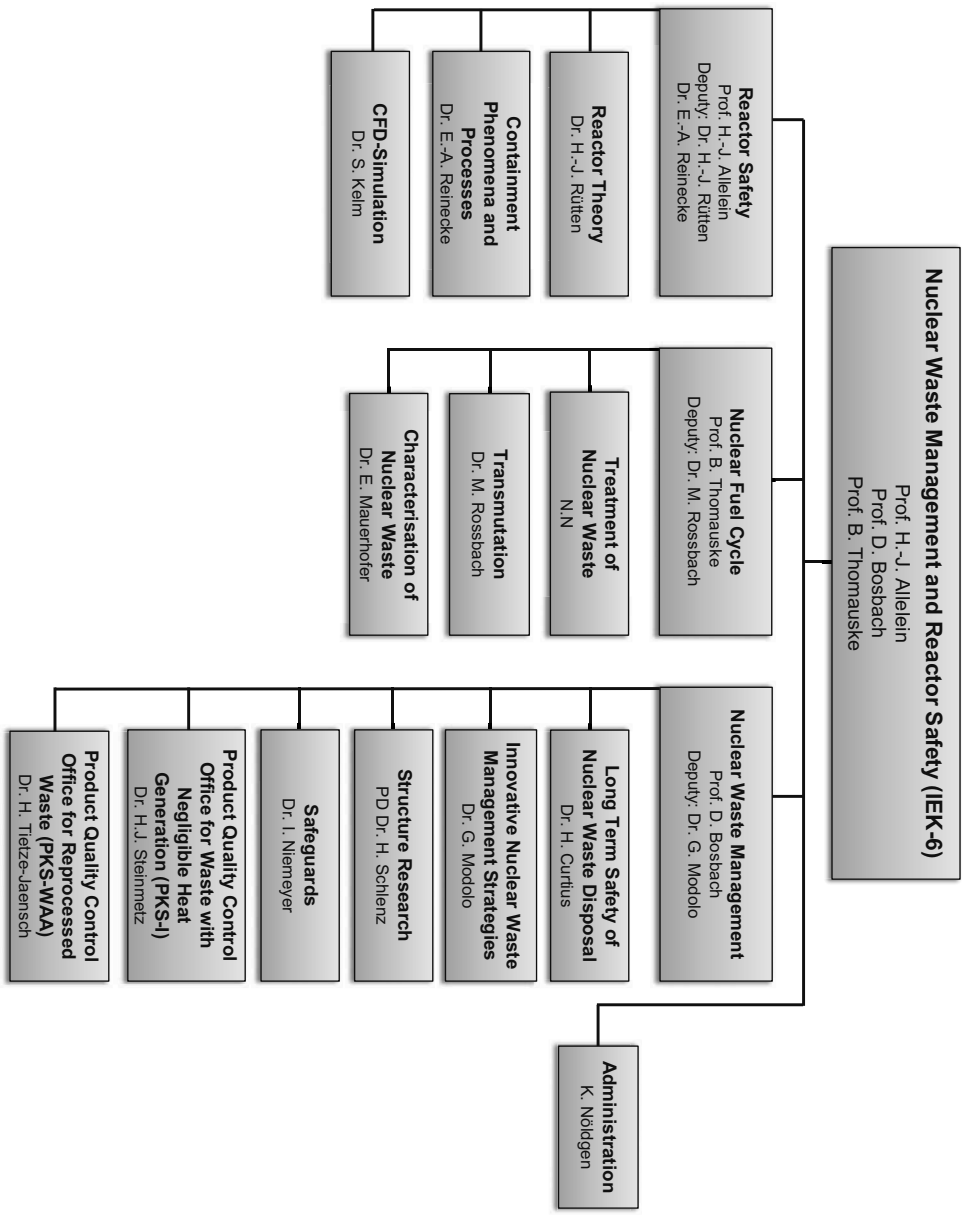

Fig. 2: Organization chart of the Institute of Energy and Climate Research (IEK-6), Nuclear Waste Management and Reactor Safety devision (July 2011).

2.3. Budget

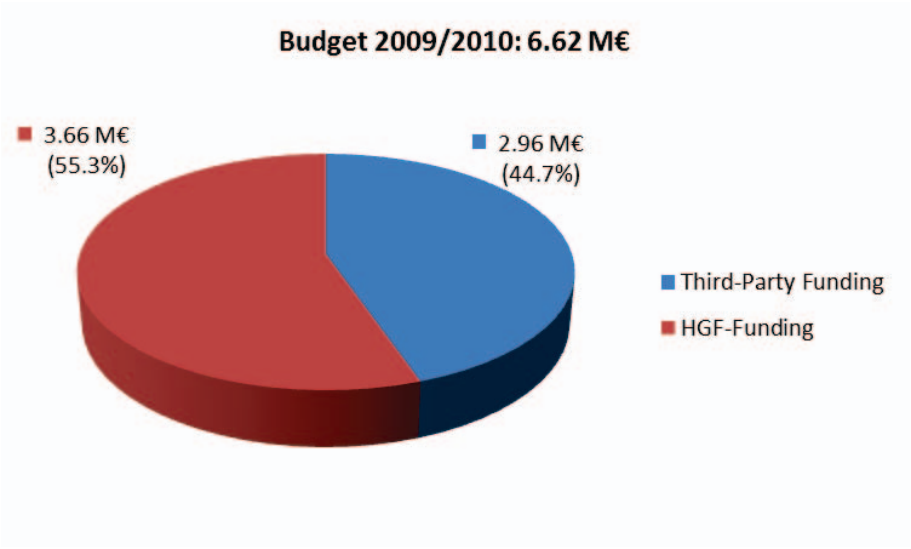
Budget 2009/2010: 6.62 M€
3.66 M€
(55.3%)
2.96 M€
(44.7%)
Third-Party Funding
HGF-Funding

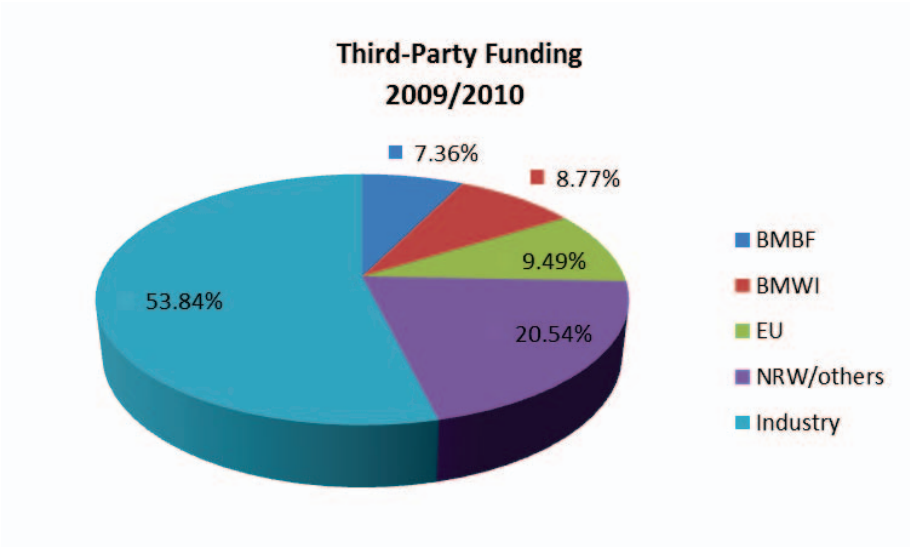
Third-Party Funding
2009/2010
7.36%
8.77%
9.49%
20.54%
53.84%
BMBF
BMWI
EU
NRW/others
Industry

3 Key Research Topics

3.1. Long Term Safety of Nuclear Waste Disposal

The disposal of high-level nuclear waste in deep geological formations poses major scientific and social challenges to be met in the next decades. One of the key issues is related to the long term safety of a waste repository system over extended periods of time - typically time frames of up to a million years are taken into account when designing waste repositories, due to the long half-live of some of the radionuclides. There is a consensus in the scientific community that deep geological disposal offers the largest long term isolation potential - it relies on the passive safety of the geological formation. There seems also to be a consensus in the scientific community that long-term predictions regarding the (radio)geochemical evolution of a waste repository system should be guided by equilibrium thermodynamics and geochemical insights.

Furthermore, a molecular-level process understanding can help improving the confidence in available data on radionuclide behaviour in the geosphere beyond a simple phenomenological description.

The principal way that radionuclides can be transported away from a deep geological disposal facility and towards the biosphere is in the form of dissolved species in ground water (Fig. 3).

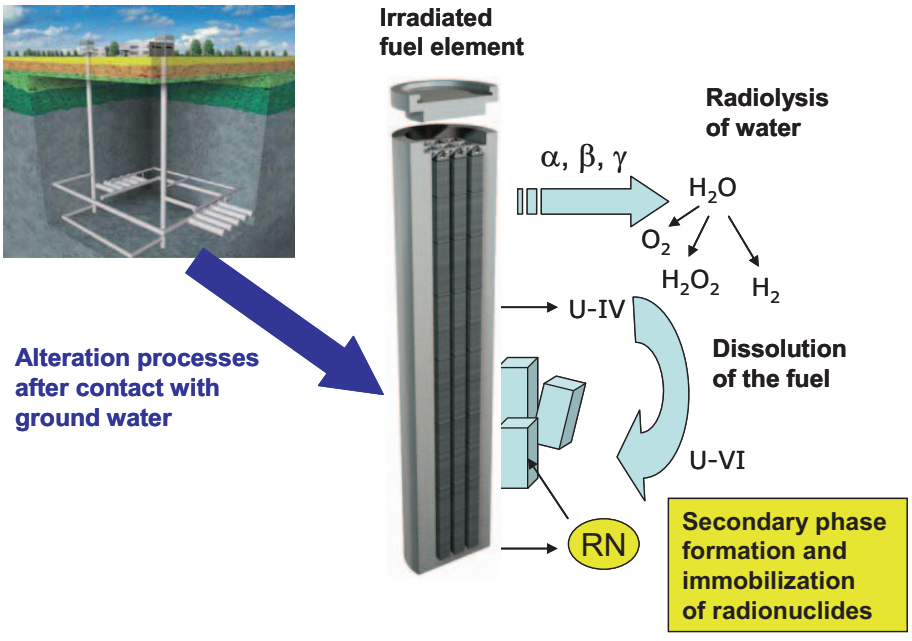

Fig. 3: Overview of geochemical processes governing the alteration of spent nuclear fuel in the presence of ground water.

Therefore, research at IEK-6 is focusing on the interaction of ground water with nuclear waste forms, in particular with spent nuclear fuel and the (geo)technical barrier (the so called near field of a repository system). Radionuclides may be released from the waste matrix upon interaction with ground water. At the same time, corrosion products form and dissolved radionuclides may bind to these secondary phases by one or more distinct sorption reactions. Characterizing the stability, reactivity and thermodynamics of the relevant secondary phases as well as the identification of the molecular level sorption reaction is an important aspect of IEK-6 research. IEK-6 performs basic science on the retention and sorption of radionuclides within the near field of a deep geological disposal facility.

Contact: Dr. Hildegard Curtius
h.curtius@fz-juelich.de

3.2. Innovative Nuclear Waste Management Strategies

The selective partitioning (P) of long-lived minor actinides from high active waste solutions and their transmutation (T) to short-lived or stable isotopes by nuclear reactions will reduce the long-term hazard of the high-level waste and significantly shorten the time needed to ensure their safe confinement in a repository. For partitioning, hydrometallurgical processes are being developed at IEK-6 for separating the trivalent actinides by means of liquid/liquid extraction. Ongoing and future R&D work is based on the highly radioactive liquid waste from reprocessing according to the PUREX process (Fig. 4).
The main objectives of our research are on the one hand fundamental research on partitioning, to improve the knowledge of the chemistry of actinides and the extraction agents and on the other hand process development involving testing of extraction devices with inactive and with genuine radioactive waste solutions.

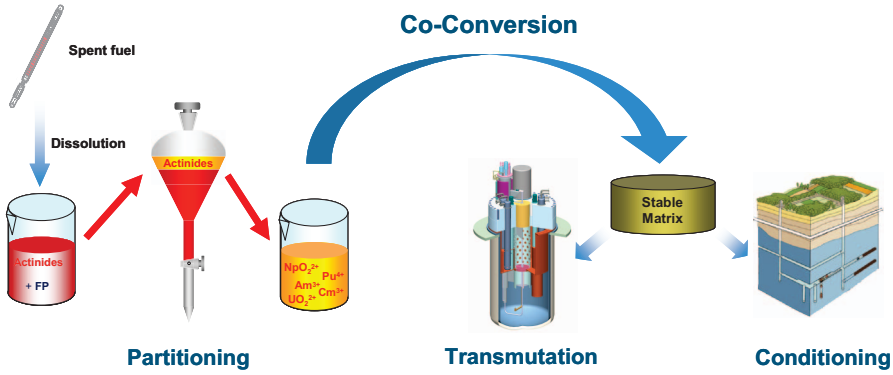

Fig. 4: Strategy for partitioning & transmutation (P&T) and partitioning & conditioning (P&C).

In order to foster and strengthen the links between partitioning and transmutation IEK-6 will carry out studies for the conversion of separated elements to solid precursors prior to fuel fabrication. The activities cover basic studies, such as the thermodynamic and kinetics of

actinide co-conversion into polyactinide solids (structural studies) to deeply understand and improve the co-conversion process.
In a complementary partitioning & conditioning strategy (P&C), new nuclear waste forms such as ceramic matrices with high radiation resistance and aqueous durability are of interest for the safe disposal. At present, high-active waste is generally vitrified. Ceramic matrices are much more stable and therefore form a final disposal product which can effectively prevent radionuclides escaping from the repository for extremely long periods of time.
P&C may help to reduce the actinide source term from a repository in case of water access. Due to their advantageous properties zirconia based compounds and monazite are considered within the R&D programme of the IEK-6.

Contact: Dr. Giuseppe Modolo
g.modolo@fz-juelich.de

3.3. Structure Research

The chemical and physical properties of a material are determined by its chemical composition, present chemical bonds and particularly by its structure, no matter if crystalline or amorphous materials (glasses) are investigated. According to nuclear waste management mainly ceramics and glasses are considered for the immobilization of actinides. For the purpose of understanding material properties and for the development of such new materials, knowing the structure is an indispensable prerequisite. As an example the crystal structure of the mineral monazite (Fig. 5, left) is determined as a function of varying amounts of Uranium (U) and Thorium (Th) using x-ray powder diffraction, in order to detect structural changes due to varying chemical composition and possible radiation damage caused by the radioactive decay of U and Th. Further candidate phases for the immobilization of actinides are e.g. pyrochlore, Ce-, U- and Th-oxides, as well as U- and Th-silicates.

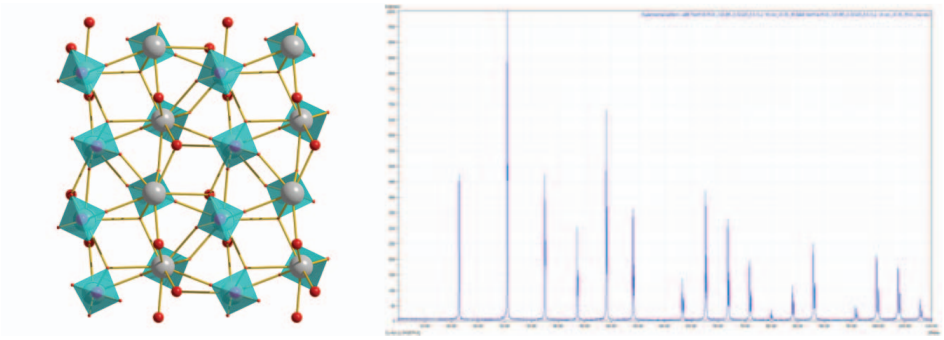

Fig. 5: Left: Crystal structure of the mineral monazite. Right: powder diffractogram of a LaB_6 standard.

At the IEK-6 structure research is performed using diffraction (Fig. 5, right) and spectroscopic analysis. X-ray synchrotron diffraction and spectroscopy experiments are performed at large

research facilities like ANKA (Karlsruhe), HASYLAB (Hamburg) or ESRF (Grenoble). Neutron diffraction experiments are performed in cooperation with the RWTH Aachen, e.g. at the nuclear research reactor FRM II (Garching). To be able to examine further structural details complementary analytical methods like Raman spectroscopy (Fig. 6) and IR spectroscopy are applied. Finally structure models are partly generated by computer simulations (Reverse Monte Carlo).

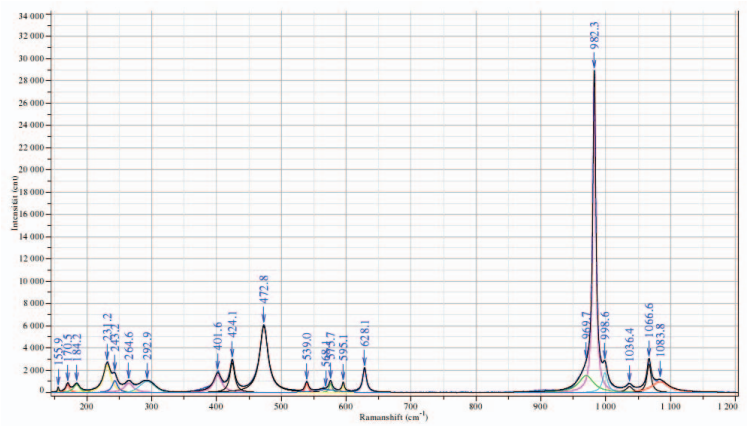

Fig. 6: Raman spectrum of synthetic $SmPO_4$.

Contact: PD Dr. Hartmut Schlenz
h.schlenz@fz-juelich.de

3.4. Characterisation of Nuclear Waste

Radioactive waste has to meet the specifications and acceptance criteria defined by national regulatory and management authorities. For this reason, appropriate quality control procedures have to be carried out to quantify relevant radioactive isotopes and non-radioactive toxic elements present in the waste. Within these procedures non-destructive assay techniques are preferred to minimize inspection time and to reduce the radiation exposure of personal. Furthermore, secondary waste by invasive sampling and subsequent radiochemical analysis of the obtained material will be avoided. The Waste Characterization group at IEK-6 is developing innovative passive and active non-destructive analytical techniques (Fig. 7) assisted by modern computational simulation tools for the accurate and reliable characterization of radioactive waste packages at industrial scale.
In support of method development nuclear data measurements are carried out at the FRM II reactor in Garching or the Budapest Neutron Centre (BNC) with cold and thermal neutrons and at the Nuclotron facility in Dubna, Russia, with spallation neutrons. Neutron capture cross sections of actinides, such as ^{237}Np, ^{242}Pu, or ^{243}Am will be determined to develop analytical methods based on active neutron interrogation.

Fig. 7: Non-destructive analytical techniques: Gamma-Scanning, Computer-Tomography, and Prompt- Gamma-Neutron-Activation-Analysis (PGNAA).

Contact: Dr. Eric Mauerhofer
e.mauerhofer@fz-juelich.de

3.5. Transmutation

Transmutation of long lived minor actinides and fission products is considered to reduce the radio toxicity of nuclear waste prior to disposal. Following separation (partitioning) of long lived minor actinides (MA) and fission products (FP) subsequent conversion (transmutation) into less toxic or stable nuclides by fast (for MA) and thermal (for FP) neutrons seems to leverage safety requirements on the long term stability for a final repository.
Current concepts for transmutation of MA and FP rely on high flux fast reactors and accelerator based spallation sub-critical systems (ADS). In a cooperative effort by the RWTH Aachen, FZJ, Siemens AG and FIAS, Frankfurt a feasibility study for an Advanced Gas-cooled Accelerator driven Transmutation Experiment (AGATE) was carried out to assess the potential of transmutation for nuclear waste produced by German Nuclear Power Plants. The proposed sub-critical reactor (Fig. 8), boosted by a proton linear accelerator and a tungsten spallation source is He cooled and due to the sub-criticality inherently safe. However, intensive R&D work is still required to solve a multitude of open questions regarding the various components of an ADS transmutation facility.

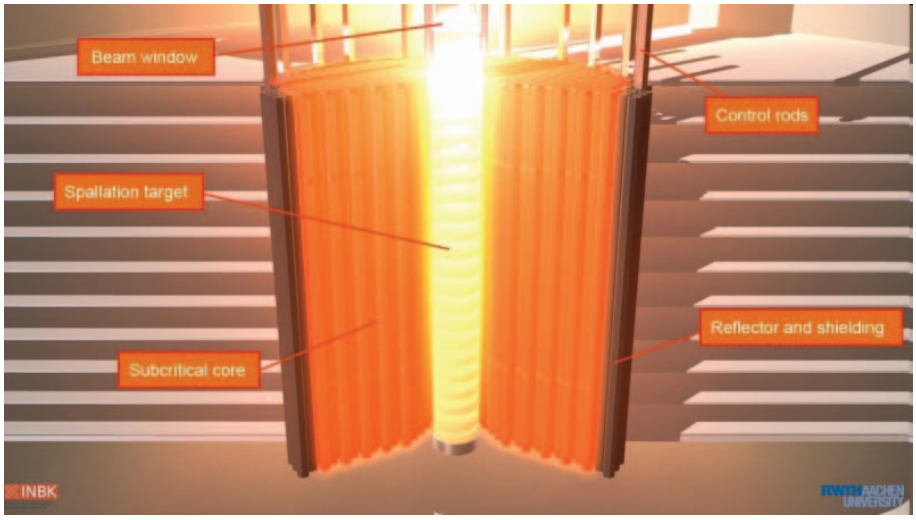

Fig. 8: Sub-critical reactor core with segmented W spallation source of the AGATE design.

Contact: Dr. Matthias Rossbach
m.rossbach@fz-juelich.de

3.6. Nuclear Waste Treatment

The application of radionuclides in science, health care and industry generates radioactive wastes which have to be collected, treated and finally disposed. Radioactive wastes are materials which consist of a non-radioactive base material which is contaminated with one or more radionuclides.

The main aim of the research activities in the Nuclear Waste Treatment Group of IEK-6 is the investigation of the chemical structures which radionuclides form in non-radioactive waste matrices. With this knowledge, methods for the nuclear decontamination of these waste matrices can be developed. Waste matrices decontaminated in such a way can be reused for new technical applications or disposed in a more favourable strategy. The removed radionuclides are also interesting if they can be separated from the nuclear waste in a highly enriched form. Such radionuclides like tritium (^{3}H) and radiocarbon (^{14}C) are commercially requested materials which are more and more difficult to provide on the international markets.

At present, the main intention of our research activities is the development of treatment methods for neutron-irradiated nuclear graphite. Nuclear graphite is high-purity graphite which was used in nuclear reactors as neutron moderator and neutron reflector. Radionuclides like ^{3}H and ^{14}C were formed in this graphite by interaction of neutrons with impurities which are present in high-purity graphite, too. These radionuclides can be removed from the graphite matrix, e.g. by thermal treatment (Fig. 9). Afterwards, the removed radionuclides as well as the decontaminated graphite can be used for further applications.

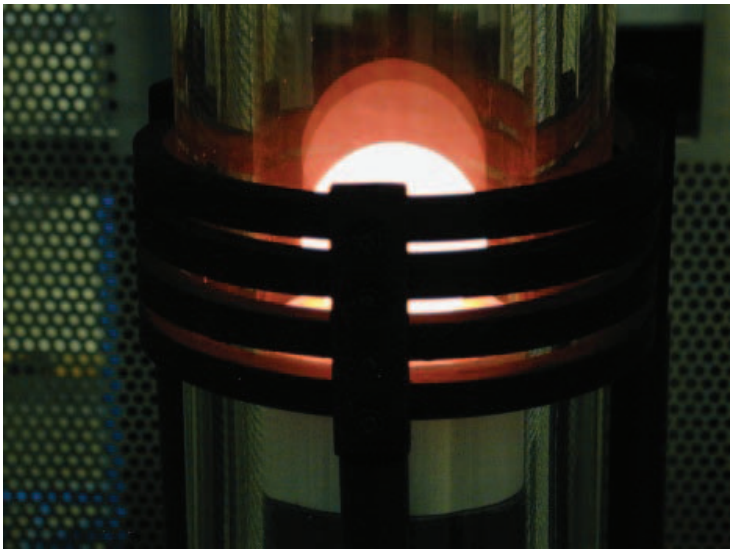

Fig. 9: Thermal treatment of an AVR graphite pebble in an induction furnace at 1000 °C.

Contact: Dr. Dirk Vulpius
d.vulpius@fz-juelich.de

3.7. Nuclear Safeguards

Under the Nuclear Non-Proliferation Treaty (NPT), non-nuclear weapon States are prohibited from, inter alia, possessing, manufacturing or acquiring nuclear weapons or other nuclear explosive devices. The Treaty has established a safeguards system under the responsibility of the International Atomic Energy Agency (IAEA). Safeguards are activities by which the International Atomic Energy Agency (IAEA) can verify that a State is in compliance with its international commitments not to use nuclear programmes for nuclear-weapons purposes. Today, the IAEA is safeguarding nuclear material and activities under agreements with more than 140 States. Safeguards are based on assessing the correctness and completeness of a State's declared nuclear material and nuclear-related activities. Verification measures include on-site inspections and other visits, on-going monitoring and evaluation.

The NPT requires the Member States to cooperate with the IAEA in order to facilitate the application of safeguards in these States. On this basis the IAEA and the German Government, then represented by the Federal Ministry of Research and Technology, agreed upon the "Joint Programme on the Technical Development and Further Improvement of IAEA Safeguards" in 1978. The programme objectives are to jointly develop safeguards methodologies and techniques, to provide consultancy and expert advice to the IAEA, and to inform the IAEA, as early as possible, about Germany's nuclear plans and projects.

Since summer 1985, the Juelich Research Centre (Forschungszentrum Jülich, FZJ) has coordinated the programme implementation in close cooperation with the German Government, now represented by the Federal Ministry of Economics and Technology (BMWi). In May 2009, the Institute of Energy and Climate Research, IEK-6, Nuclear Waste

Management and Reactor Safety devision took over the responsibility for the German Support Programme coordination within Forschungszentrum Jülich.
Since its establishment, the programme has comprised more than 150 tasks, providing research and development, training of IAEA staff, consultancy support, and the secondment of 17 cost-free experts to the IAEA. The achievements have been documented in almost 380 reports. Most of the technical developments have been implemented by the IAEA for routine inspection use. The European Atomic Energy Community (Euratom) started implementing safeguards instrumentation developed under the German Support Programme in a larger scale only after entering into force of the NPT Additional Protocol.
In 2010, the German Support Programme consisted of 27 active tasks, among them the development of containment and surveillance systems (DCM-C5, EOSS), development of nuclear measurement methods and techniques (LIBS, DMCA, HM-5, Krypton-85 analysis), geophysical measurements for detecting undeclared activities, satellite imagery analysis (Fig. 10) and the estimation of optimal inspection strategies by statistics and game theory.

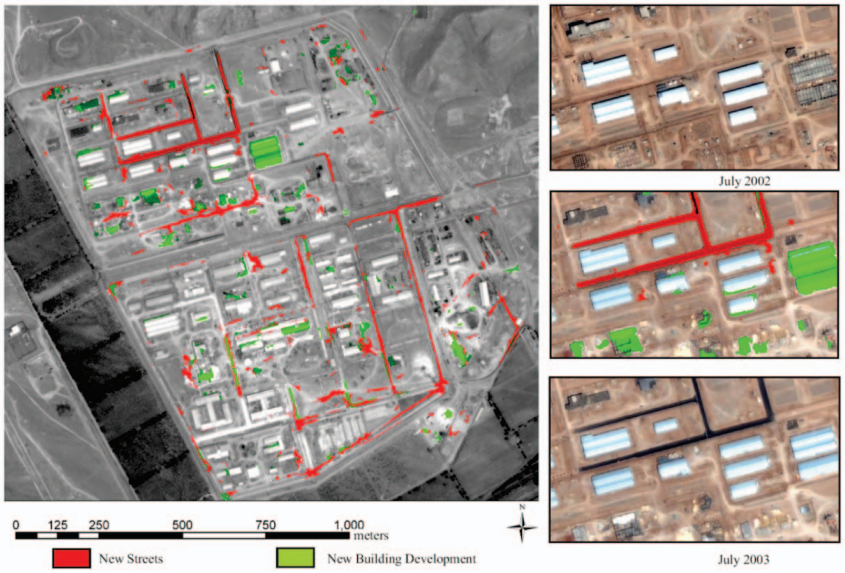

Fig. 10: Satellite imagery analysis.

Contact: Dr. Irmgard Niemeyer
i.niemeyer@fz-juelich.de

3.8. Product Quality Control of Radioactive Waste & Packages

Introduction

Product Quality Control is the examination of radioactive waste to “verify the compliance of waste properties with the acceptance criteria of a repository” (DIN 25401-9).

Already in the year 1985 the Product Quality Control Office for Radioactive Waste (PKS) has been installed at the Institute for Energy Research (IEK-6) on request of the German Federal Office for Radiation Protection (BfS). PKS advices and supports the BfS on the basis of §20 ATG (German atomic act) as an independent consulting expert group to verify the compliance of radioactive waste properties with repository relevant acceptance criteria. PKS renders expertise on technical methods for the conditioning and packaging of radiological waste and checks product quality control plans to be appropriate for the conditioning and disposal purposes. Moreover, PKS inspects reprocessing and conditioning plants, audits radwaste manufacturers and checks waste package inventory declarations and accompanying documentation prior to final disposal for the compliance with the required specifications and applicable relevant inventory limits. PKS also examines and assesses the methodological and analytical methods applied by the waste manufacturer. A large amount of PKS activities comprises the product quality control of radiological waste from the decommissioning of nuclear facilities, like phased-out nuclear power plants. The effect of product quality control contributes significantly to the safety of a nuclear waste repository.

Hosting the Product Quality Control Office for radioactive waste in Germany at the institute IEK-6 underlines its position in the field of waste characterization and in the evaluation of the long-term safety properties of radioactive waste to be acceptable for a repository in Germany.

PKS is organized two-fold:

1.) **PKS-WAA** is the sole group of experts authorized by BfS for the quality control of high- and medium-active nuclear waste from reprocessing facilities abroad (La Hague, France, and Sellafield, UK) and from the domestic high-level vitrification plant VEK of WAK Karlsruhe.

2.) **PKS-I** provides expertize for the BfS in the field of low- and medium-active German domestic waste from nuclear power plants, research institutions and Federal State Collecting Facilities to be characterized and prepared for final disposal. Basis for the quality control of waste & waste packages are the LAW / MAW Mine KONRAD waste acceptance criteria. This geological repository should be in operation in 2018.

3.8.1 Product Quality Control of Radioactive Waste – High Level Waste from Reprocessing

High-level radioactive waste requires specific care and attention for its very long-term and high radiotoxic potential. No decision on a conceivable “direct disposal” path for merely untreated high-level waste has yet been made in Germany. However, spent fuel dissolution for reprocessing has been employed until 2005, and still today residual vitrification methods are being used for the appropriate conditioning of high level waste from spent fuel of German nuclear power plants.

The expected result of nuclear waste product quality control is that all radioactive waste residues can be disposed of safely over a very long period of time. This is achieved by threefold tasks of the PKS-WAA team:

1.) **Waste conditioning process qualification:** to assess and evaluate the production processes applied to produce waste residues compliant with the officially approved waste properties and repository acceptance criteria.
2.) **Production process inspection and manufacturer’s auditing:** to make sure that all production is performed orderly within the production process guidelines and that only conform waste packages compliant with the well-defined product properties and repository acceptance criteria are being produced and prepared for their final disposal in Germany.
3.) **Documentation checking:** to assess all the documentation to accompany the waste residue packages and to check if all nuclear inventory declarations are correct, comprehensive and complete.

The PKS-WAA team, which are currently three scientists, two engineers, a Ph.D student and a project assistant, reports directly and solely to the authority in charge, the Federal Office for Radiation Protection (BfS). All reprocessing and vitrification of high-level waste residues and proportionate conditioning of the by-products are conformed in fully quality assured production processes at the reprocessing sites in La Hague in France, Sellafield in the UK and a domestic site at the WAK in Karlsruhe.

Fig. 11: Left: Documentation to verify the repository relevant properties. Right: Containers filled with vitrified and compacted waste.

Contact: Dr. Holger Tietze-Jaensch
h.tietze@fz-juelich.de

3.8.2 Product Quality Control of Low and Intermediate Level Radioactive Waste (LAW/MAW)

Radioactive waste products and waste packages have to be in compliance with the technical acceptance requirements for mine KONRAD. Repository-relevant features, radionuclide inventories and related activities as well as container parameters have to be documented and are checked by the independent experts of PKS-I.

LAW / MAW arises from nuclear power production, nuclear industry, research, medicine and technology as well as from the dismantling of nuclear installations. Accordingly, conducting a thorough and competent control and evaluation demands integrated competence in various scientific and engineering special fields. Often various technical details, complex issues and inter-relations as well as vast quantities of data have to be understood, analyzed, checked and evaluated by PKS-I. The results are summarized in written expert opinions and evaluation reports.

In executing its tasks as a Federal expert group the PKS-I in many ways is corresponding with waste producers, waste conditioning or interim storage facilities and nuclear companies, as well as nuclear licensing and supervisory authorities or government ministries of the individual German Federal States. Concerning the incineration of German LAW the control activities of PKS-I are not only limited to domestic plants but also include audits or inspections in foreign facilities, at present in France and Belgium and forthcoming in USA. Moreover, many radioactive isotopes or sealed sources used in Germany have been produced in the former Soviet Union. To be able to evaluate the completeness or reliability of corresponding waste declarations PKS-I maintains close links also to Russian organizations, in particular to Rosatom, JSC Isotop, and SIA 'RADON' (Moscow).

As a multidisciplinary group PKS-I in 2010 consisted of six scientists and engineers assisted by one office administrator. The lean management organization of PKS-I is divided into two areas of activity focusing either on "conditioning process qualification and documentation" or on "nuclear technology, nuclear reactors and computation". They are planned to be gradually completed by additional experts.

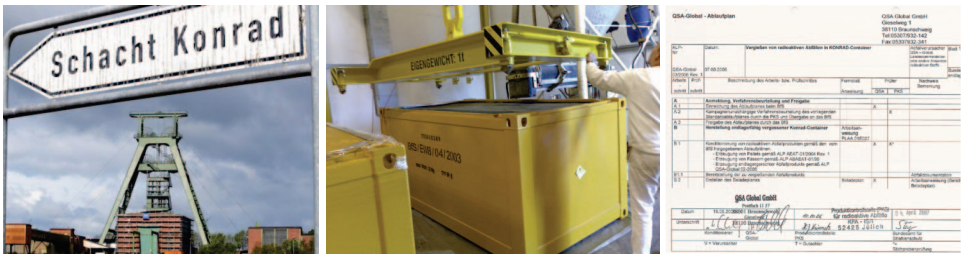

Fig. 12: Left: KONRAD repository. Middle: Container for KONRAD. Right: Quality control plan.

Contact: Dr. Hans-Jürgen Steinmetz
h.j.steinmetz@fz-juelich.de

4 Facilities

The institute operates several radiochemical laboratories (750 m^2) for experimental work with radioactive material including alpha emitters (actinides). About 500 m^2 are licensed according to the German Atomic Energy Act which permits the handling of nuclear fuels. One part of the controlled area is used for the development of non-destructive characterisation methods for radioactive waste applying neutron sources. In addition to the radiochemical laboratory equipment, the controlled area provides glove boxes which enable the handling of radioactive materials. Furthermore, analytical instruments, such as α-, β-, and γ-spectrometry, as well as x-ray diffraction, Raman spectroscopy and electron microscopy are available.

4.1. Electron Microscopy

ESEM (Environmental Scanning Electron Microscope)

The environmental scanning electron microscope Quanta 200 F from FEI (Fig. 13) is a high resolution field emission microscope, which is working at three vacuum modes: High vacuum: 10^{-2} - 10^{-4} Pa; Low vacuum: 10 - 130 Pa, and ESEM: up to 2700 Pa.

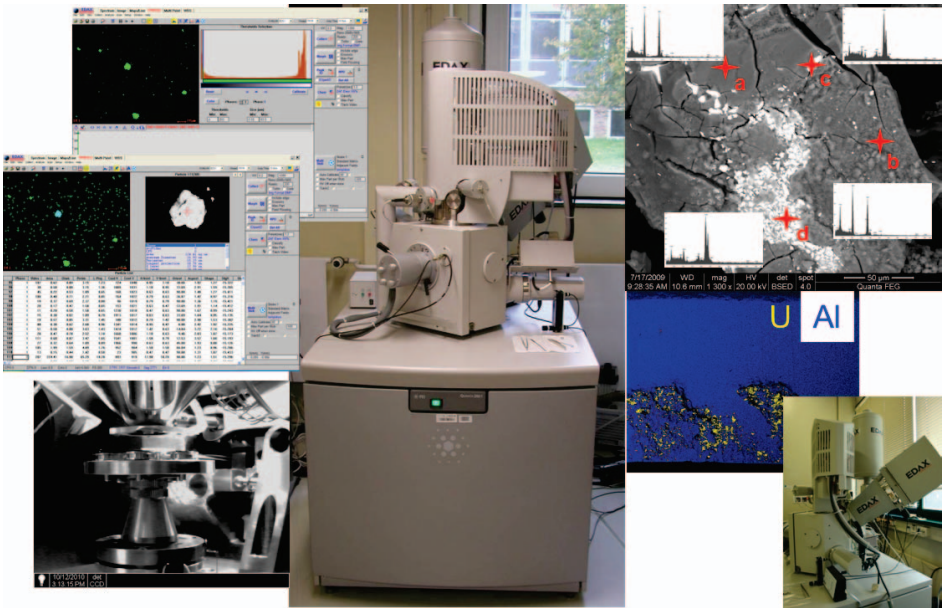

Fig. 13: Environmental scanning electron microscope Quanta 200 FEG.

The advantage of working at low vacuum is that a coating of the sample with an electrically conductive layer (e.g. C, Au) is not necessary. The investigation of wet samples is possible at ESEM-mode (in-situ wetting and drying, heating up to 55 °C and cooling down to -25 °C). The microscope is equipped with different detectors for secondary electron (SE) and backscattered electron (BSE) imaging at different pressures:

- Everhart Thornley SE-detector (high vacuum)
- Gaseous large field SE-detector (low vacuum)
- BSE-detector (high- & low vacuum)
- Gaseous analytical detector (GAD) BSE-detector (low vacuum)
- GSED (Gaseous secondary electron detector) SE-detector (ESEM)

For energy dispersive (EDS) investigations the Apollo X Silicon Drift Detector (SDD) from EDAX is installed with light element performance down to (and including) Boron. The resolution of the liquid nitrogen free detector is ≤ 131 eV for MnKα at 100.000 cps. Point and multipoint measurements, line scans, element mapping and particle analysis can be carried out with the genesis software.
For wavelength dispersive (WDX) measurements the TEXS LambdaSpec from EDAX is installed.

FIB (Focused Ion Beam)

The NVision 40 Cross Beam Workstation from Zeiss is a high resolution field emission GEMINI SEM combined with a high performance SIINT zeta FIB column and gas injection system (Tab. 1). An ensemble of detectors (In-column: EsB detector with filtering grid for BSE detection; In-lense: SE detector; chamber: Everhardt Thornley SE detector, 4Q BSE detector, GEMINI® multimode BF/DF STEM (Scanning Transmission Electron Microscopy) detector) allows high resolution investigations of the topography and morphology of the samples.

Tab. 1: Technical data of NVision Cross Beam Workstation

	SEM GEMINI column	**FIB SIINT 100 mm zeta FIB column**
Emitter	Schottky Field Emitter	Ga liquid metal ion source
Magnification	30 – 900,000x (20 kV)	475 – 500,000x (30kV)
Probe Current	4 pA- 20 nA	0.1 pA – 45 nA (30 kV)
Acceleration Voltage low voltage option	0.1 – 30 kV	1 – 30 kV, 1 - 5kV
Resolution	1.0 nm @ 15 kV, 1.5 nm @ 1 kV	4 nm @ 30 kV

Furthermore, the workstation is equipped with an INCA energy dispersive x-ray spectroscopy (EDS) and a Nordlys II Electron Backscattered Diffraction (EBSD) detector (Oxford Instruments). The combination of these detectors can be used for phase identification. EDS

provides chemical and the EBSD crystallographic and microstructural information, such as crystal orientation, grain boundary characterisation, and pole figures.
The main purpose of the FIB is the preparation of TEM lamella (Fig. 14) of ceramic materials containing radionuclides in order to investigate lattice parameters and the influence of radiation damages on the crystal structure. An integrated micromanipulator system allows an in-situ-lift-out of the TEM lamella.

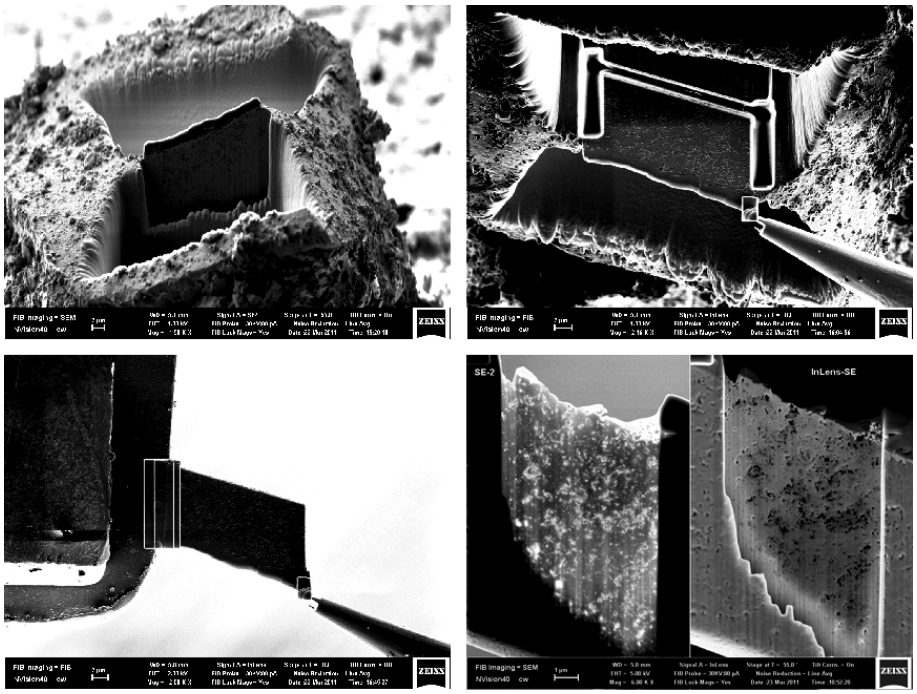

Fig. 14: TEM lamella preparation by FIB.

4.2. Raman spectroscopy

The IEK-6 runs a Horiba raman spectrometer LabRAM HR Vis (400 - 1100 nm, Fig. 15, left), currently equipped with a He-Ne laser (wave length λ = 632.81 nm, visible red light), an edge filter, two gratings (600 and 1800), focus length 800 mm, a peltier cooled solid state detector, three objectives (x10, x50 and x100) and a video camera for sample observation using reflected or transmitted visible light.
Two main applications are in the foreground according to raman spectroscopy at the IEK-6: fast phase identification (finger print method) and structure analysis with focus on short range order and medium range order, especially for irradiated (radiation damaged) samples. To this end, radioactive and non-radioactive samples can be measured alternatively with high precision and accuracy. Fig. 15 (right) shows e.g. the raman spectrum of a badly crystallized

$NdPO_4$ powder sample, directly received from hydrothermal synthesis. Even for such a sample good quality data can be obtained.
In the near future a second laser (λ = 785 nm, nodge filter) will be attached, in order to enable measurements on samples showing significant fluorescence signals at wave lengths below 785 nm.

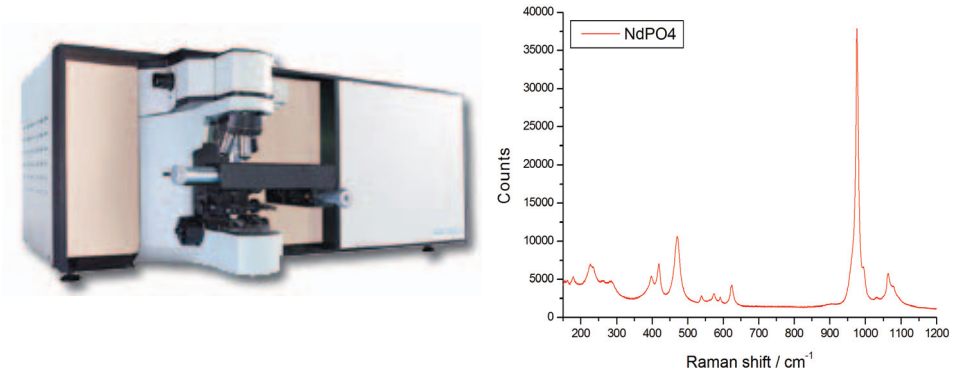

Fig. 15: Left: Horiba LabRam HR raman spectrometer. Right: Raman spectrum of $NdPO_4$ powder.

4.3. X-ray diffraction analysis

The IEK-6 runs two Bruker x-ray powder diffractometer. The first one (D8) is equipped with a copper tube (Cu K_α), a molybdenum tube (Mo K_α) and two suitable detector systems (scintillation counter and Si semiconductor detector), in order to perform x-ray diffraction analysis on crystalline, semi-crystalline and amorphous samples (Fig. 16, left). Radioactive and non-radioactive powder samples can be measured alternatively. Additionally, a climate chamber is available on request, that enables *in situ* measurements at different atmospheres and humidities and at temperatures up to 250°C.
The second diffractometer (D4) is equipped with a copper tube (Cu Kα) and a multi-sample stage (66 samples) as well as with a fast LynXEye detector, appropriate for high throughput measurements (Fig. 16, right). The D4 can also be used for any kind of analysis, with the exception of radial distribution function determination and *in situ* measurements using the climate chamber.
In principle all kinds of analysis can be performed by the structure research group according to x-ray diffraction: qualitative and quantitative phase analysis, cell constant determination, structure analysis, structure refinement (Rietveld) and the determination of radial distribution functions are possible.

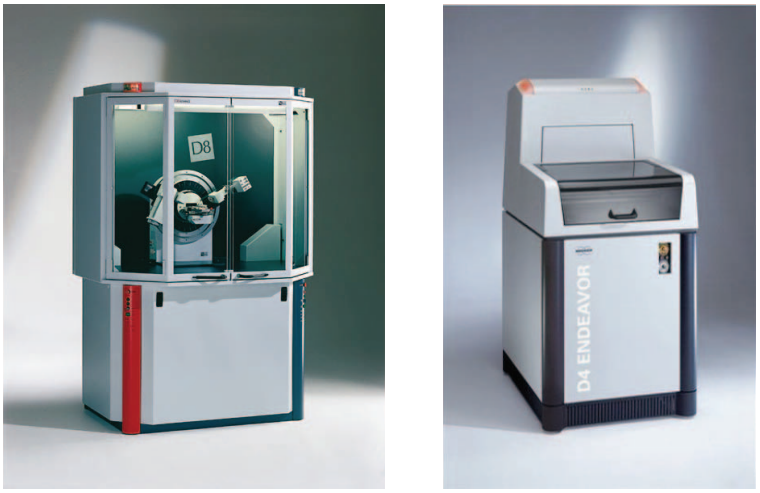

Fig. 16: Left: Bruker D8 X-ray powder diffractometer. Right: Bruker D4 X-ray powder diffractometer.

4.4. Hot Cell Facility, GHZ

In the Hot Cell building (GHZ) the hot cell line 1 is implemented (Fig. 17, left). This cell line has a length of 32 m and is divided into five working cells. The shielding consists of 110 cm of concrete.

One working hot cell (hot cell number 601, Fig. 17, right) in the hot cell line 1 can be used by the IEK-6. Hot Cell 601 has a length of 3 m and a volume of 60 m^3. Two manipulators are attached at each of the two cell windows. Hot Cell 601 is connected to an isolation cell and it is possible to bring in equipment up to a weight of 6 tons. A glove box is attached at the top of the hot cell and allows to bring in or out small devices or samples.

At the moment this cell is in preparation for leaching investigations of spent fuel samples. Also a Raman spectrometer will be connected to perform in-situ measurements.

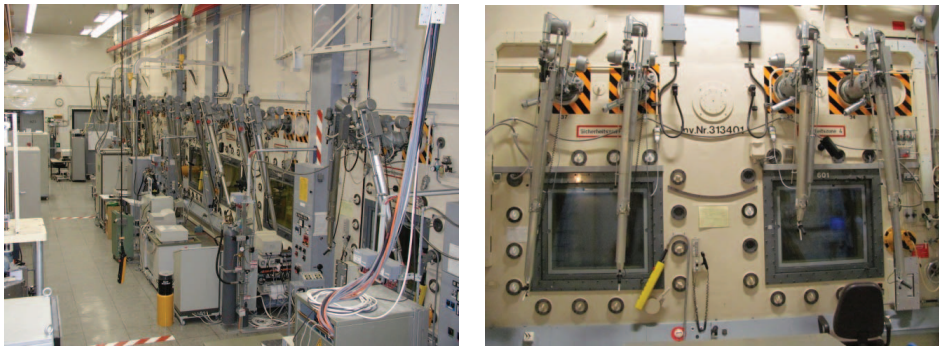

Fig. 17: Left: Hot Cell line 1. Right: Operation front of the hot cell 601.

4.5. Non-destructive assay testing

Segmented Gamma-Scanner GERNOD II.

The Segmented Gamma-Scanner GERNOD II is used for the characterization of 200-l or 400-l drums radioactive waste with wide range of matrices and isotopic compositions. The Gamma-Scanner consists of a mechanical part, a control unit, a detection system and a system unit and operator interface. The mechanical system consists basically of a turntable to accommodate different waste drums (max. weight 6000 kg) and a platform for the vertical movement of the gamma detection and collimation unit. The driving units comprise stepping motors with superior positioning capabilities. The positioning of the drum and detector is handled by a SPS control unit. This offers superior positioning capabilities together with highly reliable performance and control of the system status. Scanning programs are performed either continuously (fast measurements) or in a step by step mode (long time measurements). The detection of gamma emitting nuclides is performed by an HPGe detector connected to a digital spectrometer for signal processing and data acquisition. The detector can be used together with different collimators depending on the type of application. A dose rate meter is attached to the detector to record the dose rate at the surface of the drum over the whole assay period. All routine operator interactions are carried out via a PC-based control system using the software SCANNER32 developed in cooperation with a professional software engineering company for ease operations and reliable data handling.

Transmission and Emission Tomography System

The Transmission and Emission Tomography System developed at IEK-6 is an advanced tool for the characterization of 200-l radioactive waste drums. The radiation emitted from a Co-60 transmission source (200 GBq in DU shielding) is collimated in the direction of 4 fast scintillation detectors located in the detector collimation shielding bank to perform 4 transmission measurements at the same time. Meanwhile, the 3 HPGe-detectors are used for the emission measurements of the waste drum. An irradiation of these detectors by the transmission source is avoided by the source and detector collimation. Two stepping motors move the drum horizontally and rotate it between two measurement steps respectively. On the data collected for each measurement a pulse height analysis is performed. This leads to the basic data sets for the algorithms used for Transmission Computer Tomography, Emission Computer Tomography and Digital Radiography.

MEDINA

MEDINA (Multi-Element Detection based on Instrumental Neutron Activation) is an innovative analytical technique based on prompt and delayed gamma neutron activation analysis for non destructive assay of 200-L waste packages.

4.6. Radiochemical analytics

- **LSC (Liquid Scintillation Counter):**
  Analysis of aqueous and organic samples
  Quantulus (PerkinElmer), Autosampler, Ultra low activity determination, determination of environmental activity (14C), α,β discrimination
  TRI-CARB 2020 (PerkinElmer) Autosampler > 100 samples
- **α-spectrometry:**
  Qualitative and quantitative analysis of α-emitter, Si-detector, low level detection
- **γ-spectrometry:**
  HP Ge-detector (N_2-cooled), NaI-detector, LaBr-detecor, Radionuclide detection with low γ-energy (^{55}Fe: E_γ < 5.9 kEV), low level detection, borehole detector

4.7. Miscellaneous

- ICP-MS ELAN 6100 DRC (PerkinElmer SCIEX)
- STA 449C Netzsch
- FTIR-spectrometer: Equinox 55 (Bruker), KBr-pellets, ATR (attenuated total reflection), TGA
- Dilatometer DIL 402C (Netzsch)
- Induction furnace (Linn High Therm GmbH), max. temperature 2500 °C, mass spectrometer for analysis of combustion gases
- High temperature furnace HTK 8 (GERO GmbH), max. temperature 2200 °C
- Vacuum hot press HP W 5 (FCT Systeme), max. temperature 2200 °C, press capacity max. 50 kN, 5 x 10^{-2} mbar
- BET AUTOSORB-1 (Quantachrome Instruments)
- Spectral photometer CADAS 100
- Granulometer CILAS 920
- Autoclaves
- Gas chromatography (Siemens AG)

5 Scientific and Technical Reports 2009/2010

5.1. Radionuclide release from research reactor fuel

H. Curtius, G. Kaiser, E. Müller

Corresponding author: h.curtius@fz-juelich.de

Abstract

In order to determine the corrosion behaviour and the radionuclide release fractions of different irradiated research-reactor fuel-types in final repository relevant solutions investigations in a hot cell facility were performed. The dissolution of two dispersed research reactor fuel-types (UAl_x-Al and U_3Si_2-Al) was studied in $MgCl_2$-rich salt brine in the presence of Fe^{2+}-ions. Both fuel types corroded within the experimental time period of 3.5 years completely. In comparison, LWR spent fuel corroded only up to 0.01 % under comparable conditions after 2 years. After complete corrosion of the used research reactor fuel samples the inventories of Cs and Sr were detected in solution quantitatively. Solution concentrations of Am were lower than the solubility of $Am(OH)_3$ (s) and may be controlled by sorption processes. Pu concentrations may be controlled by Pu(VI), Pu (V) and Pu(IV) (hydr)oxides. Solution concentrations of U were within the range of the solubility limits of uranite. In comparison of both fuel samples the determined solubilities of U, Pu and Am were about one order of magnitude higher for the U_3Si_2-Al fuel sample. Here the formation of U/Si containing secondary phase components and their influence on radionuclide solubilities cannot be ruled out.

Introduction

The final disposal of spent nuclear fuel in deep geological formations is considered as waste management option. In comparison to commercial spent fuel elements (UO_2 is the fuel) used in nuclear power plants, different spent research reactor fuel-types exist. At IEF-6 the work is focused on research reactor fuel. Two different fuel-types (a dispersed metallic UAl_x-type and the U_3Si_2-Al-type) are under investigation. One back-end option for these fuel-types is final disposal [1]. Possible repositories under consideration are salt and clay formations. Clay formations always contain clay pore waters. For salt formations the contact of spent fuel with an aquatic phase is a hypothetical scenario which is taken into account with respect to long-term safety analysis. These saline solutions will then start to corrode the steel canister and then the fuel cladding while producing large amounts of hydrogen. Also radiolysis of aqueous solutions is accompanied by the formation of redox agents [2]. In salt brines, H_2 molecules are the main reductants whereas radiolytic oxidants are dominated by oxo-halogenides [2].
In the presence of hydrogen overpressure the oxidative dissolution of LWR spent fuel, (consists of UO_2 as fuel cladded with Zircalloy), is decelerated. Only 0.01% of this fuel type corroded in a concentrated salt solution in the presence of container material (iron) in 2 years [3].
Under comparable conditions this paper describes for the first time the corrosion behaviour of two different irradiated dispersed research reactor fuel-types in a highly concentrated salt brine at 90 °C under static conditions in the presence of Fe^{2+}.

Experimental details

Static corrosion tests were performed under anoxic conditions in Ar-atmosphere in a hot cell facility at 90°C using glass autoclaves. Two different irradiated research reactor fuel types were used: a.) metallic UAl_x-fuel (fifa: 45%) and b.) U_3Si_2-fuel (fifa: 63%). Details with respect to the fuel dimension, fuel mass and radionuclide inventories are given in Tab. 2 and Tab. 3. Solutions were sampled under Ar-atmosphere nine times per test and at test termination after 3.5 years. Gas sampling was performed nine times per test. More details and the analytical procedure are given in detail in [4].

Tab. 2: Details of the dispersed research reactor fuel samples.

	U_3Si_2-fuel sample	UAl_x-Al-fuel sample
Mass of U (g) before irradiation	1.93	0.28
^{235}U enrichment (%) before irradiation	19.75	80
Date of irradiation end	13.03.1985	17.06.1990
Burn up (fissions per initial fissionable ^{235}U atoms) in (%)	63	45
Mass of the sample (g)	4.5	3.4
Dimension (mm)	40 x 20 x 1.27	40 x 20 x 1.37
Mass of Al (g)	2.66	3.2
Mass of U (g)	1.7	0.19
Mass of Si (g)	0.13	

Tab. 3: Radionuclide inventory of the fuel samples (reference date: 15.05.2009).

Isotope	U_3Si_2-fuel sample Activity (Bq)	UAl_x-Al-fuel sample Activity (Bq)
^{134}Cs	1.19×10^{7}	1.63×10^{7}
^{137}Cs	2.01×10^{10}	4.92×10^{9}
^{154}Eu	2.81×10^{6}	1.50×10^{7}
^{3}H	1.55×10^{6}	1.91×10^{7}
^{90}Sr	1.54×10^{10}	4.42×10^{9}
^{238}Pu	1.95×10^{6}	2.50×10^{5}
$^{239/240}Pu$	6.80×10^{6}	8.31×10^{4}
^{241}Am	2.21×10^{6}	3.71×10^{4}
^{234}U	5.59×10^{3}	2.23×10^{4}

Results and Discussion

The irradiated UAl_x-Al and U_3Si_2-Al fuel samples corroded completely within the 3.5 years of the experimental time period. Due to the corrosion processes secondary phases were formed. Hydrogen was produced due to the corrosion of the fuel cladding and due to radiolytic processes. The complete amounts of hydrogen were determined to be in the range of 0.11 mol. At test termination the measured pH-values were in the range of 5.0 (corrected value according to [5]).

In Fig. 18 the radionuclide concentrations after complete corrosion of dispersed UAl_x-Al and U_3Si_2-Al fuels in $MgCl_2$-rich brine are summarized. The amounts of Sr in solution represent the amount of the initial Sr inventories with respect to both fuel samples. The Sr release is considered to be the indicator of the progress of matrix dissolution, hence if the complete Sr inventory is in solution the fuel did dissolve completely. This is based on the assumption that the Sr inventory is contained in the fuel matrix, where it is distributed homogeneously. The corrosion rates were determined to be 1.76 g/m^2d for the UAl_x-Al fuel sample and 2.34 g/m^2d for U_3Si_2-Al fuel sample.

The final U concentrations for both fuel types were determined to be 10^{-8} to 10^{-7} M (pH 5). The solubility of $U(OH)_4$ (am) under comparable conditions in a 5.6 M NaCl solution [6] was determined to be in the range of 10^{-9} to 10^{-7} M. Therefore the assumption can be drawn that the component $U(OH)_4$ (am) is the main U containing phase present. The solubilities of hexavalent U components like metaschoepite (UO_3 $2H_2O$(cr)) or Na-diuranate ($NaUO_2O(OH)$(cr) are significant higher and do not agree with the measured U solubilities in these experiments, hence the presence of these phases may be ruled out.

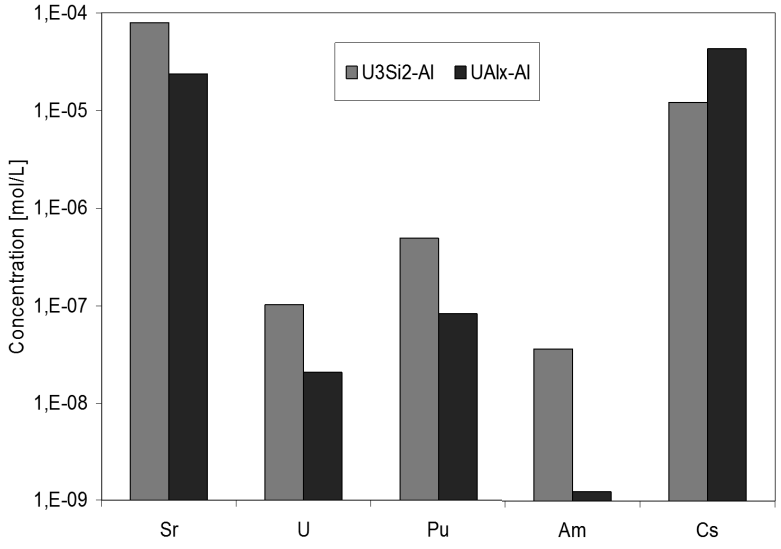

Fig. 18: Final solution concentrations of various radionuclides after corrosion of the dispersed UAl_x-Al and U_3Si_2-Al fuels in $MgCl_2$-rich brine under initial Ar atmosphere.

Nevertheless in the case of the U_3Si_2-Al-fuel different U components can be formed. It was observed during corrosion of UO_2 in spent fuel under reducing conditions that coffinite

($USiO_2$ 2 H_2O) may form [7]. Also coffinite may not be the only phase replacing uranite and spent fuel under these conditions. Recently an unnamed uranium silicate with a stoichiometry close to U_3SiO_8 has been reported [6]. In conclusion that means that in case of the U_3Si_2-fuel corrosion under reducing conditions the presence of these alteration products may not be ignored.
The measured Pu concentrations were in the range of 10^{-7} to 10^{-6} M (pH=5). As observed in other studies these concentrations might describe a mixture of Pu-IV, Pu-V and Pu-VI hydro (oxy) species [6].
The determined final Am concentrations for the UAl_x-Al fuel sample was about 10^{-9} M and about 10^{-8} M for the U_3Si_2-Al sample. These values are lower as the solubility of amorphous Am $(OH)_3$(s). Runde [8] measured that amorphous Am $(OH)_3$(s) is expected as solubility controlling phase in high concentrated salt solutions and the solubility of amorphous Am $(OH)_3$(s) was determined to be about 10^{-7} M. Processes which may retain Am are coprecipitation with secondary U phases and sorption on iron corrosion products.
In general the concentrations for the radionuclides U, Pu and Am were determined to be about one order of magnitude higher for the used U_3Si_2-Al fuel sample in comparison to the UAl_x-Al fuel sample. As discussed above the formation of U and Si containing solids as corrosion products cannot be excluded. These U/Si containing solids may influence the radionuclide concentrations through their solubilities and their retention capacities.

Conclusion and Outlook

Results of this work confirm the instantaneously corrosion of the research reactor UAl_x-Al and U_3Si_2-Al fuel types within the test period of 3.5 years in the presence of iron-II and in the $MgCl_2$-rich brine. The complete corrosion of the fuel samples was confirmed by the final Sr concentration in solution which represented the initial complete Sr inventory in the fuel. Especially the concentration of the trivalent actinide Am in solution is orders of magnitude lower than the solubility of pure Am(III) hydroxide phase and appear to be controlled by co precipitation phenomena. Comparing the behaviour of both fuel-types an influence of Si was observed. In the presence of Si the solubilities of U, Pu and Am are one order of magnitude higher. This can be due to the formation of U/Si containing solids.
Further research is recommended to determine the influence of Si in detail. The synthesis of coffinite, the determination of its solubility and the formation of solid solutions with trivalent actinides are aspired.
In conclusion, both investigated dispersed research reactor spent fuel samples completely dissolve in $MgCl_2$-rich brine in the presence of Fe^{2+} within the time period of 3.5 years. In view of the long-time scale of final disposal, this means that the radionuclides which were embedded in the fuel matrices were mobilized instantaneously. The complete inventory of Cs and Sr was found in solution. Hence, these radionuclides were classified as mobile species. To contribute to performance assessment calculations the estimation of the boundary conditions for radionuclide release from the so-called “source term” must be known. From the present results, under the experimental conditions used, clearly Cs and Sr can be regarded as mobile species. In contrast, the low concentrations of U and Pu in solution seemed to be determined by their solubility controlling solid phases. This result shows, that secondary phases which could be formed during the contact with groundwater, inhibit further radionuclide migration. For the long-lived actinide Am and for the lanthanide Eu the observed reimmobilization might be dominated by sorption on the formed secondary phases. Future

work will focus on the identification of these secondary phases in detail. This knowledge is needed in order to give reliable contributions to the radionuclide source term.

References

[1] Thamm, G.: Disposal of irradiated fuel elements from German research reactors – Status and Outlook; Trans. Int. Conf. Research Reactor Fuel Management (RRFM 1999), Bruges, Belgium, 159 (1999).

[2] Metz, V., Loida, A., Bohnert, E., Schild, D., Dardenne, K., Effects of hydrogen and bromide on the corrosion of spent nuclear fuel and γ-irradiated UO2(s) in NaCl brine, Radiochim. Acta 96, 637 (2008).

[3] Loida, A., Grambow, B., Geckeis, H., Anoxic corrosion of various high burnup spent fuel samples, Journal of Nuclear Materials, 238, 11 (1996).

[4] Curtius, H., Kaiser, G., Paprigas, Z., Ufer, K., Müller, E., Enge, R., Brücher, H., Untersuchungen zum Verhalten von Forschungsreaktorbrennelementen in den Wirtsgesteinsformationswässern möglicher Endläger, Berichte des Forschungszentrums Jülich, 4237, ISSN 0944-2952. (2006).

[5] Grambow, B., Müller, R., Chemistry of corrosion in high saline brines, Mater. Res. Soc. Symp. Proc. 176, 229 (1990).

[6] Loida, A., Grambow, B., Geckeis, H., Dressler, P., Process controlling radionuclide release from spent fuel, Mat. Res. Soc. Symp. Proc. 353, 577 (1995).

[7] Janeczek, J., Ewing, R.C., Coffinitization – A Mechanism for the Alteration of UO2 under Reducing Conditions, Mat. Res. Soc. Symp. Proc. 257, 497 (1992).

[8] Runde, W., Zum chemischen Verhalten von drei- und fünfwertigen Americium in salinen NaCl-Lösungen" Dissertation, Technische Universität München (1993).

5.2. Separation and enrichment of secondary phases of research reactor fuel elements and identification by SEM-EDX

M. Klinkenberg, H. Curtius

Corresponding author: m.klinkenberg@fz-juelich.de

Abstract

The corrosion products of research reactor fuel elements of the UAl_x-Al- and U_3Si_2-Al-type in $MgCl_2$-rich brine were investigated. This study contributes to the long-term safety analysis of directly disposed research reactor fuel elements in deep geological repositories (salt formations) because secondary phases may serve as a barrier against radionuclide migration. For a better identification of the secondary phases a sample treatment is necessary. Therefore, a grain size fractionation was carried out and different solvents were used to enrich single secondary phases. Chemical as well as phase characterisation of the secondary phases was accomplished.

Introduction

In contrast to UO_2 fuel elements which are used in commercial nuclear power plants, research reactor fuel elements are composed of metallic UAl_x-Al or U_3Si_2-Al. Batch-type corrosion experiments with non-irradiated dispersed metallic UAl_x-Al- and U_3Si_2-Al fuel in highly-concentrated synthetic $MgCl_2$-salt brine were performed [1]. The fuel elements corroded within a few months. Previous studies showed that the radionuclides were rapidly mobilized during the corrosion process, but subsequently trapped by secondary phases [2].
In order to improve the identification and quantification of these secondary phases, an enrichment of single phases is necessary. The identification by XRD is difficult due to the high amount of amorphous phases and overlapping peaks of phases like bischofite ($MgCl_2 \cdot 6\ H_2O$) which derive from the brine, as well as a high water content of the samples. The main topic of this study is the morphological and chemical characterisation of the obtained grain size fractions by SEM/EDS.

Experimental details

Sample preparation and enrichment of secondary phases – Corrosion investigations were performed with UAl_x-Al and U_3Si_2-Al fuel element plates under Ar-atmosphere in 400 mL $MgCl_2$-rich salt-brine (Tab. 4) at 90 °C. Additionally, 10 g $Fe(II)Cl_2 \cdot 4\ H_2O$ was added to simulate the presence of Fe due to the corrosion of the container.

Tab. 4: Chemical composition of the brine [3].

Ca [mol/L]	Cl [mol/L]	K [mol/L]	Mg [mol/L]	Na [mol/L]	SO_4 [mol/L]	pH corr.
0.2690	9.8456	0.0190	4.6014	0.0706	0.0005	6.03

For the enrichment of single phases a method was adopted which is successfully applied in soil science and clay mineralogy [4]. The grain size fractions > 63 µm, 2 - 63 µm, and < 2 µm of the samples were obtained by wet sieving and the use of Atterberg cylinders.

Different solvents (iso-propanol and water) were used in order to dissolve interfering phases e.g. bischofite or other salts remaining from the brine. The obtained substances were characterized by ICP-OES, LSC, alpha-spectrometry, and SEM/EDS.

Chemical analysis – The chemical composition of the untreated sample (liquid and solid phase) was determined. For the determination of Al and Fe, ICP-OES was used. The U content was determined from activity measurements by LSC and alpha-spectrometry.

Scanning electron microscopy (SEM) – For the characterisation of the solid corrosion products SEM combined with EDS (energy dispersive x-ray spectroscopy) was used. The environmental SEM Quanta 200 F manufactured by FEI and equipped with the EDX-system Genesis (EDAX) was used for the investigations. Samples were prepared as powders/grains on carbon tabs and measured in low-vacuum mode.

Results

Chemical composition – The results of the Al determination show that for all samples only a minor amount of Al is dissolved in the aqueous solution (1 - 2 wt.-% ± 0.5 wt.-%). Hence, Al is determined to be in the solid state.
About half of the iron (53 - 60 wt.-% ± 5 wt.%) is dissolved in the liquid phase.
Only a minor amount of U is dissolved in the aqueous solution (3 wt.-% ± 0.5 wt-%). The measurements of the U content reveal that U is dissolved, first, but then re-precipitated.

Characterisation by SEM/EDS – An overview of typical crystalline phases and their morphologies, which were observed for secondary phases in the obtained fractions by SEM are shown in Fig. 19. The left column shows secondary phases of UAl_x-Al fuel and the right column of U_3Si_2-Al fuel, both corroded in $MgCl_2$-rich brine. For both systems similar secondary phases could be identified.

a & f) Cubic crystals consisting of Al, Cl, and O. b) A6 2008 iso-propanol < 2 µm; g) A8 2008 iso-propanol > 2 µm. According to the morphology and chemical composition this phase is identified as lesukite ($Al_2(OH)_5Cl{\cdot}2H_2O$). This phase only occurs in iso-propanol treated samples.

b & g) Thin platy crystals, which build up a sand rose structure. These crystals are composed of Al, Mg, O, and Cl. b) A6 2008 iso-propanol > 63 µm, g) AA11 2008 iso-propanol > 63 µm. The morphology and the chemical composition are typical for MgAl-LDHs (layered double hydroxide). This phase occurs in both, water and iso-propanol treated samples.

c & h) The bright area of the large aggregates consists of U associated with Al and in case of the U_3Si_2-Al fuel of additionally Si (uncorroded fuel). These phases occur in both, water and iso-propanol treated samples. In case of water treated samples, these U-phases are surrounded by other secondary phases, mostly Al-oxides/hydroxides. c) A6 2008 H_2O > 63µm, d) A8 2008 H_2O > 63 µm.

d & i) Platy crystals of Fe-phases consisting of Fe, O, and Cl. d) AA6 2008 iso-propanol > 63 µm; i) AA11 2008 iso-propanol > 63 µm). These phases occur in both, water and iso-propanol treated samples but the content is higher in iso-propanol treated samples.

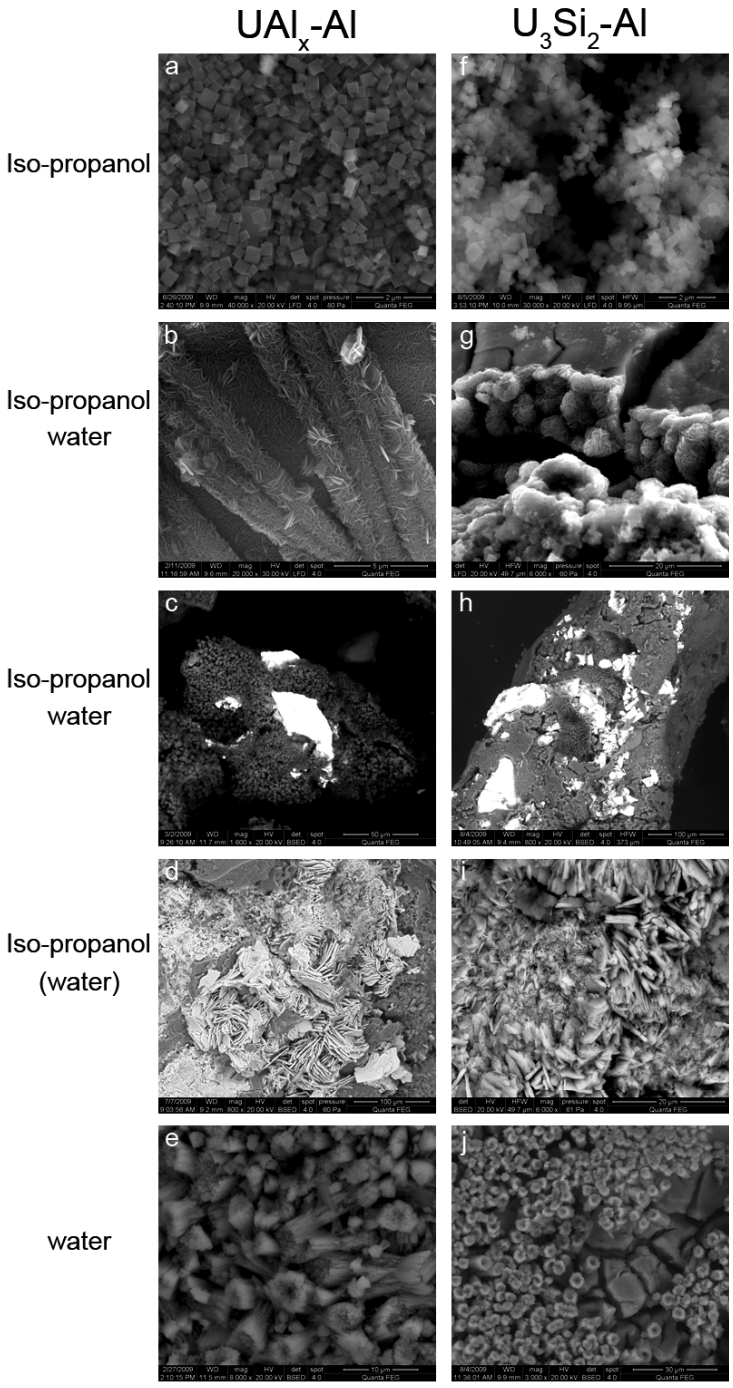

Fig. 19: Typical secondary phases of UAl_x-Al (left column) and U_3Si_2-Al (right column) fuel corroded in $MgCl_2$-rich brine a & f) Lesukite; b & g) MgAl-LDH; c & h) UAl_X and U_3Si_2-Al (white); d & i) Fe-phases; e & j) Al-oxide/hydroxide.

e & j) Aggregates of aluminium oxides/hydroxides consisting of Al and O. These phases only occur in water treated samples. c) A6 2008 H_2O > 63 µm; h) A8 2008 H_2O > 63 µm).

For the **iso-propanol treated samples** the following minerals could be identified: MgAl-LDH, lesukite, Fe-phases, U associated with Al and in case of the U_3Si_2-Al fuel additional Si (uncorroded fuel) in coarser aggregates. An enrichment of iron-minerals could be observed in the 2-63 µm fraction. Lesukite is enriched in the < 2 µm fraction. For the **water treated samples** an enrichment of Al-oxides/hydroxides, particularly in the < 2 µm fraction, could be observed. Only traces of LDH could also be found. Lesukite is completely dissolved by the water. Furthermore, small amounts of Fe-phases and uncorroded fuel occur.
An additional EDS-analysis of the < 2 µm fractions of the differently treated samples was performed. Several areas of different sites of the samples were measured, quantified, and mean values were calculated for the element contents. Salts like bischofite deriving from the brine were dissolved. The iso-propanol treated sample shows higher concentrations of Cl. Furthermore, Fe is enriched. The water treated samples show lower amounts of Mg and Cl and accordingly higher concentrations of Al and O. Due to the higher solubility of water, lesukite was dissolved completely. These results underline and confirm the observations made by SEM.

Conclusions

Due to the sample treatment various crystalline phases could be enriched successfully, which lead to a better identification of the secondary phases. From the results of the chemical investigation of the samples can be concluded, that Al and U are dissolved and re-precipitated. Hence, they are only present in the solid. The solid-phase characterisation by SEM/EDS after treatment and enrichment suggests that the following crystalline secondary phases are identified: MgAl-LDH, lesukite, Al-oxide/hydroxide, and Fe-phases. Furthermore, traces of uncorroded fuel UAl_x-Al and U_3Si_2-Al could be found. The next step will be the quantification of the crystalline secondary phases by XRD and the Rietveld method.
A high amount of amorphous phases (approximately 50 wt.-%) is contained in the samples, as well. It is assumed that U is also associated to these amorphous phases. To clarify the binding mechanisms of U, a characterisation and quantification of the amorphous phases will follow in further investigations.

References

[1] Brücher, H., Curtius, H., Fachinger, J., Kaiser, G., Mazeina, L., Nau, K.: Untersuchungen zur Radionuklidfreisetzung und zum Korrosionsverhalten von bestrahltem Kernbrennstoff aus Forschungsreaktoren unter Endlagerbedingungen, Report Forschungszentrum Jülich, Jül-4104, ISSN 0944-2952 (2002).

[2] Mazeina, L., Curtius, H., Fachinger, J., Odoj, R.: Characterisation of secondary products of uranium-aluminium material test reactor fuel element corrosion in repository-relevant brine, J. Nucl. Mater. 323, 1 (2003).

[3] B. Kienzler, A. Loida, (Hrsg.), Endlagerrelevante Eigenschaften von hochradioaktiven Abfallprodukten – Charakterisierung und Bewertung – Empfehlungen des Arbeitskreises HAW-Produkte; Wissenschaftliche Berichte FZKA 6651, Institut für Nukleare Entsorgungstechnik, Forschungszentrum Karlsruhe, (2001).

[4] Hiltmann, W. & Stribrny, B.: Tonmineralogie und Bodenphysik. Handbuch zur Erkundung des Untergrundes von Deponien und Altlasten, Band 5. BGR, Bundesanstalt für Geowissenschaften und Rohstoffe. ISBN 3-540-59465-5 Springer-Verlag (1998).

5.3. XRD-analysis of secondary phases formed under final repository conditions due to corrosion of UAl_x-Al research reactor fuel elements

A. Neumann, M. Klinkenberg, H. Curtius

Corresponding author: an.neumann@fz-juelich.de

Abstract

Corrosion experiments of unirradiated research reactor fuel elements were carried out under repository relevant conditions in order to identify and quantify the secondary phases formed by reactions with formation waters being expected in final repositories due to accidental influx from the encompassing salt formation. This analysis is important for safety assessment issues as such phases may act as a barrier against the migration of the released radioactive inventory. XRD measurements and Rietveld analysis were the major methods being applied for identification and quantification of crystalline and amorphous amount of the corrosion products.

Introduction

The final disposal of high radioactive waste of spent nuclear fuel of research reactors in deep geological formations is a very challenging task as its safety and sustainability has to be preserved for very long periods. To rule out the exposure of this hazardous material possible scenarios have to be considered which may lead to the release of the radioactive inventory disposed in a geological repository.

One of these events considered is the influx of formation waters which will corrode the waste package and facilitate the migration of the radioactive inventory outwards of the repository [1]. The chemical composition of the formation waters leading to the containment failure are strongly determined by the geology which walls the final repository. Considered favoured candidates for hosting nuclear waste are salt and clay formations.

An additional barrier to keep the radioactive isotopes fixed is represented by the corrosion products themselves. These secondary phases could immobilize the repository relevant isotopes by sorption processes. This assumption has clearly been demonstrated by hot cell experiments carried out with irradiated research reactor fuel elements and synthesized LDH compounds [2].

As the degree of immobilisation of radioactive isotopes depends on the amount of the compounds being formed in situ and/or backfilled as additional technical barrier it is necessary to identify the secondary phases and to quantify their abundances as well. Laboratory corrosion experiments under repository relevant conditions therefore have been carried out with unirradiated UAl_x-Al research reactor fuel elements in magnesium chloride rich salt brine (Type Brine 2). After the termination of the experiments the solid phases are pre-treated, prepared, and subjected to the XRD and Rietveld analysis firstly for the identification of the crystalline compounds and secondly to assess their quantity and the content of amorphous phases as well.

Experimental details

The corrosion experiments of UAl_x-Al fuel elements have been carried out in glass autoclaves which contain the salt brine of definite composition. In order to simulate the corrosion of the iron waste package $FeCl_2 \cdot 4H_2O$ has additionally been added. The experiments were carried out at 90°C and under an atmosphere being free of carbon dioxide and oxygen. The autoclaves are shown in Fig. 20.

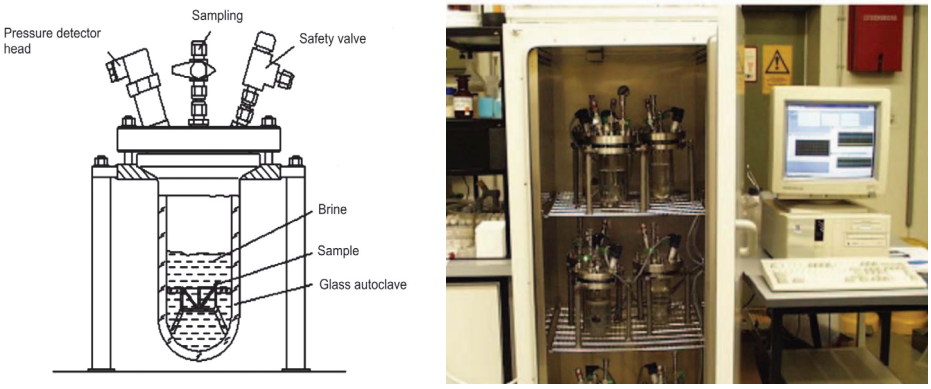

Fig. 20: Experimental setup of the corrosion experiments of unirradiated UAl_x-Al fuel elements: Left: Schematic autoclave setup. Right: Experimental autoclave setup.

After the termination of the corrosion experiments the solids were pre-treated with isopropanol and then dried. As subsequent procedure the solids were subjected to the grain size separation. This was done by sieving and by the application of the Atterberg method in order to gain fractions > 63 µm, 2 – 63 µm, and < 2 µm. More details about the technical setup and the sample pre-treatment is given elsewhere [2].

Before the XRD analysis these different grain size fractions of the secondary phases were afterwards intimately mixed with an internal zincite standard of known weight in order to assess the amount of each crystalline phase and the amorphous content as well by the Rietveld method [3].

For the XRD measurements it has to be assured that the samples were under an inert atmosphere while they were exposed to the X-rays. This was realized by the application of a climate chamber which is shown in Fig. 21.

The dedicated atmosphere was established by an inert gas flow of Nitrogen through the climate chamber. For the XRD measurements $Cu_{K\alpha}$ radiation (λ_1 = 1,54059 Å) was applied. The gained intensity was generally registered by a NaI scintillation point detector on the one hand and on the other hand with the VÅntec line detector when the gaining of huge amounts of intensity within long term measurements was important. To account for the iron fluorescence or any other parasitic radiation like $Cu_{K\beta}$ a graphite monochromator or a nickel foil filter was applied for their suppression.

For the accurate determination of the crystalline and amorphous phase content the particle dimensions of the different grain size fractions have to be measured precisely [4]. Therefore isopropanol suspensions of each fraction were subjected to supersonic treatment for homogenisation reasons and afterwards prepared for REM analysis. With image analysis

software the average diameter of the particles were determined. The REM analysis was also applied for the characterisation of the morphology of the secondary phases. In order to analyze details of the surface of dedicated phases high resolution TEM has been additionally applied.

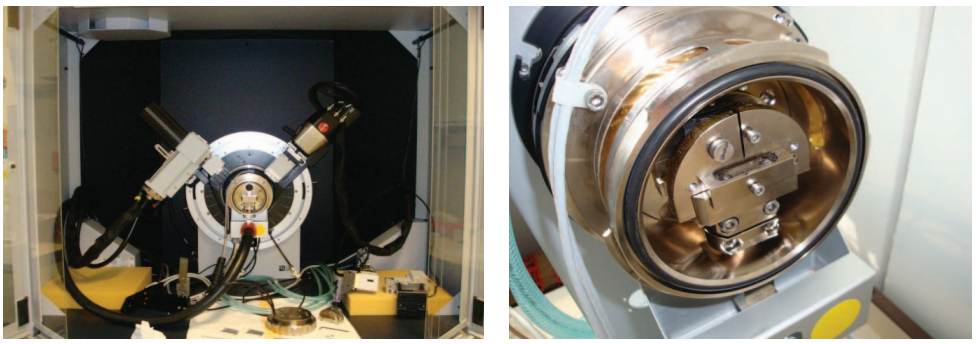

Fig. 21: Climate chamber with open sample housing: Left: Climate chamber mounted on the diffractometer. Right: Close up of the unmounted climate chamber.

Results

Due to Bragg's Law [5] crystalline phases show in dependence of the scattering angle 2θ peak unique positions which can normally be assigned to the dedicated compounds being present in the sample. This relation for the identification of the secondary phases was applied by using a database comprising numerous entries with phase specific peak positions. Fig. 22 shows exemplarily the diffractogram of the fraction < 2 µm. In detail the registered intensity in square root scale is plotted versus the angle 2θ. The coloured vertical bars represent the powder database entries which could be assigned to the observed peak positions.

Most of the observed peak positions could be assigned to Lesukite (green bars in Fig. 22). For the minor phases three additional database entries could be assigned which were not covered by the Lesukite entries of the database. The peak positions could be assigned to the iron containing phase Akaganeite (blue bars) and to layered structures (red bars) of the LDH type which contain sulphate, chloride and/or hydroxyl anions in the interlayer.

The phase content of the diffractograms of the fractions > 2 µm which are not shown are comprised in Tab. 5. It could be seen that with the increase of the grain size the amount of different observable phases is also increased. As remarkable observation for the fraction > 63 µm could be stated that negligible residues of the nuclear fuel (UAl_4) are still present and that due to the reducing environment elemental iron is formed. The presence of oxidized iron (III) compounds like Akaganeite, Lepidokrokite, and Goethite in the fraction < 63 µm could be ascribed to the fact that this fraction was additionally subjected to the Atterberg procedure for the subdivision into the fractions < 2 µm and 2 – 63 µm after sieving through a 63 µm mesh sieve. During this time consuming separation process oxidation may not be ruled out.

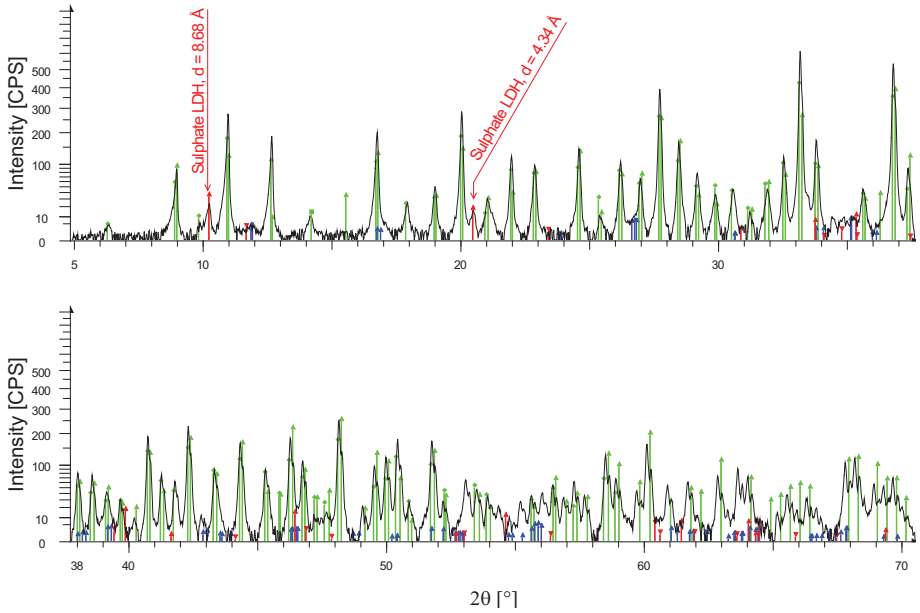

Fig. 22: Diffractogram of the fraction < 2 µm of the system UAl_x-Al in Brine 2.

Tab. 5: Observed phases in the fractions < 2 µm, 2 – 63 µm, and > 63 µm.

Phase Chemical composition	<2 µm	2 – 63 µm	63 µm
Lesukite: $Al_2(OH)_5Cl{\cdot}2H_2O$	+	+	+
Sulphate LDH: $(Mg_{0,625}Al_{0,375})(OH)_2(SO_4)_{0,188}$	+	+	+
Chloride/Hydroxid LDH: $(Mg_{0,75}Al_{0,25})(OH)_2(Cl/OH)_{0,25}(H_2O)_{0,5}$	+	+	+
Greenrust (LDH): $Fe(II)/Fe(III)(OH,Cl)_{2,55}$	-	+	+
Akaganeite: FeO(OH)	+	+	-
Lepidokrokite: FeO(OH)	-	+	+
Goethite: FeO(OH)	-	-	+
Nuclear Fuel UAlx-Al: UAl_4	-	-	+
Iron: Fe	-	-	+

After the identification of the observed crystalline phases the amount of each of these phases was determined by the Rietveld method. This method additionally allows the assessment of the amorphous content of the sample by adding an internal standard of known weight. Zincite was used as standard material.
In order to apply this method the crystallographic structure of each observed compound must be known and submitted to the appropriate Rietveld software. The crystallographic structure comprises basically the chemical composition, the lattice parameters, the space group, and the atomic positions of the asymmetric unit. These data are normally accessible through the ICSD crystallographic structural database. If the structures of the observed powder compounds are not known the structures normally have to be determined by single crystal methods which demand single crystals of certain dimensions being not smaller than few hundred micrometres.
If it is not possible to synthesize crystal individuals convenient for structure determination by X-ray diffraction other methods have to be applied to solve unknown crystal structures or to derive appropriate models at least being suitable for Rietveld calculations, respectively.
The structures of the observed secondary phases were all known with one exception considering the Lesukite. Applied REM and TEM analysis of this compound revealed unambiguously a cubic morphology of this secondary phase (Fig. 23).

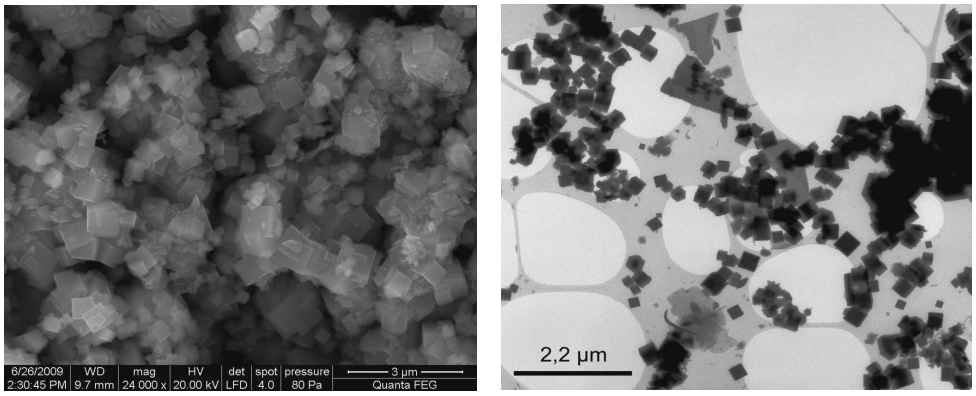

Fig. 23: Left: REM of Lesukite. Right: Low resolution TEM of Lesukite

High resolution TEM analysis of the surface shows a regular molecular arrangement (Fig. 24, left). As this electron diffraction method applies high energy which has an enormous impact of the stability of this compound the low quality of this surface picture obtained was enhanced by Fourier transformation which reduces the noise of the original measurement. The observed cubic crystals have an edge length of only few hundred nanometres. The 3D plot of the smoothed and Fourier transformed pe reveals the periodic characteristic of the molecular arrangement (Fig. 24, right). The observed ripples and valleys exhibit a distance of approximately one nanometre and a cubic arrangement as well.
These findings obtained by electron microscopy which clearly indicate the cubic nature of this structure were supported by literature data [6, 7] and additional analytical methods which have been applied considering the crystal system and unit cell parameters. This compound has a lattice parameter of approximately 2 nm which is twice the ripple distance which has been observed by HRTEM.

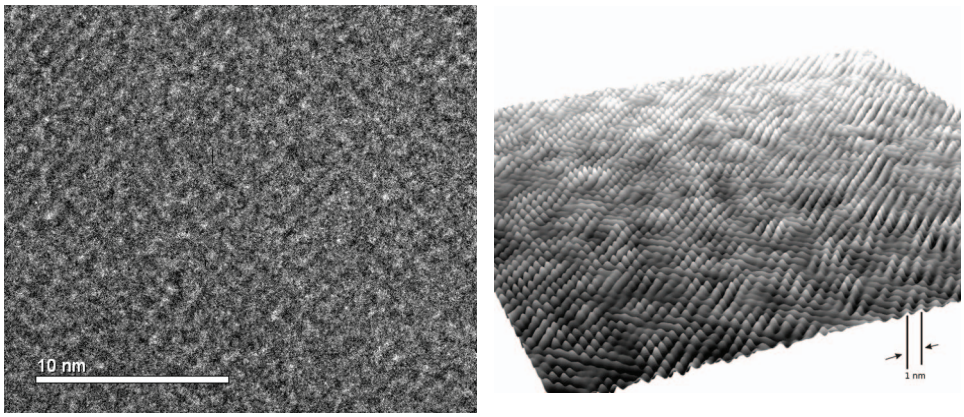

Fig. 24: Left: High resolution TEM of the Lesukite. Right: 3D depiction of the molecular arrangement in Lesukite.

The crystal system is reported to be cubic as well. An indexing procedure [8] which has been applied on the observed peak positions of Lesukite clearly favours a cubic body centred unit cell with 19,81 Å for the lattice parameter a. Afterwards a Pawley Fit [9] has been applied on basis of the best result obtained by the previous indexing procedure. The R_{wp} quality mark has a value < 9 % which is quite well. The findings of the applied indexing and the Pawley Fit are shown in the Fig. 25 and Fig. 26.

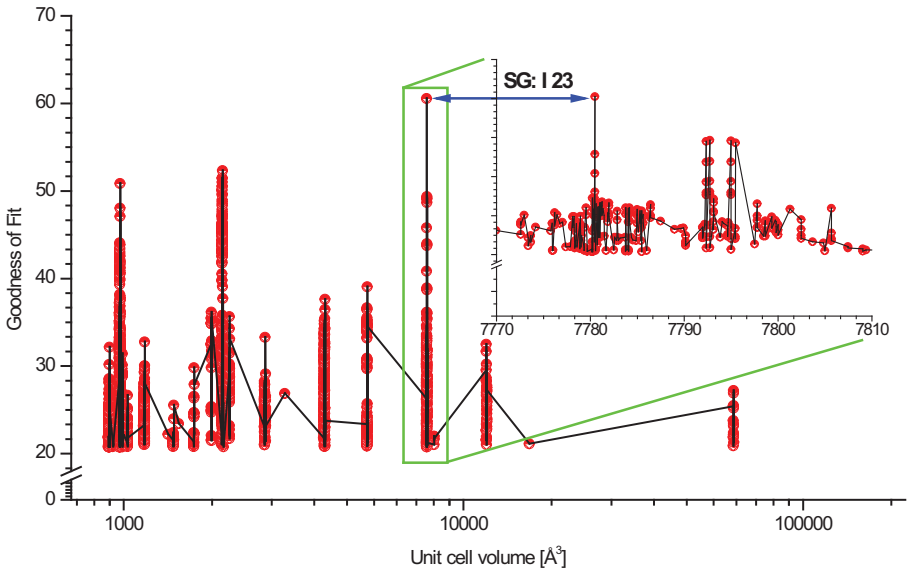

Fig. 25: Result of the LSI indexing procedure.

The indexing procedure was enabled to test all crystal systems in order to assign the observed peak positions of Lesukite to an appropriate unit cell. The number of possible solutions was constraint to 3000. This procedure favours the space group I 23. The result

represents only a little contradiction to the dedicated literature which implies a body centred space group as well but with an increased symmetry: I m-3m. Fig. 25 generally shows the quality of all 3000 solutions in dependence of the unit cell volume in logarithmic scale. The region of unit cell volumes close to 8000 $Å^3$ has been enlarged. In this sub diagram the unit cell volume is scaled linearly.

In Fig. 26 the Pawley Fit has been subdivided into 2 diffractograms from 5° to 70°and from 70° to 125° 2θ. The intensity scale of the diffractogram below, i. e. of high 2θ region has been decreased for visual reasons. It could be seen that nearly every observed peak could be assigned to the Lesukite phase. Peak positions which have not been fitted or been omitted belong to different compounds which have been identified as LDH phases and Akaganeite.

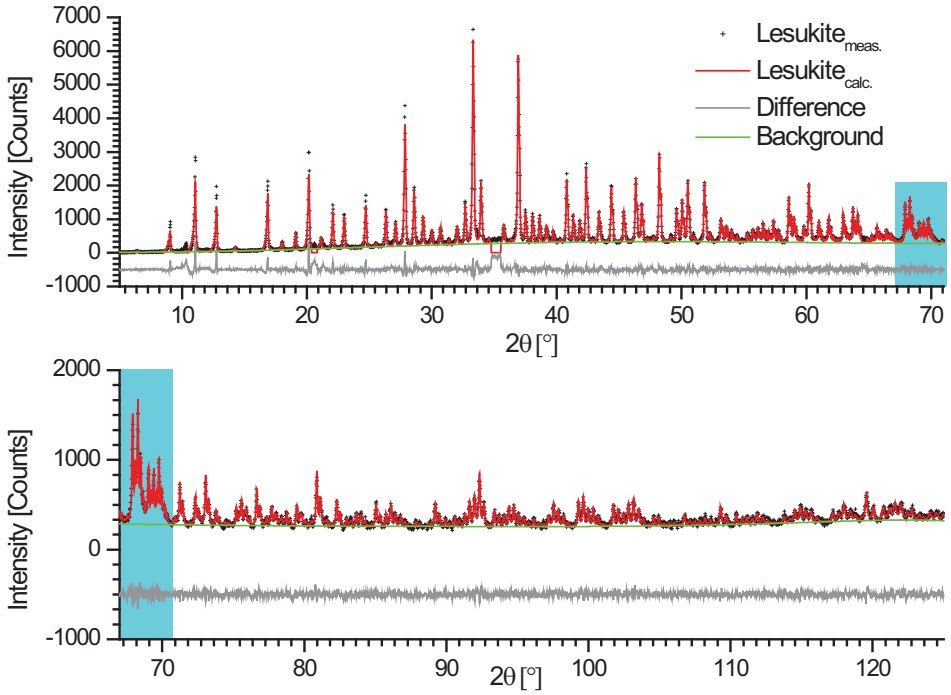

Fig. 26: Pawley Fit of Lesukite in the fraction < 2 µm.

From all these findings and other hints from literature [10] (Fig. 27a) which are not mentioned in detail following model shown in Fig. 27b) for the Lesukite has been derived.
Fig. 27a) shows the model of a dissolved Keggin molecule $(AlO_4Al_{12}(OH)_{24}(H_2O)_{12})^{7+}$ with its sevenfold positive charge which will be balanced by seven surrounding chloride ions (green). The chemical composition exhibits the elements which have been observed by EDAX analysis of this specific secondary phase as well. Fig. 27b) shows the unit cell with eight Keggin molecules. The unit cell edge has a value of approximately 19.81 Å. The Keggin molecule itself exhibits a tetrahedral symmetry which could barely be recognized due to the spherical morphology of this molecule which has a diameter of nearly one nanometre. This finding is confirmed by the HRTEM analysis.

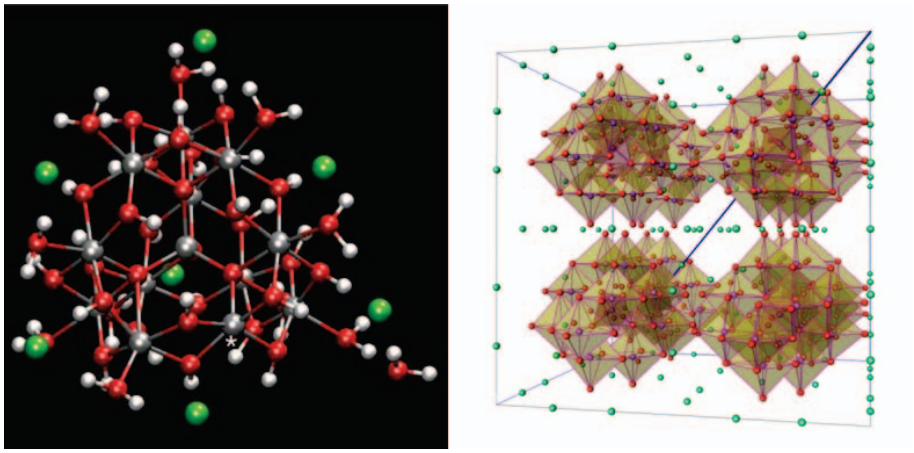

a) MD model [10] **b) Derived Lesukite structure model**

Fig. 27: Keggin structure of $AlO_4Al_{12}(OH)_{24}(H_2O)_{12})Cl_7$

Fig. 28 shows the Rietveld Plot of the fraction < 2 µm of the system UAl_x-Al. The R_{wp} is < 10 % which is comparable with that one obtained from the Pawley Fit.

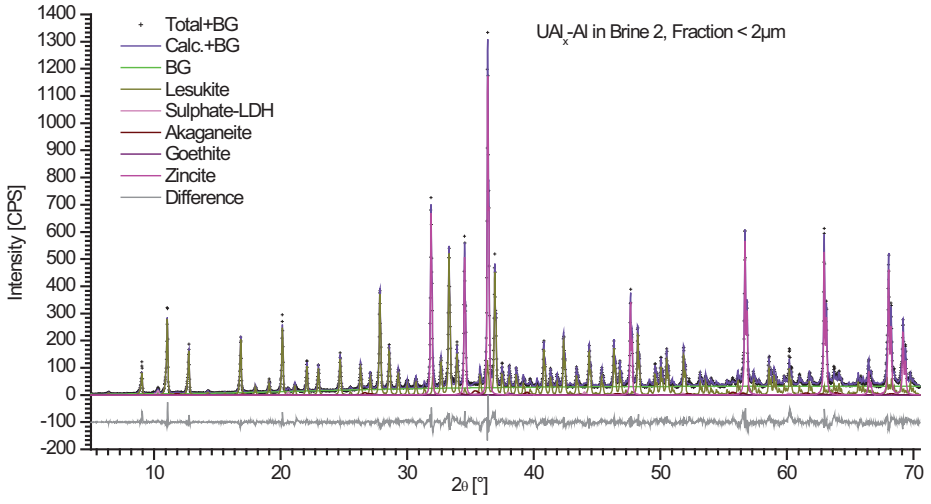

Fig. 28: Rietveld plot of the system UAl_x-Al in Brine 2, fraction < 2 µm.

The derived model was also used for the phase quantification of the fractions > 2 µm. Fig. 29 shows the results of these calculations. The major phases are Lesukite and LDH compounds. The observed amorphous content is mainly due to its abundance in the fraction > 63 µm.

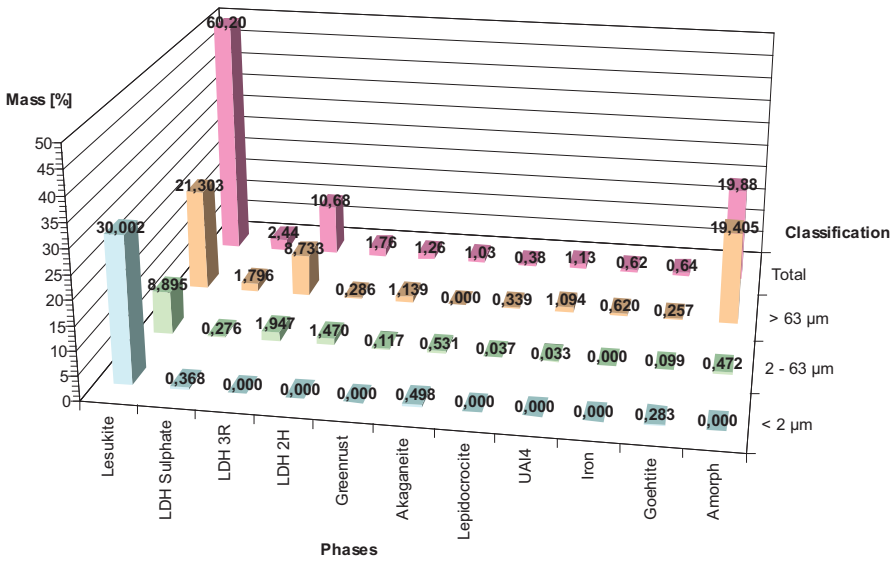

Fig. 29: Quantification of the secondary phases of the system UAl_x-Al in Brine 2.

The quantification has been carried on basis of the particle diameters previously determined by REM and image analysis. An overview about this analysis is given in Tab. 6. These results clearly show that during the formation of the secondary phases agglomeration processes are in progress as well.

Tab. 6: "True" particle size of the grain size fractions.

Grain size fraction	Determined particle size [µm]
> 63 µm	0,95
2 -63 µm	0,38
< 2 µm	0,41

For the potential of immobilisation of radio nuclides in the near field further investigations must be focused on the sorption properties of these major phases to which the amorphous phases also belong.

References

[1] E.Fein, I. Müller-Lyda, A. Rübel, GRS Bericht 247 (2008), Anh. Langzeitsicherheitsanalyse
[2] H. Curtius et al., Berichte des Forschungszentrum Jülich, Jülich-4333 (2010)
[3] H. M. Rietveld, Acta Cryst., 22 (1967) 151-152
[4] G. W. Brindley, Phyl. Mag., 36 (1945) 347-369
[5] W. L. Bragg, Proceedings of the Cambridge Philosophical Society, 17 (1913) 43–57
[6] T. Witzke, Neues Jahrbuch für Mineralogie-Monatshefte, 7 (1997) 301-308
[7] L. P. Vergasova et al. Proceedings of the Russian Mineralogical Society, 126 (1997) 104-110
[8] A. A. Coelho, Journal of Applied Crystallography, 36 (2003) 86-95
[9] G. Pawley, Journal of Applied Crystallography, 14(6) (1981) 357-361
[10] V. Pophristic et al., Chem. Phys, 6 (2004) 919-923

5.4. Minor actinide(III) recovery from high active waste solutions using innovative partitioning processes

G. Modolo[1], A. Wilden[1], A. Geist[2], R. Malmbeck[3]

[1] Institute of Energy and Climate Research – Nuclear Waste Management and Reactor Safety (IEK-6), Forschungszentrum Jülich GmbH, 52425 Jülich, Germany

[2]Karlsruher Institut für Technologie (KIT) Institut für Nukleare Entsorgung (INE), 76021 Karlsruhe, Germany

[3]European Commission, JRC, Institute for Transuranium Elements (ITU,) 76125 Karlsruhe, Germany

Corresponding author: g.modolo@fz-juelich.de

Abstract

The selective partitioning of minor actinides from the fission products and separate treatment by transmutation can considerably improve long-term safety of the residual nuclear waste for its subsequent future disposal in a deep underground repository. The present paper will summarize about the ongoing research activities at Forschungszentrum Jülich (FZJ) in the field of actinide partitioning using innovative solvent extraction processes. European research over the last few decades, i.e. in the NEWPART, PARTNEW and the recent EUROPART programs, has resulted in the development of a multicycle process for minor actinide partitioning. In this respect, numerous European partners cooperate closely in European projects. These multicycle processes are based on the co-separation of trivalent actinides and lanthanides (e.g. DIAMEX process), followed by the subsequent trivalent actinide/lanthanide group separation in the SANEX process. Apart from optimizing the properties of the solvent for optimal extraction and separation efficiency, extractant stability is a critical issue to be studied. In this paper, we will focus mainly on the development of flowsheets for the recovery of americium and curium from high active waste solutions, and testing them in centrifugal contactors. The scientific feasibility of the processes developed will be demonstrated on a laboratory scale using synthetic and genuine fuel solution. The future direction of research for the development of new processes within a new European project (ACSEPT) is briefly discussed in the conclusion.

Introduction

Reducing the radiotoxicity of spent nuclear fuel is an important objective to ensure the sustainability of nuclear energy. This objective can be attained by recovering the long-lived elements from the spent fuel constituents and their conversion into short-lived or stable nuclides by irradiation in a dedicated reactor, the so-called partitioning and transmutation strategy [1].

Plutonium, the main contributor to radiotoxicity can already be recovered today by the PUREX process, which with some modifications can also recover neptunium (advanced PUREX). In order to achieve a significant reduction in the radiotoxicity of spent fuel, we must also remove americium and curium. These trivalent minor actinides, however, are not currently industrially separated and they remain with the fission products in the high level liquid waste, which is vitrified and prepared for final disposal. This is not due to a lack of interest in separating these elements but rather due to the fact that they cannot be extracted

with tributylphosphate (TBP) within the PUREX process [2]. The chemical similarity of trivalent actinides (An) and lanthanides (Ln) combined with the unfavourable mass ratio necessitate very demanding and complex process steps. Processes developed over the last 20 years are predominantly based on the combined extraction of actinides and lanthanides from the PUREX raffinate followed by their subsequent group separation. A distinction is made here between two process variants [1].
In the single-cycle processes, An(III) + Ln(III) are simultaneously separated. Following this, the trivalent actinides are selectively back-extracted (stripped) from the loaded organic phase, e.g. using diethylenetriaminepentaacetic acid (DTPA). The most important developments in terms of this process include the reversed TALSPEAK (USA), DIDPA (Japan) and SETFICS (Japan) processes [2]. The multicycle processes, on the other hand, make use of different extractants. Following the joint co-separation of An(III) + Ln(III) from the fission product solution, e.g. using TRUEX (USA), TRPO (China), DIAMEX (France), the next process step involves the joint back-extraction of trivalent An + Ln. This is followed by selective An(III)/Ln(III) separation using a highly selective extractant, e.g. $CyMe_4BTBP$ [3].

The advantage of the latter method is the high purity of the actinide(III) product and a lower volume of secondary waste. This chapter provides an overview of important process developments for actinide separation achieved within the scope of European collaborative projects during the EU 3rd, 4th and 5th Framework Programmes [4]-[6]. Particular attention will be devoted to developments at Forschungszentrum Jülich, which were made possible through close cooperation with partners in the EU projects. The strategy employed for actinide separation is shown in Fig. 30.

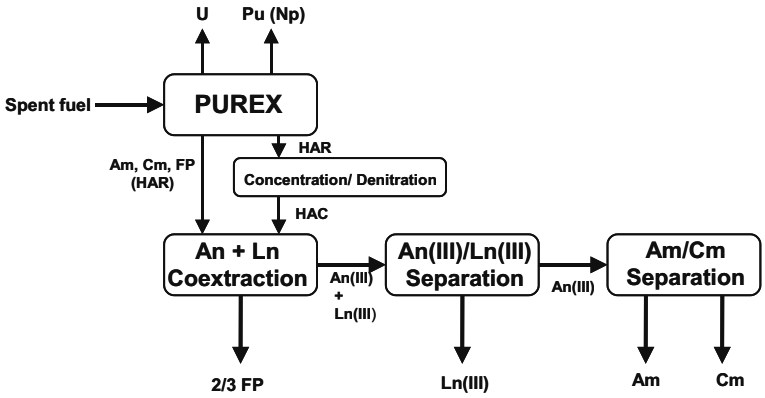

Fig. 30: European partitioning strategy for the separation of all actinides from spent fuel.

TODGA-based process developments

In the early 1990s, Stephan et al. [7] reported on the extraction of different metals using multidentate ligands such as diglycolamides (DGA). The DGA substance class with an ether group between both amide functions resembles the malonamides and therefore also satisfies the CHON principle. During the late 1990s, Japanese scientists recognized that these ligands are particularly suitable for extracting actinides from acidic waste solutions [8].

Extensive extraction studies were performed with this very promising substance class [9]-[11]. The change from a bidentate ligand (e.g. malonamide) to a tridentate diglycolamide not only significantly increased the affinity for trivalent actinides but also for the lanthanides. Different DGAs were synthesized and the N,N,N´,N´-tetraoctyl-3-oxapentan-diamide (TODGA, Fig. 31) was found to have the best properties in terms of extraction, solubility in aliphatic solvents and stability. However, TODGA had a tendency to form a third phase in aliphatic solvents such as n-dodecane, particularly at high metal and HNO_3 concentrations [12].

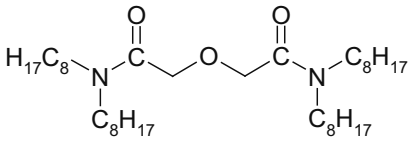

Fig. 31: The structure of TODGA.

Within the scope of the PARTNEW project, the aggregation behavior of TODGA was studied in n-dodecane as a solvent. With the aid of small-angle X-ray and neutron scattering experiments, it was shown that the reason for third-phase formation was the van der Waals interaction at low temperatures [13]. Other basic studies with TODGA and related compounds can be found in the literature, but almost no studies exist on process development including demonstration. This motivated Modolo et al. to develop a continuous reversible partitioning process, which was successfully tested for the first time in 2003 in centrifugal contactors at Forschungszentrum Jülich [14]. However, high oxalic acid concentrations of up to 0.4 mol/L were added to the PUREX raffinate in order to suppress the extraction of Zr and Mo on the one hand and third-phase formation on the other hand. At such high oxalic acid concentrations, a slow precipitation of trivalent actinides and lanthanides was observed in the PUREX raffinate. This also led to low oxalate precipitations in the scrubbing steps of the continuous process. This inevitably led to low actinide(III) losses.

Following this, Modolo et al. optimized the partitioning process and suggested a new continuous process in which the extractant was a mixture of 0.2 mol/L TODGA and 0.5 mol/L TBP in TPH [15]. The addition of TBP not only improved the hydrodynamic properties but also increased the loading capacity of the extractant and reduced the tendency to third-phase formation. In 2006, Forschungszentrum Jülich performed two tests in centrifugal extractors in cooperation with the Institute for Transuranium Elements (ITU) and CEA Marcoule [16].

In the second test run (Fig. 32) with 28 stages (4 extraction steps, 12 scrubbing steps and 12 back-extraction steps), 99.99 % of the actinides and lanthanides were selectively extracted and back-extracted from a PUREX raffinate. Problems were caused only by Ru, which was co-extracted (10 % of initial amount) and remained in the spent solvent.

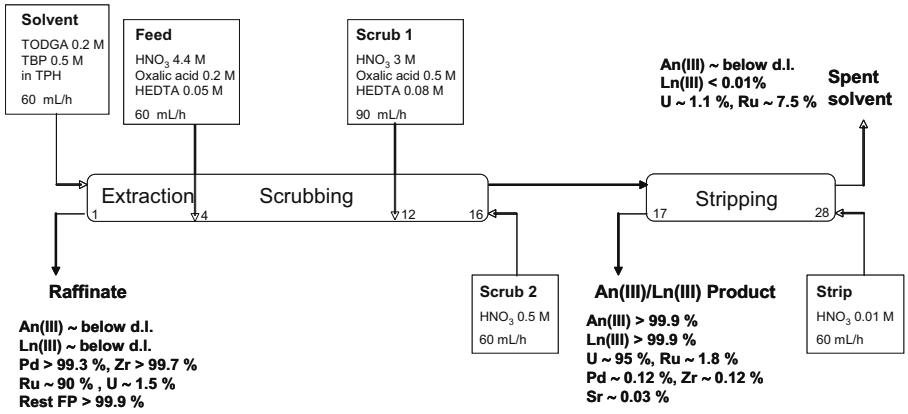

Fig. 32: Flowsheet and main results of the spiked TODGA-based process carried out at FZJ/Jülich in 2006.

Based on these positive results, a hot process run was demonstrated at the end of 2006 in ITU's centrifugal extractor battery with almost identical results [17]. In summary, we can say that the solvent composed of TODGA and TBP in an aliphatic solvent is particularly suitable for separating actinides from a process solution containing numerous fission products. This was demonstrated with a synthetic and a genuine PUREX raffinate with an optimized flowsheet. The main objective (> 99.9 % actinide separation) and a high fission product decontamination were achieved. The results generated are comparable with those for the DIAMEX processes further developed in France and the EU [17].

Selective actinide(III)/lanthanide(III) separation

The extraction systems described above separate the trivalent actinides together with the lanthanides from most of the fission products (e.g. Cs, Sr, Mo, Zr, etc.) in the liquid radioactive PUREX raffinate. For the transmutation of the minor actinides, any excess lanthanides (nuclear poison) must once again be separated. As a result of the chemical and physical similarity of both element groups, group extraction is only possible using extractants or complexants containing soft donor atoms, such as N, S, Cl, as they evidently have a stronger interaction with trivalent actinides [2].

Many extraction systems with relatively low An(III)/Ln(III) separation factors are described in the literature, but these systems are of little interest for technical application. Systems with a high selectivity are also described, but they are extremely complex (e.g. high salt loads, secondary waste), and they are incompatible with the partitioning processes described previously [1].

The SANEX concept (Selective ActiNide EXtraction) which aims to selectively extract trivalent actinides was first proposed by Musikas et al. [18]. In the early 1980s, the authors discovered two selective An(III)/Ln(III) extraction systems comprising soft N- or S-donor atoms, which subsequently formed the basis for the development of more efficient extractants.

Finally, a new class of heterocyclic N-donor SANEX ligands was developed by Foreman et al. [19], namely 6,6´-bis(5,6-dialkyl)-[1,2,4]triazin-3-yl)-[2,2´]bipyridines (BTBPs). A summary

of the extraction properties of the reference molecule $CyMe_4BTBP$ (Fig. 33) can be found in Geist et al. [3]. The slow extraction kinetics were significantly improved with a phase transfer catalyst, such as the malonamide DMDOHEMA.

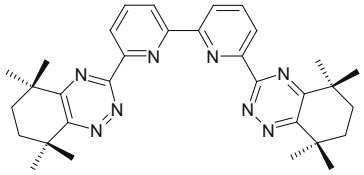

Fig. 33: 6,6´-bis(5,5,8,8-tetramethyl-5,6,7,8-tetrahydro-benzol[1,2,4]-triazin-3-yl)–[2,2´] bipyridine (CyMe4BTBP).

However, continuous tests on extraction and back-extraction using a single centrifuge showed that even at low process flows, equilibrium values could not be achieved [20]. Despite this, at the beginning of 2008, a hot test was successfully conducted for this SANEX process with a 16-stage flowsheet at ITU, Karlsruhe [21]. The product fraction contained more than 99.9 % Am(III) and Cm(III) and less than 0.1 % Ln(III).

At Forschungszentrum Jülich, Modolo et al. developed an alternative process [22]. The extractant comprised 0.015 mol/L CyMe4BTBP in n-octanol. However, instead of 0.25 mol/L DMDOHEMA, only 0.005 mol/L TODGA was used to improve the extraction kinetics. This system showed comparably good extraction properties and the process was successfully demonstrated at Forschungszentrum Jülich in February 2008.

In this 20-stage process with 12 extraction steps, 4 scrubbing steps and 4 back-extraction steps, >99.9 % Am(III), Cm(III) and Cf(III) were separated, and the product fraction contained less than 0.1 % of the initial lanthanides (Fig. 34).

The hot testing of this process (possibly at ITU, Karlsruhe) is one of the tasks of our collaborative future programme. The SANEX process variant developed at Forschungszentrum Jülich appears to be very promising for two reasons: replacing DMDOHEMA with TODGA increases the solubility of BTBPs, and the regeneration of the extractant is easier.

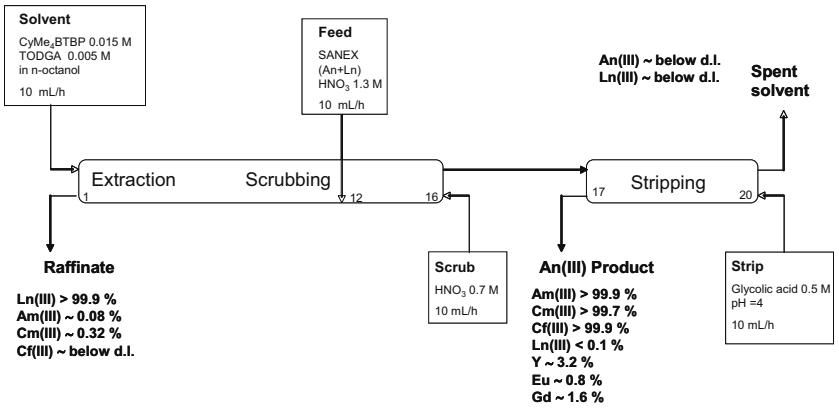

Fig. 34: Flowsheet and main results of the spiked SANEX CyMe4BTBP/TODGA process carried out at FZJ/Jülich in 2008

Americium/curium separation by the LUCA process

The separation of adjacent trivalent actinides represents an even more challenging task than the An(III)/Ln(III) separation. In principal, both elements could be transmuted together in a fast reactor or ADS system. However, because of the high heat decay and neutron emission of curium, any dry or wet fabrication process will require remote handling and continuous cooling in hot cells behind thick concrete shielding. The development of a simple, compact and robust fabrication process appears to be a great challenge [24].

Therefore, an effective method for separating Am from Cm prior to re-fabrication is a major prerequisite for the discussion of further fuel cycle scenarios. It is known that separating of americium from curium is a very difficult task due to the very similar properties of these elements. Numerous techniques, including high-pressure ion exchange, extraction chromatography, and solvent extraction using e.g. di(2-ethyl-hexyl)phosphoric acid (HDEHP) have been used for Am(III)/Cm(III) separation and purification [1], [2]. However, the Am/Cm separation factors were low and did not exceed 3, necessitating a large number of stages in order to obtain a pure product. The best separation of transplutonium elements has been obtained using methods based on the various oxidation states of the separated elements.

The synergistic mixture (Fig. 35) composed of bis(chlorophenyl)-dithiophosphinic acid [$(ClPh)_2PSSH$] and tris(2-ethylhexyl) phosphate (TEHP) shows a very high affinity for actinides(III) over lanthanides(III). Am(III)/Eu(III) separation factors over 3000 are achieved. Surprisingly high Am(III)/Cm(III) separation factors of 6 – 10 were also reported by Modolo et al [26]. Based on the extraordinary extraction properties of the above mentioned synergistic mixture, the LUCA process [27] was invented for the selective recovery of Am(III) from an aqueous nitric acid solution containing trivalent actinides (i.e. Am(III), Cm(III) and Cf(III)) and trivalent lanthanides.

LUCA is the acronym for “Lanthaniden Und Curium Americum separation”. Optimization studies were carried out to define the best conditions for extraction, scrubbing and stripping. In addition to the batch extraction studies, a single-stage extraction experiment was conducted to obtain more data on the system kinetics, and to generate data required for the flowsheet calculations.

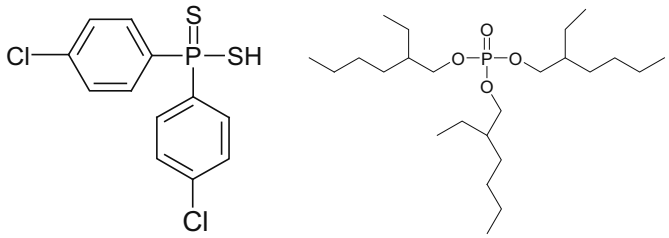

Fig. 35: Synergistic mixture of (ClPh)2PSSH and TEHP used in the LUCA process

After the data was collected, a 24-stage flowsheet was designed, and the final assessment was performed in a counter-current test using miniature centrifugal contactors [28]. The results of this counter current test (Fig. 36) showed, that the difficult recovery of Am(III) is possible from an acidic solution containing a mixture of trivalent actinides (Am(III), Cm(III) and Cf(III)) and Eu(III) as a lanthanide representative. The LUCA process can be used after a co-extraction process (e.g. after DIAMEX) for the selective extraction of Am(III), leaving

Cm(III) together with the lanthanides in the raffinate fraction. Alternatively, the process can also be run after a SANEX process for mutual Am/Cm separation.
In the future, we plan to optimize the formulation of the extractant composition, i.e. by changing the diluent. The promising results obtained here with a surrogate solution should also allow a hot demonstration to be performed in the near future with a genuine process solution. We are confident, that the aromatic dithiophosphinic acids under real process conditions (0.1 - 0.3 mol/L HNO_3, total doses up to 0.5 MGy) are sufficiently stable within the LUCA process. However, at higher acidities (> 0.5 mol/L HNO_3, e.g. during stripping) considerable degradation (by oxidation) of $(ClPh)_2PSSH$ was observed in a former study [29]. Oxidation of the ligand can be suppressed by adding HNO_2 scavengers or using hydrochloric acid as a stripping medium.

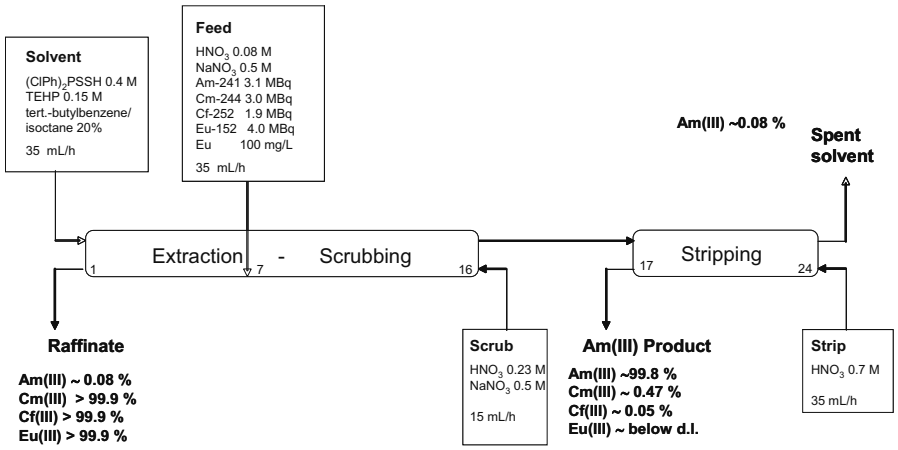

Fig. 36: Flowsheet and main results of the LUCA process for Am/Cm separation carried out at FZJ/Jülich in 2008.

Conclusion

Research on partitioning in the European Union (EU) is at such an advanced stage that serious consideration is being given to the industrialization of some separation processes. The leading nation here is France with its ambitious R&D programme on partitioning and transmutation. After decades of research in this area, separating minor actinides (americium and curium) from the PUREX raffinate still poses just as a big a challenge as in the past. The feasibility has already been demonstrated with the aid of a multicycle process (e.g. DIAMEX, TODGA, SANEX) on a laboratory scale using genuine fuel solutions. The challenge now is to optimize the developed processes in terms of their transferability and to work towards industrial process maturity. This will only be possible in the form of a large international project, and is being addressed in the EU follow-on project ACSEPT ([23]).
Within the framework of this international project, the focus is also on developing innovative processes. The objectives include simplifying processes developed in the past and reducing the number of cycles. The direct separation of trivalent actinides from the fission product solution (direct SANEX) is not yet viable as the necessary highly selective and stable extractants are not yet available. However, intensive research is being conducted on their development. Furthermore, tests must be performed to determine whether the processes

developed to date are also suitable for future reactor concepts of the third and fourth generation (GEN IV). In some GEN IV concepts, for example, the aim is to jointly recycle all transuranium elements (Np, Pu, Am, Cm). A separation technology adapted for these concepts is therefore essential. Within the framework of the ongoing EU project ACSEPT (2008 - 2012), grouped actinides extraction (GANEX concept) is therefore being studied in order to fulfill the requirements for future issues

Acknowledgement

The author would like to acknowledge the financial support of the European Commission in the projects: NEWPART (FI4I-CT96-0010), PARTNEW (FIKW-CT2000-00087), EUROPART (F16W-CT-2003-508854) and ACSEPT (No. 211267).

References

[1] Actinide and Fission Product Partitioning and Transmutation - Status and Assessment Report, OECD-NEA, Paris, France, 1999.
[2] Nash, K. L. Separation chemistry for lanthanides and trivalent actinides. Chapter 121, in Handbook on the Physics and Chemistry of Rare Earths. Gschneidner, K. A., Jr., Eyring, L., Choppin, G. R., Lander, G. H. Eds. 1994. pp. 197- 235.
[3] Geist, A.; Hill C.; Modolo, G.; Foreman, M.R.St.J.; Weigl, M.; Gompper, K.; Hudson, M.J., Madic C. Solvent Extr. Ion Exch. 2006, 24, 463–483.
[4] Madic, C.; Hudson, M.J.; Liljenzin, J.O.; Glatz, J.P.; Nannicini, R.; Facchini, A.; Kolarik, Z., Odoj, R. New partitioning techniques for minor actinides, European report, EUR 19149, 2000.
[5] Madic, C.; Testard, F.; Hudson, M.J.; Liljenzin, J.O.; Christiansen, B.; Ferrando, M.; Facchini, A.; Geist, A.; Modolo, G.;Gonzales-Espartero, A.; De Mendoza, J., PARTNEW- New Solvent Extraction Processes for Minor Actinides-Final Report, CEA-report 6066, 2004.
[6] C. Madic, M.J. Hudson, P. Baron, N. Ouvrier, C. Hill, F. Arnaud, A. G. Espartero, J.-F. Desreux, G. Modolo, R. Malmbeck, S. Bourg, G. De Angelis, J.Uhlir EUROPART. European Research Programme for Partitioning of Minor Actinides within High Active Wastes Issuing from the Reprocessing of Spent Nuclear Fuels, Proceedings of the FISA 2006, Luxembourg, 2006.
[7] H. Stephan, K. Gloe, J. Beger, P. Mühl, Solvent Extr. Ion Exch. 1991, 9(3), 459-469.
[8] Y. Sasaki, G.R. Choppin, Anal. Sci. 1996, 12, 225-230.
[9] Sasaki, Y., Choppin, G.R. Radiochim. Acta 1998, 80, 85–88.
[10] Sasaki, Y., Sugo, Y., Suzuki, S., Tachimori, S. Solvent Extr. Ion Exch. 2001, 19, 91–103.
[11] S. Tachimori, Y. Sasaki, S. Suzuki Solvent Extr. Ion Exch. 2002, 20(6), 687-699.
[12] Yaita, T., Herlinger, A.W., Thiyagarajan, P., Jensen, M.P. Solvent Extr. Ion Exch. 2004, 22, 553-571.
[13] Nave, S., Modolo, G., Madic, C., Testard, F. Solvent Extr. Ion Exch. 2004, 22(4), 527-551.
[14] Modolo, G., Vijgen, H., Schreinemachers, C., Baron, P., Dinh, B. TODGA Process Development for Partitioning of Actinides(III) from PUREX Raffinate, Proceedings of GLOBAL 2003, New Orleans, Louisiana, USA, 2003.
[15] Modolo, G., Asp, H., Schreinemachers, C., Vijgen, H. Solvent Extr. Ion Exch. 2007, 25, 703-721.
[16] Modolo, G., Asp, H., Vijgen, H., Malmbeck, R., Magnusson, D., Sorel, C. Solvent Extr. Ion Exch. 2008, 26 (1), 62 – 76.
[17] Magnusson, D.; Christiansen, B.; Glatz, J.-P.; Malmbeck, R.; Modolo, G.; Serrano-Purroy, D.; Sorel, C. Solvent Extr. Ion Exch. 2009, 27 (1), 26-35
[18] Musikas, C., Vitorge, P., Pattee, D. Progress in trivalent actinide lanthanide group separation. Proceedings of Internat. Solvent Extr. Conf (ISEC' 83). 1983.
[19] Ekberg, C., Fermvik, A., Retegan, T., Skarnemark, G., Foreman, M. R. S., Hudson, M. J., Englund, S., Nilsson, M. Radiochimica Acta 2008, 96(3-4), 225–233.
[20] Magnusson, D., Christiansen, B., Glatz, J.-P., Malmbeck, R., Modolo, G., Serrano-Purroy, D. Sorel, C. Radiochimica Acta, 2009, 97 (3), 155-159.
[21] Magnusson, D.; Christiansen, B.; Foreman, M.R.S.; Geist, A.; Glatz, J.-P.; Malmbeck, R.; Modolo, G.; Serrano-Purroy, D.; Sorel,C. Solvent Extr. Ion Exch. 2009, 27 (2), 97-106.
[22] Modolo, G.; Sypula, M.; Geist, A.; Hill, C.; Sorel, C.; Malmbeck, R.; Magnusson, D.; Foreman, M. R. St. J, Development and demonstration of a new SANEX process for actinide(III)-lanthanide(III) separation

using a mixture of CyMe4BTBP and TODGA as selective extractant, Proceedings of the 10th OECD/NEA P&T meeting, Mito, Japan, 2008.
[23] S. Bourg, C. Caravaca, C. Ekberg, C. Hill, C. Rhodes ACSEPT, Toward the Future Demonstration of Advanced FuelTreatments, Proceedings of Global 2009, Paris, France, 2009.
[24] Pillon, S., Somers, J., Grandjean, S., Lacquement, J. J. Nucl. Mater. 2003, 320, 36-43.
[25] Modolo, G., Odoj, R., Solvent Extr. Ion Exch. 1999, 17 (1), 33-53.
[26] Modolo, G., Nabet, S. Solvent Extr. Ion Exch. 2005, 23, 359-373.
[27] Modolo, G., Odoj, R. Method for separating trivalent americium from trivalent curium. European patent EP 1664359B1, 03.01.2007.
[28] Modolo, G., Kluxen, P., Geist, A., Radiochimica Acta, 2010, 98, 193-201.
[29] Modolo, G., Seekamp, S. Solvent Extr. Ion Exch. 2002, 20(2), 195-210.

5.5. 1-cycle SANEX process development studies and lab-scale demonstrations for the direct recovery of trivalent actinides from PUREX raffinate

A. Wilden, M. Sypula, C. Schreinemachers, J. Assenmacher, S. Gülland, G. Modolo

Corresponding author: a.wilden@fz-juelich.de

Abstract

The direct selective extraction of trivalent actinides from a simulated PUREX raffinate solution (1-cycle SANEX) was studied using a mixture of $CyMe_4BTBP$ and TODGA. The solvent showed a high selectivity for trivalent actinides with a high lanthanide separation factor. However the co-extraction of some fission products, such as Cu, Ni, Zr, Mo, Pd, Ag and Cd was observed. The extraction of Zr and Mo could be suppressed using oxalic acid but the use of the well-known Pd complexant HEDTA was unsuccessful. During screening experiments with different amino acids, the sulphur-bearing amino acid L-cysteine showed good complexation of Pd and prevented its extraction into the organic phase without influencing the extraction of trivalent actinides. The development of a process-like batch extraction series and a continuous counter-current test using a single centrifuge contactor showed very promising results in view of further optimizing the process. A strategy for a single-cycle process is proposed within this paper.

Introduction

The development of new and innovative processes for the processing of spent nuclear fuel solutions is a very intensively studied topic in nuclear research all over the world [1, 2]. As the liquid aqueous waste solution from reprocessing contains approx. 40 different elements in concentrations ranging from a few milligrams up to several grams per litre, the selective separation of trivalent actinides from this multi-element solution is one of the most challenging problems. The separation of the trivalent actinides from the lanthanides is a particularly difficult step, as the two groups of f-elements have very similar chemical properties.

In Europe, the DIAMEX-SANEX (DIAMide EXtraction - Selective ActiNide EXtraction) partitioning process is one of the most promising strategies to be converted from lab scale to industrial scale. The first step of this process (DIAMEX) uses a diamide extractant to co-extract lanthanides and minor actinides from the highly acidic PUREX (Plutonium-Uranium Recovery by EXtraction) raffinate [3, 4]. In the subsequent step (SANEX), the trivalent actinides are separated from the lanthanides e.g. by the highly selective $CyMe_4BTBP$ extractant [5, 6]. A drawback of such a process design is the need for two separate processes using two different ligands. Within the current European project ACSEPT (Actinide reCycling by SEParation and Transmutation), a new process design is envisaged, the so-called “innovative-SANEX” concept. In this strategy, the trivalent actinides and lanthanides are co-extracted in a DIAMEX-type process. Then, the loaded solvent is subjected to several stripping steps. The first one concerns selectively stripping the trivalent actinides with selective water-soluble ligands followed by the subsequent stripping of trivalent lanthanides [7].

A more challenging route studied within this paper is the direct actinide (III) separation from the PUREX raffinate using a mixture of $CyMe_4BTBP$ and TODGA (structures shown in Fig. 37) as extractants, the so-called 1-cycle SANEX process. A single process directly using the PUREX raffinate would reduce the number of cycles, thus saving the DIAMEX process, making the complete advanced reprocessing process more economical and easier.

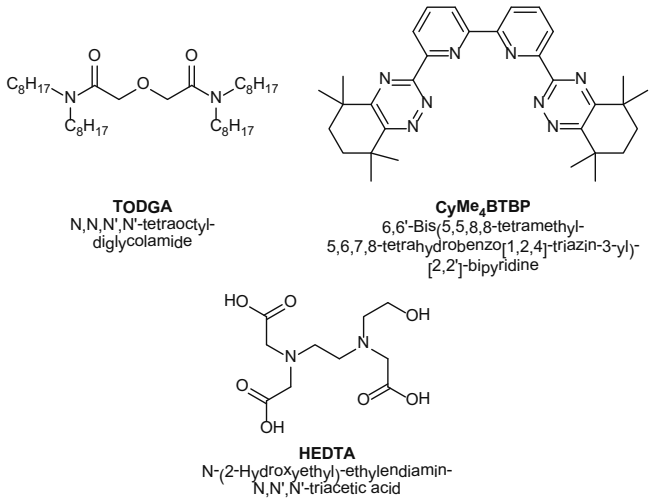

Fig. 37: Structures of TODGA, CyMe4BTBP and HEDTA.

Geist et al. have shown the $CyMe_4BTBP$ molecule to be a very selective extractant for the separation of actinides from lanthanides [8]. Magnusson et al. demonstrated the performance of $CyMe_4BTBP$ in a hot SANEX test using 0.25 mol/L of the malonamide DMDOHEMA as phase transfer reagent [5]. The use of a phase transfer reagent is necessary owing to the slow kinetics of the $CyMe_4BTBP$-molecule which can be significantly improved by the use of DMDOHEMA. Modolo et al. recently proposed that 0.25 mol/L DMDOHEMA can be substituted with 0.005 mol/L TODGA [9]. This system shows comparably good extraction properties and kinetic behaviour compared to DMDOHEMA, and the performance of the system was demonstrated in a spiked test. Both experiments used a DIAMEX raffinate solution containing actinides and lanthanides as a SANEX feed solution for the experiments. After a 20-stage counter-current process, an actinide product fraction containing >99.9% of the actinides with less than 0.1% lanthanides was obtained. Despite these very successful tests, the question arose as to whether it would be possible to directly and selectively extract the actinides from a PUREX raffinate solution leaving the lanthanides and the other fission products in the aqueous phase.

Results and discussion

Batch extraction studies in 2 mL glass vials were carried out with a synthetic PUREX raffinate solution. An organic phase consisting of 0.015 mol/L $CyMe_4BTBP$ and 0.005 mol/L TODGA diluted in a mixture of TPH and 1-octanol (40/60 v/v) was used as solvent. The composition of the synthetic PUREX raffinate solution and the corresponding distribution ratios of the elements for the extraction without adding any complexants are given in Tab. 7 (see column 3).

Tab. 7: The extraction of actinides and fission products from a simulated PUREX-raffinate with $CyMe_4BTBP/TODGA$.

Solute	Concentration [mg/L or as shown]	Without complexant	$C_2H_2O_4$	HEDTA	$C_2H_2O_4$ + HEDTA
		Distribution ratio			
^{241}Am	trace amounts	10.8	9.1	14.8	9.4
^{244}Cm	trace amounts	4.3	3.6	6.1	3.8
Y	90	0.04	0.85	0.15	0.73
La	239	<0.01	0.02	0.01	0.01
Ce	567	<0.01	0.03	0.01	0.02
Pr	223	0.01	0.04	0.02	0.03
Nd	718	0.02	0.06	0.04	0.05
Sm	149	0.07	0.14	0.1	0.13
Eu	34	0.16	0.24	0.14	0.25
^{152}Eu	trace amounts	0.06	0.22	0.1	0.2
Gd	51	0.08	0.17	0.08	0.15
Ni	40	30	18.4	32.1	37.3
Cu	19	4.88	15.7	19.1	5.6
Zr	1071	0.5	0.01	0.23	0.01
Mo	678	2.57	0.21	3.76	0.18
Pd	168	6.19	8.81	6.63	4.69
Ag	12	0.88	2.48	3.59	0.51
Cd	15	12.3	6.92	14.2	4.03
Cr	93	0.02	0.03	0.03	0.04
Sn	11	0.12	0.31	0.46	0.05
Sb	4.6	0.12	0.07	0.09	0.08
Rb	63	0.08	0.1	0.11	0.09
Ru	356	0.09	0.07	0.1	0.05
Rh	73	<0.01	<0.01	<0.01	<0.01
Te	165	0.03	<0.01	0.01	<0.01
Sr	177	<0.01	<0.01	0.01	<0.01
Ba	259	<0.01	<0.01	<0.01	<0.01
Cs	542	<0.01	<0.01	<0.01	<0.01
Al	2	n.d.	n.d.	n.d.	n.d.
Fe	1900	n.d.	n.d.	n.d.	n.d.
Se	10	n.d.	n.d.	n.d.	n.d.
Na	1600	n.d.	n.d.	n.d.	n.d.
HNO_3	3.2 mol/L				

n.d.: not determined.

These preliminary results show that the direct extraction of Am and Cm from a synthetic PUREX raffinate solution is possible with good extraction of the actinides and a high Am/Eu separation factor of 68. However, some non-lanthanide fission products were co-extracted with the actinides, namely Zr, Ag, Cd, Mo, Ni, Cu and Pd. Zirconium and molybdenum play a major role, because their concentration in the PUREX-raffinate solution is very high (1071 and 678 mg/L, respectively). Even a relatively low distribution ratio in this case leads to a considerable loading of the organic phase, thereby reducing the free extractant concentration available for the actinide extraction. Palladium (168 mg/L) must also be considered due to the higher concentration, whereas Ag (12 mg/L), Cd (15 mg/L), Ni (40 mg/L) and Cu (19 mg/L) are contained in smaller amounts.
The co-extraction of Zr, Mo and Pd is a problem that was often overcome by the use of the complexing agents oxalic acid and HEDTA (Fig. 37) in experiments concerning the DIAMEX process [10].

Tab. 7 shows the results for the addition of oxalic acid. It shows that the distribution ratios of Zr and Mo are reduced significantly by oxalic acid, as expected. The extraction behaviour of Ag, Cd, Ni, Cu and Pd is not affected very much by oxalic acid and the results furthermore show that Y is extracted much better due to the lower overall loading of the organic phase.
Tab. 7 also shows the results for experiments with the addition of HEDTA alone, and those with a mixture of oxalic acid and HEDTA. The experiment with HEDTA alone shows that the Zr distribution ratio is approximately halved compared to the experiment without the addition of complexants, but there is no influence on the extraction of Pd. This was not expected and experiments with Pd single-element solutions showed no influence of the HEDTA concentration on the extraction of Pd. The experiment with a mixture of oxalic acid and HEDTA shows that the addition of HEDTA is not advantageous compared to the experiment with oxalic acid alone and that the use of HEDTA can be omitted.
The aim of this work was to find a suitable masking agent for Pd [11]. A number of amino acids and some amino acid derivatives were therefore tested for their influence on the Pd distribution ratio, together with ^{241}Am and ^{152}Eu. An overview of the tested complexants is shown in Fig. 38. Amino acids were chosen because of their relatively complex coordination chemistry due to the presence of different donor atoms (O, N, S) in diverse structural constitutions thus allowing different chelate ring sizes, and because of their well solubility in aqueous solutions.

They were all tested in two concentrations, 0.1 and 0.2 mol/L. The results of the test with 0.1 mol/L amino acid are shown in Fig. 39. The results of the test with 0.2 mol/L amino acid show a similar behaviour and therefore are not shown.

Just two of the 22 tested amino acids showed a significant influence on the distribution ratio of Pd: L-cysteine 5 and L-cystine 6 (structures are shown in Fig. 38). The Pd distribution ratios are reduced considerably and reach values below 1. Furthermore, the amino acids had no influence on the extraction of Am(III) and Eu(III). The distribution ratios of Am(III) and Eu(III), as well as the separation factor, remained unchanged. L--cysteine was chosen for further studies, because of the structural similarity of the two molecules. L-cystine is a dimer of two L-cysteine molecules.

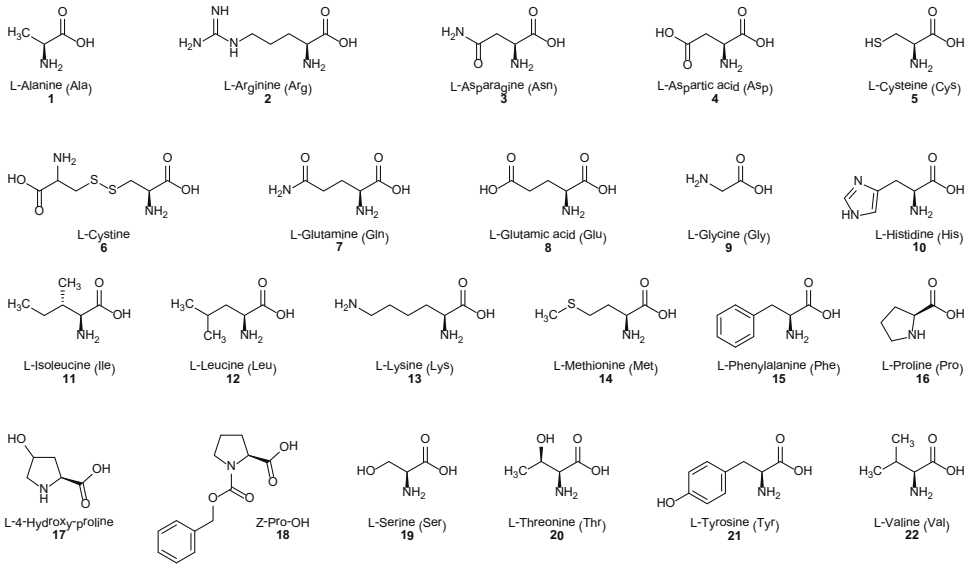

Fig. 38 Overview of the tested amino acids and derivatives.

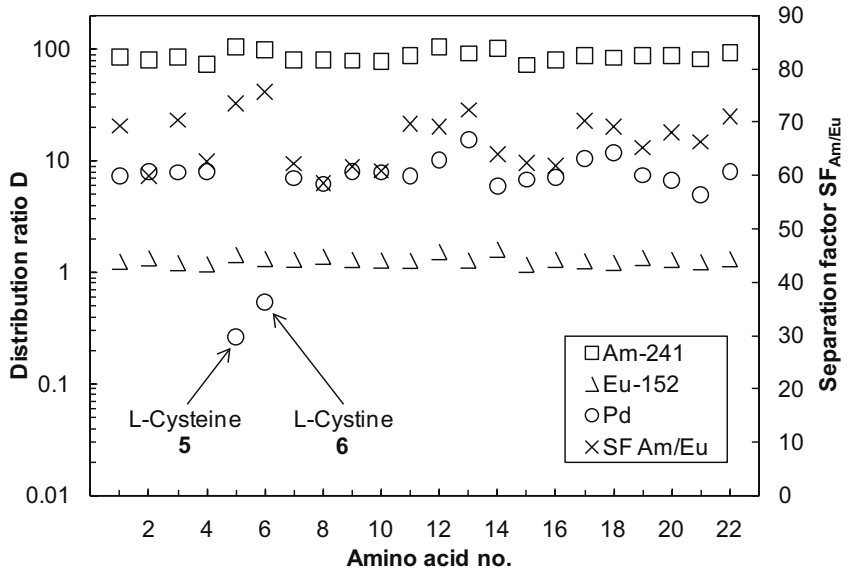

Fig. 39: Amino acid screening using CyMe4BTBP + TODGA in TPH/1-octanol = 40/60 and different amino acids in 3 mol/L HNO3 as aqueous phases.

The 1-cycle SANEX process is intended to be used to separate the minor actinides from a PUREX-raffinate solution. To test the new complexant under process relevant conditions a simulated PUREX-raffinate solution had been prepared with the composition shown in Tab. 7.
In the following batch experiments, a process-like extraction series was used. The composition of the aqueous phases is shown in Tab. 8.
In the first step, the extraction step, 4 mL of the simulated PUREX-raffinate solution were contacted for 15 min. with 4 mL of a freshly prepared organic phase with the same composition as in the previous experiments (0.015 mol/L $CyMe_4BTBP$ + 0.005 mol/L TODGA in TPH/1-octanol = 40/60). After phase separation, aliquots of each phase were taken for analysis and 3.0 mL of the remaining organic phase were contacted with 3.0 mL of a freshly prepared aqueous phase (Scrub I). Again after phase separation, aliquots of each phase were taken for analysis and 2.0 mL of the remaining organic phase were contacted with 2.0 mL of a freshly prepared aqueous phase (Scrub II). In the last step, called Strip, 1.0 mL of the separated organic phase was contacted with 1.0 mL of a freshly prepared aqueous phase.

Tab. 8: Composition of the aqueous phases used in the first experiment.

concentration / mol/L	Step 1: Ex	Step 2: Scrub I	Step 3: Scrub II	Step 4: Strip
HNO_3	3.2	1	1	0.01
oxalic acid	0.3	0.2		
L-cysteine			0.01	

During this first extraction experiment, L-cysteine caused a voluminous precipitation, which is unwanted in a counter-current process. Therefore, the extraction series was altered as shown in Tab. 9. The experiment was conducted as described above.

Tab. 9: Composition of the aqueous phases used in the second experiment.

concentration / mol/L	Step 1: Ex	Step 2: Scrub I	Step 3: Scrub II	Step 4: Strip
HNO_3	3.2	1	1	0.01
oxalic acid	0.3	0.2		
L-cysteine	0.05	0.05		

During this experiment, no precipitate formed and no third phase formation was observed. Fig. 40 shows that americium and curium are well extracted and that they stay in the organic phase during the washing steps. In the last step (Strip), they were back extracted into the aqueous phase. The trivalent lanthanides were not extracted well (with the highest distribution ratios for europium) and therefore a high separation between the trivalent lanthanides and the actinides was achieved. The good back-extraction behaviour of the $CyMe_4BTBP$ system is advantageous for the development of a reversible process with recycling of the organic phase which could be reused after a possible solvent treatment.

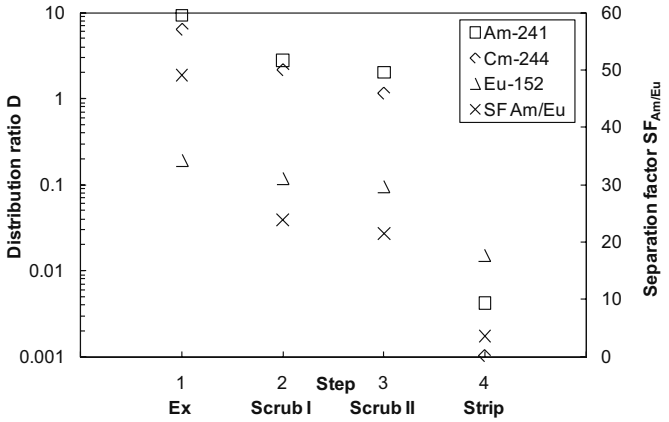

Fig. 40: Distribution ratios and separation factor of ^{241}Am, ^{244}Cm and ^{152}Eu in a simulated four-step process using CyMe$_4$BTBP + TODGA in TPH/1-octanol = 40/60 and aqueous phases as shown in Tab. 9.

Fig. 41 shows the results from ICP-MS analysis for some selected inactive elements. In this figure, the concentration of the elements in the organic phase is depicted instead of the distribution ratio because the D-values of copper and nickel could not be determined due to their low concentration in the aqueous phase. The results show that copper and nickel are nearly completely extracted and that they stay in the organic phase during the whole experiment. They could possibly be scrubbed in an alkaline solvent treatment, but this topic was not investigated during this work. The extraction of zirconium and molybdenum was prevented by the use of oxalic acid and yttrium was scrubbed during the first two steps. Furthermore, the results show that palladium and silver were effectively scrubbed from the organic phase in the third step, the section with L-cysteine addition.

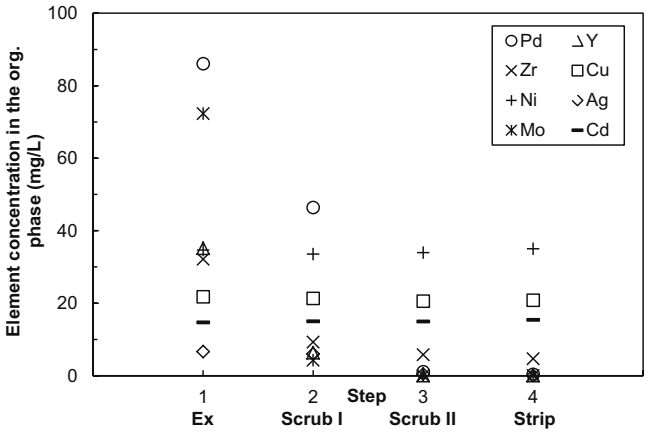

Fig. 41: Organic phase concentrations of selected stable elements as determined by ICP-MS in a simulated four-step process using CyMe$_4$BTBP + TODGA in TPH/1-octanol = 40/60 and aqueous phases as shown in Tab. 9.

Continuous counter-current tests using a single centrifugal contactor were conducted for three steps, selective actinide (III) extraction, Pd-scrubbing and stripping of the actinides. For the extraction test a mixture of HAR feed solution with the first scrub solution was used, resulting in an overall HNO_3 concentration of 2 mol/L and an oxalic acid concentration of 0.25 mol/L. Freshly prepared solvent was used and the test was run at three different flow rates: org./aq.=20/40 mL/h (Ex1), org./aq.=10/20 mL/h (Ex2) and org./aq.=5/10 mL/h (Ex3). Fig. 42 shows the Am and Eu concentrations in the org. phase against the experiment time. It shows that approx. 3-4 exchanges of the mixing chamber volume (ca. 5.5 mL) were needed to reach a steady state. The steady state is indicated by the development of a constant org. phase concentration.

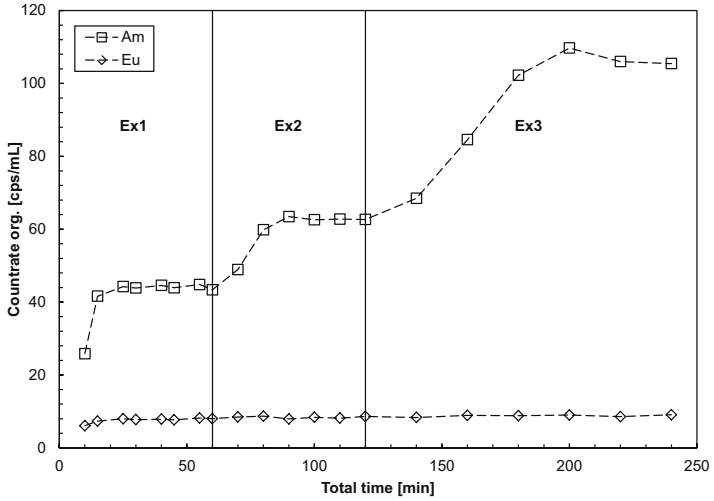

Fig. 42: Am(III) and Eu(III) concentration in the org. phase during the extraction test.

The results show that the stage efficiency increases with decreasing flow rates (Fig. 42 and Tab. 10). For the further scrubbing and stripping tests a flow rate of 10 mL/h for both, the aqueous and organic phase, was chosen. Like in the batch experiments co-extraction of Cu, Ni, Cd, Ag and Pd was observed to a larger extend and minor co-extraction of Y. The lanthanides follow the same trend as observed previously and Mo and Zr were sufficiently masked by oxalic acid.

Tab. 10: Results of the extraction test.

	Flow rate org. [mL/h]	Flow rate aq. [mL/h]	Distribution ratio Am	Eu	SF Am/Eu
Ex1	20	40	0.85	0.18	4.7
Ex2	10	20	1.38	0.17	8.1
Ex3	5	10	5.72	0.21	27
Equilibrium value by shaking the content of the mixing chamber after Ex3			12.3	0.23	53

The scrubbing test using L-cysteine showed a decrease of the Pd distribution ratio of 2.46 (Ex2) to 0.34 during the scrubbing test. The equilibrium value of 0.03 was not reached due to the slow kinetics of the system. Cu, Ni and Cd quantitatively stayed in the organic phase and were not scrubbed. The slightly co-extracted elements Mo, Ru, Y and the lanthanides were further scrubbed to the aqueous phase.

For the stripping test, different aqueous phases were used. First a solution of glycolic acid (0.5 mol/L), set to pH 4 with NH_3 (St1) was used, then the aqueous phase was changed to a nitric acid solution of pH 3 (St2) and after that to pH 2 (St3). The results of the stripping test are shown in Tab. 11.

Tab. 11: Results of the stripping test.

	pH	Complexant	Distribution ratio	
			Am	Eu
St1	4	0.5 M glycolic acid	0.11	0.08
St2	3	-	0.74	0.15
St3	2	-	0.67	0.13
Equilibrium value by shaking the content of the mixing chamber after St3			0.01	0.01

The best stripping results were obtained with 0.5 mol/L glycolic acid at pH 4. Thermodynamic stripping at pH 3 or even pH 2 was possible but equilibrium values were not reached owing to the slow kinetics of the system. Cu, Ni and Cd stayed in the organic phase during the stripping test, thus being effectively separated from americium. The product fraction, besides americium, contained smaller concentrations of Pd, Ru, Y, Mo and some lanthanides. These contaminations should be avoided using a higher number of stages for the extraction, scrubbing and stripping parts. A possible flow sheet of a spiked one-cycle SANEX process is shown in Fig. 43.

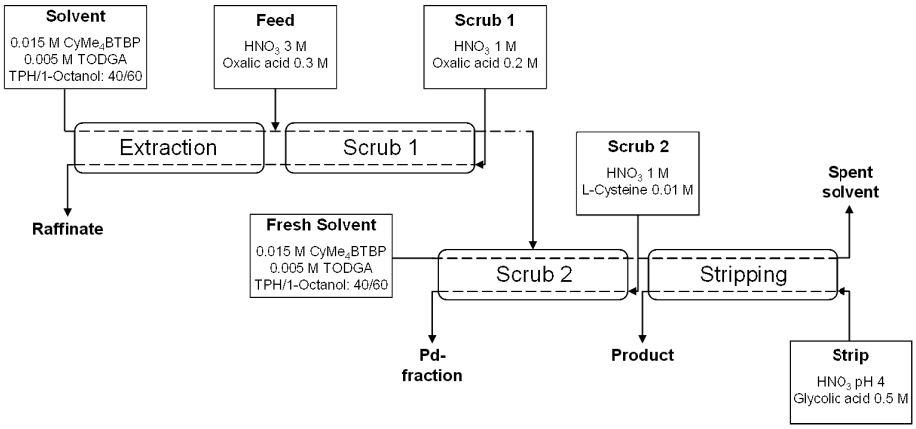

Fig. 43: Flow sheet proposal of a spiked one-cycle SANEX process.

Conclusion

In this work, it was shown that the direct and selective extraction of trivalent actinides from a synthetic PUREX raffinate solution as 1-cycle SANEX seems to be possible. Distribution ratios for trivalent actinides and the separation factor from the trivalent lanthanides were high. Nonetheless the reported system suffered from the co-extraction of some of the non-lanthanide fission product elements.

22 amino acids and derivatives were tested and L-cysteine showed good complexation behaviour of Pd, without influencing the extraction of trivalent actinides. In a process-like extraction series, the practicability of the use of L-cysteine as complexant for Pd and Ag was shown.

Continuous counter-current experiments using a single centrifuge contactor gave very promising results and a flow sheet for a spiked test was proposed.

The high distribution ratios of Ni and Cu could be problematic for a continuous working industrial process. More investigations have to be done to examine stripping conditions for these elements. A possible solvent clean-up step has to be developed for the design of an industrial process.

Acknowledgements

Financial support for this research was provided by the European Commission (project ACSEPT – Contract No. FP7-CP-2007-211 267) and the German Federal Ministry of Education and Research (Contract No. 02NUK012E). Frank Lewis, University of Reading, is greatly acknowledged for providing $CyMe_4BTBP$.

References

[1] M. Nilsson, K. L. Nash, Solvent Extr. Ion Exch. 25 (2007) 665-701.
[2] C. Ekberg, A. Fermvik, T. Retegan, G. Skarnemark, M. R. S. Foreman, M. J. Hudson, S. Englund, M. Nilsson, Radiochim. Acta 96 (2008) 225-233.
[3] O. Courson, M. Lebrun, R. Malmbeck, G. Pagliosa, K. Romer, B. Satmark, J. P. Glatz, Radiochim. Acta 88 (2000) 857-863.
[4] R. Malmbeck, O. Courson, G. Pagliosa, K. Romer, B. Satmark, J. P. Glatz, P. Baron, Radiochim. Acta 88 (2000) 865-871.
[5] D. Magnusson, B. Christiansen, M. R. S. Foreman, A. Geist, J. P. Glatz, R. Malmbeck, G. Modolo, D. Serrano-Purroy, C. Sorel, Solvent Extr. Ion Exch. 27 (2009) 97-106.
[6] D. Magnusson, B. Christiansen, J.-P. Glatz, R. Malmbeck, G. Modolo, D. Serrano-Purroy, C. Sorel, Radiochim. Acta 97 (2009) 155-159.
[7] X. Hérès, C. Sorel, M. Miguirditchian, B. Camès, C. Hill, I. Bisel, D. Espinoux, C. Eysseric, P. Baron, B. Lorrain, Proc. of the GLOBAL 2009, Paris, France (2009) 9384.
[8] A. Geist, C. Hill, G. Modolo, M. R. S. J. Foreman, M. Weigl, K. Gompper, M. J. Hudson, C. Madic, Solvent Extr. Ion Exch. 24 (2006) 463-483.
[9] G. Modolo, M. Sypula, A. Geist, C. Hill, C. Sorel, R. Malmbeck, D. Magnusson, M. R. S. J. Foreman, Proc. of the Tenth Information Exchange Meeting on Actinide and Fission Product Partitioning and Transmutation, Mito, Japan (2008).
[10] D. Serrano-Purroy, P. Baron, B. Christiansen, R. Malmbeck, C. Sorel, J. P. Glatz, Radiochim. Acta 93 (2005) 351-355.
[11] A. Wilden, C. Schreinemachers, M. Sypula, G. Modolo, Solvent Extr. Ion Exch 29 (2011) 190-212.

5.6. Innovative SANEX process for actinide(III) separation from PUREX raffinate using TODGA-based solvents

M. Sypula, A. Wilden, C. Schreinemachers, G. Modolo

Corresponding author: g.modolo@fz-juelich.de

Abstract

We studied an innovative SANEX process using N,N,N',N'-tetraoctyl diglycolamide (TODGA) based solvents for the selective separation of trivalent actinides from a PUREX raffinate. TODGA was chosen for actinide(III)/lanthanide(III) co-extraction and 1-octanol was used as an organic phase modifier to avoid third-phase formation. A new masking agent, trans-1,2-cyclohexanediaminetetraacetic acid (CDTA) was successfully used for Pd and Zr. N-(2-hydroxyethyl)ethylenediaminetriacetic acid (HEDTA) and diethylenetriamine pentaacetic acid (DTPA) were used as complexing agents for selective actinide(III) stripping. The organic phase modifier used partly extracted HNO_3 which decreased the pH of the actinide stripping solution and resulted in a lower Ln(III)/An(III) separation. Therefore several buffers were studied with the aim of minimising the pH change during An(III) stripping. Good An(III) stripping conditions were obtained using DTPA + citric acid or DTPA + glycine. All the established conditions were applied in single centrifugal contactor tests to obtain the data for future flow-sheet design and spiked counter-current runs using a battery of centrifugal contactors.

Introduction

The P&T strategy (Partitioning and Transmutation) aims to decrease the radiotoxicity of nuclear waste and thereby minimise the cost and time associated with its storage. After the recovery of U, Pu and optionally Np in the PUREX process (Plutonium Uranium Recovery by EXtraction), the main contributors to the total radiotoxicity of the remaining waste are the trivalent minor actinides Am+Cm (~0.1% of the total spent fuel mass). Therefore, their transformation into stable or short-lived isotopes is highly desirable. Prior to the transmutation, the separation of lanthanides (Ln) is necessary since large neutron-capture cross-sections would hinder an efficient transmutation. One of the concepts for trivalent actinide separation being studied in the European ACSEPT project **[1]** is the innovative SANEX concept (Selective ActiNide EXtraction). It consists of an An(III)/Ln(III) co-extraction step, followed by selective An(III) stripping using hydrophilic complexing agents. In the final step, lanthanides are stripped to the aqueous phase using diluted nitric acid. The most challenging part of this process is the selective An(III) stripping, where the pH value of the stripping solution and the choice of an appropriate hydrophilic An(III) complexing agent are crucial.

Methodology

Batch extraction experiments were performed in 2 mL glass vials. 500 µL of organic and aqueous phases were spiked with 10 µL of radiotracer (^{241}Am, ^{152}Eu, approx. 25 kBq/mL) and

shaken by a vortex mixer for 15 minutes at 22 °C to reach equilibrium. Separation of the phases by centrifugation was followed by the sampling of each phase for gamma analysis. Stable lanthanides and fission products were determined by ICP-MS.
The distribution ratio D was measured as the ratio between the radioactivity of an isotope in the organic and the aqueous phase. Distribution ratios between 0.01 and 100 exhibit a maximum error of ± 5 %. The error may be up to ± 20 % for smaller and larger values.
The single centrifuge test was performed using a Chinese-type centrifugal contactor with a rotor diameter of 10 mm and an approximate chamber volume of 3 mL. The aqueous and organic phases were introduced at the required flow-rate controlled by two calibrated syringe pumps. The samples from the outlets of the contactor were collected after the achievement of the steady state and analysed as described above.

Results and discussion

In 2001, Sasaki et al. [2] introduced a new organic ligand N,N,N',N'-tetraoctyl diglycolamide (TODGA), which showed very high extraction affinity towards An(III) and Ln(III) from highly concentrated nitric acid combined with a very good solubility in non-polar diluents. However, the poor loading capacity of TODGA can cause the organic phase to split when it is loaded with high amounts of extracted metals [3]. Therefore, Modolo et al. [4] additionally used TBP as an organic phase modifier, thus increasing the limit of the solvent metal loading in order to avoid the third-phase formation. In 2007, a new process for An partitioning from the PUREX raffinate was developed [5] at Forschungszentrum Jülich and successfully tested with a genuine spent fuel solution at ITU, Karlsruhe [6]. The solvent consisted of TODGA/TBP dissolved in TPH. The co-extraction of Pd and Zr was suppressed by well-known masking agents HEDTA and oxalic acid, respectively, which had been used previously by French researchers in DIAMEX process [7,8].
Recently, the French CEA developed an innovative process for An(III) separation from the PUREX raffinate and successful cold and spiked demonstration tests were conducted [9]. The organic solvent was based on TODGA + TBP. The extraction and scrubbing step of this process were adapted from the German TODGA/TBP process for An+Ln partitioning [5] and the selective actinide stripping step was added.

New masking agent for Zr

The co-extraction of nitric acid by TBP has a major impact on the actinide stripping efficiency, as its later back-extraction decreases the pH of the actinide stripping solution and hence the An(III)/Ln(III) separation yield. Therefore, the substitution of TBP by 1-octanol was proposed by Geist et al. [10]. This decreases the nitric acid co-extraction from 0.041 mol/L (TBP) to 0.013 mol/L (1-octanol) ($[HNO_3]_{ini,aq}$=0.5 mol/L]). Oxalic acid, which is used as a masking agent, is also party extracted by the organic solvent. Its substitution was therefore desirable. Moreover, at high oxalic acid concentrations, lanthanide oxalates can be formed and cause precipitation. For these reasons, a new masking agent was introduced to substitute oxalic acid: trans-1,2-cyclohexanediaminetetraacetic acid (CDTA). CDTA suppresses the extraction of both Pd and Zr by their efficient complexation in the feed solution (Tab. 12).

Tab. 12: The extraction of metals by TODGA + TBP and TODGA + 1-octanol with and without a masking agent.

TODGA +	TBP		1-octanol	
	Without masking agent	CDTA	Without masking agent	CDTA
	Distribution ratios		Distribution ratios	
Zr	202	0.005	324	0.004
Pd	9.23	0.09	4.8	0.09
Sr	1.81	2.2	1.2	2.4
Mo	0.21	0.14	0.24	0.22
Ru	0.29	0.38	0.21	0.21
^{241}Am	> 100	> 100	> 100	> 100
Ln	> 100	> 100	> 100	> 100

Org. phase: 0.2 mol/L TODGA + 0.5 mol/L TBP (or 5 vol-% 1-octanol) in TPH (not pre-equilibrated with HNO_3)

Aq. phase: 3.1 mol/L HNO_3, PUREX-type raffinate solution [5], 0.05 mol/L CDTA + tracers (^{241}Am, ^{152}Eu)

Re-investigation of the formulation of the solution for An(III) stripping

The substitution of the masking agents with CDTA and the use of 1-octanol as an organic phase modifier required the re-investigation of the formulation of the An-stripping solution.
To improve the separation of Ln(III) from An(III), two hydrophilic complexing agents were tested, HEDTA and DTPA. The use of DTPA gave the lowest $SF_{Ln/Am}$ for neodymium ($SF_{Nd/Am}$=9.6), while for HEDTA lanthanum was the least-extracted lanthanide ($SF_{La/Am}$=2.3) (Tab. 13). In general, better separation of Am from Ln was obtained using DTPA. Further optimisation studies were therefore carried out with this hydrophilic complexant.

Tab. 13: The influence of DTPA and HEDTA on the Ln/Am separation factors

	Separation factor of Ln/Am							
	Y	La	Pr	Eu	Gd	Nd	Ce	Sm
HEDTA	325	2.35	2.66	16.8	6.09	3.46	2.63	9.48
DTPA	183	22.7	11	16.5	14.7	9.6	18	12.1

Org. phase: 0.2 mol/L TODGA + 5 vol-% 1-octanol in TPH (preloaded with lanthanides at 0.5 mol/L HNO_3),

Aq. phase: 0.05 mol/L DTPA or 0.05 mol/L HEDTA, 1 mol/L $NaNO_3$, 1 mol/L glycine + tracers (^{241}Am, ^{152}Eu).

The influence of the DTPA concentration and the initial pH of the An-stripping solution on the Am and lanthanides back-extraction is shown in Fig. 44 (left) and Fig. 44 (right). By increasing the DTPA concentration, the distribution ratio of ^{241}Am decreased, while D_{Ln} did not change significantly (Fig. 44 left). A concentration of 0.05 mol/L DTPA was sufficient to effectively separate Am(III) from the Ln(III). The increase in the pH of the An-stripping solution decreased both D_{Am} and D_{Ln}, resulting in an optimum pH range of 1.7–1.9. This allowed a good Am(III) back-extraction without stripping the Ln(III). $NaNO_3$ was used as a salting-out agent to keep the Ln in the organic phase.

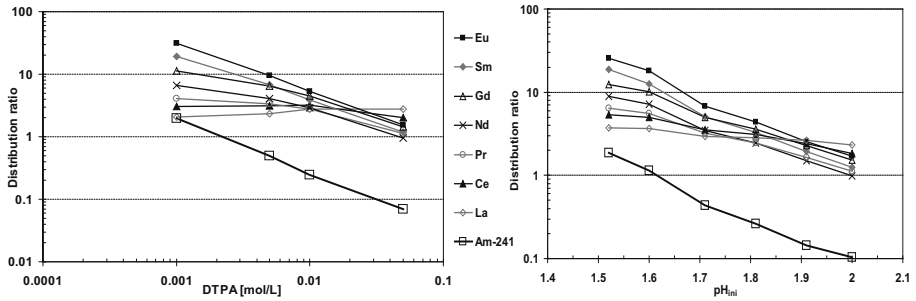

Fig. 44: The influence of left) DTPA and right) initial pH of the An-stripping solution on the distribution ratios of ^{241}Am and Ln. Org. phase: 0.2 mol/L TODGA + 5 vol-% 1-octanol in TPH loaded with Ln, Aq. phase: 1 mol/L glycine, 1 mol/L $NaNO_3$ + tracers (^{241}Am, ^{152}Eu), a) variable DTPA concentration, pH_{ini}=2 b) 0.05 mol/L DTPA, variable pH_{ini}.

Buffering of the An-stripping solution

The nitric acid extracted in the first step of the process (co-extraction of An/Ln) was partly back-extracted into the aqueous phase in the selective An-stripping step. This caused an increase in the acidity of the aqueous phase. To minimise this effect, the aqueous phase has to be buffered. Several buffers were tested (malic acid, glycine, lactic acid, citric acid, glycolic acid). Citric acid and glycine resulted in the smallest pH change (-ΔpH=0.13 and 0.15, respectively) combined with a high $SF_{Ln/Am}$ (Tab. 14). Glycine led to the best combination of good pH stabilisation and high Ln/Am separation, and was therefore used in further studies.

Tab. 14: The separation factors Ln/Am for TODGA + 1-octanol.

Buffer	Citric acid	Glycine
	$SF_{Ln/Am}$	
La	3	5
Pr	3	6
Eu	15	25
Gd	9	14
Nd	4	8
Ce	3	6
Sm	10	14

Org. phase: 0.2 mol/L TODGA + 5 vol-% 1-octanol in TPH (preloaded with lanthanides at 0.5 mol/L HNO_3),

Aq. phase: 0.05 mol/L DTPA, 1 mol/L $NaNO_3$, pH_{ini}=2, 1 mol/L citric acid (or glycine) + tracers (^{241}Am, ^{152}Eu).

Single-centrifuge tests

A series of single-centrifuge tests were performed using TODGA + 1-octanol in TPH as the solvent. The flow-sheets of the tests are shown in Fig. 45. The optimised conditions for extraction, scrubbing and the An-stripping step were applied in these tests.

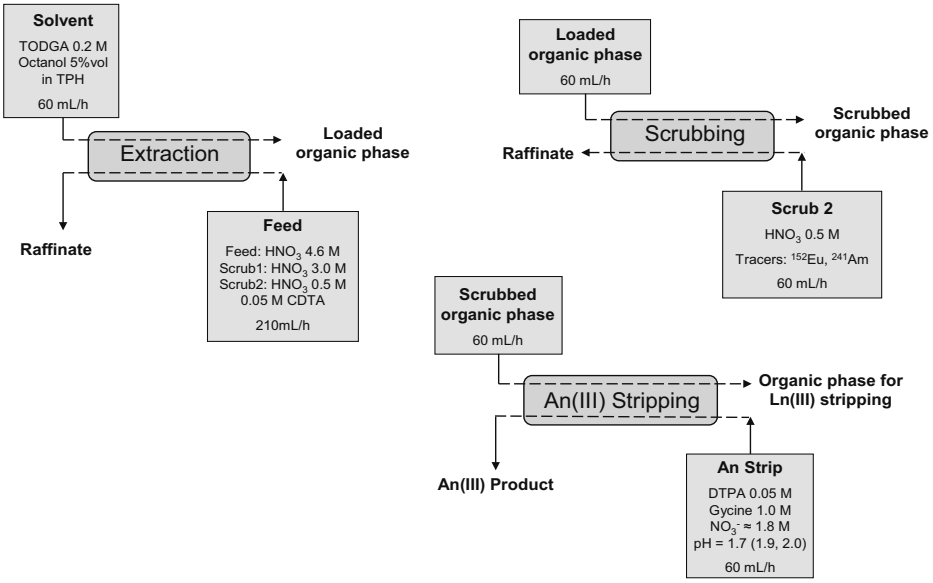

Fig. 45: The flow-sheets for the single centrifugal contactor tests

The results of the single centrifugal contactor tests are summarised in the Tab. 15. The lanthanides and Am(III) were quantitatively extracted in the first step (Extraction) with distribution ratios over 200 and they remained in the loaded organic phase through the nitric acid scrubbing step (Scrubbing). Three An-stripping solutions of different initial pHs were tested, namely 1.7, 1.9 and 2.0. The solution with a pH of 2.0 appeared to be the best choice for selective Am back-extraction (Stripping 2.0). The extraction of Pd and Zr was suppressed by using CDTA in the feed. Strontium and molybdenum were partly extracted by TODGA. However in the scrubbing step most of their content was removed from the organic phase.
The D_{Am} and D_{Ln} obtained in the An-stripping step (Stripping 2.0; see last column in Tab. 15) of the single-centrifuge test were higher than in the batch tests (Fig. 44) with much lower Ln/Am separation factors. This could be a result of inefficient nitric acid scrubbing from the organic phase in the previous step (Scrubbing) and/or the low efficiency of a single contactor in the stripping step. Therefore, these two steps must be further tested by increasing the number of the centrifugal contactors, which should increase their efficiency.

Tab. 15: The distribution ratios of metals in each tested step of the process (n.d. – not detected).

	Extraction	Scrubbing	Stripping 1.7	Stripping 1.9	Stripping 2.0
	Distribution ratios				
^{241}Am	-	24.3	4.78	0.79	0.42
Y	> 200	> 200	> 200	> 200	> 200
La	> 200	7.88	14.5	7.77	6.03
Ce	> 200	14.9	21.1	7.64	4.53
Pr	> 200	27.2	23.8	5.64	2.86
Nd	101	59	32	5.66	2.73
Sm	> 200	> 200	93.3	8.33	4.15
Eu	> 200	> 200	> 200	12.3	6.04
Gd	> 200	> 200	67.9	14.4	6.87
Sr	2.81	0.24	0.16	< 0.001	0.14
Mo	0.42	0.68	0.34	0.36	0.45
Ru	0.15	≈ 5	> 100	> 100	> 100
Pd	0.042	> 30	> 30	> 30	> 30
Sb	< 0.05	n.d.	n.d.	n.d.	n.d.
Cd, Rb, Rh	< 0.01	n.d.	n.d.	n.d.	n.d.
Te	< 0.005	n.d.	n.d.	n.d.	n.d.
Ba, Cs, Zr	< 0.001	n.d.	n.d.	n.d.	n.d.

Extraction: Org. phase: 0.2 mol/L TODGA + 5 vol-% 1-Octanol in TPH.
Aq. phase: synthetic PUREX raffinate with 4.6 mol/L HNO_3, 0.05 mol/L CDTA, 3 mol/L HNO_3 (Scrub1), 0.5 mol/L HNO_3 (Scrub2).
Scrubbing: Org. phase coming from the extraction step.
Aq. phase: 0.5 mol/L HNO_3 + tracers (^{241}Am, ^{152}Eu).
Stripping: Org. phase coming from the scrubbing step.
Aq. phase: 0.05 mol/L DTPA, 1 mol/L glycine, 1.8 mol/L $NaNO_3$, pH_{ini}=1.7, 1.9, 2.0

Conclusions

Within the framework of the ongoing European project ACSEPT (2008–2012), the focus is on the development of challenging partitioning processes. The objectives include simplifying processes developed in the past and reducing the number of cycles. The innovative SANEX concept using TODGA as the main extractant was studied as part of the European collaborative project. The French CEA achieved good results with the TODGA/TBP solvent. Further batch extraction studies were carried out at Forschungszentrum Jülich to further simplify the formulation of the solvent. First single-centrifuge tests were performed as the basis for developing a continuous counter-current process, which will be adapted with a battery of centrifugal contactors.

Acknowledgments

Financial support for this research was provided by the European Commission (project ACSEPT – Contract No. FP7-CP-2007-211 267).

References

[1] Bourg, S., Caravaca, C., Ekberg, C., Hill, C., Rhodes, C. ACSEPT, Toward the Future Demonstration of Advanced Fuel Treatments. Proceeding of International Conference GLOBAL 2009 (The Nuclear Fuel Cycle: Sustainable Options & Industrial Perspectives), Paris, 6–11 September 2009, paper 9185, pp. 937–943. , www.acsept.org

[2] Sasaki, Y., Sugo, Y., Suzuki, S., Tachimori, S. (2001) The novel ex-tractants diglycolamides, for the extraction of lanthnides and actinides in hno3-n-dodecane system. Solvent Extraction and Ion Exchange, 19(1), pp. 91–103.

[3] Tachimori, S., Sasaki, Y., Suzuki, S. (2002) Modification of TODGA-n-dodecane Solvent with a Monoamide for high loading of Lanthanides(III) and Actinides(III). Solvent Extraction and Ion Exchange, 20(6), pp. 687–699.

[4] Modolo, G., Asp, H., Schreinemachers, C., Vijgen, H. (2007) Development of a TODGA based Process for partitioning of actinides from a PUREX raffinate Part I: Batch extraction optimization studies and stability tests. Solvent Extraction and Ion Exchange, 25(6), pp. 703–721.

[5] Modolo, G., Asp, H., Vijgen, H., Malmbeck, R., Magnusson, D., Sorel, C. (2008) Demonstration of a TODGA-Based Continuous Counter-Current Extraction Process for the Partitioning of Actinides from a Simulated PUREX Raffinate, Part II: Centrifugal Contactor Runs. Solvent Extraction and Ion Exchange, 26(1), pp. 62–76.

[6] Magnusson, D., Christiansen, B., Glatz, J.P., Malmbeck, R., Modolo, G., Serrano-Purroy, D., Sorel, C. (2009) Demonstration of a TODGA based Extraction Process for the Partitioning of Minor Actinides from a PUREX Raffinate Part III: Centrifugal Contactor Run using Genuine Fuel Solution. Solvent Extraction and Ion Exchange, 27(1), pp. 26–35.

[7] Serrano-Purroy, D., Baron, P., Christiansen, B., Malmbeck, R., Sorel, C., Glatz, J-P. (2005) Recovery of minor actinides from HLLW using the DIAMEX process. Radiochimica Acta, 93(3), pp. 351–355.

[8] Serrano-Purroy, D., Christiansen, B., Glatz, J-P., Malmbeck, R., Modolo, G. (2005) Towards a DIAMEX process using high active concentrate. Radiochimica Acta 2005, 93 (3), 357–361.

[9] Hérès, X., Sorel, C., Miguirditchian, M., Camès, B., Hill, C., Bisel, I., Espinoux, D., Eysseric, C., Baron, P., Lorrain, B. (2009) Results of recent counter-current tests on An(III)/Ln(III) separation using TODGA extractant. Proceeding of International Conference GLOBAL 2009 (The Nuclear Fuel Cycle: Sustainable Options & Industrial Perspectives), Paris, 6–11 September 2009, paper 9384, pp. 1127–1132.

[10] Geist, A., Modolo, G. (2009) TODGA Process Development: an Improved Solvent Formulation. Proceeding of International Conference GLOBAL 2009 (The Nuclear Fuel Cycle: Sustainable Options & Industrial Perspectives), Paris, 6–11 September 2009, paper 9193, pp. 1022–1026.

5.7. Synthesis and thermal treatment of uranium-based microspheres through internal gelation

H. Daniels, S. Neumeier, G. Modolo

Corresponding author: g.modolo@fz-juelich.de

Abstract

An alternative to the direct final disposal of long-lived radionuclides is their separation (partitioning) from the original waste in connection with a subsequent appropriate treatment. The general aim is to lower the risk potential coming along with the radioactivity (radiotoxicity).

A promising concept after the partitioning step is the embedding of Am, Cm & Np, the “Minor Actinides” (MA), in uranium-based nuclear fuel (co-conversion). Through this the MAs can be eliminated by nuclear reactions with fast neutrons (transmutation) in upcoming reactor concepts.

One way to obtain such fuel is the internal-gelation process: Amorphous gel-spheres are created and thermally treated at comparably low temperatures to become crystalline. The main advantages are the high automation potential as well as the co-conversion being carried out predominantly in aqueous solutions without dust-creation.

The formulation of stable precursor solutions for the gelation is one crucial step towards a reliably working process. Therefore MA-surrogates were utilised for basic research on reaction mechanisms and speciation in the corresponding aqueous phases. Subsequently, the UO_2-based ceramics obtained through thermal treatment of the gels were characterised to optimise the calcination and sintering process.

Introduction

Advanced nuclear fuel management with the help of new reactor generations needs appropriate fuel matrices. A UO_2 based fuel with addition of minor actinides can serve as a fuel and transmutation matrix in parallel. Fabrication of such fuels has high demands due to radiotoxicity and contamination issues. A procedure minimising the connected risks is highly beneficial.

Internal gelation is a well known method to produce microspheres suitable as sphere-pac fuel or as precursors for fuel pellet fabrication. One variant of internal gelation was developed in Forschungszentrum Jülich by Förthmann et al. [1] In contrast to KEMA- and similar processes [2], the gelating agents were added in solid form. The advantage of this variant is the resulting higher effective uranium concentration in the precursor solution due to a less overall volume of water needed for solvation of the chemicals. Therefore, the preparation of acid deficient uranyl nitrate (ADUN), which leads to a higher uranyl solubility, is nonessential [1].

The work in 2010 focused on the investigation of chemical interactions between the involved species in solution and the thermal treatment of obtained uranium / neodymium microspheres through internal gelation. For the experiments, neodymium was utilized as a surrogate for a trivalent actinide such as americium. Additionally, creation ADUN through

dissolution of uranium oxide was undertaken to combine the advantages of the Jülich gelation process with the benefits of ADUN.

Interaction of the chemical species in a gelation precursor solution

As it is known that the gelation chemicals urea and HMTA can form complexes with uranyl-ions [3], a look was taken at the behaviour of neodymium in this environment. In Fig. 46, UV/Vis measurements at room temperature of pure neodymium-nitrate and additions of urea and HMTA in suprapure water can be seen. All three measurements show peaks at the same wavelengths without shifts. Hence, under the given conditions no measureable interaction of the compounds can be assumed. Therefore, pre-hydrolysis mechanisms as with the uranyl-ion [3] are also unlikely to take place. Fig. 47 shows a UV/Vis with pure uranyl-nitrate and an addition of urea and HMTA for comparison. With HMTA present, a shift of the uranyl-peak with a related increase of absorption can be seen, illustrating HMTA – uranyl interaction.

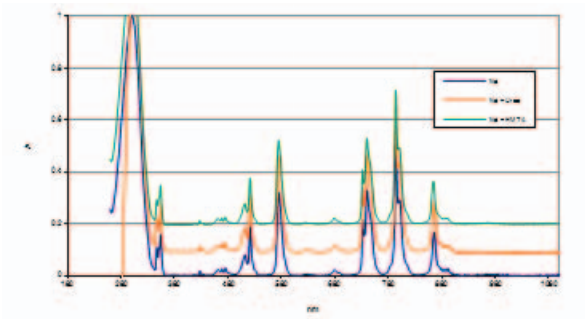

Fig. 46: UV/Vis of neodymium and with influence of urea/HMTA[Nd] = 2.5 mol/L, R_{HMTA}[1] = R_{Urea}[2] = 2; dilution: 1:1000; RT

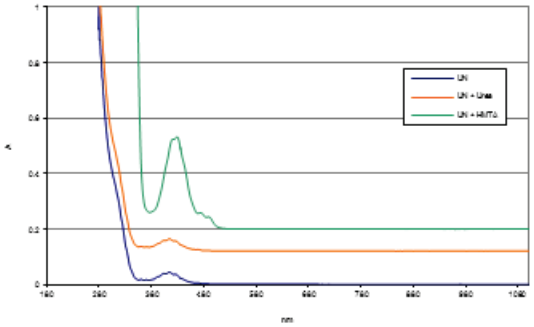

Fig. 47: UV/Vis of uranium and with influence of urea/HMTA [U] = 2.1 mol/L, R_{HMTA}= R_{Urea} = 2; dilution: 1:1000; RT

[1] R_{HMTA} = [HMTA] / [Me]; [Me]: [U] and/or [Nd] present in solution

[2] R_{Urea} = [Urea] / [Me]

Acid-Deficient Uranyl-Nitrate via dissolution of uranium oxide

Despite previous research about extractive denitration, a decision was made to utilise dissolution of β-UO_3 for ADUN creation. Reason for this is the corporation with the team of S. Grandjean at CEA, Marcoule and the need for a well known creation method.
Advantageous is the increase of the uranium concentration above the solubility limits of uranyl-nitrate with a stoichiometric nitrate amount. This allows a general higher specific uranium loading of the created gels.
First, ammonia-di-uranate (ADU) was obtained through precipitation out of 1 mol/L uranyl nitrate solution with subsequent filtration. The product was then heated up in air with a gradient of approximately 15 °C / min, leaving it at 430 °C for 1h before cooling to obtain β-UO_3. XRD measurements (Fig. 48) showed the β-UO_3 to be pure. The β-UO_3 was added to a 2.1 molar uranyl-nitrate solution and continuously stirred for 3 days. Not all of the solid matter dissolved, leaving the solution with a measured uranium concentration of 2.9 mol/L.
Accidentally, at one experiment the furnace temperature was too high, resulting in a lot of U_3O_8 being present in the sample after thermal treatment. Although not expected, a conducted dissolution experiment with this sample went well resulting in also 2.9 mol/L uranyl-nitrate solution. The [NO_3^-] / [U] ratio in the prepared solutions was calculated to be 1.45 which suits well to the gelation procedures, where a ratio of 1.5 is recommendable.

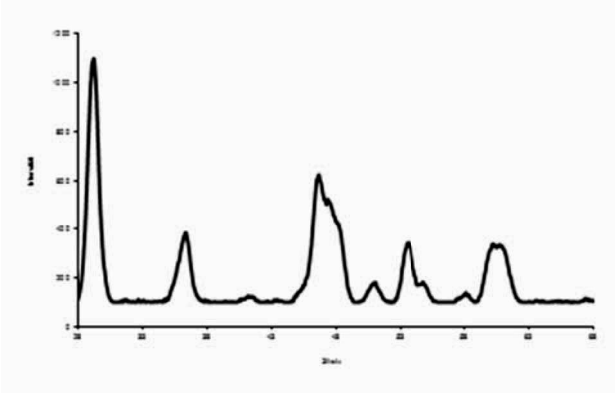

Fig. 48: XRD of prepared β-UO_3.

Investigations on precursor solution stability

Determination and verification of gelation points

Determination of gelation points (GPs) was started first with a conductivity-based measurement variant. The measured values were now verified with the more reliable viscosity-based method, also described in the literature. [4]
Fig. 49 shows a typical diagram in which viscosity over temperature is plotted. The point of dramatic viscosity increase marks the GP. The obtained values result in the gelation field shown in Fig. 50. In the gelation field the GPs are plotted in dependence on the relative amount of the gelation agents, urea and hexa-methylene-tetraamine (HMTA).
It was found that the results of the conduction-based and the viscosity-based method. Compared to the gelation of zirconium, investigated by Benay et. al. [5] the GPs are comparably low with temperatures of less than 30 °C. This gives important borders of

applicability of the gelation in dependence on the formulation, as the GP always has to be higher than the ambient temperature. Therefore, a certain minimum of the urea amount is necessary to stabilize the precursor solution.

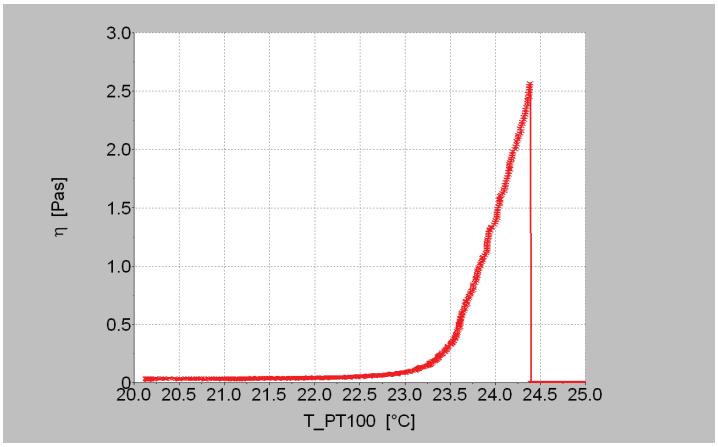

Fig. 49: Determination of the gelation point via viscosity

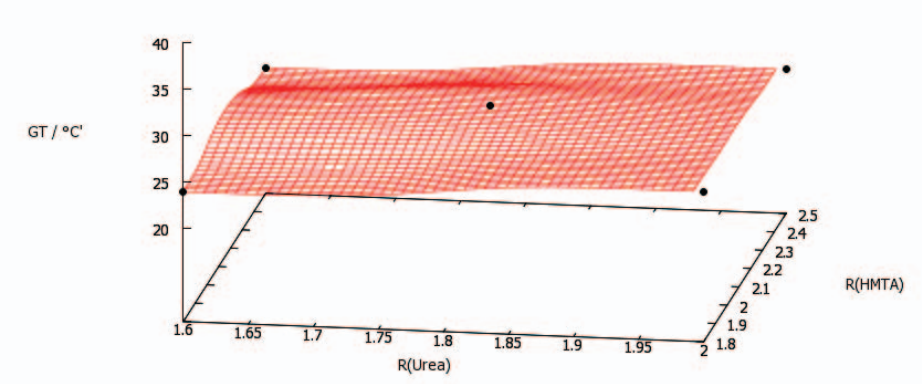

Fig. 50: Gelation field $U_{0.9}/Nd_{0.1}$ (red mesh area for illustration only).

Irradiation of urea and/or hexa-methylene-tetraamine containing solutions

As the stability of a precursor solution may be altered by radiation fields introduced by the present nuclides, as for example Am, it is important to investigate radiolysis mechanisms of these compounds. Therefore, irradiations with different dose rates of urea and HMTA containing solutions were carried out. These experiments took place in corporation with Chalmers University, Gothenburg, Sweden. After irradiation, the samples were sent to Jülich research centre for characterisation. Tab. 16 gives an overview about the samples and their irradiation.

Optical investigation showed a noticeable change of colour in all HMTA containing solutions. Nevertheless, the IR spectra (see Fig. 51) of the samples before and after radiation with the highest dose rate show no noticeable difference. It can be assumed that only a very small amount of the chemicals underwent radiolytic reactions. This stability against radiolysis is crucial for the future steps of the gelation, substituting a minor-actinide simulate with Pu or Am.

Tab. 16: Samples for γ-irradiation.

Number	Content	Dose
1	Urea-Solution, 2.8 mol/L	9,1 kGy
2	HMTA-Solution, 2.8 mol/L	9,1 kGy
3	HMTA/Urea-Solution, 2.8 mol/L	9,1 kGy
4	Urea-Solution, 2.8 mol/L	91 kGy
5	HMTA-Solution, 2.8 mol/L	91 kGy
6	HMTA/Urea-Solution, 2.8 mol/L	91 kGy
7	Urea-Solution, 2.8 mol/L	910 kGy
8	HMTA-Solution, 2.8 mol/L	910 kGy
9	HMTA/Urea-Solution, 2.8 mol/L	910 kGy

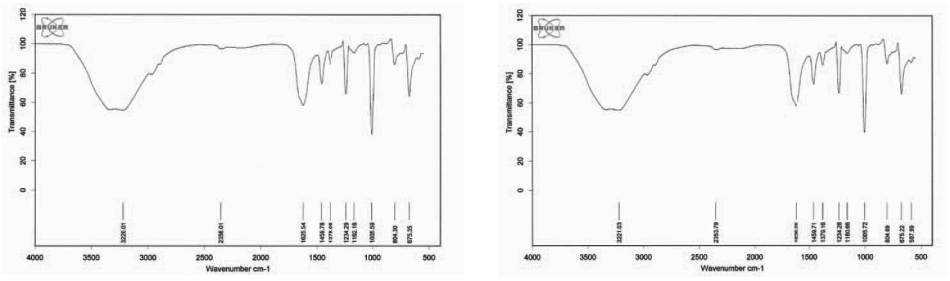

Fig. 51: IR-Spectra of unirradiated (left) and irradiated (right) (1000 kGy) solution Nr. 9.

Fabrication of uranium / neodymium spheres using acid-deficient-uranyl-nitrate

Subsequent to the work carried out before, microspheres utilising acid-deficient-uranyl-nitrate (ADUN) were synthesised.

According to the flowsheet shown in Fig. 52, the fabrication took place. As can be seen from Tab. 17, the advantage of using ADUN is the lower amount of needed HMTA in relation to the amount of metal-ions, as well as a higher metal-density in the gel due to a higher initial uranium concentration. The lower relative HMTA amount finds reason in the also lower acidity related to the uranium-concentration. Therefore less base is needed for a hydrolysis reaction that causes gelation.

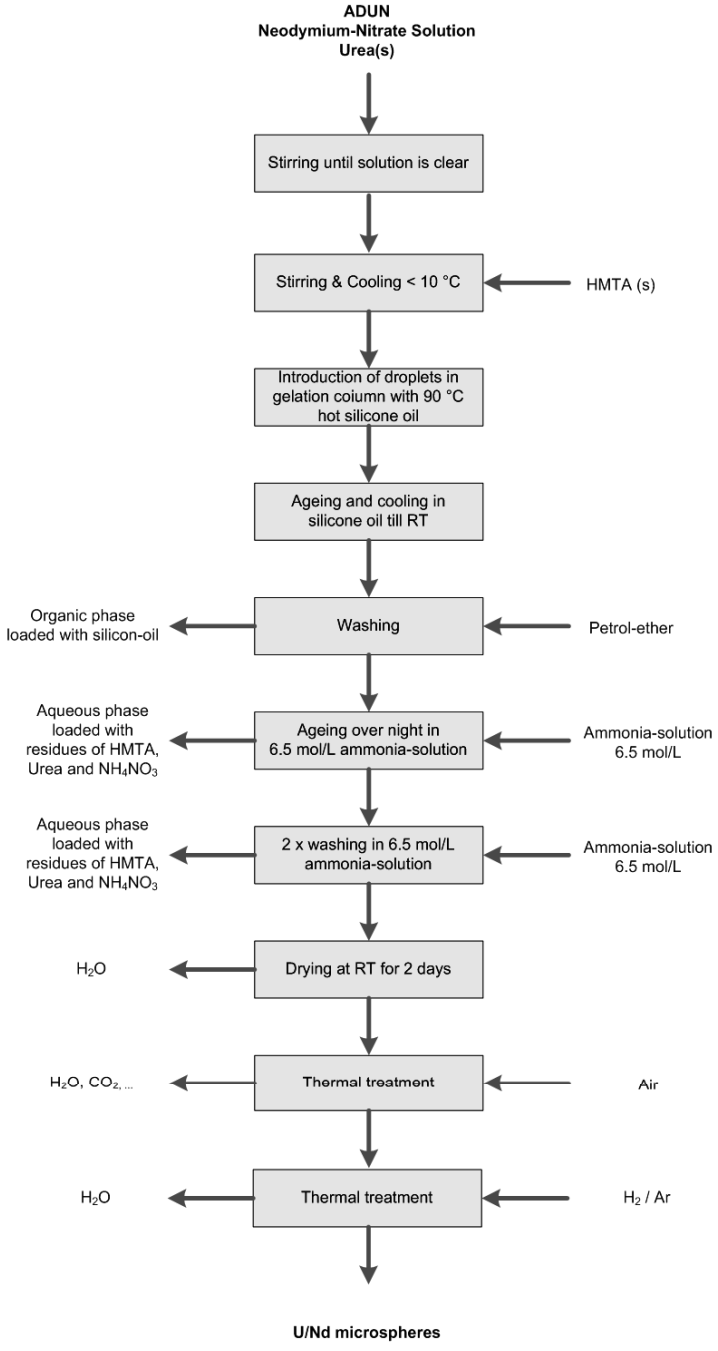

Fig. 52: Gelation flowsheet.

Tab. 17: Composition of precursor solution for gelation

Number	R(Urea)	R(HMTA)
1	2	1,875
2	2	1,65
3	2	1,35
4	1,8	1,88
5	1,8	1,65

Thermal treatment of the uranium / neodymium gels

Previous research showed that, although it is possible to achieve crack free gels, the thermal treatment leads with high certainties to crack formation in the spheres. This is due to decomposition of rests of the gelation chemicals urea and HMTA during the treatment, as well as to multiples phase changes until the final UO_2 fluorite-lattice is achieved. [3, 5, 6] As these effects put significant stress on the structure of the microspheres, efforts have to be taken to understand mechanisms and to improve the program of thermal treatment in a way that the formerly mentioned factors are counteracted.

Using the available literature as orientation [7], a modified calcination profile was developed. The temperature programme with the corresponding TG-DSC is illustrated in Fig. 53. Also the sintering was altered by letting it completely take place in reductive atmosphere (forming gas). The TG-DSC is illustrated in Fig. 53.

SEM investigations of the microspheres after sintering showed a high integrity with barely visible crack formation Fig. 54.

These parameters were applied in an oven for a thermal treatment of spheres with different gel formulations. After sintering, most of the spheres were macroscopically intact but showed cracks under an optical microscope. Nevertheless, XRD investigations of theses spheres revealed them to have a UO_2 fluorite-lattice without any other (Fig. 55). With the old calcination and sintering programmes this could not be achieved.

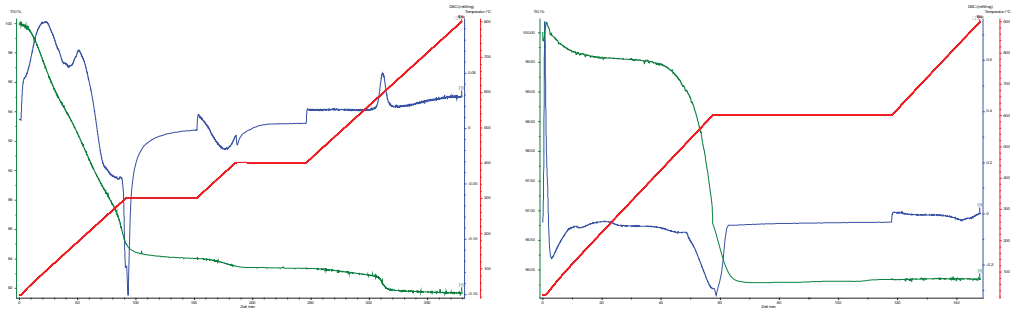

Fig. 53: TG-DSCs of new calcination (left) and sintering (right) programme.

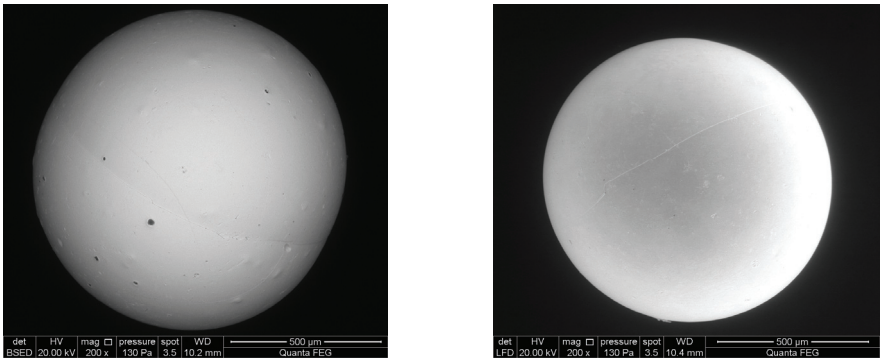

Fig. 54: SEM of sintered microspheres.

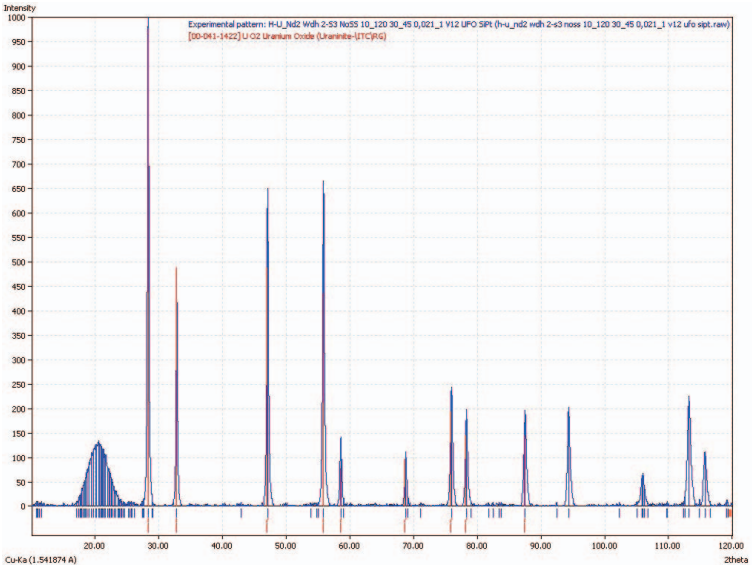

Fig. 55: XRD of sintered microspheres.

Conclusions

The work carried out in 2010 in Jülich Research Centre is further clarifying the influences of the gelation chemicals on the precursor-solution stability. Also, ADUN was started to be integrated in the Jülich internal gelation process. Better parameters of the thermal treatment of the gels were found to minimize the intermediate structural stress and to obtain a pure UO_2 matrix.

The precursor formulation for the Jülich internal gelation process is not trivial, as the bandwidth of variation of the amount of gelation chemicals has close limits to both sides. The investigation of GPs is a helpful instrument and it was shown in this and the last HYBAR with two different methods that the preferable R(Urea) and R(HMTA) are around 2.

Radiolysis in the aqueous solutions has to be taken into account and therefore needs to be investigated. First experiments have shown a certain resistance of Urea and HMTA against γ-irradiation. Successive experiments should take place with solutions that are closer to the real precursor solutions for gelation, as soon as the analysis of the current set of samples is finished.

Although being able to synthesise almost integer U/Nd-microspheres with a 100 % UO_2-lattice, it is important to make the thermal treatment more reliable. This part of the process is still a weakness that needs further research. Investigations on this topic are taking place at the moment.

Acknowledgements

Financial support for this research was provided by the European Commission (project ACSEPT – No. 211267).

References

1. Förthmann R, Naoumidis A, Nickel H, Burck W. Investigations on the Preparation of UO_2 Microspheres by Internal Gelation of a UO_2 Sol and from a Uranium(VI) Solution. Forschungszentrum Jülich GmbH; 1970.
2. Deptula A, Majani C. Sol-Gel Processes and their Applications. ENEA; 1986.
3. Allen GC, Holmes NR. A mechanism for the UO_2 to a-U308 phase transformation. J Nucl Mater. 1995;223:231–237.
4. Vaidya VN, Mukerjee SK, Joshi JK, Kamat RV, Sood DD. A study of chemical parameters of the internal gelation based sol-gel process for uranium dioxide. J Nucl Mater. 1987;148:324 – 331.
5. Benay G, Hubert F, Modolo G. Preparation of yttria-stabilized zirconia-ceria kernels as fuel precursors using internal gelation. Radiochim Acta. 2008;96:285–291.
6. Keller C, Boroujerdi A. Phasengleichgewichte in den Systemen UO_2-UO_3-$NdO_{1,5}$ und NpO_{2+x}-$NdO_{1,5}$. J inorg nucl chem. 1972;34:1187–1193.
7. Hunt RD, Collins JL. Uranium kernel formation via internal gelation. Radiochim Acta. 2004;92:909–915.

5.8. Conditioning of Minor Actinides in Monazite-type Ceramics

C. Babelot, S. Neumeier, A. Bukaemskiy, G. Modolo, D. Bosbach

Corresponding author: s.neumeier@fz-juelich.de

Abstract

Monazite-type ceramics are promising candidates for the conditioning of minor actinides. Pure monazite ($LaPO_4$) and doped-monazite $La_{(1-z)}X_zPO_4$ (X = Eu and z = 0.05, or X = Cm and z = a few ppm) were prepared by hydrothermal synthesis and its hydrated form ($LaPO_4{\cdot}0.5H_2O$) was synthesised by precipitation. The first characterisation results, structural and morphological combined with thermal behaviour, physical properties and state-of-the-art spectroscopy (TRLFS), are presented.

Introduction

In Germany, spent nuclear fuel and relatively small amounts of vitrified high level waste (from reprocessing in France and the UK) will be disposed in a deep geological formation. In principle, these waste forms seem to be suitable to accommodate the long-term safety of a waste repository system over extended periods of time. However, by using significantly more stable waste forms, the long-term safety of nuclear disposal could be significantly improved. Various ceramic waste forms seem to be promising materials in particular for tri- and tetravalent actinides, which dominate the long-term radiotoxicity [1; 2].

Here, we are studying lanthanide and actinide bearing monazite with respect to its stability under repository relevant conditions and in particular because of its stability against radiation damage [3]. XPO_4 ceramics are named after their natural mineral analogue: monazite for X = La to Gd (monoclinic structure) and xenotime for X = Tb to Lu and Y (tetragonal structure).

The processes used to synthesise these samples were aqueous chemical routes such as hydrothermal synthesis and precipitation. Indeed, to avoid radioactive dust formation, synthesis routes like conventional solid state reaction are not advisable. Structural and morphological results applying XRD and SEM are presented here combined with thermal behaviour and physical properties. Time resolved laser fluorescence spectroscopy (TRLFS) was used to probe the incorporated Eu(III) or Cm(III) in order to obtain structural information on its local environment.

Monazite and Rhabdophane

Wet-chemical methods were applied in this work for the preparation of monazite ($LaPO_4$) and rhabdophane ($LaPO_4{\cdot}0.5H_2O$). Monazite samples were prepared by hydrothermal synthesis (T=200 °C). This fabrication process partly followed that described by Meyssamy [4]. Rhabdophane powders were synthesised by precipitation from lanthanum–citrate chelate solution and phosphoric acid (at room temperature). This process was partially adapted from the route described by Boakye et al. [5].

In order to study the impact of calcination on these ceramics, the thermal behaviour of the dried powders was investigated from room temperature up to 1000 °C by thermogravimetry (TG) coupled with differential scanning calorimetry analysis (DSC) in air atmosphere with a heating rate of 10 K/min. Fig. 56 shows the comparison of the TG-DSC measurements for monazite and rhabdophane (at pH=5 after washing). The mass loss of the monazite sample

is about 4% while the one of the rhabdophane is about 10% after a thermal treatment up to 1000 °C. This difference is partly caused by the residual crystal water contained in the rhabdophane structure.

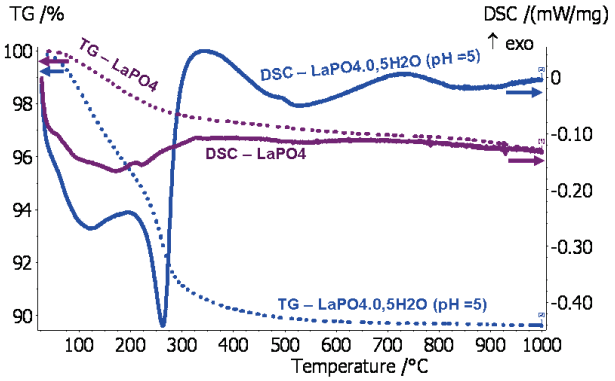

Fig. 56: TG-DSC measurements of monazite and rhabdophane (washed until pH=5) powders.

For both powders a broad endothermic peak is observed between 100 and 200°C, which can be explained by the elimination of adsorbed gas and residual water. For the rhabdophane powder, an additional endothermic peak at ~270 °C is observed which is linked to the elimination of the 0.5 mol of the crystal water.

The broad exothermic peak between 600 and 800 °C belongs to the phase transformation from hexagonal to monoclinic (from rhabdophane to monazite) structure. Naturally, this peak does not appear on the monazite plot (magenta plot).

Fig. 57 shows the X-ray diffraction patterns of the dried monazite (left) and rhabdophane (right) powders.

The XRD result of the monazite ($LaPO_4$) sample confirms that the phase is pure within the limits of the method. After calcination of the rhabdophane powder at 1000 °C, XRD data show the similitude of the monazite (light blue) and the calcined rhabdophane (dark blue). The hexagonal to monoclinic phase transformation occurs. The FWHM (full width at half maximum) decreased for the 1000°C-calcined rhabdophane due to beginning of the material recrystallization (microstrain ε, crystallite size *d*). The diffractogram of rhabdophane powder also confirms the purity of this phase just after the precipitation.

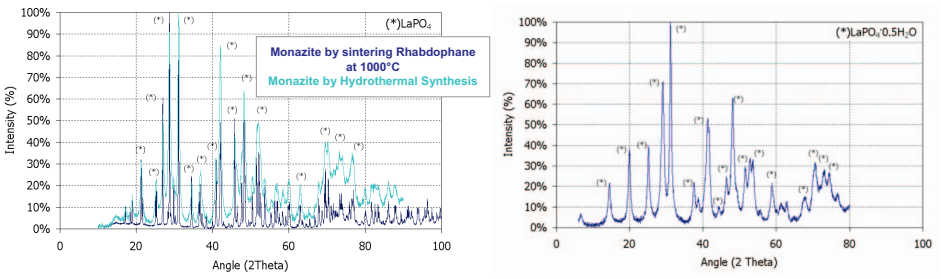

Fig. 57: XRD patterns of monazite obtained after hydrothermal synthesis and by calcination of rhabdophane (left). XRD of rhabdophane for comparison (right).

The morphology of the powder was studied with scanning electron microscopy (SEM) as shown in Fig. 58. The rhabdophane particles were round and their diameters is between 0.1 and 2 µm.
Since the phase transformation (hexagonal to monoclinic) ends around 850 °C, the rhabdophane particles were heated up to 1000 °C, where they consolidate together. This is the beginning of the sintering process. The comparison between the left and the right photo in Fig. 58 shows significantly the beginning of the densification.

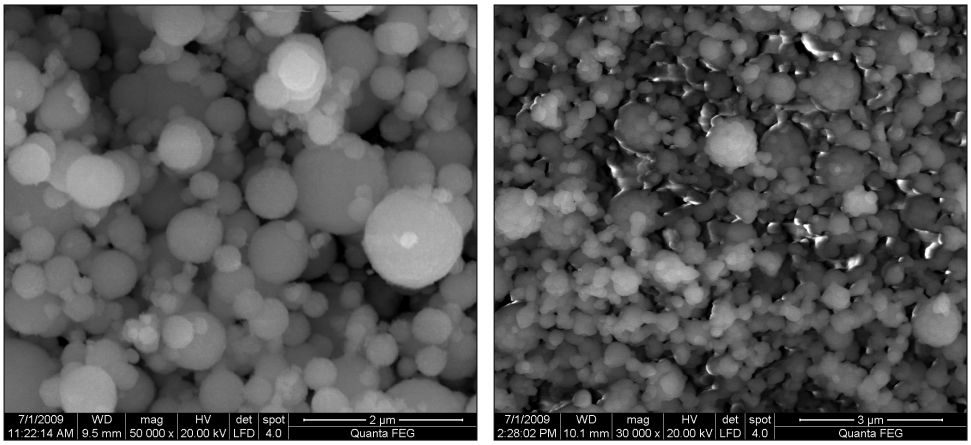

Fig. 58: SEM images of $LaPO_4 \cdot 0.5H_2O$ sample (left) and of calcined (1000°C) $LaPO_4 \cdot 0.5\ H_2O$ sample (right).

In this work, leaching tests are planned to be done on both powder and pellets. Indeed leaching tests on pellets is a standard method (e.g. Soxhlet method) and a study on pellet density is necessary.
The investigated powders were compacted by cold uniaxial pressing, applying pressures between 130 and 510 MPa. The pellets were made by powder prepared by hydrothermal synthesis. The relative green density and the relative sintered density both depend on the applied pressure (Fig. 59). The results of the relative green density in relation to the logarithm of the pressure show that the values form a linear function. This is a typical behaviour for ceramic materials [6]. After the sintering at 1400°C [7], the relative sintered density of the pellets was determined by Archimedes method, i.e. by hydrostatic weighing in water (see lower figure).
The value of the pressure related to the maximal density - optimal pressure - is between 250 and 400 MPa. The sintered density at this optimal pressure is above 98% of theoretical density.

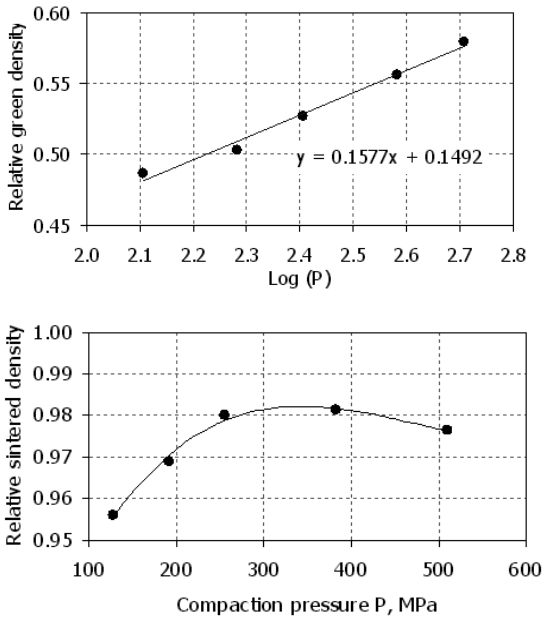

Fig. 59: Compressibility curve for monazite powders (upper figure) and relative sintered density of monazite pellets, as a function of compaction pressure (lower figure).

The SEM image (Fig. 60) shows the microstructure of a $LaPO_4$ pellet sintered at 1400°C. Porosity is observed neither in the grains nor at the groundboundaries.

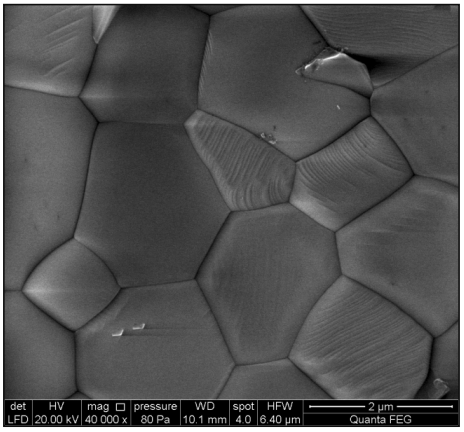

Fig. 60: SEM image of $LaPO_4$ pellet sintered at 1400°C.

Monazite matrices were doped with 5 mol% Eu(III) (as a non-radioactive chemical homologue for Am(III)) and a few ppm Cm(III). Time Resolved Laser Fluorescence Spectroscopy (TRLFS) was used to explore the local structural environment of Eu and Cm

within the monazite crystal structure. Indeed Cm has a high fluorescence rate of yield which allows running TRLFS measurements with a very low Cm concentration.
These experiments revealed that Eu^{3+} and Cm^{3+} are incorporated in the La site as expected. Indeed the emission spectrum of Eu^{3+} resolves all peaks in the F_2 transition (see Fig. 61). A minor site in the Eu^{3+} doped sample is identified as coordinated with a hydroxide molecule.
The resolution of the ground state splitting with direct excitation of Cm^{3+} doped samples show the presence of "satellite" sites [8]. Fig. 62 shows the excitation of four different sites, each with four-fold splitting. Their origin has been discussed in a recent publication [9].

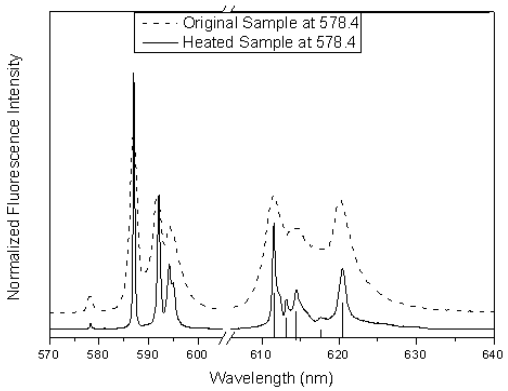

Fig. 61: Emission spectra of the major Eu species from direct excitation at 578.4 nm before and after calcining $LaPO_4$.

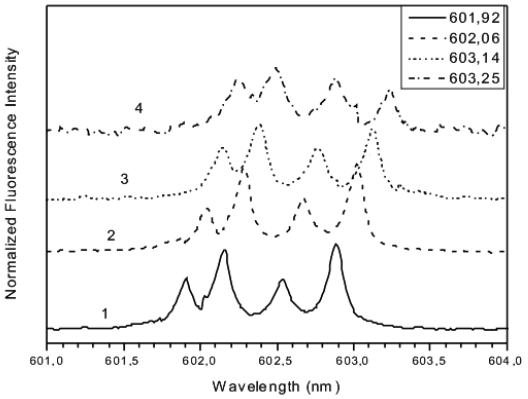

Fig. 62: High resolution emission spectra from direct excitation of Cm in calcined $LaPO_4$(T_c=1000°C).

An essential parameter describing the stability of the host phases is the resistance to radiation. Radiation damage to the monazite type ceramics has been induced by means of ion bombardment. See Schlenz et al. (this issue) for the description of the first experiments and results.

Conclusion and outlook

Monazite-type ceramics, as a promising candidate for the conditioning of minor actinides, were studied in this work. Monazite ($LaPO_4$) and rhabdophane ($LaPO_4 \cdot 0.5H_2O$) powders were prepared by hydrothermal synthesis (T=200°C) and by precipitation (room temperature). The thermal analysis and XRD show that the monazite powders are already crystalline after synthesis and subsequent drying, whereas the rhabdophane transforms at temperatures over 800°C to the monoclinic monazite structure. On the base of the synthesised monazite powder, pellets with a 98% of the theoretical density were prepared by cold pressing and sintering. TRLFS confirms the substitution of Eu(III) and Cm(III) on the La site of $LaPO_4$.

The corrosion behaviour of synthetic ceramics will be investigated soon. To this end, the ceramics will be subjected to leach tests under conditions of relevance for final repositories.

Aknowledgements

This work is supported by the Ministerium für Innovation, Wissenschaft, Forschung und Technologie des Landes (MIWFT) Nordrhein-Westfalen; AZ: 323-005-0911-0129.
We would like to thank Kiel Holliday and Thorsten Stumpf (KIT-INE, Karlsruher Institut of Technology - Institut für Nukleare Entsorgung, Germany) for the cooperation and the TRLFS measurements.

References

[1] G. R. Lumpkin, Elements 2 (2006) 365-72.
[2] P. Trocellier, Annales De Chimie-Science Des Materiaux 26 (2001) 113-30.
[3] E. H. Oelkers and J. M. Montel, Elements 4 (2008) 113-16.
[4] H. Meyssamy, K. Riwotzki, A. Kornowski, S. Naused, and M. Haase, Advanced Materials 11 (1999) 840.
[5] E. E. Boakye, P. Mogilevsky, and R. S. Hay, Journal of the American Ceramic Society 88 (2005) 2740-46.
[6] A. A. Bukaemskiy, D. Barrier, and G. Modolo, Journal of the European Ceramic Society 29 (2009) 1947-54.
[7] D. Bregiroux, S. Lucas, E. Champion, F. Audubert, D. Bernache-Assollant, Journal of the European Ceramic Society 26 (2006) 279-287.
[8] Murdoch, K.M., Edelstein, N.M., Boatner, L.A., Abraham, M.M., J. Chem. Phys. 105 (1996), 2539.
[9] Site-selective time resolved laser fluorescence spectroscopy of Eu and Cm doped $LaPO_4$, K. S. Holliday, C. Babelot, C. Walther, S. Neumeier, D. Bosbach, Th. Stumpf – *submitted to Radiochimica Acta (2011).*

5.9. Synthesis and characterization of ZrO_2 based ceramics for innovative nuclear waste strategies

S. Finkeldei, S. Neumeier, A. Bukaemskiy, H. Schlenz, G. Modolo, D. Bosbach
Corresponding author: s.finkeldei@fz-juelich.de

Introduction

One of today's strategies for the disposal of spent fuel is the vitrification of the high level liquid waste issuing the PUREX process leading to amorphous waste forms. A different approach is to consider crystalline ceramic materials as potential host matrices for the disposal of long-lived radionuclides in a deep geological repository. Therefore, several ceramic materials, such as monazite or pyrochlore are investigated. The advantage of crystalline over amorphous materials such as borosilicate glasses is their high physical and chemical stability. Moreover, the possibility of release of the radionuclides is low due to their fixed placement at well-defined lattice sites. Lumpkin [1] reviews different crystalline phases with respect to their suitability as host matrices. This work points out that zirconates, such as $Gd_2(Zr,Hf)_2O_7$ stand out among crystalline phases due to their high radiation tolerance. Pyrochlores in nature, e.g. $Gd_2(Ti,Hf)_2O_7$ are well known for their high durability in aqueous environments. Combining the advantages of zirconates with the pyrochlore structure yields a promising candidate for a host matrix for the disposal of actinides.
In this work the synthesis and characterization of zirconia-based pyrochlore-type ceramics is described. Different routes of synthesis are compared. Moreover, their assets and drawbacks are outlined. The results of the characterization of the products with x-ray diffraction, secondary electron microscopy and thermal analysis are discussed.

The general pyrochlore formula is $^{VIII}A_2{}^{VI}B_2{}^{IV}X_6{}^{IV}Y$. The Roman numerals denote coordination numbers of the corresponding ion. The A- and B-positions are occupied by tri- and tetravalent cations. The oxygen ions are located at the X-positions while the Y-positions may be occupied by fluoride, hydroxide or oxygen ions. In the case of zirconia based pyrochlores the A-positions can be filled with any element of the lanthanide series from La – Gd. Moreover, actinides in different valence states (3+, 4+ and 5+) can form the pyrochlore structure occupying the A or B-position [2,3]. Fig. 63 shows an illustration of the unit cell of the pyrochlore structure on the left and the coordination polyhedra of a Nd- and a Zr-ion in detail on the right.

It can be seen that the A-cations are coordinated by scalenohedra (blue polyhedra) of eight oxygen atoms each. The scalenohedra are joined along their edges with the octahedra (green polyhedra) of oxygen ions surrounding the B-cations. The octahedra themselves are connected along corners. The pyrochlore structure can only be obtained in a specific range of the ionic radii [4]: r_A/r_B= 1.46 – 1.78 with r_A=0.087 – 0.151 nm and r_B=0.040 – 0.078 nm. Otherwise, the less ordered defect-fluorite structure is formed.

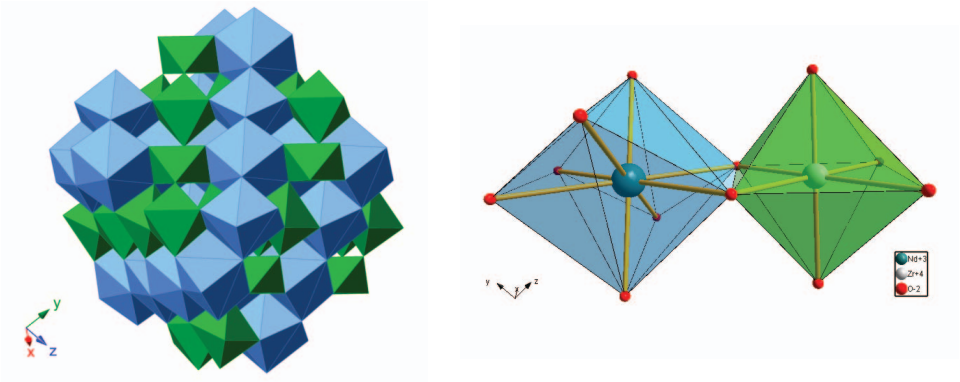

Fig. 63: Description of the unit cell of the pyrochlore structure (left) and a pair of edge linked coordination polyhedra of the Nd- and Zr-ions (right).

Synthesis of pyrochlore-type ceramics

One aspect of this study was the comparison of various synthesis routes. We synthesized pyrochlore-type ceramics via solid state reaction, hydrothermal synthesis, a coprecipitation route and a sol-gel process. Working with radionuclides, especially with alpha emitters such as actinides, reactions involving dust should be avoided due to the risk of contamination. Neodymium serves as a non-radioactive surrogate for trivalent actinides, such as Americium.
Solid state reactions are very common for the synthesis of ceramics [5]. A lanthanum zirconate ($La_2Zr_2O_7$) with pyrochlore structure was obtained after sintering a stoichiometric mixture of La_2O_3 and $ZrOCl_2$ with potassium carbonate at 1600 °C. A temperature of 900 °C that can be found in the literature [5] was not high enough to synthesize pure pyrochlore in a single reaction step. The main disadvantage of the solid state reaction is the formation of dust during synthesis. Therefore the focus was laid on wet synthesis routes.
One of the wet synthesis routes is the hydrothermal synthesis. Its main advantage is the crystallinity of the products at relatively low temperatures [6]. A final sintering step is usually not needed. The synthesis was carried out according to a procedure by Chen and Xu [7]. Even though the reaction temperature and primary pressure were varied in the range of 200 - 240 °C and 20 - 25 bar, respectively, no pyrochlore-type lanthanum zirconate could be synthesized. In all cases, a mixture of segregated phases consisting of $La(OH)_3$ and ZrO_2 were obtained. Additional high temperature sintering (1600 °C) of the product mixture led to the single phase solid solution with pyrochlore structure. However, the additional sintering step leaves the main advantage of the hydrothermal synthesis unutilised.
Coprecipitation was a successful wet chemical route for the preparation of pyrochlore-type neodymium zirconate ($Nd_2Zr_2O_7$). During the coprecipitation the intermediate product is synthesized by formation of the hydroxides in ammonia solution (equation 1 and 2) and subsequent thermal treatment delivers the final product (equation 3).

$$ZrOCl_2 + 2\ NH_3 + 3\ H_2O \rightarrow Zr(OH)_4 \downarrow + 2\ (NH_4^+, Cl^-) \quad (1)$$

$$Nd(NO_3)_3 + 3\ NH_3 + 3\ H_2O \rightarrow Nd(OH)_3 \downarrow + 3\ (NH_4^+, NO_3^-) \quad (2)$$

$$2\ Zr(OH)_4 + 2\ Nd(OH)_3 \rightarrow Nd_2Zr_2O_7 + 7\ H_2O \quad (3)$$

As precipitation agents, either gaseous or liquid ammonia can be used. The reaction with gaseous ammonia was carried out to investigate the reaction kinetics. The precipitation of $Zr(OH)_4$ starts at a pH value of 2.13 and finishes before the $Nd(OH)_3$ precipitation reaches its maximum. Accordingly there is only a small pH region in which an actual coprecipitation can occur. Therefore, the “reverse dropping method” [8] was carried out for the synthesis. Its main advantage over the use of gaseous ammonia as precipitation agent is the high pH value at the beginning of the reaction that can be kept constant over the entire reaction time. The high pH value enforces the actual coprecipitation of the neodymium hydroxides and the zirconium hydroxides. Using the “reverse dropping method”, neodymium zirconate and lanthanum zirconate with pyrochlore structure as well as gadolinium zirconate with a defect-fluorite-structure were prepared. The products were analysed by x-ray powder diffraction and scanning electron microscopy. Fig. 64 shows the x-ray diffraction pattern of $Nd_2Zr_2O_7$ with pyrochlore structure.

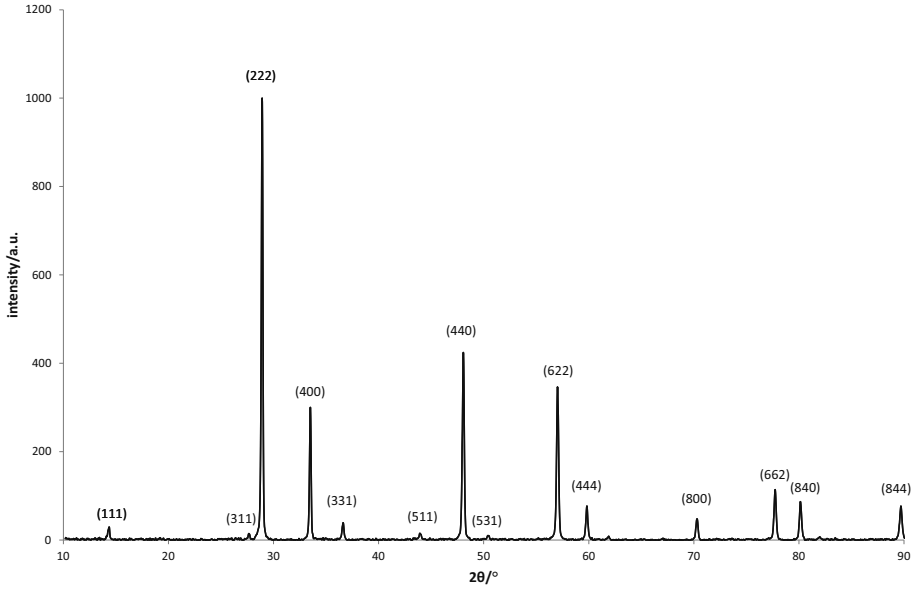

Fig. 64: X-ray diffraction pattern of a $Nd_2Zr_2O_7$ compound with pyrochlore structure, synthesized by coprecipitation reaction.

All Bragg reflexes of the pyrochlore structure could be indexed. Via coprecipitation single-phase $Nd_2Zr_2O_7$ pyrochlore was obtained within the limit of detection.

Zirconates with pyrochlore structure were synthesized by a sol-gel process. The internal gelation is a dust-free process. This process is especially favourable in combination with a prior partitioning step, because the actinide solutions that are obtained from the separation can be used directly. Using the internal gelation a kernel-like product is formed, which is appropriate for subsequent treatment. The challenge of the sol-gel route is the sol-formulation. The precise sol-formulation is very important for the integrity of the produced kernels. If the HMTA/urea ratio is not adjusted to the system one will receive a slurry product instead of well sharped kernels. HMTA and urea were used as gelation and complexation

agents for the synthesis of neodymium zirconate with pyrochlore structure. Collins et al.[9,10] postulate a complexation of the zirconium with urea at a temperature of 0 °C (equation 4) that suppresses the hydrolysis of the zirconium. The solution is dropped into hot silicone oil.

$$2\ CO(NH_2)_2 + Zr^{4+} \rightleftharpoons Zr[CO(NH_2)_2]_2^{4+} \quad (4)$$

$$Zr^{4+} + x\ H_2O \rightleftharpoons Zr(OH)_4 \cdot yH_2O + 4\ H^+ \quad (5)$$

$$(CH_2)_6N_4 + H^+ \rightleftharpoons (CH_2)_6N_4 \cdot H^+ \quad (6)$$

$$(CH_2)_6N_4 \cdot H^+ + 3\ H^+ + 6\ H_2O \rightleftharpoons 4\ NH_4^+ + 6\ CH_2O \quad (7)$$

A decomplexation of the zirconium occurs and the hydrolysis begins (equation 5). The hydrolysis is accompanied by a release of protons leading to a protonation of the HMTA (equation 6). The high temperature of the silicone oil causes the HMTA to decompose into ammonia and formaldehyde. The result is an increasing pH value that leads to the formation of gel-like metal hydroxides. Subsequent thermal treatment yields kernels with pyrochlore structure. The product was analyzed with scanning electron microscopy (SEM) and energy dispersive x-ray spectroscopy. Fig. 65 shows the SEM image of a crushed $Nd_2Zr_2O_7$ kernel with pyrochlore structure (left) and a close-up of the surface (right).

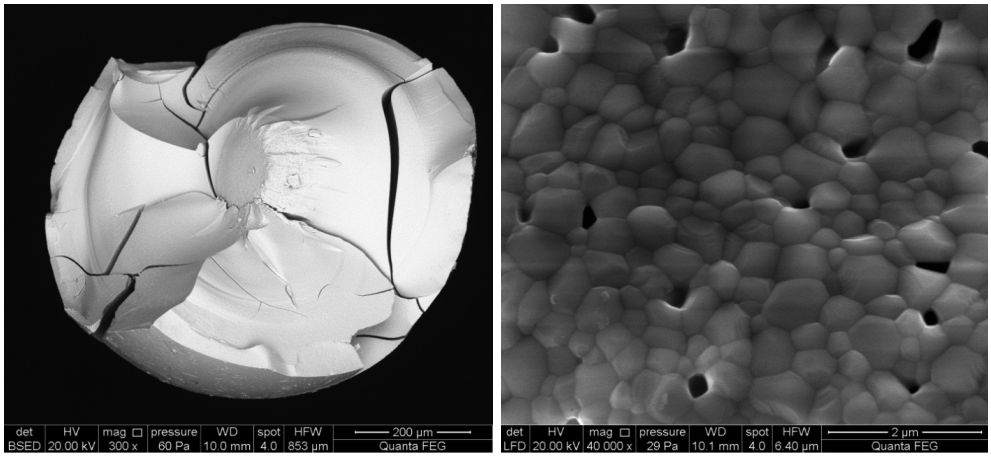

Fig. 65: Backscattered electron micrograph of a crushed $Nd_2Zr_2O_7$ kernel (left) and close-up of its inside (secondary electron micrograph).

The picture on the right exhibits the porous inside of the kernel. A composition of 70.1 at% of oxygen, 15.4 at% of zirconium and 14.5 at% of neodymium was determined by EDX measurements. The difference of the at% of the Zr and Nd is less than 1 at% and therefore within the limit of error. The at% value of oxygen is highly overrated by the EDX. This is caused by the low-vacuum mode that was used to perform the EDX measurements at uncoated samples. The EDX-measurement in combination with the XRD is proof for the single phase of the synthesized pyrochlore.

Characterization of the synthesized pyrochlores by thermal analysis

To get a deeper understanding about the process of crystallization of the neodymium zirconate systems the products of the internal gelation and the coprecipitation were analysed by thermogravimetry (TG) and differential scanning calorimetry (DSC). The samples were heated up from room temperature to 1300 °C with a heating rate of 10 K/min. Fig. 66 shows the TG/DSC thermogram of a neodymium zirconate synthesized by coprecipitation. Between the temperatures of 109 °C – 344 °C the DSC-curve exhibits four endothermic peaks. These peaks can be attributed to the desorption of adsorbed water and a possible decomposition of impurities. To investigate the process of crystallization in detail, x-ray measurements were carried out in addition to the TG/DSC-measurements. The x-ray measurements were taken from samples that were heated to temperatures right before and after the four exothermic peaks at 407 °C, 514 °C, 684 °C and 811 °C and subsequently quenched to room temperature. Using these x-ray measurements we were able to attribute the peaks to the solid solution formation.

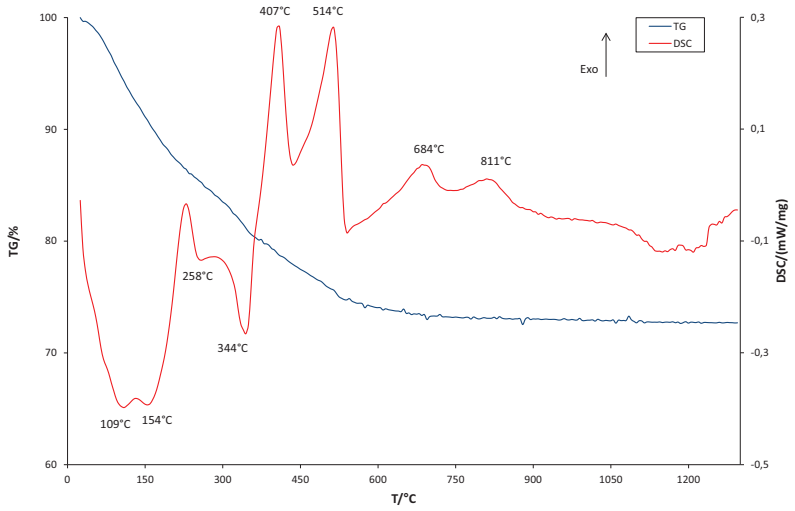

Fig. 66: TG/DSC-curves of a neodymium zirconate by coprecipitation with gaseous ammonia as precipitation agent.

Fig. 67 shows the TG/DSC thermogram of a neodymium zirconate from the internal-gelation process.

The thermogram exhibits only one endothermic and a single exothermic effect. The endothermic peak at 120 °C is caused by the desorption of adsorbed water. The exothermic peak at 785 °C indicates the solid solution formation of $Nd_2Zr_2O_7$.

Comparing the synthesis routes described above the process of crystallization for the sol-gel route is straightforward while the crystallization process of the coprecipitation product occurs in several steps. Nevertheless the coprecipitation seems more favourable than the internal gelation due to the difficulties involved with the sol-formulation.

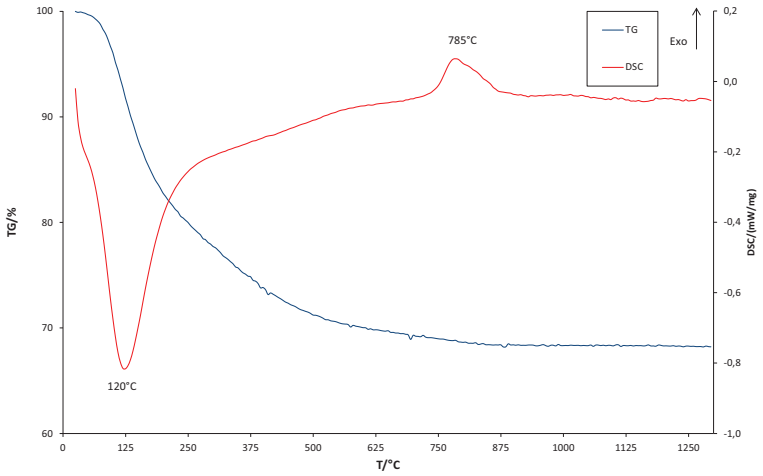

Fig. 67: TG/DSC thermogram of a neodymium zirconate by internal gelation.

Conclusion

Among the three wet chemical synthesis routes conducted in this work coprecipitation and the sol-gel route were successful for the preparation of pyrochlore-type zirconates. The characterization of the products with XRD and SEM exhibits single phase $Nd_2Zr_2O_7$ pyrochlore. The scanning electron microscopy image shows that coprecipitation as well as internal gelation lead to a homogeneous product which was proofed by backscattered electron images.

In summary, the sol-gel synthesis is a straightforward synthesis-route for the preparation of $Nd_2Zr_2O_7$. However, any variation in the Nd/Zr-system complicates the internal gelation process because the sol-formulation needs to be adjusted every time. Despite its multi stage formation process coprecipitation is easy to control and therefore has great potential for the preparation of zirconia-based pyrochlores even with changes in the Nd/Zr-system.

Acknowledgements

This work is supported by the Ministerium für Innovation, Wissenschaft, Forschung und Technologie des Landes (MIWFT) Nordrhein-Westfalen; AZ: 323-005-0911-0129.

References

[1] G. R. Lumpkin, Elements 2 (2006) 365-372.
[2] R. C. Ewing, C. R. Geoscience 343 (2011) 219-229.
[3] B. C. Chakoumakos, R. C. Ewing, Mater. Res. Soc. Symp. Proc. 44 (1985) 641-646.
[4] R. C. Ewing, W. J. Weber, J. Lian, J. Appl. Phys. 95 (2004) 5949-5971.
[5] Y. P. Tong, J. W. Zhu, L. D. Lu, X. Wang, X. J. Yang, J. Alloy. Comp. 465 (2008) 280-284.
[6] N. Hingant, N. Clavier, N. Dacheux, N. Barre, S. Hubert, S. Obbade, F. Taborda, F. Abraham, J. Nucl. Mater. 385 (2009) 400-406.
[7] D. Chen, R. Xu, Mater. Res. Bull. 33 (1998) 409-417.
[8] H. F. Chen, Y. F. Gao, Y. Liu, H. J. Luo, J. Alloy. Comp. 480 (2009) 843-848.
[9] J. L. Collins, M. H. Lloyd, R. L. Fellows, Radiochim. Acta 42 (1987) 121-134.
[10] J. L. Collins, K. K. Anderson, Report Number ORNL/CP-96463, 1998.

5.10. Synthesis and Characterization of $Sm_{1-x}Ce_xPO_4$ Ceramics used for Nuclear Waste Management

J. Heuser, H. Schlenz, G. Modolo, M. Klinkenberg, C. Schreinemachers, A. Neumann,

S. Schmitz, D. Bosbach

Corresponding author: j.heuser@fz-juelich.de

Abstract:

Samarium-Cerium-monazites $Sm_{1-x}Ce_xPO_4$ (x = 0-1) can be used as simulation phases for radionuclide-doped matrices. Thirteen different compositions of the aforementioned solid solution were prepared by hydrothermal synthesis at T = 220 °C and $p \approx 25$ bar. The sample properties were analysed chemically by electron microscopy (EDX), structurally by powder x-ray diffraction (XRD) and Raman spectroscopy and thermally by TG-DSC. By means of our characterizations we could show that the solid solution with endmembers $SmPO_4$ and $CePO_4$ doesn`t reveal an ideal behaviour. Accordingly we assume a melting point minimum in the compositional range $Sm_{0.7}Ce_{0.3}PO_4$ - $Sm_{0.6}Ce_{0.4}PO_4$.

Introduction

The conditioning of nuclear waste from nuclear power plants is an important issue according to science and society. Therefore the research on an appropriate matrix for the immobilization of e. g. actinides is of great interest. Beyond the widely used borosilicate glasses, ceramics are promising materials for conditioning. In many cases natural analogues can demonstrate the different properties of possible matrices for radionuclide conditioning. Monazite-type ceramics with compositions $LnPO_4$ (*Ln* = La, Ce, Nd, Sm, Eu, Gd), e. g., represent an important material in this field. To obtain a suitable host matrix for radionuclides, the characterization of monazites of different chemical composition and their thermal and structural behaviour is essential. Monazite was chosen because of its outstanding properties according to radiation resistance and chemical durability. Our aim is to find a composition with a melting point minimum or an eutectic mixture in order to improve the production design for future industrial synthesis.

Experimental

Sm-Ce-Monazites of thirteen different chemical compositions were prepared by hydrothermal synthesis using diammonium hydrogen phosphate ($(NH_4)_2HPO_4$; *MERCK*, purity > 99,0 %) as the phosphorus-component. Hydrated Sm- and Ce-Nitrates, respectively, were mixed with specific amounts of distilled water to obtain aqueous solutions of 1 $mol \cdot l^{-1}$ concentration (*Alfa Aesar GmbH & Co.KG*: $Sm(NO_3)_3 \cdot 6\ H_2O$ (99,9 % REO), $Ce(NO_3)_3 \cdot 6\ H_2O$ (99,5 % REO)). The Sm^{3+}- and Ce^{3+}-concentrations in the aqueous solutions were checked by ICP-MS measurements. These solutions were poured to a NaOH-solution (c = 1 $mol \cdot l^{-1}$) in specific ratios while stirring on a magnetic stirrer, following the admixture of $(NH_4)_2HPO_4$ (aq). The chosen (Sm+Ce):P - ratio in the mixture was 1:1. The mixture was poured in a Teflon liner inserted in a stainless-steel-autoclave and heated to 220 °C using an oven by *Nabertherm GmbH*.

The following reaction took place:

$$Ln(NO_3)_3 \cdot 6\ H_2O + (NH_4)_2HPO_4 \rightarrow LnPO_4 + HNO_3 + 2\ NH_4NO_3 + 6\ H_2O.$$

After synthesis the product was centrifuged and the supernatant was separated. The product was mixed with an aqueous solution of nitric acid (c = 1 mol·l^{-1}) and stirred for three days to make sure that unlikely formed Sm- or Ce-Hydroxides are solved.
Centrifuging again after three days, the product was washed three times with distilled water, afterwards oven-dried at 80 °C and ground in an agate mortar.
Chemical analyses were performed using a scanning electron microscope with an energy dispersive x-ray detector (*FEI, Quanta 200 F, EDX,* 60 Pa, 30 kV).

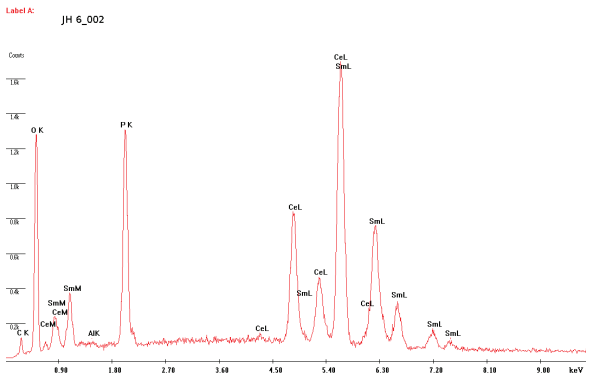

Fig. 68: EDX-spectrum of the composition $Sm_{0.7}Ce_{0.3}PO_4$ (JH 6).

Supplementary the Ce content of two samples with chemical compositions $Sm_{0.8}Ce_{0.2}PO_4$ and $Sm_{0.2}Ce_{0.8}PO_4$ was analysed by XPS/ESCA (*electron spectroscopy for chemical analysis*; *ESCALAB 250, Thermo VG Scientic*). The monazite powders were thermally analysed by coupled TG-DSC (*Netzsch STA 449C Jupiter*). Filled in platinum-rhodium crucibles they were heated in air up to 1300 °C, at a heating rate of 10 K·min^{-1} and cooled down at the same rate. Seven samples (x = 1, 0.8, 0.7, 0.5, 0.3, 0.2, and 0 in $Sm_{1-x}Ce_xPO_4$) were chosen for additional TG-DTA measurements, heated up to 1200 °C in N_2-atmosphere at a heating rate of 10 K·min^{-1} using corundum crucibles (*Netzsch STA 420 Jupiter*).

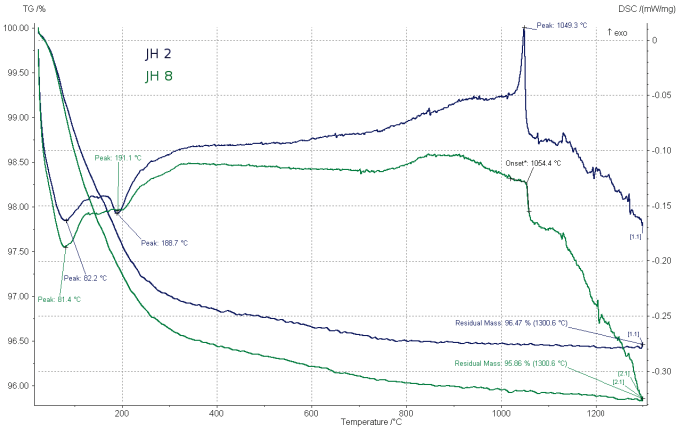

Fig. 69: As an example two TG-DSC-curves are displayed: JH 2 – $Sm_{0.96}Ce_{0.04}PO_4$ (blue) and JH 8 -$Sm_{0.5}Ce_{0.5}PO_4$ (green).

X-ray powder diffraction measurements were conducted in the 2 θ-range of 10-100° using a *D8 ADVANCE*, *Bruker AXS GmbH* (θ-θ-geometry). For the measurements Cu Kα-radiation, a variable aperture (4 mm), soller slits, a secondary monochromator and a scintillation counter running in step-scan-mode (0.02 / 2 θ, t = 15 s) were used. The 13 samples and the five TG-DTA-samples were analysed by XRD.
Using a *LabRAM HR Vis* (*HORIBA Scientific*) for Raman-spectroscopy, equipped with a He-Ne-laser (λ = 632.81 nm) and a focal length of 80 cm, all samples were analysed according to their short range order and medium range order.

Results and discussion

Fig. 70 shows the ratios Sm:Ce and (Sm+Ce):P and their mean squared errors are displayed in [at.%]. The true values of Sm:Ce are in good agreement with the theoretical values. The (Sm+Ce):P-ratio is too low in many cases which might be a problem of the method`s precision. P:O- and (Sm+Ce):O-ratios showed an overestimation of the O-contents mostly due to the H_2O-gas used to generate the vacuum. Beside Sm, Ce, P and O there could be observed small amounts of Al and C in the EDX-spectra (Fig. 68). These impurities are caused by the sample holder.

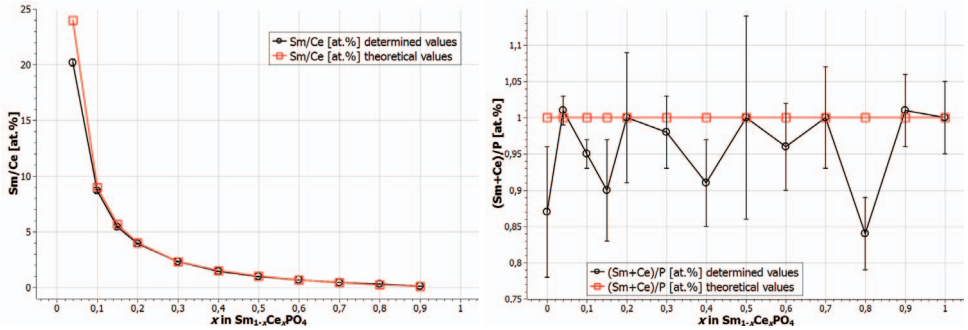

Fig. 70: Left: Theoretical and determined values of the Sm/Ce-ratios [at.%]. Right: Theoretical and determined values of the (Sm+Ce)/P-ratios [at.%].

XPS measurements on samples JH 5 and 11 ($Sm_{0.8}Ce_{0.2}PO_4$ and $Sm_{0.2}Ce_{0.8}PO_4$) were made to exclude the existence of $Ce^{IV}O_2$-impurities. In both samples the typical u'''-band could not be observed, so the existence of Ce^{4+} can almost be ruled out.
The mean total mass loss of the different samples was 1.6 % and the TG-curves showed no clear sections of weight loss. However we could observe three main events in the DSC-curves: two endothermic ones at temperatures about 80 °C and $T \approx$ 155-190 °C (Fig. 69 and Fig. 71 left) and moreover a broad exothermic peak in the temperature-range $T \approx$ 700-1000 °C finishing with a sharp exothermic event around $T \approx$ 1000-1100 °C that is more or less distinctive (Fig. 69). The first endothermic event is caused by the loss of adsorbed water, the second one by the loss of rhabdophane-like bounded water. Fig. 71 (left) shows that the first endothermic peaks have more or less constant values in contrast to the second endothermic events where the peak-temperatures decrease in the compositional range $Sm_{0.6}Ce_{0.4}PO_4$ - $Sm_{0.3}Ce_{0.7}PO_4$ from $T \approx$ 200 °C to $T \approx$ 155 °C. This change in temperature according to the loss of water may indicate a structural change in this range as a function of chemical composition. The exothermic events can be interpreted as a recrystallization

process of monazite and additional grain growth. The sharp peaks at $T \approx$ 1000-1100 °C are lambda-shaped.

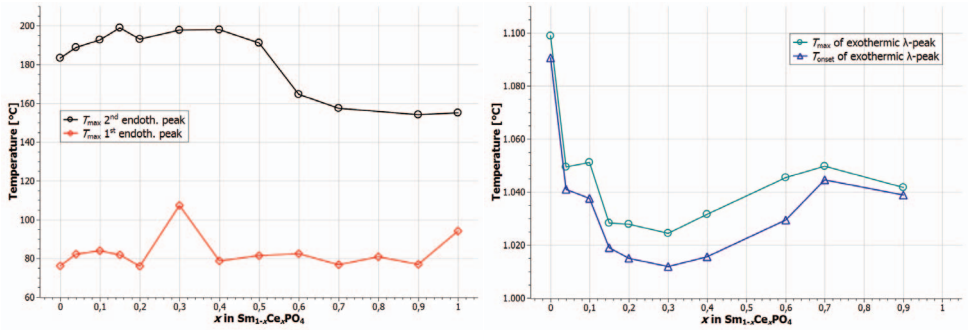

Fig. 71: Left: Peak-temperatures of the 1st and 2nd endothermic events. Right: Onset- and Peak-temperatures of the exothermic event at $T \approx$ 1000-1100 °C.

Typically for lambda-transitions the heat capacity increases already before the transition occurs and decreases steeply in the end. The lambda-transitions observed in this work can be interpreted as solid-solid-phase reactions. Where there are no clear peaks in the heating phase they can be observed in the cooling phase in most cases, respectively. In fig. 6 the peak temperatures and onset temperatures of the "lambda-peaks" are displayed. These effects have not been described in literature yet. DSC-curves of Montel et al. (2006) [1] showed a kind of the observed peak shape, but have only described the broad peak as formation of their investigated solid solution. JH 8 (Sm:Ce = 0.5:0.5) and JH 13 (Sm:Ce = 0:1) showed no clear peaks in the heating phase and JH 11 (Sm:Ce = 0.2:0.8) was taken as an outlier from several points of view, so these values are missing in Fig. 71 (right). Up to amounts of 30 at.% Ce^{3+} the temperatures of the exothermic peaks decrease and increase afterwards. So there is no linear behaviour as has to be expected for an ideal solid solution. We could show that sintering temperatures higher than 1200 °C are not necessary for these phases. We assume a melting point minimum close to the chemical composition $Sm_{0.7}Ce_{0.3}PO_4$.

In addition seven samples were measured by differential thermoanalysis (DTA), but without a baseline correction. The DTA-curves also showed exothermic events in the mentioned temperature range and decreasing peak temperatures up to JH 6 ($Sm_{0.7}Ce_{0.3}PO_4$). The number of measured values is too small to yield more information according to the assumption of a melting point minimum by the DTA results, but the temperature values show a similar tendency.

Diffraction patterns of the 13 samples showed broad bragg peaks due to low crystallinity. After grain growth while heating the samples up to 1200 °C during DTA-measurements, the reflections` FWHM *(full width at half maximum)* decreased and sharp bragg peaks could be observed (see Fig. 72 for comparison). Using the software *Topas (Bruker AXS GmbH)* cell parameters for all compositions were determined based on structure models of Ni et al. (1995) [2] (PDF-2 entry-No.: $SmPO_4$ [01-083-0655 46-1329] and $CePO_4$ [01-083-0652 32-199]). The cell parameters showed small deviations from a linear behaviour which would be expected in an ideal solid solution.

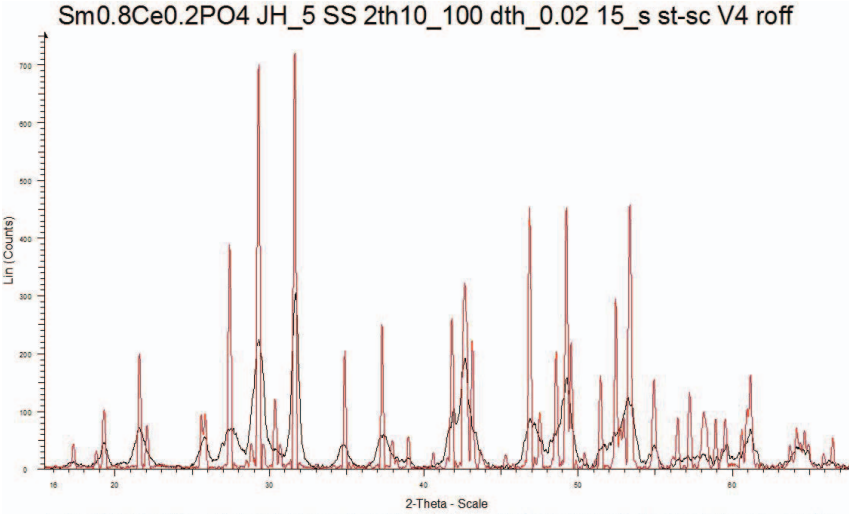

Fig. 72: Comparison of sample JH 5 ($Sm_{0.8}Ce_{0.2}PO_4$) unsintered (black) and after heating to 1200 °C in DTA (red).

For some compositions the lattice parameters were also determined by *Dicvol06 (A. Boultif & D. Louer, J. Appl. Cryst. 37, 724-731, 2004)* without a structure model (Tab. 18: $SmPO_4$- and $CePO_4$-values in comparison with reference values). These results showed sharp rises in cell parameters a_0 and c_0 in the compositional range of $Sm_{0.6}Ce_{0.4}PO_4$ to $Sm_{0.5}Ce_{0.5}PO_4$ (see Fig. 73). In the case of step by step insertion of Cerium in $Sm_{1-x}Ce_xPO_4$ the monazite structure expands and $[PO_4]^{3-}$-tetrahedra and LnO_9-polyhedra are distorted.

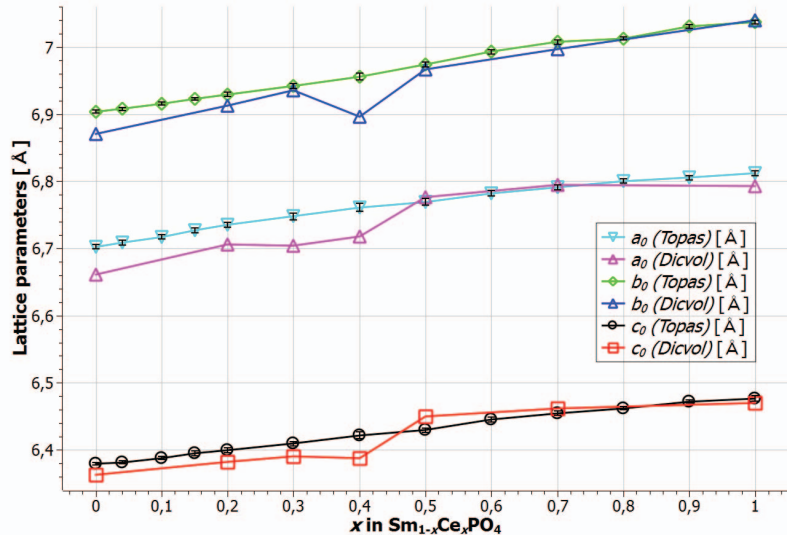

Fig. 73: Lattice parameters determined in *Topas* and *Dicvol06*. a_0 and c_0 show a sharp rise from 40 at.% to 50 at % Cerium.

Tab. 18: Lattice parameters determined by *Dicvol06* within this work (JH) and reference data (Kizilyalli and Welch (1976) [3], Pepin and Vance (1981) [4], Aldred (1984) [5], Ni et al. (1995) [2], Ushakov et al. (2001) [6]. Indices: a = powder data, b = single crystal data

Ref.	$SmPO_4$				$CePO_4$			
	a_0 [Å]	b_0 [Å]	c_0 [Å]	β [°]	a_0 [Å]	b_0 [Å]	c_0 [Å]	β [°]
[3][a]	6.67	6.88	6.36	103.47	6.78	7.01	6.45	103.5
[4][a]	6.693	6.897	6.374	103.87	6.8	7.023	6.472	103.47
[5][a]	6.6878(6)	6.8943(3)	6.3712(5)	103.89(1)	6.7984(5)	7.0234(5)	6.4731(5)	103.44(1)
[2][b]	6.6818(12)	6.8877(9)	6.3653(9)	103.86(1)	6.7880(10)	7.0163(8)	6.4650(7)	103.43(1)
[6][b]	6.6891(3)	6.8958(3)	6.3770(6)	103.9(1)	6.7968(5)	7.0258(5)	6.4743(6)	103.5(1)
JH[a]	6.661	6.8709	6.3627	103.626	6.793	7.0398	6.4696	103.536

The Raman shifts of the endmembers $SmPO_4$ and $CePO_4$ are in good agreement with the reference values of Begun et al. (1981) [7], Poloznikova and Fomichev (1994) [8], Silva et al. (2006) [9] and Huang et al. (2010) [10] (Tab. 19). Silva et al. (2006) [9] described the Raman spectrum of monazite by vibrations of $[PO_4]^{3-}$- and Ln^{3+}-"units". There are 36 Raman bands expected caused by the internal and external modes of the "free" $[PO_4]^{3-}$-tetrahedron and the external modes of the Ln^{3+}-cation. Although the tetrahedra are slightly distorted their internal modes can be described by the point symmetry $\bar{4}3m$ (T_d). Lowered by its site symmetry 1 (C_1) and assigned to the factor group of monazite 2/m (C_{2h}) 9 A_g + 9 B_g internal modes can be expected. Raman active 9 A_g + 9 B_g external modes are evoked by the transitional and rotational degrees of freedom of the $[PO_4]^{3-}$-tetrahedron and the transitions of the LnO_9-polyhedron. For the different compositions of the solid solution $Sm_{1-x}Ce_xPO_4$ no Raman data have been published so far. According to Zotov et al. (2003) [11] v_1 and the modes between v_1 and v_3 (≈ 1025-1035 cm^{-1}) can be related to the linking of the tetrahedra: Q^0 and Q^1, where Q^0 stands for isolated tetrahedra and Q^1 for two corner-sharing tetrahedra. Within this work the recorded Raman spectra also revealed that synthesized Sm-Ce-orthophosphates don`t show a behaviour as expected for an ideal solid solution. Especially the two vibrations concerning to stretching of the $[PO_4]^{3-}$-tetrahedra (symmetrical v_1 and antisymmetrical v_3): Fig. 74 shows the two Raman frequencies plotted vs. the amount of Ce^{3+} in $Sm_{1-x}Ce_xPO_4$, compared to reference values of $SmPO_4$ and $CePO_4$ (Begun et al. (1981) [7]). The wavenumbers do not vary linearly within the whole compositional range but decrease rapidly from $Sm_{0.7}Ce_{0.3}PO_4$ to $Sm_{0.6}Ce_{0.4}PO_4$. Similar to the XRD-results there can be seen a structural change according to short-range order.

The decrease of the wavenumbers in general due to the increasing atomic number and the decreasing ionic radius of the cations is described by a compression of the $[PO_4]^{3-}$-tetrahedra that causes a shortening of the P-O-distance and therefore increasing frequencies for the P-O-stretching (Begun et al. (1981) [7], Hobart et al. (1983) [12]). Influences on the P-O-bond are based on polarization effects of Ln^{3+} (Hezel and Ross (1966) [13], Poloznikova and Fomichev (1994) [8]). However, Podor (1995) [14] described the effect by the shortening of the *Ln*-O-distance.

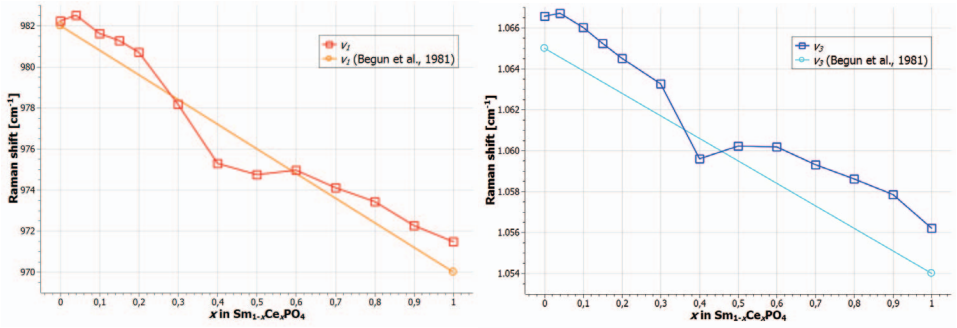

Fig. 74: **Left: Raman shifts [cm^{-1}] of symmetric $[PO_4]^{3-}$ stretching v_1 versus chemical composition $Sm_{1-x}Ce_xPO_4$. Right: Raman shifts [cm^{-1}] of antisymmetric $[PO_4]^{3-}$ stretching v_3 versus chemical composition $Sm_{1-x}Ce_xPO_4$.**

Tab. 19: **Experimental and reference Raman frequencies [cm^{-1}]: Begun et al. (1981) [7], Poloznikova and Fomichev (1994) [8], Silva et al. (2006) [9], Huang et al. (2010) [10]. * = orthophosphates were doped with 0.1 wt.% Gadolinium.**

$SmPO_4$				$CePO_4$					Assign.	Symm.
[7]*	[8]	[9]	JH	[7]*	[8]	[9]	[10]	JH		
88	88	88		88	88	88			Lattice	B_g
107	107	107		100	100	100			Lattice	A_g
123	123			118	118				Lattice	A_g,B_g
132	132			129	129				Lattice	B_g
156	156	155	155.87	152	152			151.25	Lattice	B_g,A_g
		159				158		155.59	Lattice	B_g
170	170	177	170.49	172	172	172	170.7	171.61	Lattice	B_g,A_g
185	185	185	184.15			183		183.43	Lattice	A_g
				188	188			188.19	Lattice	
232	232	231	231.42	219	219	219	218.4	219.94	Lattice	A_g,B_g
242	242	243	242.39	227	227	227		227.15	Lattice	A_g,B_g
265	265	265	265.4	254	254	254	253.0	256.01	Lattice	A_g
294	294	293	293.10	270	270	270	270.5	273.43	Lattice	A_g
402		404	402.07	396		396	395.1	397.43	Lattice	A_g,B_g
423	423	424	424.01	414	414	414	412.9	415.11	Lattice	A_g,B_g
473	473	474	472.80	467	467	467	465.7	467.55	v_2	A_g,B_g
538	538	542	539.02	536	536	535		537.60		A_g
575	575	577	575.57	571	571	568	570.9	572.05		A_g
595		603	595.16	589	589	588		589.37		B_g
627	627	629	628.13	618	618	618	619.7	620.17	v_4	A_g,B_g
			907.09					899.25		
982	982	983	982.24	970	970	970	971.1	971.47	v_1	A_g,B_g
999	999	999	999.41	990	990	990	992.4	992.22		A_g
1035	1035	1035	1036.00	1024	1024	1024	1026.4	1025.67		B_g
1065	1065	1065	1066.57	1054	1054	1054	1056.3	1056.2	v_3	A_g,B_g
1083	1083	1084	1083.87	1070	1070	1071	1072.3	1072.37		B_g

Conclusions

For $Sm_{1-x}Ce_xPO_4$ monazites new experimental data could be generated and so far unknown properties be determined.

It was possible to show that max. sintering temperatures of 1200 °C are sufficient for the several chemical compositions $Sm_{1-x}Ce_xPO_4$ to obtain a high densification of the material. Beneath this temperature unlikely rhabdophane impurities transform to monazite, the monazite recrystallizes and a significant grain growth takes place. Finally the material is densified by the formation of a new microstructure.

Appreciable changes in crystal structure could be observed by structural analyses using Raman spectroscopy and powder x-ray diffraction in the compositional range $Sm_{0.7}Ce_{0.3}PO_4$ to $Sm_{0.6}Ce_{0.4}PO_4$. A sudden decrease of wavenumbers in the Raman spectra was observed and furthermore an abrupt increase in the lattice parameters a_0 and c_0 could be recognized. These observations disprove the existence of an ideal solid solution, where a linear behaviour concerning Vegard`s Law should be observed. This non-ideal behaviour of $Sm_{1-x}Ce_xPO_4$ is described for the first time.

Reference data do only exist for the pure endmembers $SmPO_4$ and $CePO_4$. Synthesis and characterization of synthetic *Ln*-orthophosphate solid solutions have rarely been described so far.

In order to receive more information about a possible melting point minimum, additional orthophosphates in the compositional range of $Sm_{0.8}Ce_{0.2}PO_4$ - $Sm_{0.5}Ce_{0.5}PO_4$ will be synthesized and analysed in the near future. The crystal structures of the solid solution will be determined in detail (Rietveld). Furthermore electronic charge distributions of single crystals might give more information about chemical bonds within the monazite structure.

Based on these new phases actinides like U and Th will be incorporated. Using coupled substitutions of $2\ Ln^{3+} \rightarrow Th^{4+} + Ca^{2+}$ and $Ln^{3+} + P^{5+} \rightarrow Th^{4+} + Si^{4+}$ solid solutions of Sm-Ce-monazites, cheralite ($ThCa(PO_4)_2$) and huttonite ($ThSiO_4$) will be synthesized. In a similar way U^{4+} can be inserted. Different compositions of $Sm_{1-x}(Th,U)_xP_{1-x}Si_xO_4$ (x = 0-0.5) will be synthesized in order to find a melting point minimum or even an eutectic mixture. Phase diagrams will be determined by thermal analyses and additional model calculations.

Finally irradiation experiments and leaching tests on cold or hot pressed and sintered pellets will be performed for testing the radiation resistance and the chemical durability of the new phases, respectively.

The results of these experiments and calculations will be presented within the context of the next department report 2012.

References

[1] J.-M. Montel, B. Glorieux, A.-M. Seydoux-Guillaume, R. Wirth, Journal of Physics and Chemistry of Solids 67 (2006) 2489

[2] Y. Ni, J. M. Hughes, A. N. Mariano, American Mineralogist 80 (1995) 21

[3] M. Kizilyalli, A. J. E. Welch, Journal of Applied Crystallography 9 (1976) 413

[4] J. G. Pepin, E. R. Vance, Journal of Inorganic and Nuclear Chemistry 43 (1981) 2807

[5] A. T. Aldred, Acta Crystallographica Section B 40 (1984) 569

[6] S.V. Ushakov, K.B. Helean, A. Navrotsky, L.A. Boatner, Materials Research Society 16 (2001) 2623

[7] G. M. Begun, G. W. Beall, L. A. Boatner, W. J. Gregor, Journal of Raman Spectroscopy 11 (1981) 273

[8] M. E. Poloznikova, V. V. Fomichev, Russian Chemical Reviews 63 (1994) 399

[9] E.N. Silva, A.P. Ayala, I. Guedes, C.W.A. Paschoal, R.L. Moreira, C.-K. Loong, L.A. Boatner, Optical Materials 29 (2006) 224

[10] T. Huang, J.-S. Lee, J. Kung, C.-M. Lin, Solid State Communications 150 (2010) 1845

[11] N. Zotov, H. Schlenz, B. Brendebach, H. Modrow, J. Hormes, F. Reinauer, R. Glaum, A. Kirfel, C. Paulmann, Zeitschrift für Naturforschung Section A 58 (2003) 419

[12] D. E. Hobart, G. M. Begun, R. G. Haire, H. E. Hellwege, Journal of Raman Spectroscopy 14 (1983) 59
[13] A. Hezel, S.D. Ross, Spectrochimica Acta 22 (1966) 1949
[14] R. Podor, European Journal of Mineralogy 7 (1995) 1353

5.11. Raman Spectra of Synthetic Rare Earth Orthophosphates

H. Schlenz, J. Heuser, S. Schmitz, C. Babelot

Corresponding author: h.schlenz@fz-juelich.de

Abstract

Rare earth orthophosphates were synthesized and investigated by raman spectroscopy. The data were compared to the available literature and the subsequent analysis of all data revealed new insights into crystal structures of monazite type and their properties, respectively. Extraordinary correlations between cell parameters and raman frequencies were observed and will be explained on the basis of crystallographic considerations in the course of this report.

Introduction

One of the central tasks of nuclear waste management is the immobilization of actinides (U, Th, etc.) from spent fuel [1,3]. For the immobilization phosphate ceramics including monazite appear to be ideal [2,4,5], since such phases are able to take up large amounts of actinides on regular positions in their crystal structures and keep such elements savely and permanently. Natural monazite, with an age of up to 3.2 billion years, contains up to 27 weight percent UO_2 and ThO_2, without achieving any significant radiation damage. For this and other reasons, ceramic monazite phases are potential candidates for future management strategies. Therefore new ceramic monazite phases shall be synthesized and structurally characterized by x-ray diffraction and raman spectroscopy. Goal is the development of new phases for the permanent integration of U and Th and the investigation of the ongoing operations at an exposure within the crystal structure. In particular the reversible phase transformation crystalline ↔ amorphous has to be investigated in detail in order to be able to judge the long-term durability. The development of such new ceramics provides a new option for the safe disposal of nuclear waste.

Experimental

Rare earth orthophosphates of compositions $LaPO_4$, $CePO_4$, $NdPO_4$, $SmPO_4$ and $EuPO_4$ were prepared by hydrothermal synthesis and partly subsequently cold pressed and sintered. See Heuser et al. and Babelot et al. (this issue) for more detailed descriptions of the applied synthesis routes. Raman spectra were recorded with a Horiba LabRam HR spectrometer. The spectra were excited with the 632,81 nm line of a He-Ne laser. The samples were mostly in the form of small crystalline powders. Some difficulties were encountered with the excitation of electronic bands, especially in the case of Eu orthophosphate, but the observed additional bands caused by photoluminescence appear only at wavenumbers greater than 1200 cm^{-1} and therefore do not disturb the structural information available through the observed raman frequencies at smaller wavenumbers. Raman measurements were also performed on $LaPO_4$ and $EuPO_4$ pellets. Because of the improved crystallinity these spectra show significantly sharper peaks and reveal more details (see e.g. Fig. 76), respectively. Some $LaPO_4$ pellets were irradiated by 400 keV Kr^{2+} ions at increasing dose rates in order to simulate α-recoil effects. Subsequently some of the samples were measured by raman spectroscopy for the detection of potential radiation damage. Using the program SRIM [21]

computer simulations could be performed that deliver valuable information about possible ways of damage caused by the irradiation mentioned above.

Results and discussion

Up to 25 different raman frequencies (cm^{-1}) could be detected for the investigated powder samples (Fig. 75, Tab. 20) and up to 30 different raman frequencies for the cold pressed and sintered samples (Fig. 76 & Fig. 77, Tab. 20). The determined values are in good agreement with literature data [5,10,19,20] and additionally exceed the existing data partially (Tab. 20), an observation that documents the quality of the new Horiba raman spectrometer just gone into service. Fig. 76 demonstrates the impressive increase in data quality when pellets were measured instead of powders. Here the spectra of powdered and cold pressed and sintered $LaPO_4$ are compared. The zoom of the high frequency region (Fig. 76, right) clearly verifies the significantly increased resolution. Six different bands can easily be distinguished for the region of stretching vibrations (≈ 800 - 1200 cm^{-1}) instead of only three or four for the powder sample of identical composition.

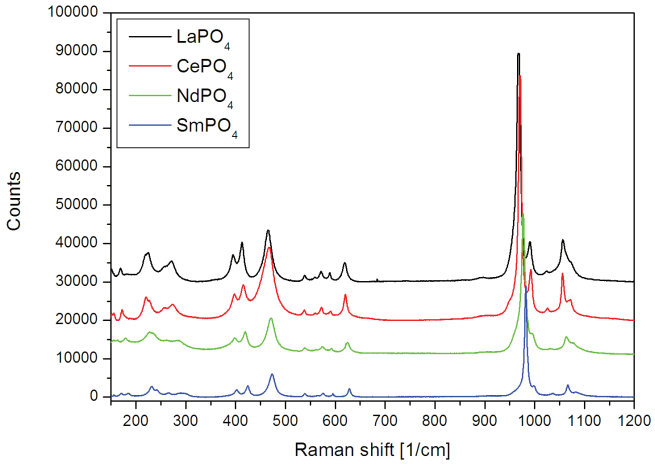

Fig. 75: Raman spectra of synthetic rare earth orthophosphate powders.

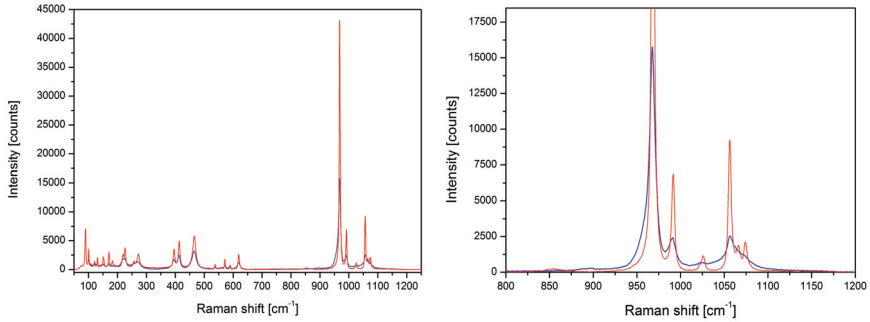

Fig. 76: Left: Raman spectra of synthetic $LaPO_4$, cold pressed and sintered (red) and without pressing and sintering after hydrothermal synthesis (blue). Right: Zoom of the high frequency region.

The numerical values of all measured raman frequencies were determined using the software LabSpec 5 (Horiba), including a preceding data reduction using the same software. The values were determined by peak fitting using Gaussian-Lorentzian profiles. As an example Fig. 77 shows the fitting result for the synthetic cold pressed and sintered $LaPO_4$ sample. The adjustment of the spectrum is very good and allows for the assured determination of the maximum peak positions. Tab. 20 summarizes the determined values for all investigated samples and compares the results to the available literature. The raman frequencies between 87 cm^{-1} and 429 cm^{-1} are assigned as lattice vibrations. The frequencies v_2 and v_4 denote the symmetrical and anti-symmetrical bending vibrations of the $[PO_4]$ tetrahedra, respectively. Symmetrical and anti-symmetrical stretching vibrations of the $[PO_4]$ tetrahedra are assigned as v_1 and v_3, respectively. Therefore three main regions in all monazite raman spectra can be distinguished: lattice, bending (≈ 430 - 650 cm^{-1}) and stretching vibrations (with increasing wave numbers). The remaining bands not explicitly assigned in Table 1 are mainly caused by vibrations of the $[LnO_9]$ polyhedra.

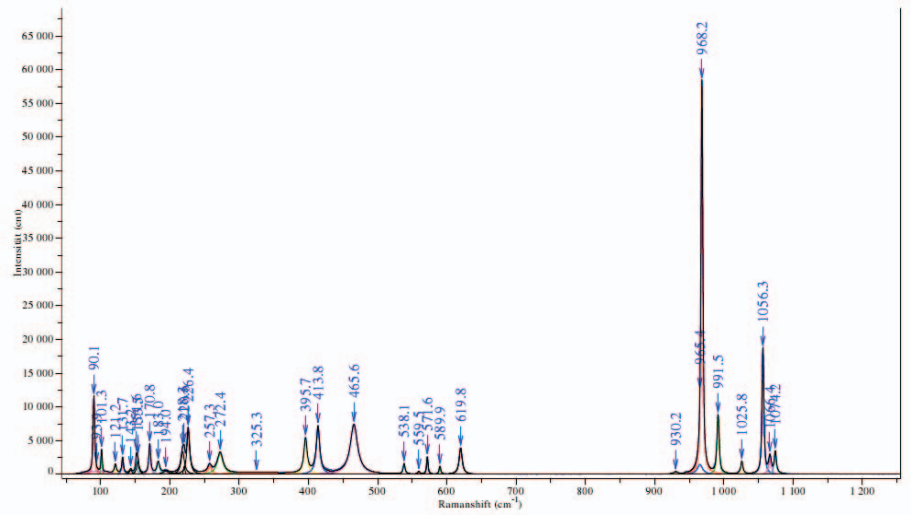

Fig. 77: Fitted raman spectrum of synthetic cold pressed and sintered $LaPO_4$.

In the following, however, the main focus will be on the $[PO_4]$ vibrations, because the associated raman frequencies deliver the necessary structural information for the interpretation of structural differences caused by the exchange of the lanthanide ions. Plotting the received values for the bands v_1, v_2, v_3 and v_4 versus cell constants (Fig. 78 & Fig. 79) reveals new insights into the chemical and structural correlations according to synthetic rare earth orthophosphates. Fig. 78 and Fig. 79 show the correlation between the four different $[PO_4]$ vibrational bands v_i [cm^{-1}] and the cell constant c_0 [Å], respectively. Plotting v_i versus a_0 or b_0 yields the same picture. Figure 4 (left) shows a linear correlation between the decreasing cell constant c_0 and decreasing atomic number, respectively, and the raman frequency v_1 of the symmetrical $[PO_4]$ stretching vibration. The data point for $Eu[PO_4]$ doesn't really fit to this correlation, regardless of whether our own data or literature data [5,10,19,20] are applied. A similar discrepancy for the case of $Eu[PO_4]$ can also be observed in Fig. 79 (left), where the symmetrical $[PO_4]$ bending vibration v_2 is plotted versus

c_0. A linear correlation could only be justified by the exclusion of Eu[PO_4], otherwise a fourth-order polynomial yields the best fit.

Tab. 20: Experimentally determined raman frequencies (cm^{-1}) of synth. $LnPO_4$ (Ln: La, Ce, Pr, Nd, Sm, Eu, Gd) compared to literature data [Mean values of Ref. 5,10,19,20]. Data marked by an asterix (*) are from this work. The accuracy of all data is ± 1 cm^{-1}.

La*	La [Ref.]	Ce*	Ce [Ref.]	Pr [Ref.]	Nd*	Nd [Ref.]	Sm*	Sm [Ref.]	Eu*	Eu [Ref.]	Gd [Ref.]	Assignment
90	90	---	88	90	---	89	---	88	88	87	87	Lattice
101	100	---	100	105	---	106	---	107	109	108	108	Lattice
121	120	---	118	122	---	123	---	123	125	124	123	Lattice
132	131	---	129	133	---	133	---	132	133	132	130	Lattice
143	---	---	---	---	---	---	---	---	---	---	---	Lattice
151	151	151	152	159	155	155	156	157	159	159	158	Lattice
---	---	156	---	---	163	162	---	---	---	---	162	Lattice
171	170	172	172	177	179	175	171	172	174	175	178	Lattice
183	183	183	186	185	184	182	184	185	190	189	192	Lattice
194	---	188	---	---	---	---	---	---	---	---	---	Lattice
220	220	220	219	---	---	---	---	---	---	---	---	Lattice
226	227	227	227	226	226	228	231	232	235	233	236	Lattice
---	---	---	---	---	236	---	243	242	245	244	247	Lattice
258	256	256	254	256	261	264	265	265	267	265	269	Lattice
272	272	274	270	282	283	289	293	294	302	306	306	Lattice
396	395	398	396	399	398	399	402	403	404	404	405	Lattice
414	414	415	414	417	419	420	424	423	427	424	429	Lattice
466	465	468	467	470	471	471	473	473	473	471	478	v_2
538	536	538	535	538	540	539	539	539	539	540	542	
560	---	559	---	---	---	---	568	---	---	---	---	
572	570	572	570	572	574	575	576	576	577	576	579	
590	588	589	589	592	592	598	595	598	597	599	602	
620	619	620	618	623	624	625	628	628	631	630	632	v_4
---	---	899	---	---	901	---	---	---	---	---	---	
931	---	---	---	---	---	---	---	---	---	---	---	
947	---	948	---	---	---	---	---	---	---	---	---	
965	---	963	---	---	---	---	970	---	---	---	---	
968	967	970	970	975	977	977	982	982	990	990	988	v_1
992	990	992	990	995	997	998	999	999	---	1002	1004	
1026	1024	1026	1025	1029	1031	1033	1036	1035	1033	1036	1042	
1056	1055	1056	1054	1058	1064	1062	1067	1065	1070	1069	1072	v_3
1066	1065	---	---	---	---	---	---	---	---	---	---	
1074	1072	1073	1071	1075	1074	1079	1084	1083	1083	1084	---	
---	---	---	---	---	1089	---	---	---	1093	1093	1092	

For the anti-symmetrical [PO_4] stretching vibration v_3 (Fig. 78, right) and the anti-symmetrical [PO_4] bending vibration v_4 (Fig. 79, right) a divergent observation can be made. Here Eu[PO_4] fits to the whole dataset in an excellent way (third-order polynomial for v_3 and second-order polynomial for v_4), but La[PO_4] and Ce[PO_4] behave nearly identical. Only for atomic numbers $Z \geq 59$ a none constant correlation between c_0 and v_3, v_4 can be observed. To our

knowledge, these special relationships haven't been discussed in literature so far. As a basis for a first explanation of this somewhat extraordinary behaviour of synthetic rare earth orthophosphates Tab. 21 can serve. In this table selected structure properties and [PO_4] raman frequencies are listed with focus on properties that are obviously influenced by the chemical composition. The following conclusions can be drawn from Tab. 21:

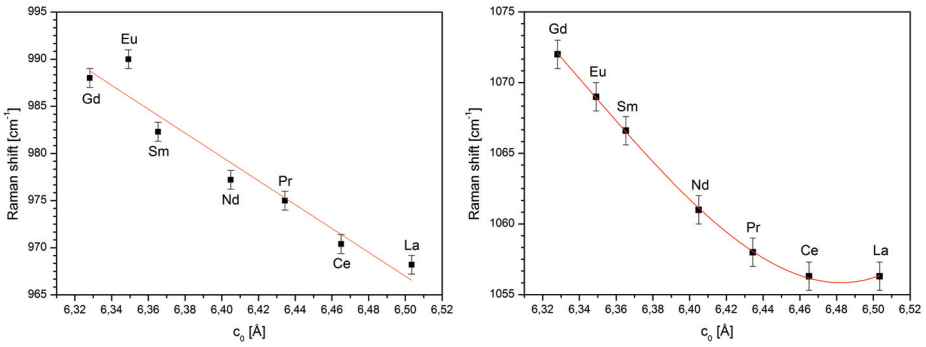

Fig. 78: Cell constant c_0 [Å] plotted as a function of raman frequencies [cm^{-1}]: v_1 (left) and v_3 (right).

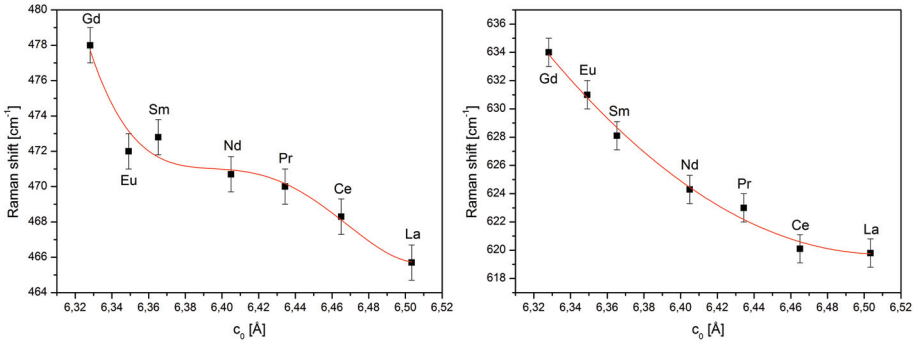

Fig. 79: Cell constant c_0 [Å] plotted as a function of raman frequencies [cm^{-1}]: v_2 (left) and v_4 (right).

The ionic radii r_K and the cell constants a_0, b_0 and c_0 (as well as the volume of the unit cell) decrease constantly with increasing atomic number Z (only the cell constant β increases slightly with Z). The reason for this is the well known lanthanide contraction. The raman frequencies v_1 and v_2 also decrease with increasing atomic number, but a jump can be observed for Eu[PO_4]: v_1 increases exceptionally and v_2 decreases unexpectedly (Fig. 78 & Fig. 79). A precise look at the existing bond lengths (Tab. 21) delivers the explanation. From La to Gd the [LnO_9] polyhedra become smaller and less regular, whereas the [PO_4] tetrahedra simultaneously become larger and keep quite regular. An increasing [PO_4] volume automatically results in an increase of the symmetrical [PO_4] stretching vibration and the corresponding raman band v_1. At the same time the increasing [PO_4] volume reduces the symmetrical bending vibration v_2, because the vibrating oxygen atoms which move together

have to travel longer distances during a single vibration. The change of the Ln electronic configuration from [Xe] $4f^6 6s^2$ (Sm) to [Xe] $4f^7 6s^2$ (Eu) induces a sudden increase of the $[PO_4]$ volume from $Sm[PO_4]$ to $Eu[PO_4]$ and a similar decrease of the $[LnO_9]$ volume, respectively. $Gd[PO_4]$ defines the phase boundary to the tetragonal xenotime phases ($Tb[PO_4]$ to $Lu[PO_4]$). From Gd to Tb the $[LnO_9]$ polyhedra collaps and $[LnO_8]$ polyhedra are build as new structure units. The small difference between the ionic radii of La^{3+} and Ce^{3+} (Tab. 21) prevents significant structural differences between $La[PO_4]$ and $Ce[PO_4]$, even though the lanthanide contraction is already active. These two crystal structures are the most stable ones within the monoclinic orthophosphate system, even because all polyhedra are quite regular. On the basis of the aforementioned crystallographic considerations, the very low recrystallization temperature of e.g. $La[PO_4]$ (30 - 35 °C) compared to the remaining orthophosphates can be understood quite easily. In order to reach an even more deeper understanding of the crystal structure of $La[PO_4]$ and its properties, we started irradiation experiments using 400 keV Kr^{2+} ions. Because the energy of 400 keV ions is too small to produce severe damage of the structure, the performed raman measurements only show small differences with increasing dose rates (Fig. 80) and no amorphous phases being build.

Tab. 21: Comparison of selected structure properties and $[PO_4]$ raman frequencies of synthetic rare earth orthophosphates (Ln = La, Ce, Pr, Nd, Sm, Eu or Gd). Average raman frequencies are mean values calculated from Tab. 20. CN denotes the coordination number and r_K the ionic radius, respectively. Cell constants were taken from Ni et al. [17] (standard deviations are given in parenthesis).

Structure	$La[PO_4]$	$Ce[PO_4]$	$Pr[PO_4]$	$Nd[PO_4]$	$Sm[PO_4]$	$Eu[PO_4]$	$Gd[PO_4]$
CN (Ln - O)	9	9	9	9	9	9	9
r_K (Ln^{3+}) [Å]	1,213	1,188	1,170	1,162	1,131	1,120	1,109
No. of different Ln-O bond lengths	9	9	9	9	9	9	9
Average Ln-O bond length [Å]	2,5785	2,5552	2,5391	2,5245	2,5000	2,4876	2,4756
Ln electronic configuration	$5d^1 6s^2$	$4f^1 5d^1 6s^2$	$4f^3 6s^2$	$4f^4 6s^2$	$4f^6 6s^2$	$4f^7 6s^2$	$4f^7 5d^1 6s^2$
No. of different P-O bond lengths	4	4	4	4	4	4	4
Range of P-O bond lengths [Å]	1,5203 - 1,5556	1,5323 - 1,5422	1,5310 - 1,5510	1,5285 - 1,5448	1,5270 - 1,5397	1,5331 - 1,5405	1,5308 - 1,5491
Cell constant a_0 [Å]	6,8313(10)	6,7880(10)	6,7596(8)	6,7352(10)	6,6818(12)	6,6613(10)	6,6435(9)
Cell constant b_0 [Å]	7,0705(9)	7,0163(8)	6,9812(10)	6,9500(9)	6,8877(9)	6,8618(9)	6,8414(10)
Cell constant c_0 [Å]	6,5034(9)	6,4650(7)	6,4344(9)	6,4049(8)	6,3653(9)	6,3491(8)	6,3281(6)
Cell constant β [°]	103,27(1)	103,43(1)	103,53(1)	103,68(1)	103,86(1)	103,96(1)	103,98(1)
$< v_1 >$ [cm^{-1}]	968	970	975	977	982	990	988
$< v_2 >$ [cm^{-1}]	466	468	470	471	473	472	478

Computer simulations (SRIM) can explain the least damage, since the Kr^{2+} ions are just able to scratch the surface (Fig. 81) and cannot produce recoil atoms in depth. Future experiments will switch to different ions (e.g. La^{3+}, Au^{2+}) and to higher energies (1 - 8 MeV) in order to produce real damage to the material and to get data that will allow the detailed investigation of the crystalline - amorphous phase transition.

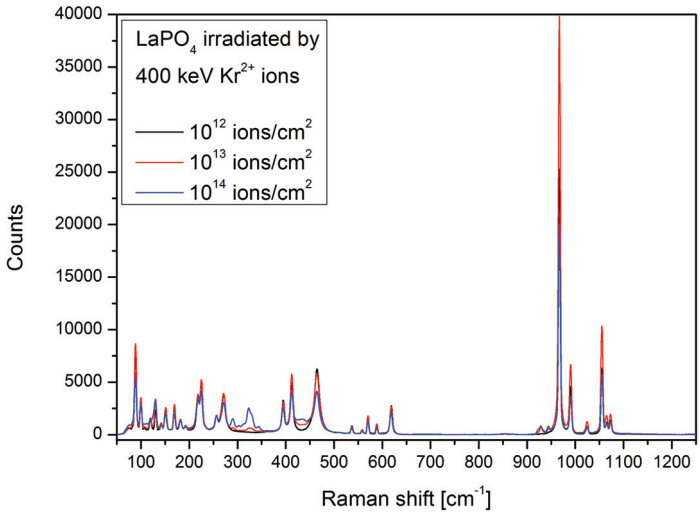

Fig. 80: Raman spectra of $LaPO_4$ irradiated by 400 keV Kr^{2+} ions.

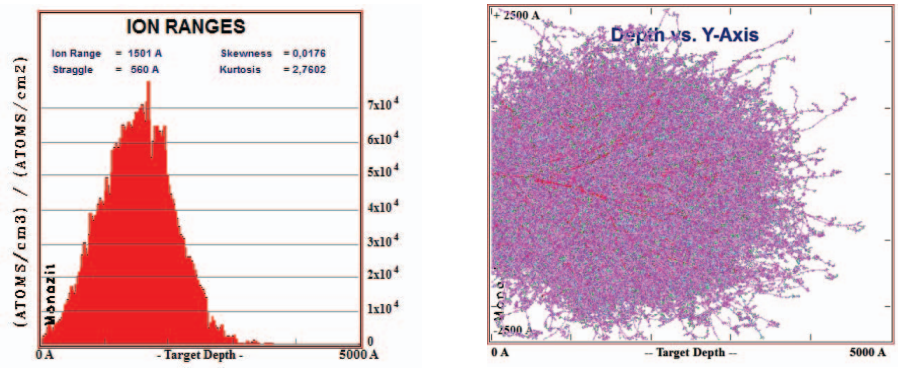

Fig. 81: Left: Computer simulation of the ranges of 400 keV Kr^{2+} ions shot on synthetic $LaPO_4$ (incident angle: 7°) using the program suite SRIM. Right: Computer simulation (SRIM) of collision events (primary caused by Kr^{2+} (RED) and secondary caused by recoil atoms (GREEN, PURPLE)) for the same sample and experiment. In this picture the Kr^{2+} beam hits the target from the left.

Conclusions

Rare earth orthophosphates with monazite structure type of different compositions could be synthesized and well characterized by raman spectroscopy. The results reveal a somewhat unusual behaviour of i) $Eu[PO_4]$ as well as of ii) $La[PO_4]$ und $Ce[PO_4]$, when precise and accurate raman and x-ray data are taken into account. From La to Gd the crystal structures and the related properties of Ln-orthophosphates do not change linearly. By changing the chemical composition of $Ln[PO_4]$ from Ln = La to Gd, the lanthanide contraction induces non-linear structural correlations, which were not yet properly addressed. In order to receive a deeper understanding of such lanthanide orthophosphates, that shall serve as simulation phases for monoclinic actinide orthophosphates, which are the actual goal as new waste

forms, more research has to be done to answer remaining questions and to clear up not well understood issues. This includes the detailed investigation of the reversible crystalline - amorphous phase transition, caused by irradiation and recoil processes.

References

[1] L.A. Boatner, B.C. Sales, In: W. Lutze, R.C. Ewing (Eds.): *Radioactive waste forms for the future*, Amsterdam, North-Holland (1988).

[2] Y. Hikichi, T. Nomura, Y. Tanimura, S. Suzuki, M. Miyamoto, *J. Am. Ceram. Soc.* **73** (1990) 3594.

[3] G.R. Lumpkin, *Elements* **2** (2006) 365.

[4] W.J. Weber, A. Navrotsky, S. Stefanovsky, E.R. Vance, E. Vernaz, *MRS Bulletin* **34** (2009) 46.

[5] G.M. Begun, G.W. Beall, L.A. Boatner, W.J. Gregor, *J. of Raman Spectroscopy* **11** (1981) 273.

[6] D.E. Hobart, G.M. Begun, R.G. Haire, H.E. Hellwege, *J. of Raman Spectroscopy* **14** (1983) 59.

[7] G.M. Begun, C.E. Bamberger, *J. of Raman Spectroscopy* **13** (1982) 284.

[8] R. Podor, *Eur. J. Mineral.* **7** (1995) 1353.

[9] N. Zotov, H. Schlenz, B. Brendebach, H. Modrow, J. Hormes, F. Reinauer, R. Glaum, A. Kirfel, C. Paulmann, *Z. Naturforsch.* **58a** (2003) 419.

[10] E.N. Silva, A.P. Ayala, I. Guedes, C.W.A. Paschoal, R.L. Moreira, C.-K. Loong, L.A. Boatner, *Optical Materials* **29** (2006) 224.

[11] L. Nasdala, R. Grötzschel, S. Probst, B. Bleisteiner, *Canadian Mineralogist* **48** (2010) 351.

[12] H. Assaaoudi, A. Ennaciri, A. Rulmont, *Vibrational Spectroscopy* **25** (2001) 81.

[13] D. Uy, A.E. O'Neill, L. Xu, W.H. Weber, R.W. McCabe, *Appl. Catalysis B: Environmental* **41** (2003) 269.

[14] G.W. Beall, L.A. Boatner, D.F. Mullica, W.O. Milligan, *J. inorg. nucl. Chem.* **43** (1981) 101.

[15] J.G. Pepin, E.R. Vance, G.J. McCarthy, *Mat. Res. Bull.* **16** (1981) 627.

[16] J.G. Pepin, E.R. Vance, *J. inorg. nucl. Chem.* **43** (1981) 2807.

[17] Y. Ni, J.M. Hughes, A.N. Mariano, *Am. Mineralogist* **80** (1995) 21.

[18] A.T. Aldred, *Acta Cryst.* **B40** (1984) 569.

[19] M.E. Poloznikova, V.V. Fomichev, *Russian Chem. Rev.* **63** (1994) 399.

[20] C.T. Dinh, P.V. Huong, R. Olazcuaga, C. Fouassier, *J. of Optoelectronics and Advanced Materials* **2** (2000) 159.

[21] J.F. Ziegler, M.D. Ziegler, J.P. Biersack, Nucl. Instr. and Meth. in *Phys. Res.* **B 268** (2010) 1818.

5.12. MC simulation of thermal neutron flux of large samples irradiated by 14 MeV neutrons

Y. Bai[1,2], E. Mauerhofer[1], J. Kettler[1], D. Wang[2]

[1] Institute of Energy and Climate Research – Nuclear Waste Management and Reactor Safety (IEK-6), Forschungszentrum Jülich GmbH, 52425 Jülich, Germany

[2] School of Nuclear Science and Engineering, Shanghai Jiao Tong University, 200240 Shanghai, China

Corresponding author: e.mauerhofer@fz-juelich.de

Abstract

The response of a 14 MeV neutron-based prompt gamma neutron activation analysis (PGNAA) system, i.e. the prompt gamma-rays count rate and the average thermal neutron flux, is studied with a large concrete sample and with a homogeneous large sample, which is made of polyethylene and metal with various concentrations of hydrogen and cadmium using the MCNP-5 (Monte Carlo N-Particle) code. The average thermal neutron flux is determined by the analysis of the prompt gamma-rays using the thermal neutron activation of hydrogen in the sample, and the thermal and fast neutron activation of carbon graphite irradiation chamber of the PGNAA-system. Our results demonstrated that the graphite irradiation chamber of the PGNAA-system fairly operates, and is useful to estimate the average thermal neutron flux of large samples with various compositions irradiated by 14 MeV neutrons.

Introduction

In Germany, the declaration and balancing of toxic substances in low and intermediate level radioactive waste (LILW) have become obligatory as a result of the plan-approval for disposal Konrad [1]. Depending on its origin, LILW may contain toxic elements (Pb, Cd, Hg, and alkali metals), anions (nitrates, sulphates, chlorides, and chlorates), and toxic organic chemical compounds [2]. Radioactive waste containing such toxic substances must comply with the regulations defined by the German authority and their properties need to be taken into account for a safe disposal.

In order to achieve this, the limiting values for toxic elements and substances were defined by the Federal Office of Radiation Protection (BfS)[3] for the final disposal of radioactive waste packages in the mine Konrad. To determine toxic elements in radioactive waste packages, a non-destructive analytical technique based on PGNAA (Prompt- Gamma-Neutron-Activation-Analysis) with a 14 MeV neutron generator is in development at the Institute of Energy Research-Safety Research and Reactor Technology, Forschungszentrum Jülich, Germany. In the first step, a PGNAA-system consisting of a 14 MeV neutron generator for sample irradiation, an HPGe detector for prompt-gamma ray measurement, and a graphite irradiation chamber was designed for the investigation of large samples with a maximal volume of 50 L.

In this paper, the prompt γ-ray count rate and the average thermal neutron flux in the sample for the PGNAA-system was studied with a large concrete sample and with a homogeneous large sample made of polyethylene (PE) and metal with various H and Cd contents using the MCNP-5 code. To determine the average thermal neutron flux in large samples of various compositions, a new method was proposed using the prompt-gamma rays at 2.22 MeV

produced by thermal neutron activation of hydrogen in the sample, and at 4.44 MeV and 4.95 MeV produced by fast and thermal neutron activation of carbon in the graphite chamber and in the sample, respectively.

MCNP5 modelling

The PGNAA-system was modelled according to the experimental setup (Fig. 82). The investigated drum was placed in an irradiation chamber made exclusively of graphite as neutron moderator and reflector. Out of radioprotection purpose, the chamber wall was about 40 cm thick, and the inner volume was 40 cm × 40 cm × 50 cm. Hydrogenous materials like PE or paraffin were prohibited in the irradiation chamber, so as to determine hydrogen content of the drum matrix using the 2.22 MeV γ-ray.

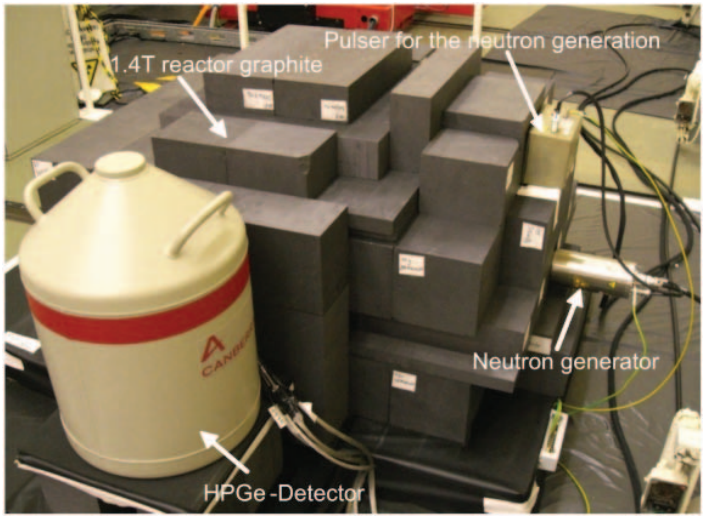

Fig. 82: Side views of the PGNAA-system in the experimental hall with the HPGe-detector in front, the neutron generator on the right side and the graphite irradiation chamber.

The drum was irradiated with 14 MeV neutrons from a D-T neutron generator (GENIE 16GT, EADS SODERN). The deuterium beams irradiate the tritium target located at mid-height of the drum, and a 35-cm distance was kept from its centre. The prompt γ-rays was detected with a 104% n-type HPGe detector (Canberra). The detector was surrounded by ^{6}LiF plates to avoid thermal neutron capture in the Ge crystal. The distance between the detector window and the drum centre was 35 cm so that a 50 L drum was fully analysed.

In the MCNP model, the 14 MeV neutron source was defined as a disc source emitting 10^{8} $n \cdot s^{-1}(4\pi)$, and the HPGe detector was described as a 8×8 cylinder of natural germanium. To be like with a real HPGe detector, track lengths of the γ-rays were simulated using the so called “pulse height tally” and the Gaussian Energy Broadening function (GEB), which is related to energy resolution of the physical detector. The 50 L steel drum with 1.5 mm wall was filled with dry concrete or a mixture of PE and metal.

Contents of the dry concrete were: O, 51.6%; Si, 37%; Ca, 8.9%; Al, 0.85%; K, 0.7%; Mg, 0.57%; Fe, 0.45%; H, 0.41%; Mn, 0.0294%; and Cl, 0.0097%. It was about 115 kg, with a density of 2.35 $g \cdot cm^{-3}$. In order to simulate the samples with higher H content, the silicon

content was replaced by hydrogen. Composition of the PE and metal mixture was: O, 24.7 α%; Na, 5.9 α%; Al, 11.8 α%; Si, 28.2 α%; Ca, 11.8 α%; Fe, 11.8 α%; and Cu, 5.9 α%, where $\alpha = (1–C_{PE}/100)$ and C_{PE} is the PE content. For polyethylene, the carbon content changes with hydrogen content at a mass ratio of 6/1. And the mixture of PE and metal was 115 kg, with an average density of 2.3 $g \cdot cm^{-3}$.

In the simulations, Cd content of the samples increased from 0 to 1000 ppm, and hydrogen content from 0 to 4%. Each simulation calculated 10^9 particles, for a high statistical precision in terms of relative error and variance of variance (vov), within an accuracy interval of 0.2% (1σ).

Prompt gamma ray count rates

As an example, the prompt gamma spectrum (Fig. 83) was obtained by MCNP5 with the concrete sample of 500-ppm cadmium. A large number of prompt γ-rays were observed from the fast and thermal neutron activation of the sample, the graphite chamber and the steel drum. The prompt γ-rays at 2.22 MeV produced by thermal neutron activation of hydrogen in the sample, and at 4.44 MeV and 4.95 MeV produced by fast and thermal neutron activation of carbon in the graphite chamber and in the sample were labelled. They were used to monitor the average thermal neutron flux of the samples. The major prompt γ-ray of Cd at 0.558 MeV was also marked in the figure.

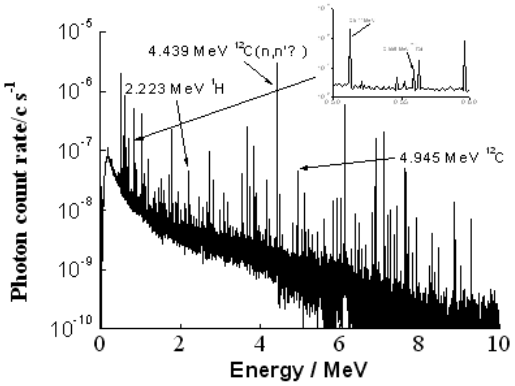

Fig. 83: Simulated prompt gamma spectrum of concrete sample (115 kg) of 500 ppm cadmium. The simulation was performed by MCNP5, with 108 $n \cdot s^{-1}$ of 14 MeV neutrons, which was normalized to 1.

The count rate at 2.22 MeV with the H and Cd in the two samples is shown in Fig. 84. Under given Cd concentration, the count rate at 2.22 MeV increases with the H concentration, which acted as fast neutron moderator, hence an increase of the average thermal neutron flux. The concrete sample had higher counts than the PE and metal mixture, reflecting a difference in the absorption of thermal neutrons. Given the H concentration, the count rate at 2.22 MeV decreased with the Cd concentration due to the absorption of its thermal neutrons. This was more remarkable in the concrete sample than in the mixture of PE and metal because of the composition difference, and the higher the Cd concentration, and the lower the difference for the two samples. Thus, the count rate at 2.22 MeV may be used to monitor the average thermal neutron flux in a specific sample.

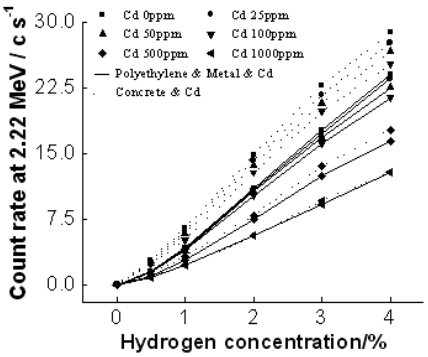

Fig. 84: Count rate of the prompt γ-ray at 2.22 MeV calculated by MCNP5 with thermal neutron activation of H in the sample, as function of the H and Cd concentration in the two materials.

The dependence of the count rate at 4.44 MeV on the H and Cd contents in the two samples is shown in Fig. 85. The value, which was independent of the Cd content, i.e. the thermal neutron absorption, only depends on moderation properties of the sample, and decreased linearly with the H concentration. In the mixture of the samples, however, a break of the linearity was observed due to containing 3% to 4% hydrogen except for a large amount of polyethylene. Given the H concentration, the count rate was lower in the concrete sample than in the mixed samples, as the former is a better absorber of fast neutrons than the latter. The macroscopic neutron cross section of 14 MeV neutrons was 0.115 cm^{-1} for the concrete sample, and was 0.0827 cm^{-1} for the mixture without polyethylene, and that was 0.0964 cm^{-1} for the mixture of 24% PE (4% H). Thus the count rate at 4.44 MeV may be used to monitor the moderation and absorption of fast neutrons in the sample.

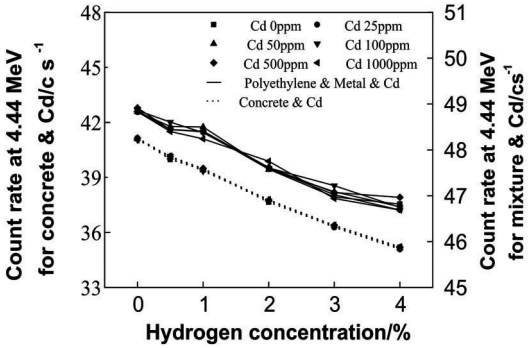

Fig. 85: Count rate of the prompt γ-ray at 4.44 MeV calculated by MCNP5 with fast neutron activation of carbon (graphite cell), as a function of the H and Cd contents in the two materials.

The count rate at 4.95 MeV varied with the H and Cd contents in the two samples (Fig. 86). The behavior was much more complex than at 2.22 MeV and 4.44 MeV. Given the Cd concentration, the count rate increased for a lower than 1% hydrogen, and reached a

constant for hydrogen concentrations of 1% to 2% in the concrete sample, and for that of 1% to 3% in the PE and metal mixture. At the highest H concentrations, the count rate decreased in the concrete sample due to its thermal neutron absorption, and increased in the mixed samples due to the large amount of the carbon. Given the H concentration, the count rate at 4.95 MeV decreased with increasing Cd concentrations due to its thermal neutron absorption, which reflected the moderation of fast neutrons and the absorption of thermal neutrons in the sample.

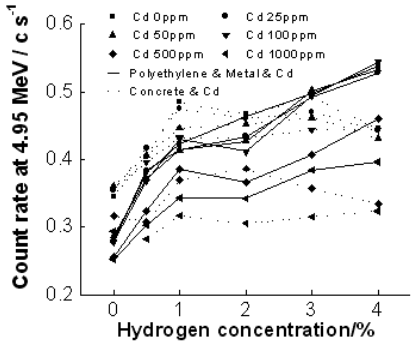

Fig. 86: Count rate of the prompt γ-ray at 4.95 MeV calculated by MCNP5 with thermal neutron activation of carbon (graphite cell) as a function of the H and Cd contents in the two materials.

The count rate at 0.558 MeV depended on the H and Cd concentration in the two samples (Fig. 87). Given the Cd concentration, the rate increased non-linearly for a lower than 2 % hydrogen in the concrete sample, and lower than 3% hydrogen in the mixed samples. For high hydrogen and lower cadmium than 500 ppm, the rate decreased due to the thermal neutron absorption by hydrogen. For higher cadmium than 500 ppm, the rate increased. Given the H content, the rate increased with the Cd concentration and reached a saturation value due to the absorption of thermal neutrons by cadmium.

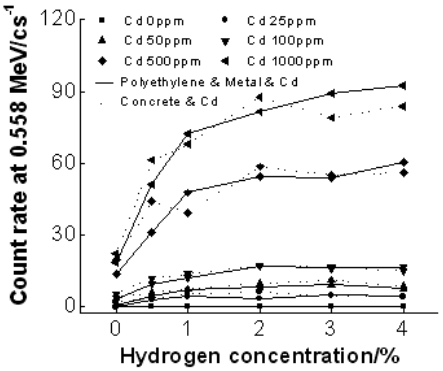

Fig. 87: Count rate of the prompt γ-ray at 0.558 MeV calculated by MCNP5 with thermal neutron activation of cadmium in the sample as a function of the H and Cd concentration in the two materials.

Thermal neutron flux

Fig. 88 shows dependence of the average thermal neutron flux on the H and Cd concentration in the two samples. Given the Cd concentration, the average thermal neutron flux increased non-linearly with the H concentration, whereas it decreased non-linearly with increasing Cd concentration under given H content.

In order to find a general analytical expression of the average thermal neutron flux based on the count rates, the average thermal neutron flux, Φ_{th}, was calculated by MCNP5 without cadmium in the two materials, i.e. the strong thermal neutrons absorber was first fitted by function of the prompt γ-ray count rate of hydrogen at 2.22 MeV, Z_H, using Eq. (1),

$$\Phi = \Phi_0 + \Phi_{max} Z_H / (C + Z_H) \quad (1)$$

where, Φ_0 was the average thermal neutron flux without hydrogen, Φ_{max} was its maximum value, and C was sample composition dependent corrective factor taking into account the moderation of the fast neutrons. In the concrete sample, fitting the Φ should lead to Φ_0 = 3138 ± 355 n·cm^{-2}·s^{-1}, Φ_{max} = 15063 ± 488 n·cm^{-2}·s^{-1}, and C = 4.11 ± 0.49 counts·s^{-1} with a regression coefficient of 0.998. In the PE and metal mixture, Φ_0 = 2173 ± 242 n·cm^{-2}·s^{-1}, Φ_{max} = 15352 ± 547 n·cm^{-2}·s^{-1}, and C = 7.44 ± 0.49 counts·s^{-1} with a regression coefficient of 0.999. The Φ_0 values are in good agreement with of that of the MCNP5 calculation (3162 and 2021 n·cm^{-2}·s^{-1}). Taking into account the errors, the two materials have the same Φ_{max} and the averaged Φ_{max} of 15207 ± 204 n·cm^{-2}·s^{-1}) was used for the following calculation.

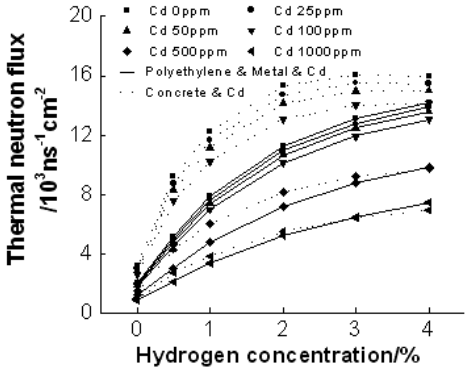

Fig. 88: Average thermal neutron flux calculated by MCNP-5 varied as function of the hydrogen and cadmium concentration for the two materials.

In a next step, a factor taking into account the relative effect of the concrete sample on the moderation of the fast neutrons was defined using the prompt γ-ray count rate at 4.44 MeV, $Z_{C,fast}$, which was produced by the fast neutron activation of carbon as,

$$\alpha = Z_{C,fast} / Z^{ref}_{C,fast} \quad (2)$$

where, $Z^{ref}_{C,fast}$ is the average count rate at 4.44 MeV in the concrete samples without cadmium, to be free from Cd influence on fast neutron moderation (Fig. 4). The count rate at 2.22 MeV, Z_H, can be calculated by:

$$Z^{ref}_{C,fast} = a_0 + a_1 Z_H + a Z_H^2 \quad (3)$$

with a_0 = 41.08 ± 0.06, a_1 = –183.88 ± 8.55 and a_2 = 889.77 ± 41.37 the coefficients of the fit with a regression coefficient of 0.999.

A factor considering the relative influence of the concrete sample on the absorption of the thermal neutron without cadmium was derived from the prompt gamma-ray count rate at 4.95 MeV, $Z_{C,thermal}$, which was produced by the thermal neutron activation of carbon as follows:

$$\beta = Z_{C,thermal}/Z^{ref}_{C,thermal} \qquad (4)$$

where, $Z_{C,thermal}$ = 0.453 ± 0.035 counts·s^{-1} is the mean count rate at 4.95 MeV in the cadmium-free concrete samples.

Finally, the average thermal neutron flux, Φ_{th}, can be calculated for any samples with the lower than 4% hydrogen, and with the lower than 1000 ppm cadmium, as well as other elements, which showed a strong absorption of thermal neutron using the following semi empirical formula:

$$\Phi_{th} = \alpha\,\beta^2\,[\alpha^2\Phi_0 + \Phi_{max}Z_H/(\alpha^{5/2}\,C + Z_H)] \qquad 5)$$

where, Φ_0 = 3138 ± 355 n·cm^{-2}·s^{-1}, Φ_{max} 15207 ± 204 n·cm^{-2}·s^{-1}, and C = 4.11 ± 0.49 counts·s^{-1}, obtained from the analysis of the average thermal neutron flux without Cd in the concrete sample. The values of Φ_{th} obtained by Eq. (5) were compared with that of the MCNP5 calculation, both were in good agreement within a relative error of 16 % (Fig. 89), and the deviation for the two data sets was –11 ± 23%.

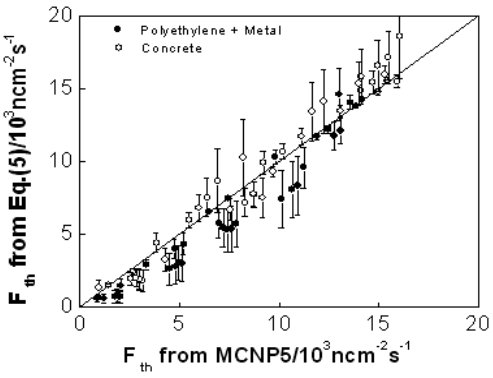

Fig. 89: The comparison of the average thermal neutron flux calculated by mean of Eq. (6) with by MCNP5 for the two materials.

According to the PGNAA system, therefore, Eq.(5) led to a fairly good estimation for the average thermal neutron flux in a homogeneous large sample of 50 L, irradiated by a 14 MeV neutron source emitting the 108 n·s^{-1}(4π). Any modification of the PGNAA system and a change of the sample volume should impact on the prompt gamma-ray count rates, and was necessary for a new parameterization.

Conclusion

In this work, the demonstration that the average thermal neutron flux in large samples irradiated by 14 MeV neutrons may be estimated from the prompt gamma-rays produced by the thermal neutron activation of hydrogen in the sample, and by the thermal and fast

neutron activation of carbon in the sample and the graphite irradiation chamber has been proved based on the simulation by MCNP-5. The analytical expression to calculate the average thermal neutron flux is specific to the PGNAA-system described in this work i.e. to the amount and thickness of graphite surrounding the sample and to the relative position of the gamma-ray detection system to the 14 MeV neutron source.

References

[1] Niedersächsisches Umweltministerium; Planfeststellungsbeschuss für die Errichtung und den Betrieb des Bergwerkes Konrad in Salzgitter als Anlage zur Endlagerung fester oder verfestigter radioaktiver Abfälle mit vernachlässigbarer Wärmeentwicklung, Bekanntmachung des NMU vom 20.05.2002. Niedersächsisches Ministerialblatt, Hannover, Nds. MBl. Nr. 21/2002, 808.

[2] International Atomic Energy Agency. IAEA-TECDOC- 1325: Management of low and intermediate level radio- active wastes with regard to their chemical toxicity, IAEA, Vienna, December 2002, 3-10.

[3] Bundesamt für Strahlenschutz. Planfeststellungsbeschluss für die Errichtung und den Betrieb des Bergwerkes Konrad in Salzgitter. 2002, 191-196.

5.13. An Improved Method for the non-destructive Characterization of Radioactive Waste by Gamma Scanning

E. Mauerhofer[1], Y. F. Bai[1,2], D. Z. Wang[2], R. Odoj[1]

[1] Institute of Energy and Climate Research – Nuclear Waste Management and Reactor Safety (IEK-6), Forschungszentrum Jülich GmbH, 52425 Jülich, Germany

[2.]School of Nuclear Science and Engineering, Shanghai Jiao Tong University, 200240 Shanghai, China

Corresponding author: e.mauerhofer@fz-juelich.de

Abstract

A method to improve the reliability and accuracy of activity results in segmented gamma scanning of radioactive waste drums with non-uniform isotope and matrix distribution has been developed. The improved method which is based on numerical simulations of the measured angular dependent count rate distribution during drum rotation in segmented gamma scanning has been validated through the measurement of Cs-137 and Co-60 activities in 13 real radioactive waste drums with heterogeneous activity and matrix distributions. The results were compared to that obtained for the conventional method assuming homogeneous activity and matrix distributions.

Introduction

Radioactive waste has to meet the specifications and acceptance criteria defined by national regulatory and management authorities for its intermediate and final storage. The non-destructive determination of the isotope specific activity content in quality checking of radioactive waste drums is most widely performed by segmented gamma scanning (SGS). Generally it is assumed that the matrix and the activity are uniformly distributed in each drum segment that is measured. Corrections for gamma attenuation in the waste matrix are usually performed by methods like density estimation by drum weighing or calculation of corrective factors based on assumptions regarding the average distribution of density and activity in the waste. However, waste drums are often heterogeneous, and span a wide range of matrix composition and activity distribution. Hence, uncertainties will be introduced which cannot be accounted for by standard correction procedures. Thus SGS errors are mainly related to non-uniform measurement responses associated with unknown radioactive sources spatial distribution and matrix heterogeneity including internal shielding structures of unknown design [1,2,3,4].

In this paper we describe an improved method to quantify the activity of spatially concentrated gamma-emitting isotopes ('hot spots') in heterogeneous waste drums. This method is based on the analysis of the angular dependent count rate distributions recorded during the waste drum rotation in SGS to localize 'hot spots' inside the waste package and to determine the gamma attenuation properties of the waste matrix. To achieve this, numerical simulations and χ^2 fits of the angular dependent count rate distributions were performed using an analytical expression derived from a geometrical model. The application of the improved method to the quantification of non-uniform distributed Cs-137 and Co-60 activities in real heterogeneous radioactive waste drums is demonstrated.

The improved method

A heterogeneous waste matrix may be considered as a composite of active waste components containing 'hot spots' assimilated as point sources, and passive waste components containing shielding structures. Based on this consideration the angular dependent count rate of a collimated γ-ray detector exposed to point sources of 1 Bq activity located at different radial and angular positions (p_i,β_i) in the central horizontal section of a drum segment may be calculated in function of the rotation angle θ of the waste drum as:

$$Z_\gamma(\theta) = \varepsilon_0 \cdot I_\gamma \cdot e^{-\left(\mu/\rho_w \cdot \rho_w \cdot d_w\right)} \cdot \sum_{(p_i,\beta_i)} \left(\frac{d_0}{d_i(\theta)}\right)^2 e^{-\left(\mu/\rho_a \cdot \rho_a \cdot l_a(\theta)\right)} \cdot e^{-\left(\mu/\rho_s \cdot \rho_s \cdot l_s(\theta)\right)} \cdot e^{-\left(\mu/\rho_c \cdot \rho_c \cdot l_c(\theta)\right)} \qquad (1)$$

where d_0 and $d_i(\theta)$ are the distances of the segment centre and of the point source from the centre of the γ-ray detector surface, respectively; ε_0 is the photopeak efficiency of the considered γ-ray energy for a point source at the distance d_0; I_γ is the intensity of the considered γ-ray energy; ρ_w, ρ_a, ρ_s and ρc are the densities of the drum wall, the active waste matrix, the passive waste matrix and the collimator of the γ-ray detector, respectively; μ/ρ_w, μ/ρ_a, μ/ρ_s, μ/ρ_c are the corresponding mass attenuation coefficients at the considered γ-ray energy; d_w is the wall thickness of drum and $l_a(\theta)$, $l_s(\theta)$ and $l_c(\theta)$ are the mean distances covered by the γ-ray in the active waste matrix, the passive waste matrix and the collimator of the γ-ray detector, respectively to reach the centre of the γ-ray detector surface. The geometric model used to evaluate $Z_\gamma(\theta)$ is shown in Fig. 90.

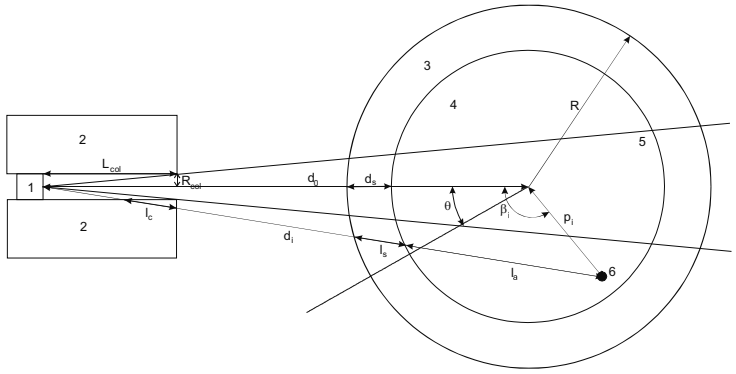

Fig. 90: Geometric model used to simulate the angular count rate distribution. 1: HPGe-detector, 2: lead collimator; 3: passive matrix; 4: active matrix; 5: volume of the drum segment seen by the collimated HPGe-detector; 6: hot-spot.

The distance of the point source from the centre of the γ-ray detector surface is expressed by:

$$d_i(\theta) = \sqrt{(d_0 - p_i \cdot \cos(\theta + \beta_i))^2 + (p_i \cdot \sin(\theta + \beta_i))^2} \qquad (2)$$

where p_i and β_i are the radial and angular positions of the point source, respectively. The mean distance covered by the γ-ray in the active waste matrix is given by:

$$l_a(\theta) = d_i(\theta) - \alpha \cdot d_0 + \sqrt{(\alpha \cdot d_0)^2 + \cdot (R - d_s)^2 - d_0^{\,2}} - d_w \qquad (3)$$

where R is the drum radius, d_s the mean thickness of the passive matrix and α a parameter calculated as following:

$$\alpha = \frac{d_0 - p_i \cdot \cos(\theta + \beta_i)}{d_i(\theta)} \qquad (4).$$

The mean distance covered by the γ-ray in the passive matrix is given by:

$$l_s(\theta) = d_i(\theta) - \alpha \cdot d_0 + \sqrt{(\alpha \cdot d_0)^2 + R^2 - d_0^{\,2}} - l_a(\theta) - d_w \qquad (5).$$

The mean distance covered by the γ-ray in the collimator (cylindrical) of the γ-ray detector is given by:

$$l_c(\theta) = 0 \qquad \text{for } d_i(\theta) \le d_{col} \qquad (6)$$

$$l_c(\theta) = \frac{L_{col}}{\alpha} - \frac{R_{col}}{\sqrt{1 - \alpha^2}} \qquad \text{for } d_i(\theta) > d_{col}$$

where L_{col} is the collimator length, R_{col} the collimator radius and d_{col} calculated as:

$$d_{col} = \alpha \cdot d_i(\theta) \cdot \sqrt{1 + \left(\frac{R_{col}}{L_{col}}\right)^2} \qquad (7).$$

The density of the active waste matrix ρ_a in a drum segment may be expressed as:

$$\rho_a = \rho_s + \frac{V}{V_a} \cdot (\rho_m - \rho_s) \qquad (8)$$

where ρ_m is the apparent drum waste density determined by weighing; ρ_s is the density of the passive matrix and V and V_a are the volumes of the drum segment and of the active matrix seen by the collimated γ-ray detector, respectively. V is expressed for a cylindrical collimator by:

$$V = \frac{2 \cdot \pi}{3} \cdot \left(\frac{R_{col}}{L_{col}}\right)^2 \cdot (R - d_w) \cdot \left(3 \cdot d_0^{\,2} + (R - d_w)^2\right) \qquad (9)$$

and V_a by:

$$V_a = \frac{2 \cdot \pi}{3} \cdot \left(\frac{R_{col}}{L_{col}}\right)^2 \cdot (R - d_s - d_w) \cdot \left(3 \cdot d_0^{\,2} + R^2 + (d_s + d_w)^2 - 2 \cdot R \cdot (d_s + d_w)\right) \qquad (10).$$

The volume of the passive matrix V_s is calculated as the difference between V and V_a.
The above equations enable to simulate the angular dependent count rate distributions for various point source configurations and different properties of the active and passive matrix and a given counting geometry. For the localization of the 'hot spots' within a drum segment and the determination of the gamma attenuation properties of the drum segment, the simulated count rates $Z_\gamma(\theta)$ are fitted to the measured count rates $T_\gamma(\theta)$ using the following χ^2 minimization:

$$\chi^2 = \sum_{\theta}^{n} \left(\frac{Z_\gamma(\theta)}{Z_\gamma(\theta)_{max}} - \frac{T_\gamma(\theta)}{T_\gamma(\theta)_{max}} \right)^2 \qquad (11)$$

where $Z_\gamma(\theta)_{max}$ and $T_\gamma(\theta)_{max}$ are the maxima of the simulated and measured angular dependent count rate distributions, respectively; and n is the number of distributions recorded for a segment ($n = 360/\Delta\theta$). The lowest χ^2-value obtained from the fit of the angular dependent count rate distributions recorded for 'hot spots' at various gamma energies i.e. for different gamma-emitting isotopes will lead first to the gamma attenuation properties of the drum segment under investigation. Then a second fit of the angular dependent count rate distributions is performed to determine the radial and angular positions of the 'hot spots' by keeping constant the gamma attenuation properties previously determined for the drum segment. Finally the 'hot spots' activity in Bq for the investigated drum segment is calculated as:

$$A = \frac{\sum_{\theta}^{n} T_\gamma(\theta)}{\sum_{\theta}^{n} Z_\gamma(\theta)^{\rho_i,\beta_i,\rho_a,d_s}_{\chi^2_{min}}} \qquad (12).$$

The relative uncertainty of the activity is estimated as:

$$\sigma_A = \frac{\sqrt{n \cdot \chi^2_{min}}}{\sum_{\theta}^{n} T_\gamma(\theta)} \cdot 100 \qquad (13).$$

If the angular dependent count rate distribution is homogeneous and if the gamma attenuation properties of the drum segment have been previously determined (at least one 'hot spot' analysis for an other angular dependent count rate distribution to determine the matrix properties), then the activity of the corresponding isotope in the drum segment is calculated as [1]:

$$A = \frac{T_\gamma(\theta)_{mean}}{I_\gamma \cdot \varepsilon_0 \cdot F_0 \cdot} \cdot \frac{\mu/\rho_a \cdot \rho_a \cdot V_a}{1 - e^{\left(-\mu/\rho_a \cdot \rho_a \cdot 2 \cdot (R - d_s - d_w)\right)}} \cdot e^{\left(\mu/\rho_s \cdot \rho_s \cdot d_s\right)} \cdot e^{\left(\mu/\rho_w \cdot \rho_w \cdot d_w\right)} \qquad (14)$$

where $T_\gamma(\theta)_{mean}$ is the mean value of the measured angular dependent count rate distribution and F_0 is the area of the spherical zone formed by the intersection of the (conical) volume of the drum segment seen by the collimated γ-ray detector and the drum at the distance d_0.
If the angular count rate distribution is homogeneous and if the gamma attenuation properties of the drum segment cannot be determined, then the activity of the corresponding isotope in the drum segment is calculated assuming a homogeneous matrix with the apparent density ρ_m as [1]:

$$A = \frac{T_\gamma(\theta)_{mean}}{I_\gamma \cdot \varepsilon_0 \cdot F_0 \cdot} \cdot \frac{\mu/\rho_m \cdot \rho_m \cdot V}{1 - e^{\left(-\mu/\rho_m \cdot \rho_m \cdot 2 \cdot (R - d_w)\right)}} \cdot e^{\left(\mu/\rho_w \cdot \rho_w \cdot d_w\right)} \qquad (15)$$

The relative uncertainty for the activity calculated by Eq. (14) or (15) is estimated from the mean standard deviation of $T_\gamma(\theta)_{mean}$.

Application

The improved method was applied to the quantification of non uniform distributed Cs-137 and Co-60 activities in 13 real waste drums (200 L). These drums were selected from a batch of drums with a typical signature of heterogeneous activity and matrix distribution. The waste matrix was made of lead canisters embedded in concrete containing dismounted radioactive sources for industrial application of well known activity. Based on *a priori* information, the mass of lead was ranging between 142 and 470 kg. The apparent density of the waste ρ_m determined by weighing was ranging between 2.61 and 4.04 g/cm^3. The drum height was 80 cm, the drum radius R was 28.15 cm and the wall thickness d_w was 0.15 cm. The waste drums were assayed by means of segmented gamma scanning with stepwise drum rotation. For that, the drums were subdivided into 20 equidistant segments and each segment rotation was subdivided into 12 sectors ($\Delta\theta$ = 30°) for which complete γ-spectra were measured and stored. The gamma-emitting isotopes were detected with an high resolution HPGe coaxial detector, 30% relative efficiency, shielded by means of a lead cylinder with a cylindrical collimation window. The length L_{col} and the radius R_{col} of the detector collimator were 20.5 and 2 cm, respectively. The thickness of the lead collimator was 9 cm. The distance of the drum segment centre from the centre of the detector surface d_0 was 74.65 cm. From this counting geometry, the volume of a drum segment seen by the collimated detector was 9769 cm^3 and the parameter F_0 was 166.63 cm^2. The detector was connected to a digital electronics DSPEC PLUS™ (ORTEC) for signal processing and the spectra were recorded with GAMMAVISION®-32 (ORTEC). The assay time was 1 hour i.e. 15 s for each sector corresponding to the assay time set for routine scanning of drums. The gamma scanner was operated via a PC-based system with the software SCANNER 32 which was designed in collaboration with a professional software engineering company (HM Ingenieurbüro Marschelke) to support all aspects of the gamma scanning such as: full hardware control for detector lifting and drum rotation, nuclear instrumentation control for gamma-spectrometry and dose rate measurements, visualisation of measurement progress (engine's status, spectral data, gamma count rate and dose rate distribution), data evaluation and analysis (spectrum analysis, activity determination) and result reporting and archiving. Detailed technical specifications of the gamma scanner employed for the routine characterization of radioactive waste drums may be found elsewhere [5].

The angular dependent count rate distributions measured at 661.6 keV for Cs-137 and at 1173.2 keV for Co-60 were used to determine the activity of the isotopes. Numerical simulations were performed with a computer program written in Visual Basic and running as a macro file under the software SigmaPlot® 8.0.2 (SYSTAT Sofware Inc.). The presence of 'hot spots' in drum segments was obtained from the statistical treatment of the measured angular dependent count rate distributions taking into account that a second maximum of the count rate at θ + 180° could correspond to a maximum of the count rate observed at θ. Due to the low spatial resolution of the collimated detector it was assumed that no more than two 'hot spots' of the same isotope could coexist in a drum segment. The radial position of the sources p_i was varied from 1 cm to (R - d_s - d_w) cm with a step of 2 cm. The angular position of the sources β_i was varied from 0° to 330° with a step of 30°. The mean thickness of the passive matrix d_s was varied from 0 to 20 cm with a step of 0.5 cm. The density of the active matrix ρ_a was restricted to vary between 1g/cm^3 and the apparent waste density ρ_m. Matrix

configurations leading to negatives values of ρ_a were systematically rejected. The radiological parameters used to simulate the count rate distributions of Cs-137 and Co-60 are given in Tab. 22.

Tab. 22: Radiological parameters used to simulate the angular dependent count rate distributions.

Isotope	Cs-137	Co-60
Eγ, keV	611.6	1173.2
Iγ, %	85.1	99.97
ε_0, %	62.335 10^{-4}	40.900 10^{-4}
μ/ρ_m, μ/ρ_a (concrete), cm^2/g	77.551 10^{-3}	58.943 10^{-3}
μ/ρ_s, μ/ρ_c (lead), cm^2/g	111.22 10^{-3}	61.987 10^{-3}
μ/ρ_w (iron), cm^2/g	73.499 10^{-3}	55.263 10^{-3}

The densities of iron and lead are 7.63 and 11.34 g/cm^3, respectively. Additionally, the activity was calculated assuming a homogeneous density distribution using the apparent waste density ρ_m; setting thus the mean thickness of the passive matrix d_s to zero.

Results and discussion

As examples, the angular dependent count rate distributions of Cs-137 and Co-60 measured for a drum with an apparent waste density of 2.63 g/cm^3 are shown in Fig. 91.

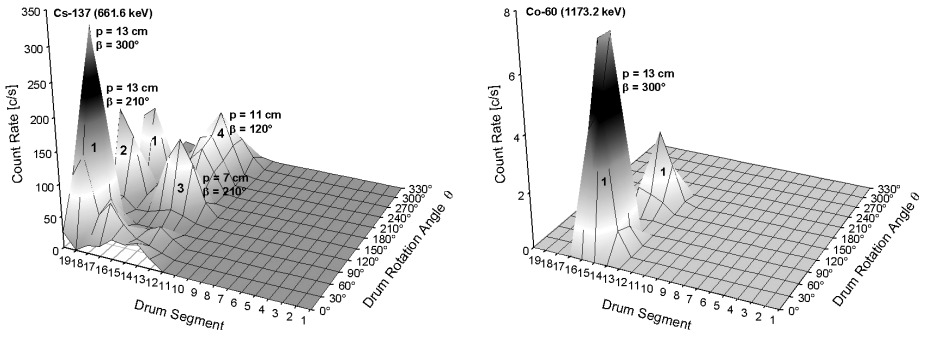

Fig. 91: Count rate distribution of Cs-137 (left diagram) and Co-60 (right diagram) measured for a drum with an apparent waste density of 2.63 g/cm^3. The determined radial and angular positions of the 'hot spots' are indicated on the diagrams. The counting time is 15 s per sector.

The drum contained 5 Cs-137 sources (0.7, 235, 821, 1237 and 5195 MBq) and 2 Co-60 sources (0.1 and 22 MBq). The source activities above are given at the time of the measurement. The radial and angular positions of the 'hot spots' within the drum segments as a result of the numerical simulations are given also in Fig. 91.

In the drum, 4 'hot spots' for Cs-137 and 1 'hot spot' for Co-60 were identified. Two Cs-137-'hot spots' are positioned at a drum height of about 76 cm with the same radial position (13 cm) but different angular positions (210° and 300°). The two other Cs-137-'hot spots' and the Co-60-'hot spot' are positioned at a drum height of about 60 cm with different radial and angular positions: (7 cm, 210°) and (11cm, 120°) for Cs-137 and (13 cm, 300°) for Co-60. It may be noted that the maximum of the count rate for a 'hot spot' occurred at a drum rotation angle $\theta = 360° - \beta$, which corresponds to the closest distance between the 'hot spot' and the detector during drum rotation. A second maximum may be observed at $\theta = 180° - \beta$ depending on the 'hot spot' activity and position, the γ-ray energy and the attenuation properties of the matrix. The radioactive sources with an activity lower than 1 MBq are not detected because of the lead shielding structures. The mean thickness of the lead shielding in the drum segments containing the 'hot spots' was found to be 4 cm. The resulting activities of Cs-137 and Co-60 in the segments of the drum are shown in Fig. 92. They reflect well the axial distribution of the isotopes within the drums.

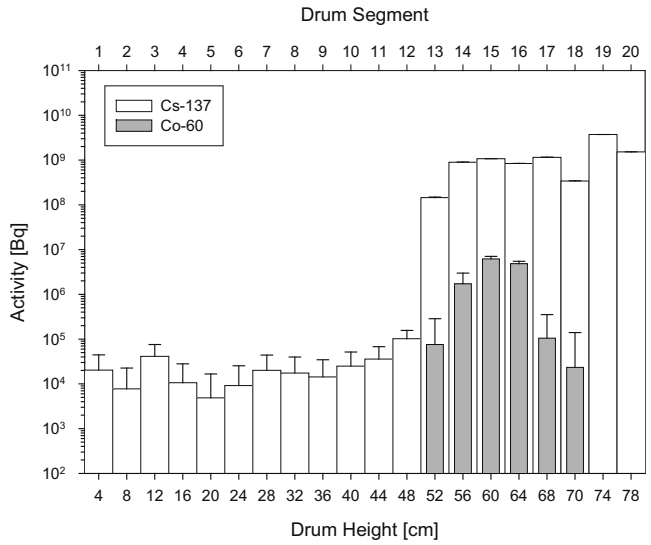

Fig. 92: Activity of Cs-137 and Co-60 in the segments of the drum with an apparent waste density of 2.63 g/cm^3. The activity is calculated for a non uniform distribution of the isotopes and a heterogeneous sample matrix (see Fig. 3).

The results obtained with the improved method compared to the true activity and to the activity calculated by the conventional method which assumes a homogeneous distribution of activity and matrix inside the drum segments are summarized for Cs-137 in Tab. 23. The mean ratio of calculated to true activity is shown for the different methods applied in Fig. 93.

Tab. 23: Results for the determination of the Cs-137 activity in the investigated radioactive waste drums by the conventional and improved method. The true activity is the sum of the sources activities. The activity is given at the time of the measurement.

Cs-137 Activity in Bq					
Drum Nr.	Waste density g/cm^3	True activity	Conventional method	Improved method	
				Homogeneous matrix	Heterogeneous matrix
1	3.99	$4.68 \cdot 10^{10}$	$1.48^{+0.59}_{-0.59} \cdot 10^{8}$	$2.65^{+0,58}_{-0,58} \cdot 10^{9}$	$4.27^{+0.94}_{-0.94} \cdot 10^{10}$
2	2.94	$6.59 \cdot 10^{10}$	$1.42^{+0.22}_{-0.22} \cdot 10^{9}$	$1.81^{+1.61}_{-1.61} \cdot 10^{10}$	$6.08^{+5.41}_{-5.41} \cdot 10^{10}$
3	3.64	$1.73 \cdot 10^{10}$	$8.08^{+2.98}_{-2.98} \cdot 10^{6}$	$2.27^{+2.51}_{-1.20} \cdot 10^{8}$	$7.30^{+8.10}_{-3.87} \cdot 10^{9}$
4	2.63	$7.49 \cdot 10^{9}$	$6.70^{+0,94}_{-0.94} \cdot 10^{7}$	$7.97^{+12.67}_{-4.86} \cdot 10^{8}$	$9.68^{+15.39}_{-5.90} \cdot 10^{9}$
5	2.61	$3.46 \cdot 10^{11}$	$1.69^{+0.29}_{-0.29} \cdot 10^{8}$	$2.19^{+2.10}_{-2.10} \cdot 10^{9}$	$1.10^{+1.06}_{-1.06} \cdot 10^{11}$
6	3.47	$1.58 \cdot 10^{11}$	$4.40^{+0.46}_{-0.46} \cdot 10^{8}$	$3.49^{+5.06}_{-2.06} \cdot 10^{10}$	$4.54^{+6.58}_{-2.68} \cdot 10^{11}$
7	3.48	$9.08 \cdot 10^{10}$	$1.16^{+0.12}_{-0.12} \cdot 10^{9}$	$7.49^{+13.56}_{-4.79} \cdot 10^{10}$	$9.60^{+17.38}_{-6.14} \cdot 10^{11}$
8	3.66	$4.48 \cdot 10^{11}$	$4.87^{+0,81}_{-0.81} \cdot 10^{8}$	$2.05^{+1.58}_{-1.58} \cdot 10^{10}$	$1.67^{+1.28}_{-1.28} \cdot 10^{11}$
9	4.04	$9.86 \cdot 10^{10}$	$3.03^{+0.10}_{-0.10} \cdot 10^{7}$	$7.34^{+1.54}_{-1.54} \cdot 10^{9}$	$6.57^{+1.38}_{-1.38} \cdot 10^{10}$
10	3.57	$6.99 \cdot 10^{10}$	$1.29^{+0.04}_{-0.04} \cdot 10^{7}$	$1.84^{+0.66}_{-0.66} \cdot 10^{9}$	$1.50^{+0,54}_{-0,54} \cdot 10^{10}$
11	2.68	$2.02 \cdot 10^{10}$	$4.12^{+0.35}_{-0.35} \cdot 10^{9}$	$7.71^{+1.54}_{-1.54} \cdot 10^{10}$	$3.95^{+0.79}_{-0,79} \cdot 10^{11}$
12	2.71	$2.93 \cdot 10^{12}$	$4.77^{+1.12}_{-1.12} \cdot 10^{8}$	$7.48^{+3.74}_{-3.94} \cdot 10^{9}$	$1.04^{+0.52}_{-0,52} \cdot 10^{11}$
13	3.61	$3.83 \cdot 10^{11}$	$3.88^{+0.53}_{-0.53} \cdot 10^{7}$	$5.54^{+5.37}_{-5.37} \cdot 10^{9}$	$3.24^{+3.14}_{-3.14} \cdot 10^{10}$
Total		$4.68 \cdot 10^{12}$	$8.58^{+1.04}_{-1.04} \cdot 10^{9}$	$2.53^{+2.08}_{-1.27} \cdot 10^{11}$	$2.42^{+2.75}_{-1.36} \cdot 10^{12}$

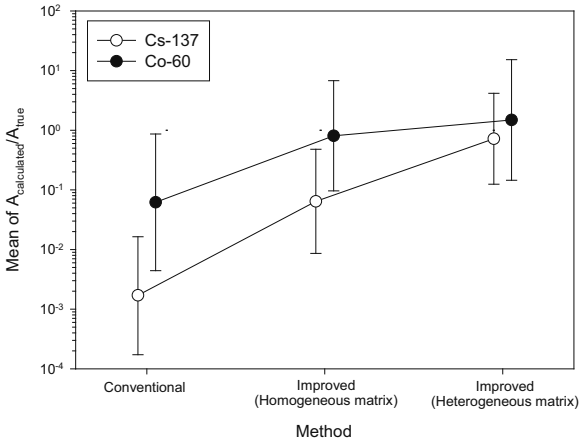

Fig. 93: Mean ratio of the calculated to true activity for the different methods applied.

The conventional method leads to a large underestimation of the activity since the non-uniform distribution of the isotopes and the shielding structures inside the drums are not considered. The mean factor of underestimation is 586 for Cs-137 and 16 for Co-60. The

activity of Cs-137 is much more underestimated compared to that of Co-60 due to a higher absorption of the γ-rays of Cs-137 by the lead shielding structures inside the waste. By applying the improved method for a **homogeneous** waste matrix, the activity values are somewhat higher as the non uniform distributions of the isotopes are now taken into account. The activity of Cs-137 and Co-60 is underestimated by a mean factor of 16 and 1.2, respectively. This corresponds to a mean improvement factor of 37 for Cs-137 and of 13 for Co-60 with respect to the conventional method due to correction for the non-uniform distribution of the isotopes. The results of the improved method for a **heterogeneous** waste matrix considering the presence of the lead shielding structures show a much better agreement with the true value, demonstrating its applicability and the validity of the geometric model used to simulate the angular dependent count rate distributions. In this case, the activity of Cs-137 is underestimated by a mean factor of 1.4 and the activity of Co-60 overestimated by a mean factor of 1.5. The mean improvement factor due to the correction of the γ-rays absorption by the heterogeneous matrix is 11 for Cs-137 and 2 for Co-60 compared to the case of a homogeneous waste matrix.

Conclusion

A method to improve the reliability and accuracy of activity results in segmented gamma scanning of radioactive waste drums exhibiting non-uniform isotope and density distributions has been developed and validated. In comparison to the conventional method, the quality of the activity results obtained by the improved method is largely enhanced. However, the application of the method needs a good counting statistics for the analysis of the angular dependent count rate distributions, which depends on the 'hot spot' activity, the γ-ray energy and the attenuation properties of the waste matrix. The presence of internal shielding structures inside the waste drum may be obtained from *a priori* information and controlled by weighing. An implementation of the improved method to the gamma scanner operation software SCANNER 32 will be performed to enhance the routine quality checking of radioactive waste packages.

References

[1] Filß P. (1995) Relation between the activity of a high-density waste drum and its gamma count rate measured with an unshielded Ge-detector. Appl. Radiat. Isot. 46, 805.

[2] Tran Quoc Dung (1997) Calculation of the systematic error and correction factors in gamma waste assay system. Ann. Nucl. Energy 24, 33.

[3] Tran Quoc Dung (1998) Some theoretical results of gamma techniques for measuring large samples. Nucl. Instrum. Methods Phys. Res. A 416, 505.

[4] Report WG-A-03 (2002) Non-destructive analyses for the quality checking of radioactive waste packages; Proceedings of the workshop "Past, present and future of QA/QC on radioactive waste", 19 and 20 June 2002 at NRG Petten, The Netherlands; Editor: L.P.M van Velzen; European Network of Testing Facilities for the quality checking of Radioactive waste Packages (ENTRAP).

[5] Report WG-A-01 (1998) Synopsis of gamma scanning systems; Comparison of gamma determining systems and measuring procedures for radioactive waste packages; Editors: T. Bücherl, E. Kaniciel, Ch. Lierse; European Network of Testing Facilities for the quality checking of Radioactive waste Packages (ENTRAP).

5.14. Reconstruction of the Activity of Point Sources for the Accurate Characterization of Nuclear Waste Drums by Segmented Gamma Scanning

T. Krings, E. Mauerhofer

Corresponding author: tho.krings@fz-juelich.de

Abstract

This work improves the reliability and accuracy in the reconstruction of the total isotope activity content in heterogeneous nuclear waste drums containing point sources. The method is based on X^2-fits to the angular dependent count rate distribution measured during a drum rotation in segmented gamma scanning. A new description of the analytical calculation of the angular count rate distribution is introduced based on a more precise model of the collimated detector. The new description is validated and compared to the old description using MCNP5 simulations of angular dependent count rate distributions of Co-60 and Cs-137 point sources. It is shown that the new model describes the angular dependent count rate distribution significantly more accurate compared to the old model. Hence, the reconstruction of the activity is more accurate and the errors are considerably reduced which leads to more reliable results. Furthermore, the results are compared to the conventional reconstruction method assuming a homogeneous matrix and activity distribution.

Introduction

Radioactive waste must be characterized in order to verify its conformance with the national regulations for intermediate and final storage. Segmented gamma scanning (SGS) is the most widely applied non destructive analytical technique for the characterization of radioactive waste drums. The isotope specific activity content is generally calculated assuming a homogeneous matrix and activity distribution for each measured drum segment [1]. However, real radioactive waste drums exhibit non-uniform isotope and density distributions heavily affecting the reliability and accuracy of activities reconstruction in SGS [2,3]. The presence of internal shielding structures in the waste drum contributes generally to a strong underestimation of the activity in particularly for radioactive sources emitting low energy gamma-rays independently of their spatial distribution.

In a previous work an improved method to quantify the activity of spatially concentrated gamma-emitting isotopes (point sources or hot spots) in heterogeneous waste drums with internal shielding structures has been developed [4]. The activity of the isotope was determined by numerical simulations and X^2-fits of the angular dependent count rate distribution recorded during the drum rotation in SGS using an analytical expression derived from a geometric model. From the quantification of Cs-137 and Co-60 activities in real heterogeneous waste drums it was demonstrated that the improved method enhances largely the accuracy of the reconstructed activity in comparison to the conventional method which assumes a homogeneous density and activity distribution. However, the isotope activity was estimated with a high uncertainty mainly due to the response of the collimated

gamma-ray detector approximated by a pseudo Dirac function in the applied geometric model.
In this work the analytical expression of the improved method is revised for a more precise calculation of the angular dependent count rate distribution and thus of the activity by modifying the collimated detector response. Further, the new and the old collimator functions are compared by analyzing the angular dependent count rate distributions of Co-60 and Cs-137 point sources simulated with MCNP5 (Monte Carlo N-Particle Code) in different matrices. The obtained results are compared to the conventional method.
different matrices. The obtained results are compared to the conventional method.

Geometric Setup

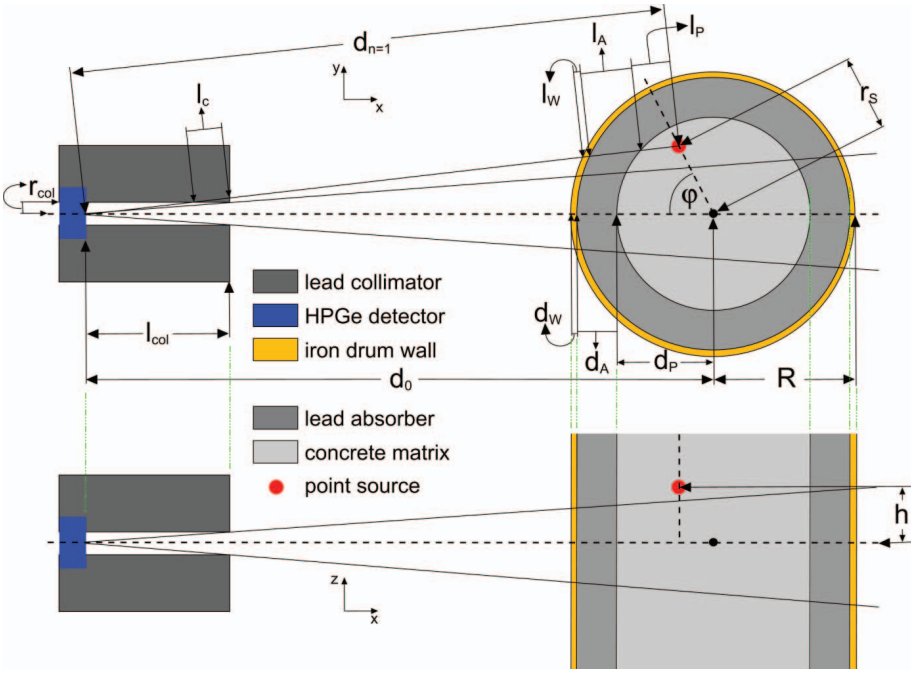

Fig. 94: Geometric model of the experimental setup used for segmented gamma scanning. The upper part shows the top view and the lower part shows the side view of the detector with a drum segment containing an activity point source.

Fig. 94 shows the geometric model of the segmented gamma scanner used for the characterization of nuclear waste at our institute. The emitted photons are detected with an n-type coaxial HPGe detector (30% relative efficiency). The active detector crystal has a diameter of 4.96 cm and a length of 5.31 cm. The detector is shielded by means of a lead cylinder with a cylindrical collimation window. The collimator has a length of 20.6 cm and a diameter of 22 cm. The collimation window has a radius of 2 cm. The distance from the center of the nuclear waste drum to the detector surface is 74.6 cm. Each segment is scanned in 12 steps which leads to a rotation of the drum of 30° in each step. Each geometric quantity in Fig. 94 can thus be calculated according [5]. We also refer to this work

regarding to the calculation of the analytical expression to calculate the count rate expectation and regarding to the activity reconstruction.

Collimator Response Function

The collimator response function is based on the solid angle that is subtended by the collimated detector to the source. It is therefore necessary to calculate the part of the active detector surface which is illuminated beam cone formed by the collimator entrance window. A systematical sketch of this can be seen in Fig. 95.

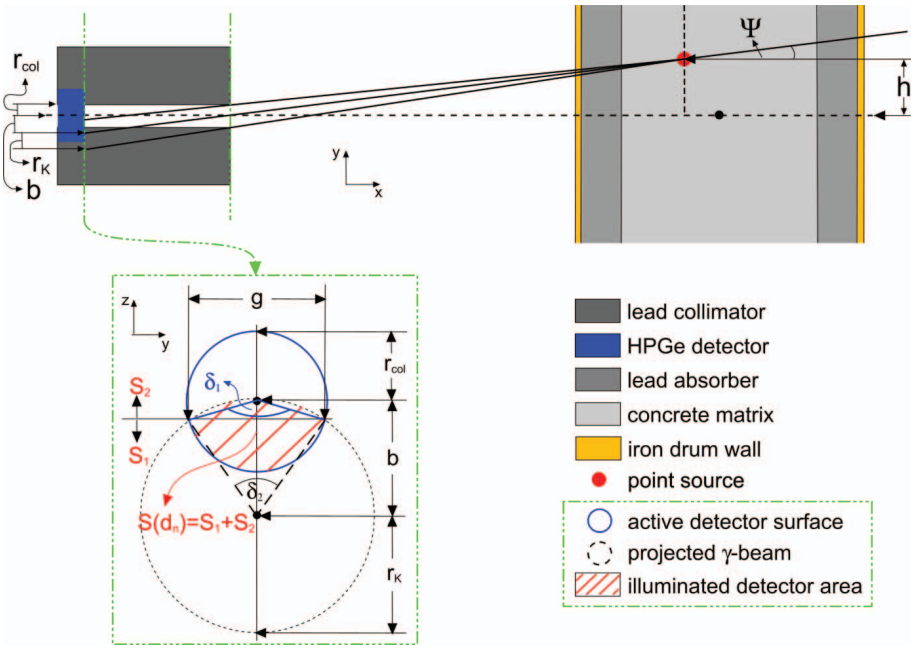

Fig. 95: Sketch of the beam geometry and active detector area illuminated with a photon-beam. The diagram in the green box shows the illuminated active detector area.

Details on the calculation of the illuminated active detector surface can be found in [5].

MCNP Simulations

To validate the described analytical model, various angular dependent count rate distributions are simulated with different combinations of point source positions and matrix configurations. The detector response and the photon tracking are simulated with the MCNP code in its current version 5.1.50.

Results

MCNP5 is used to simulate count rate distributions as a function of the height position for a Co-60 point source in air at a given radial position (r_S = 10 cm) and n = 1 to validate equation the analytical model including the collimator response function. The simulated and per incident particle normalized count rates can be compared to the analytically calculated count rate distributions derived in [5] and derived in [4] (old). The results for various heights are

shown in Fig. 96. In both cases the old formulation leads to a strong overestimation of the count rates up to a factor of about 2 when the source partially illuminates the active detector surface. In contrast, the count rates based on the new model are in excellent agreement with the simulated ones. The small discrepancies between the new analytical count rate calculation and the simulation for increasing source displacements are due to edge penetration phenomena which are only roughly implemented in the new analytical model.

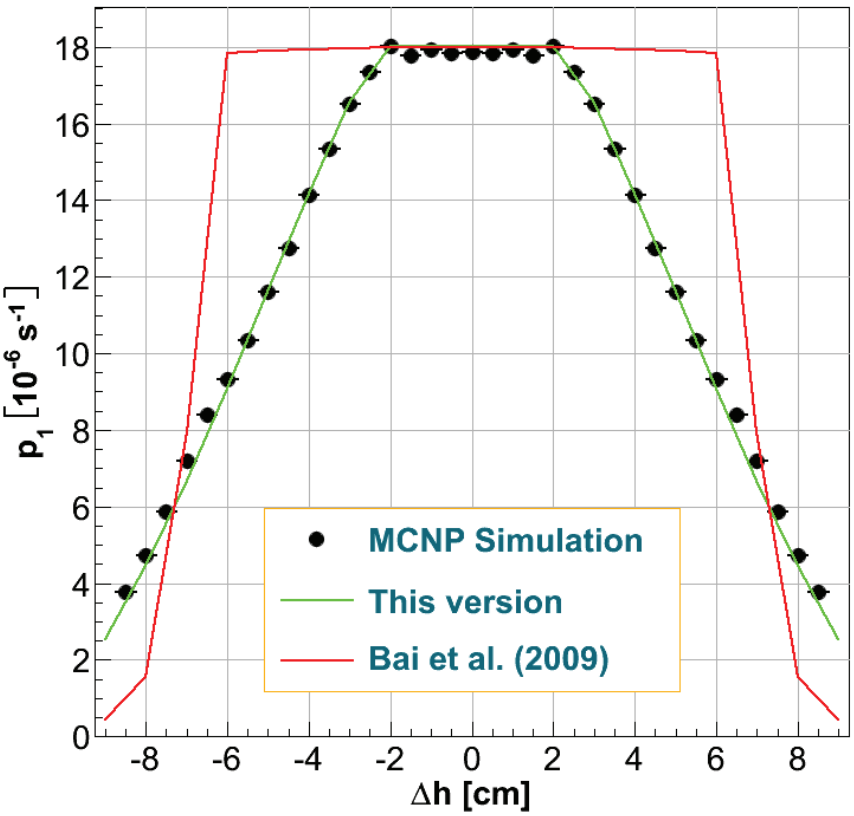

Fig. 96: Comparison of the count rates obtained for the old and new collimator model for a source (rS = 10 cm) at different heights to the detector normal.

Next, MCNP5 simulations of angular count rate distributions such as measured in SGS are performed for Co-60 and Cs-137 point sources in a segment of a drum filled with concrete (ρ_{con} = 1.6 g cm^{-3}). The 0.15 cm thick drum wall consists of stainless steel with a density of ρ_W = 7.87 g cm^{-3}. As an example, the angular dependent count rate distributions simulated for the E_γ = 1.173 MeV photons of a Co-60 point source located at radial positions of 10 cm are shown in Fig. 97.

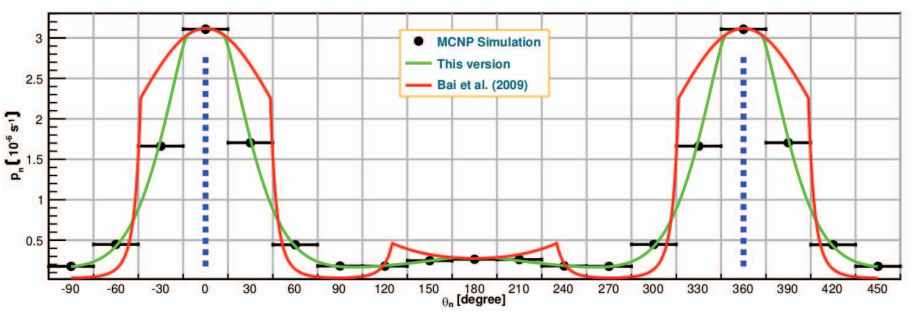

Fig. 97: Angular count rate distribution normalized per incident particle of a Co-60 point source in a concrete filled drum segment (E_γ = 1.1725 MeV) at r_S = 10 cm.

Generally, the angular count rate distributions calculated with the new model agree significantly better to those calculated with the old model. The activity reconstruction is benchmarked assuming the position of the point source and the matrix configuration are known (biased reconstruction). In a second step the position of the source is fitted according the X^2-procedure under the constraint of a known matrix. Hence, the activity is reconstructed using the best fit parameter (fitted reconstruction). These results are compared with the activity reconstruction assuming a homogeneous activity and matrix distribution (conventional reconstruction). The corresponding results are summarized in Tab. 24 for Co-60.

Tab. 24: Results from the reconstruction of the activity and point source position in the old and new analytical model for a 1 GBq Co-60 source (E_γ = 1.175 MeV) placed in an concrete environment. B means biased reconstruction; The here given source position is the input for the MCNP5 simulation. F means fitted reconstruction. C means the conventional reconstruction.

	New model							Old model						
	r_S [cm]	h [cm]	φ [deg]	χ^2 [10^{-3}]	A [GBq]	σ_A [%]	$\lvert\Delta A/A\rvert$ [%]	r_S [cm]	h [cm]	φ [deg]	χ^2 [10^{-3}]	A [GBq]	σ_A [%]	$\lvert\Delta A/A\rvert$ [%]
B	5	0	0	6.31	0.971	4.5	2.92	5	0	0	146	0.856	21.7	14.4
F	5	1.5	-1	1.71	1	2.35	0.13	7	0	-1	54.1	0.857	13.2	14.3
C												0.0247		97.5
B	10	0	0	1	0.989	3.85	1.1	10	0	0	220	0.873	57	12.7
F	10	1.25	0	0.472	1.01	2.64	0.954	13	1.5	0	56.6	0.881	28.9	11.9
C												0.0213		97.9
B	15	0	0	0.0407	1.02	1.48	1.71	15	0	0	31.6	1.2	41.1	19.7
F	15	0	0	0.0407	1.02	1.48	1.71	14	1	0	1.26	1.2	8.22	19.7
C												0.0213		97.9
B	20	0	0	0.24	1.02	5.16	1.73	20	0	0	0.209	1.01	4.81	1.46
F	19	0	0	0.0475	1.14	2.29	13.9	21	1.75	8	0.162	1.14	4.24	13.8
C												0.0279		97.2
B	9	1	3	9.34	1.02	9.7	1.78	9	1	3	147	0.864	38.4	13.6
F	9	0	3	0.851	1	2.93	0.243	9	1.5	4	135	0.847	37	15.3
C												0.0223		97.8
B	4	0	10	24.1	0.976	7.59	2.38	4	0	10	99.1	0.915	15.4	8.53
F	4	1.75	7	1.3	1.01	1.76	1.28	5	0	6	36.4	0.916	9.35	8.41
C												0.0255		97.5

In comparison to the conventional method, both improved methods enhance largely the accuracy in the activity reconstruction. However, the new method employed for the calculation of the angular dependent count rate distributions leads to a more precise activity

reconstruction than the old calculation method. The mean deviation from the true activity lies around 1% to 10% in the new model and around 8% to 42% in the old model depending on the source position. The improvement in the accuracy of the activity reconstruction becomes less important for point sources at increasing radial positions. Furthermore, the error of the reconstructed activity is considerably reduced leading to a high reliability. The new method allows also a better position reconstruction than the old method. We refer to [5] for more detailed results and discussion.

Conclusion

In comparison to the old model, the new model describing the angular dependent count rate distribution presented in this work provides a more accurate reconstruction of the activity and the position of a point source. Improvements of the precision in the activity and position reconstruction can be further obtained by incorporating the height dependent count rate distribution in the fitting process. Additionally, the effects of extended and multiple sources in the scanned segment have to be investigated.

References

[1] Filß, P., 1995. Relation between the activity of a high-density waste drum and its gamma count rate measured with an unshielded ge- detector. Applied Radiation and Isotopes 46 (8), 805 – 812

[2] Dung, T. Q., 1997. Calculation of the systematic error and correction factors in gamma waste assay system. Annals of Nuclear Energy 24 (1), 33 – 47.

[3] Dung, T. Q., 1998. Some theoretical results of gamma techniques for measuring large samples. Nuclear Instruments and Methods in Physics Research Section A: Accelerators, Spectrometers, Detectors and Associated Equipment 416 (2-3), 505 – 515

[4] Bai, Y., Mauerhofer, E., Wang, D., Odoj, R., 2009. An improved method for the non-destructive characterization of radioactive waste by gamma scanning. Applied Radiation and Isotopes 67 (10), 1897 – 1903

[5] Krings, T., Mauerhofer, E., 2011, Reconstruction of the activity of point sources for the accurate characterization of nuclear waste drums by segmented gamma scanning, Applied Radiation and Isotopes 69 (6), 880-889

5.15. Prompt Gamma Characterization of Actinides

M. Rossbach, C. Genreith, G. Caspary, E. Mauerhofer

Corresponding author: m.rossbach@fz-juelich.de

Abstract

In an attempt to collect integral and partial thermal neutron cross section data $^{237}NpO_2$ samples were prepared for irradiation in the guided cold neutron beam of the Budapest reactor. Gold was mixed to some samples and used as a neutron flux monitor. Prompt and delayed spectra were taken and are under evaluation to extract the relevant nuclear data. Other actinide isotopes, such as ^{242}Pu or ^{243}Am will be investigated to create a data base for a future non-destructive analysis tool for quantification of minor actinides in heterogeneous waste packages.

Introduction

Due to their pronounced role in nuclear waste management transuranic actinides are of particular interest in research and technology. Chemical behavior of actinides has been investigated widely. However, non-destructive determination of minor actinides (Np, Am, Pu, Cm etc.) in heterogeneous waste packages is still hampered and, due to their potentially hazardous nature, not fully developed. Radiotoxicity, longevity and decay radiation render these elements interesting for development of innovative non-destructive analytical methods.
Unlike other destructive wet-chemical techniques such as atomic spectrometric or mass spectrometric techniques prompt gamma activation analysis (PGAA) is a direct, non-destructive approach based on prompt gamma emission after neutron capture. This active neutron interrogation technique allows investigation of hazardous bulk materials difficult to partition due to high radiation doses. Standard gamma spectroscopy techniques are often not adequate because of high radiation background from fission products, long half-life or low gamma ray intensities emitted from the actinide nuclides. High energy prompt gamma rays emitted after neutron capture may offer an alternative to identify and quantify transuranic actinides in complex matrices.
Current non-destructive assay techniques have been developed mainly for monitoring the fissile content of well characterized samples or products from fuel processing, and not all are suitable or fully developed for the more demanding task of monitoring waste materials of generally unknown composition, e.g. compacted metal scrap in CSD-C containers. Passive Neutron Coincidence Counting (PNCC) using shift register electronics is a well-established technique for the non-destructive assay of spontaneous fission sources (^{238}Pu, ^{240}Pu, ^{244}Cm, ^{252}Cf) whether in mg quantities which occur in low level contaminated waste or in kg quantities which are encountered in fissile material inventory control or in safeguards inspections. For waste containing ^{235}U, ^{239}Pu or ^{241}Pu active neutron interrogation has the potential for quantitative assessment only after extended data reduction [1]. Monte Carlo simulation is required to optimize geometric or counting conditions.
Concerning quantification of minor actinides, such as ^{237}Np, ^{242}Pu, or ^{243}Am in waste from reprocessing of used fuel the situation is much worse as accurate nuclear data are missing or are incomplete. Direct gamma spectrometry of the decay radiation is difficult or impossible due to heavy self-shielding and/or absence of intense gamma lines suitable for detection.

Neutron capture cross sections and gamma line intensities have not been experimentally determined or are not known for fast neutron energies. Therefore, experiments have been designed to study the basic neutron capture data of selected actinides in a guided beam of cold neutrons at the Budapest Reactor (BNC), Institute of Isotopes, Hungary to establish a data base for numerical simulation to design a possible analytical instrument for actinide quantification in waste forms.

Materials and Methods

$^{237}NpO_2$ powder was obtained from Oak Ridge National Laboratory through TU München. ^{237}Np was in equilibrium with its decay daughter ^{233}Pa. Small quantities (7 to 15 mg each) of the powder were pressed into 3 mm diameter pills using a pill press (max. pressure: 1 T) from SPECAC, UK. The pills were sealed between two circular aluminum slabs (Alfa Aesar, 99,99%, 0.25 mm thick) held in a screw cap frame from Al. For neutron flux determination some samples were prepared by mixing homogeneously $^{237}NpO_2$ powder with known amount of gold powder (Alfa Aesar, 99.96+%, 0.5-0.8 microns). All samples were carefully prepared in a glove box and checked for external contamination before removing from the box.
Sample irradiation was carried out at the prompt gamma-ray facility of the Budapest Reactor. The instrument set up and characteristics are described in ref. [2]. Thermal equivalent neutron flux of the facility has been determined to be 1.2×10^8 cm^{-2} s^{-1} [2]. The estimated promt gamma activity generated by 12 h irradiation of 10 mg of the nuclides at a flux of 10^8 $cm^{-2} \cdot s^{-1}$ is shown in Tab. 25:

Tab. 25: Estimated activity for irradiation of 10 mg of ^{237}Np, ^{242}Pu and ^{197}Au at the Budapest facility, σ_{th} = thermal neutron cross section, σ_f = fission cross section.

Isotope	s_{th} (barn)	s_f (barn)	Activity (Bq)	Capture rate (1/s)	Gamma capture rate (1/s)	Total gamma capture for 12 h irradiation
^{237}Np	180	0.08	2.61E+05	4.56E+05	1.82E+03	7.87E+07
^{242}Pu	19	0.2	1.47E+06	4.71E+04	1.88E+02	8.14E+06
^{197}Au	98.6	0	-	3.00E+05	1.20E+03	5.19E+07

Experimental

The samples were located in the cold neutron beam at a distance of 23.5 cm from the detector tilted by 30° to the beam axis (see Fig. 98). The prompt gamma ray spectrum of a blank sample (no actinide) consisting of pure Al sheets and frame has been measured for 22 h to assess the background. A pure $^{237}NpO_2$ sample was positioned in front of the detector and measured with the neutron beam off to assess the decay spectrum from ^{237}Np and ^{233}Pa. Finally, the same sample has been measured with neutron beam on for 20 h to obtain the combined spectrum containing gamma rays of $^{237}Np/^{233}Pa$ decay, and prompt and delayed gamma rays from $^{237}Np(n,\gamma)^{238}Np$ and $^{27}Al(n,\gamma)^{28}Al$. After irradiation the sample was removed from the sample holder and positioned in front of a calibrated low level HPGe detector (13% rel. eff., 2.0 keV resolution) at 17.5 cm distance to measure decay lines from ^{238}Np (half-life: 2.117 d) with better accuracy. The same procedure was applied to samples including small amounts (2 to 4 mg) of gold. The 411 keV delayed gamma ray of ^{198}Au (half-life: 2.6943 d) was used to assess the equivalent thermal neutron flux in the sample during irradiation. In Fig. 99 the delayed gamma rays of ^{198}Au, ^{233}Pa and ^{238}Np can be seen. Spectra are under evaluation using the Hypermet software obtained from Budapest. Identification of prompt and

delayed gamma rays and their respective intensities will be used to extract partial neutron capture cross sections.

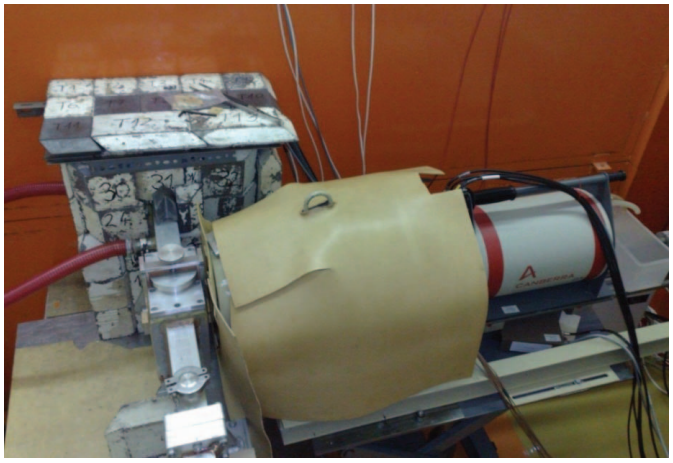

Fig. 98: PGAA setup with beam line, sample chamber and BGO shielded HPGe detector at the guide hall of the Budapest reactor. The BGO detector is surrounded by ^{6}Li-plastic to shield the detector array from scattered neutrons.

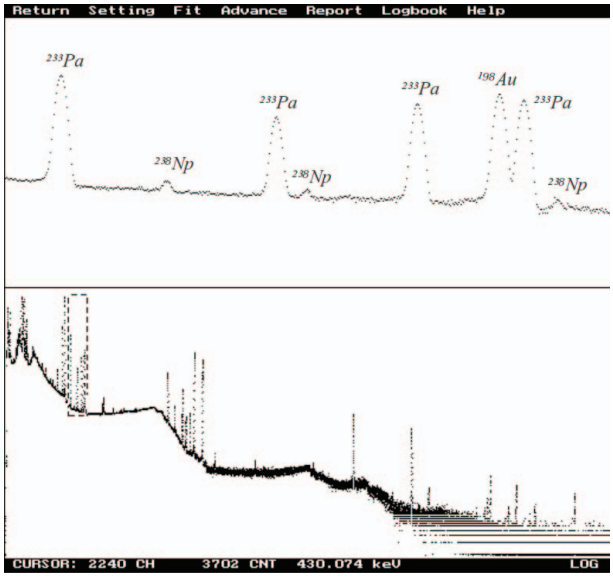

Fig. 99: Decay spectrum of a $^{237}NpO_2$ sample with gold (11.11 mg Np, 1.965 mg Au), after 12.5 h irradiation. Counting time was 43 h. Lower part is the full spectrum; the upper part represents a zoomed region around the ^{198}Au gamma ray at 411 keV.

Outlook

The evaluated data will be used as input data for numerical simulation of prompt gamma ray spectra using MCNP-X or GEANT 4 and to develop and optimize a non-destructive analytical technique for assay of minor actinides in heterogeneous waste packages. Further experiments are planned using fast neutrons from a 14 MeV neutron generator to extract also high energy data [3]. First attempts to generate synthetic spectra using the geometric arrangement in Budapest (see Fig. 100) have shown good agreement with experimental data; however, simulating a neutron emission of 10^8 n cm^{-2} s^{-1} and a detector of 0.1% efficiency requires very large computer capacity to obtain spectra of sufficient statistical significance.

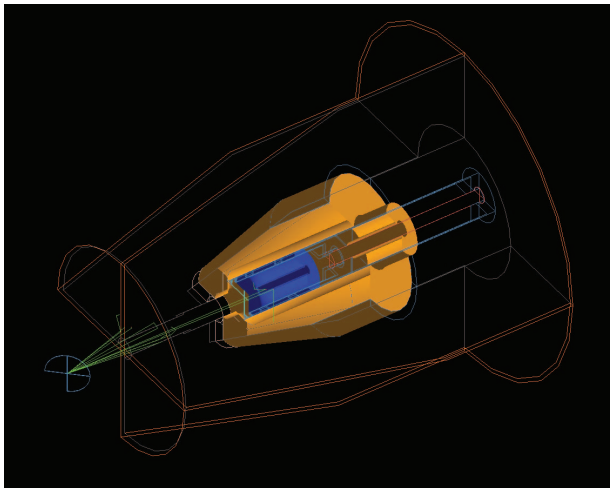

Fig. 100: Simulation of photon trajectories for the Budapest PGAA detector arrangement with GEANT 4.

Acknowledgement:

We gratefully acknowledge the support of the colleagues from BNC Budapest, Dr. Z. Revay, Dr. T. Belgya and Dr. L. Szentmiklosi.

References

[1] B.H. Armitage, P.M.J. Chard, S. Croft, T.W. Packer, D.B.C. Syme: Limitations to the accurate assessment of waste actinide content by neutron interrogation. *Nuclear Science Symposium and Medical Imaging Conference, 1992., Conference Record of the 1992 IEEE* , Orlando, FL, USA, IEEE pp. 703-705

[2] Z. Revay: Determining Elemental Composition Using Prompt γ Activation Analysis. Anal. Chem., 2009, 81 (16), pp 6851–6859

[3] L. W. Campbell, L. E. Smith, and A. C. Misner: High-Energy Delayed Gamma Spectroscopy for Spent Nuclear Fuel Assay. IEEE TRANSACTIONS ON NUCLEAR SCIENCE, VOL. 58, NO. 1, FEBRUARY 2011, 231-240

5.16. Treatment and disposal of irradiated graphite and other carbonaceous waste

W. von Lensa[1], D. Vulpius[1], H.-J. Steinmetz[1], N. Girke[1], D. Bosbach[1], B. Thomauske[1], A. W. Banford[2], D. Bradbury[3], B. Grambow[4], M. J. Grave[5], A. N. Jones[6], L. Petit[7], G. Pina[8]

[1] Institute of Energy and Climate Research – Nuclear Waste Management and Reactor Safety (IEK-6), Forschungszentrum Jülich GmbH, 52425 Jülich, Germany

[2] National Nuclear Laboratory, UK

[3] Bradtec Decon Technologies, UK

[4] École des Mines de Nantes, FR

[5] Doosan Babcock Energy, UK

[6] The University of Manchester, UK

[7] Électricité de France, FR

[8] CIEMAT, ES

Corresponding author: d.vulpius@fz-juelich.de

Introduction

The very first generation of nuclear reactors relied on graphite for the moderation of fission neutrons in the core. The extremely low neutron capture cross section of carbon allowed the use of natural, non-enriched uranium fuel for this type of reactors. Since mid of the 1950s, CO_2-cooled graphite-moderated reactors were built as the first commercial nuclear power stations. High-Temperature Reactors (HTR), water-cooled graphite-moderated reactors (RBMK) as well as diverse Material Test Reactors (MTR) also utilise graphite as moderator and reflector. Many of these facilities are now facing decommissioning and raise the need for the management of irradiated graphite waste, which contains varying fractions of radionuclides including ^{3}H, ^{14}C, ^{36}Cl, ^{60}Co etc., due to neutron activation of the natural ^{13}C isotope and of impurities within the graphite or coolant gas (e.g. nitrogen).

The European project on 'Treatment and Disposal of Irradiated Graphite and other Carbonaceous Waste (CARBOWASTE)' was launched in 2008 under the 7th EURATOM Framework Programme and addresses the retrieval, characterisation, treatment, reuse and disposal of irradiated graphite including other carbonaceous waste such as non-graphitized carbon materials or pyrocarbon.

Since the end of 2010, the complementary German project 'Disposal of irradiated Graphite (CarboDISP)' is dealing with the specific requirements for irradiated graphite in the German KONRAD waste repository and is funded by the German Federal Ministry of Education and Research. Both projects are coordinated by the Research Centre Jülich.

The Objectives

The main objective of the CARBOWASTE project is the development of best practices in the retrieval, characterisation, treatment and disposal of irradiated graphite (i-graphite) including other i-carbonaceous waste like structural material made of graphite or non-graphitised carbon bricks and fuel coatings (pyrocarbon, silicon carbide) [1]. It addresses both existing legacy waste from past and actually operated graphite-moderated reactors as well as waste

from carbon-based HTR fuel elements or from the heat-resistant walls of future fusion reactors.

After defining the various targets (end points) for an integrated waste management approach, analysis of the key stages of the road map (i.e. from in-reactor storage to final disposal) can then be undertaken with regard to safe and the most economic, environmental and sustainable options. This methodological approach will enable EU Member States to select the most appropriate options to meet their specific criteria and considerations. Emphasis will therefore be given to legacy i-graphite as this currently represents a significant problem that will have to be addressed, in the short and medium term.

Some Member States and other countries are beginning to evaluate strategies and develop options for the identification, retrieval, characterisation, treatment and final disposal of this waste. It is important that this project takes account of them and assimilates their considerations against appropriate end points. The project unites organisations from most EU Member States being faced with a need for i-carbonaceous waste management (GB, FR, LT, ES, IT, DE, BE, NL, SE, RO). It thus permits quantification of the magnitude of the problem and to identify the most relevant grades and sources of i-carbonaceous waste.

The waste issue has not been well managed in earlier generations of gas-cooled reactors (Magnox, AGR, UNGG, HTR) and in other graphite-moderated reactors such as RBMK or in Materials Test Reactors (MTR) as well as in early production reactors. Irradiated and contaminated graphite from reactor moderators and reflectors or thermal columns, and other related carbonaceous materials, represent the greatest volume of irradiated waste materials from these reactors. Up to now, about 250,000 tons have been accumulated, worldwide. In addition, these reactors have not been designed for decommissioning as can be seen from Fig. 101, which illustrates the assembly of graphite blocks in a French UNGG reactor. This complex assembling process de facto needs to be reversed, for retrieving the irradiated blocks by remote techniques or shielding to handle the graphite.

Fig. 101: Chinon A3 Core Assembly in 1965 (EDF Médiathèque / Brigaud Michel).

A specific problem related to i-carbonaceous waste stemming from the structures of the core is the varying content of long-lived radioisotopes, especially of radiocarbon (^{14}C), resulting from activation processes under neutron irradiation. If other long-lived radioisotopes are present in smaller quantities, their management might also be an important issue because of the particular properties of some of them under disposal conditions like chlorine (^{36}Cl). Dependent on the specific national legislation, they can be a crucial parameter for a final disposal. Therefore, this type of waste is handled as Intermediate-Level Waste (ILW), in some countries, and Long-lived Low-level Waste (LLLW) or Low-Heat-Generating Waste, in others. Burning i-graphite has been discussed in the past as an alternative to the disposal option but will most probably not be politically and ecologically accepted due to the radiocarbon releases to the environment if not separated or reduced in the exhaust gas. Recycling or reuse of treated i-graphite in the nuclear industry might be a preferable new option to minimize waste streams for disposal.
The CARBOWASTE consortium regards the present unsatisfactory status in this waste disposal area as an opportunity to build upon previous work, to review technological advances and innovative ideas which have arisen in more recent years, and thus to identify the most technologically appropriate, environmentally sustainable, and cost-effective procedures, at all stages in the retrieval, treatment and disposal of all types of carbonaceous wastes.
The previously employed procedures are not necessarily appropriate for the future. The special character of i-graphite wastes can lead to problems such as electrochemical corrosion and the potential leaching of long-lived isotopes if they are handled by the standard methods though appropriate for other wastes. A special issue arises from the fact that radiocarbon (^{14}C) has to be safely isolated from the biosphere due to its biocompatibility. Stored Wigner-Energy is another concern, which has to be addressed especially for graphite being operated at temperatures below about 250 °C where significant annealing of radiation effects does not yet take place.

Characterisation of irradiated graphite

Characterisation within the CARBOWASTE Project is a “key issue” in the scheme of radioactive carbonaceous waste management and life-cycle. It is not a goal of the waste management itself but facilitates a better understanding of the nature of contaminants; contamination mechanisms that allows the prediction of isotopes by inventory modelling; the determination of decontamination factors; the selection of appropriate treatment methodologies and ultimately nuclide inventory determination for long term disposal.
Correlation and the scientific interpretation of the results from the innovative characterisation procedures for impurities location, structural analyses and modelling applied on virgin and irradiated graphite gives the validation and underlying principles for accurate data and a basis for making decisions in any step of the waste life-cycle: retrieval, treatment, conditioning, interim storage and final disposal. A novel example of the structural characterisation techniques currently being applied with the CARBOWASTE project is through the use of X-ray tomography. Manchester University has employed this technique to give 3D volume information of irradiated graphite microstructure, porosity size and shape distributions and to identify the location of high attention inclusions within the material which may be associated with contaminates and isotopes. A volume reconstruction of irradiated British Experimental Pile Zero reactor graphite is shown in Fig. 102 and clearly shows the porosity distribution (blue) and inclusions of high attenuation (red).

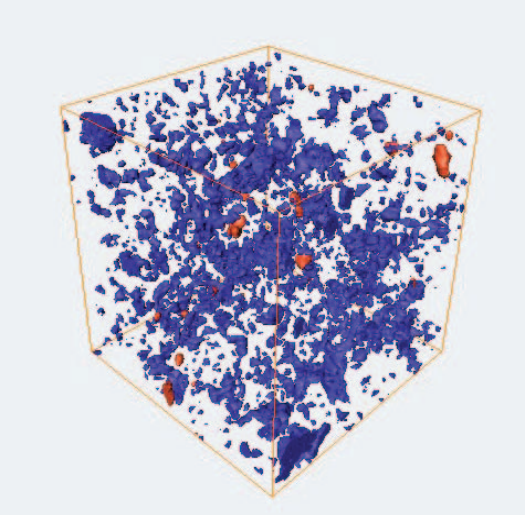

Fig. 102: 3D volume reconstructions of 1 mm^3 BEPO Graphite showing porosity.

The laboratories involved in this characterisation have applied these methodologies over the main legacy waste in EU focusing not only in i-graphite from the most abundant reactors (Magnox, UNGG and MTR) but also i-graphite from RBMK or HTR reactors.
In order to upgrade, check and harmonise the radiochemical methodology a proficiency test (Collaborative mode) based on international standards has been carried out. The nuclides determined are ^{3}H, ^{14}C, ^{36}Cl, ^{63}Ni and ^{60}Co by ten Lab's for two samples of i-graphite powder whose homogeneity is probed by ANOVA test, before distribution of samples. Preliminary results from the expert laboratories within the consortium have been consistent, which increases the confidence in the reliability of the analytical results and facilitates the validating and/or accreditation of test procedures.
Radiochemical analyses methodologies have been developed for this matrix and for the specific nuclides within this waste. In this field technology for sample preparation, dissolution of the matrix, accurate determination of gamma emitting nuclides, as well as beta-emitting ^{3}H, ^{14}C, ^{36}Cl, ^{63}Ni, ^{99}Tc, ^{129}I and alpha emitting nuclides has been developed and applied.

Treatment & Purification

The knowledge on the location and the chemical bond of contaminating radionuclides is a necessity for the development of methods for treatment and purification of i-graphite. Nuclear graphite is a technical product composed of filler and binder materials [2]. For filler, mainly coke (made from coal or petrol pitch) or natural graphite and additions of carbon black are used and, for binder, e.g. pitch or resins. These components are then heat-treated, impregnated and graphitized at temperatures beyond 3000 °C, e.g. by the Acheson process. Carbon brick as also used in the German HTR (AVR, THTR) is only 'baked' to about 1200 °C and can be considered as a nuclear carbon material with crystalline filler and highly amorphous binder regions. Fig. 103 shows that the binder regions are the main place where impurities are located. The white dots indicate diverse impurities which have been detected by back-scattering electrons. These impurities mainly consist of oxides and carbides of

aluminium, silicon and iron, but the easily neutron-activable elements cobalt and nickel are often affiliated to these main impurities as has been analysed by Secondary Ion Mass Spectroscopy (SIMS).

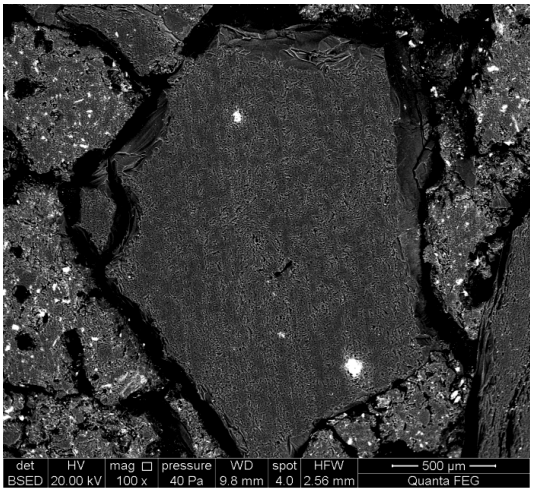

Fig. 103: Scanning electron micrograph of carbon brick in back-scattering electron mode.

It is evident, that non-carbon contaminants like ^{3}H, ^{36}Cl, ^{60}Co etc. can principally be removed from the carbon matrix by specific separation processes due to their different chemical behaviour compared to carbon. But is it possible to remove ^{14}C from material that consists predominantly of ^{12}C and 1.07% of ^{13}C atoms; all of which have identical chemical features and are differentiated only by atomic weight?

The main routes for the generation of ^{14}C are via neutron activation of ^{13}C (n, γ / 0.0014 barn), ^{14}N (n, p / 1.93 barn) and ^{17}O (n, α / 0.257 barn). Due to the fact that ^{17}O is only present in natural oxygen by 0.038%, ^{14}C generation via ^{17}O is much less than by ^{13}C or by ^{14}N, in most i-graphite cases. As the activation cross section for nitrogen is about 1,400 times larger than for ^{13}C, the same ^{14}C production rate is therefore already reached at a nitrogen concentration of about 8 ppm within the graphite. Much higher nitrogen concentrations (up to 40-300 ppm) have been measured in nuclear graphite, which has been exposed to air. However, the nitrogen content of graphite being irradiated under CO_2 as is the case for UNGG, MAGNOX and AGR can significantly differ from these results, due to nitrogen desorption under operational temperatures and coolant gas conditions. Reverse calculation methods based on the measured values of ^{14}C specific activity and their distribution within the core of shut-down reactors are therefore often applied to determine the sources of the ^{14}C generation [3].

It is known that graphite has a high affinity to nitrogen, which is chemisorbed on the surfaces of the graphite, up to a depth of about 50 nm [4]. Under this background, it can be assumed that the ^{14}C atoms created by neutron activation of nitrogen will stay near to the location of the activated nitrogen atom, despite considerable recoil energy from the nuclear (n, p) reaction.

^{13}C is mainly bound in the graphite lattice and is part of other deposited carbon-particulate matter in the graphite. In case of the $^{13}C(n, \gamma)^{14}C$ reaction the recoil energy is high enough to

dislocate the ^{14}C atom from its previous place in the lattice. It will either recombine with vacancies or stay as an interstitial between the graphene layers.
Experiments at Forschungszentrum Jülich [5] first revealed that ^{14}C was preferentially released when heating i-graphite in the range of 870–1300 °C, in an inert atmosphere or in water steam.
The high ^{14}C release fractions when 'roasting' i-graphite under inert gas atmosphere can be explained by the fact that oxygen is also physi- and/or chemisorbed at the surfaces of the crystalline structures [6], in the direct 'neighbourhood' of the ^{14}C atoms. At higher temperatures, the oxygen reacts with all carbon atoms around including those ^{14}C isotopes formed by nitrogen activation until all available oxygen is exhausted. The graph in Fig. 104 also includes experiments with water vapour as oxidant. It can be seen that the ^{14}C release is rather sensitive to a variation of the process parameters and that there is still a lot of potential for improvements. A ^{14}C vs. total C release ratio of 5:1 can be seen as a lower limit for an industrial process development for ^{14}C removal. The ratios beyond 20:1 may even allow the development of ^{14}C extraction processes, e.g. for medical uses.

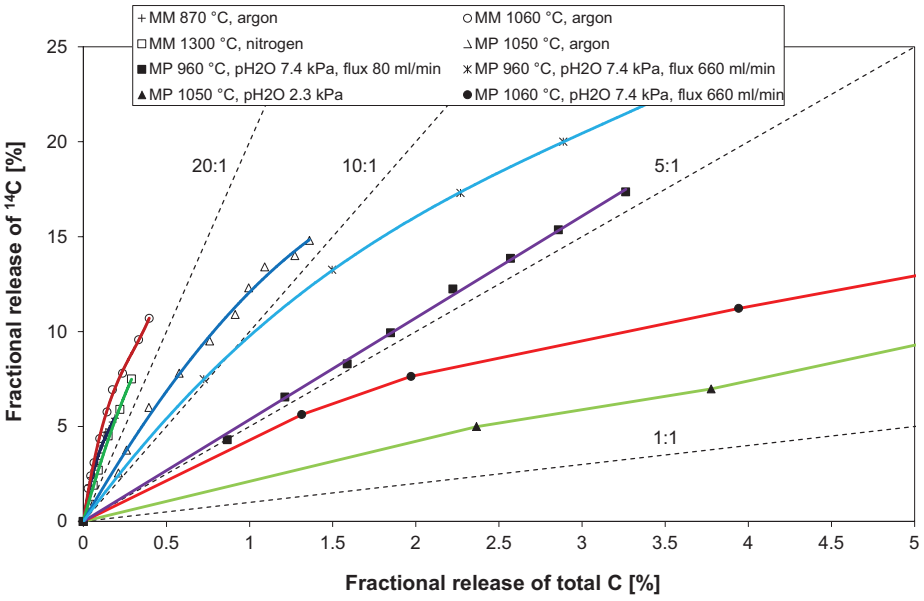

Fig. 104: Fractional release of ^{14}C vs. total carbon releases of i-graphite from the FRJ-1 MTR (MERLIN) thermal column (MM-massive sample; MP-powdered sample).

Recent studies at Forschungszentrum Jülich and at University of Manchester have shown that significant activities of the ^{14}C can also be removed through the use of thermal treatment with oxygen. The latest research carried out in Manchester has employed computerised X-ray tomography in conjunction with thermal treatment (*ex situ*) in order to decontaminate the graphite and identify the location of ^{14}C within the graphite matrix. Samples have been identified with laser markers to align in the CT scanner prior to thermal oxidation. Oxidation is then performed up to 1000 °C in a 2% O_2/Ar environment. A bubbler system is connected to the catalytic furnace which traps ^{14}C and ^{3}H, which is then analysed using liquid scintillation

counting. The irradiated graphite sample is then rescanned with X-ray tomography to determine and weight loss and structural changes to the material.
However, it must be stated that such ^{14}C release processes already occur under operational conditions being mainly triggered by radiolytical and chemical corrosion of the graphite, in dependence of the specific coolant gas (e.g. air, CO_2, helium), the impurities within the coolant gas (e.g. oxygen, nitrogen), the operational temperatures and the final neutron dose, which increasingly leads to an amorphisation of the graphite crystals. Therefore, it is difficult to compare different i-graphite features without taking their specific operational history into account. The final content of the ^{14}C is an equilibration of the generation vs. release processes already during operation.
In case of shutdown UNGG reactors, reverse calculation methods have shown that the remaining ^{14}C is even less than ^{14}C generated by the ^{13}C contribution route. This clearly shows the strong competition of ^{14}C generation by neutron activation of ^{14}N and ^{13}C against the ^{14}C release in operational conditions due to chemical and radiolytic corrosion, at temperatures up to about 550 °C.
Provisional interpretations of the ^{14}C releases indicate that a varying part of the ^{14}C is easier to remove than the remaining rest. This might be due to the fact that ^{14}C created by activation of ^{13}C will mainly be integrated into the lattice of graphite crystallites or as an interstitial atom between the graphene layers. For disposal purposes, it will be decisive that the mobile fraction of ^{14}C is preferentially removed or fixed, whereas the stable part will presumably not be released under disposal conditions.

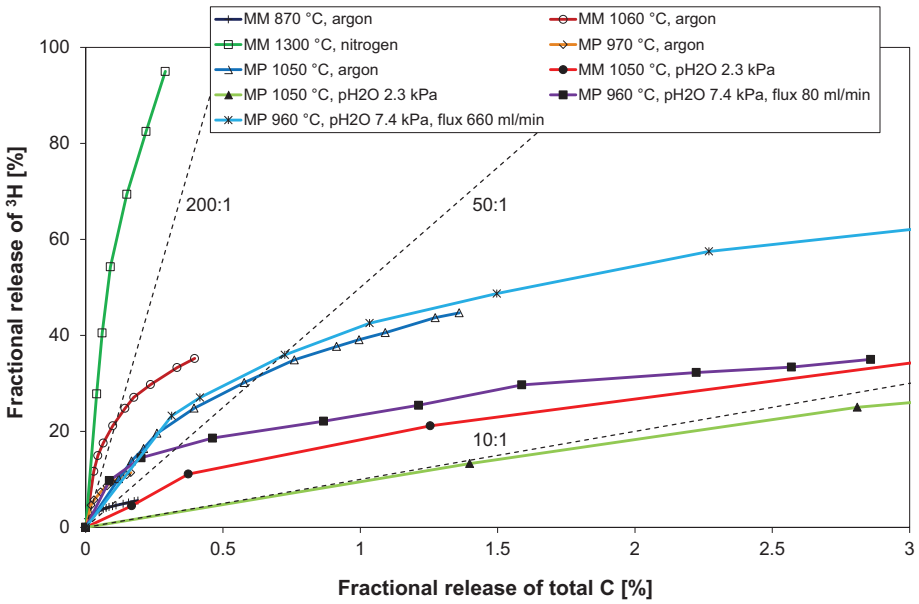

Fig. 105: Fractional release of ^{3}H vs. total carbon releases of i-graphite from the FRJ-1 MTR (MERLIN) thermal column (MM-massive sample; MP-powdered sample).

Other problematic radioisotopes, ^{3}H and ^{36}Cl, can also be removed by such treatment processes. Fig. 105 shows the release of tritium during the 'roasting' under inert atmosphere.

It can be seen that nearly all tritium can be removed at temperatures around 1300 °C, at reasonable exposition times. It is assumed that the main effect is based on a pyrolysis of CH bonds, which degrade in relation to temperature.
Further treatment processes are investigated with several acidic leachants (HNO_3, HCl, H_3PO_4, H_2SO_4, and mixtures of the aforementioned with oxalic and citric acid) in order to determine the decontamination factor e.g. for ^{60}Co, ^{94}Nb, ^{137}Cs, ^{154}Eu, $^{239,240}Pu$, ^{241}Am as well as for ^{3}H and ^{14}C. In addition, decontamination processes using diverse liquid detergents, molten salt, spark erosion, plasma, laser, blasting and electrochemical techniques are also under consideration. Another interesting study has been performed by the South African partners with microbiological treatment, which also shows certain selectivity for ^{14}C removal.

Disposal

With regards to the disposal behaviour of i-graphite it has to be reminded that nuclear graphite is rather porous (typically ~ 20%) and that porosity even increases by irradiation and mass loss during operation in the reactor. The radiation and radiolytic corrosion cause breakage of the C-C bonds in the crystallites and/or the joints in the grains of graphite to form more hydrophilic C-H or C-O bonds. Under this background, access of groundwater to the pore space within i-graphite has been studied for the release of radionuclides from graphite. The results show that small hydraulic gradients are sufficient for water infiltration into the pore space. Water saturation of a significant fraction of the open pore volume is rapid even at low pressures. Water access leads to almost instantaneous leaching e.g. of a significant part of the ^{36}Cl inventory of small sized graphite samples. Both diffusive and advective transport properties for radionuclide transport in graphite are analysed as well as the influence of operating conditions during irradiation.
It is known that the reaction rate of graphite with water increases with an increase of the concentration of radiolytic water decomposition products such as H_2O_2. This may lead to a release of the matrix bound fraction of the ^{14}C inventory. However, new calculations have shown that after decay of ^{60}Co inventories, the expected dose rates will become so low that any radiolytic processes will be insignificant for any additional ^{14}C release. Neither, pore water chemistry nor radionuclide release will be controlled by radiolytic graphite dissolution. This means that pore water chemistry will be similar to the composition of the groundwater, which might access the i-graphite disposal location in a geological formation.
The mechanism which governs the mobility of long-lived radionuclides like ^{14}C and ^{36}Cl under repository conditions prior to and after groundwater access is an important concern. XPS experiments carried out on virgin and annealed samples show that around 30% of chlorine is inorganic (chloride or chlorate compounds) whereas around 70% is organic (aromatic C-Cl bonds). The release of inorganic compounds increases with temperature whereas the organic chlorine remains more stable. Only the latter is expected to resist to a certain degree under disposal conditions.
Radionuclides released from graphite may in principal be retained by engineered barrier materials surrounding the waste. However, first results show that e.g. ^{36}Cl retention on cementitious barriers is rather weak. Inorganic ^{14}C releases (e.g. $^{14}CO_2$) might well be kept in a concrete waste package whereas organic ^{14}C compounds (e.g. $^{14}CH_4$) might permeate through the concrete. Recent results indicate that only a small fraction of the ^{14}C inventory appears to be susceptible to mobilisation upon groundwater contact.
Deep or shallow geological disposal of i-graphite is being studied in many countries. Fig. 106 shows an illustration for a specific i-graphite repository in a clay / marl sedimentary and low

permeability layer, at a shallow depth ranging from 100 to 200 m. The layers should be at least 50 m thick and being located in a geologically stable zone over the next tens of thousands years and possess a low hydraulic gradient.

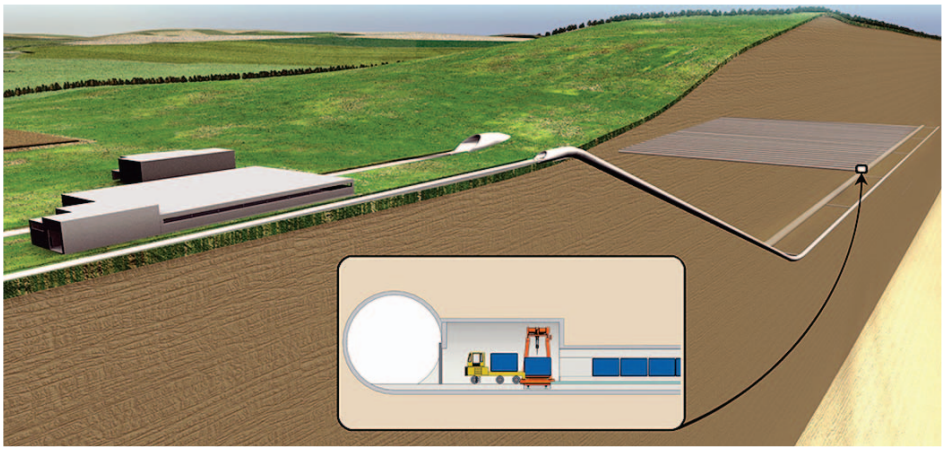

Fig. 106: Concept of shallow disposal of i-graphite (courtesy of ANDRA).

cementitious backfill provides a strong chemical barrier for ^{14}C and that a clay backfill offers potential advantages for ^{36}Cl but the consequences of a reduced chemical barrier for ^{14}C need to be more fully understood. Increased ^{14}C flux to the geosphere in groundwater is unlikely to be significant, except where the geosphere is a poor barrier and ^{14}C does not substantially decay in the geosphere, e.g. due to the presence of fracture network to the surface. Potential hydro-fracturing of backfill also requires consideration. Coupled gas generation and multiphase flow calculations are required.

The disposal of i-graphite in the German KONRAD repository is investigated within the German CarboDISP project, which is complementary to the European CARBOWASTE project. The total ^{14}C activity being allowed for KONRAD is only $4 \cdot 10^{14}$ Bq. With an overall storage capacity of 303,000 m^3 this results in $1.32 \cdot 10^9$ Bq/m^3, as an average. For the disposal of ^{14}C waste in KONRAD, different limits result from safety analyses, which have to be considered. Most restrictive ^{14}C limits arise from safety issues for internal operation (T ~ 50 °C), classified by ^{14}C release from the waste container. If a maximum release of < 1% of the total ^{14}C inventory can be guaranteed, the limit is $1.8 \cdot 10^{10}$ Bq per container either individual or in average within a batch of containers. This means that about 22,000 waste-containers will be needed to accommodate the allowed total ^{14}C activity of $4 \cdot 10^{14}$ Bq. Taking as a basis a typical Type V KONRAD Container volume of 10 m^3, this number of containers corresponds to 70% of the total repository volume. If the 1% limit cannot be kept but ^{14}C releases may range up to 10%, then the maximum ^{14}C activity of a waste container must not exceed $1.8 \cdot 10^9$ Bq resulting in a ten times higher repository volume which exceeds the KONRAD capabilities. And if ^{14}C release cannot be specified, the limit is even more restrictive being $1.8 \cdot 10^8$ Bq per container. Under this background, the CarboDISP project will focus on the ^{14}C release mechanisms under KONRAD operating and disposal conditions for German i-graphite waste including irradiated carbon brick, which contains a much higher ^{14}C contamination because of rather high nitrogen concentrations already present in the virgin material.

Acknowledgement

The authors like to thank the European Commission for co-funding the CARBOWASTE project (FP7-211333), the German Federal Ministry for Education and Research for supporting the CarboDISP project (02S8790) as well as other national authorities sponsoring complementary R&D, in this field. It is acknowledged that the paper is built upon diverse collaborative contributions of all other CARBOWASTE partners including additional own funds of these organisations.

References

[1] A. W. Banford, H. Eccles, M. J. Graves, W. von Lensa, S. Norris, CARBOWASTE - An Integrated Approach to Irradiated Graphite, Nuclear Futures, Sept/Oct 2008.

[2] R. E. Nightingale (Ed.), Nuclear graphite, Academic Press, New York, 1962.

[3] Carbon-14 in Irradiated Graphite Waste: A Study of the Formation and Distribution of ^{14}C in Graphite Moderators Relevant to the Decommissioning of Graphite Moderated Reactors, EPRI, Palo Alto, CA, 2010, 1021109.

[4] R. Takahashi, M. Toyahara, S. Maruki, H. Ueda, T. Yamamoto, Investigation of morphology and impurity of nuclear grade graphite, and leaching mechanism of carbon-14, Proceedings IAEA Technical Committee, October 1999, Manchester (UK).

[5] T. Podruzhina, Graphite as radioactive waste: Corrosion behaviour under final repository conditions and thermal treatment, Forschungszentrum Jülich, Jül-4166, February 2005.

[6] T. Fromherz, C. Mendoza, F. Ruette, Chemisorption of atomic H, C, N and O on a cluster-model graphite surface, Mon. Not. R. Astron. Soc. 263 (1993) 851–860.

5.17. Advanced Gas-cooled Accelerator-driven Transmutation Experiment – AGATE

John Kettler[1,3] , Bruno Thomauske[1], Rahim Nabbi[1], Peter Bourauel[1], Klaus Biß[1], Nikhil Shetty[1], Giuseppe Modolo[2], Matthias Rossbach[2], Rudolf Maier[3], Klaus Bongardt[3], Frank Esser[4], Jörg Wolters[4], Salun Hamzic[4], Harald Cura[5], Nikolay Kolev[5], Alexander Wank[5], Rainer Nies[5], Igor Mishustin[6], Igor Pshenichnov[6]

[1]Institute for Nuclear Fuel Cycle – RWTH Aachen University

[2]Institute of Nuclear Waste Management and Reactor Safety – Research Centre Jülich

[3]Institute of Nuclear Physics – Research Centre Jülich

[4]Central Technology Division – Research Centre Jülich

[5]SIEMENS AG

[6]Frankfurt Institute for Advanced Studies

Corresponding author: m.rossbach@fz-juelich.de

Abstract

The reduction of risks associated with high radioactive waste is a big challenge in the future of nuclear power. There are several concepts and studies to incinerate radioactive wastes, including long lived minor actinides (MA) and fission products (FP), in Accelerator Driven Systems (ADS). Several concepts based on different cooling systems are being discussed. Currently, concepts based on liquid metal coolant like lead or lead-bismuth are being preferred. The Institute of Nuclear Fuel Cycle (RWTH-Aachen), the Research Centre Jülich (FZJ), the Frankfurt Institute for Advanced Studies (FIAS) and the SIEMENS company investigate the feasibility of a gas-cooled ADS, which has been previously considered also by French and other European research groups. This study will demonstrate the coupling of a linear accelerator, a neutron spallation target and a subcritical core. Complementary to the design of the basic system, the critical points of the whole system will be addressed, to identify the research & development (R&D) needs, to define the safety and licensing issues and last but not least to preliminary assess the cost of the installation. The paper will present the preliminary results of the study.

Introduction

Transmutation is a method to reduce the high level wastes (HLW), which also contain long-lived minor actinides. Those can be transmuted into short-lived isotopes in a high neutron flux [1]. Apart from fission reactors, the accelerator driven system (ADS) is predestinated as a high intensity fast neutron source. The fundamental reaction is the spallation process, which yields 20-30 neutrons per initial proton. This is one order of magnitude more than in a fission reaction. Spallation sources can also be used for basic research (SNS, J-PARC, ESS).

In former European and national projects, different gas-cooled ADS concepts were developed (e.g. XADS, EUROTRANS, GNEP, TEF, HYPER) [2, 3], up to preliminary designs of 100 MW_{th} experimental facilities. Within the European Facility for Industrial Transmutation (EFIT), the gas-cooled concept was chosen as back-up solution. However, further research was focused on lead-cooled concepts [4]. It is proposed to complement the ADS

development by investigations of gas-cooled ADS and benefit from synergies with other ADS and gas-cooled fast reactor developments (e.g. MYRRHA, GoFastR, ALLEGRO) [5].

The feasibility study

The motivation of the feasibility study is to investigate the technical properties of a gas-cooled ADS. In this study the goals are to identify by simulations a nuclear fuel, which comply with the specifications of transmutation. The technical properties of the accelerator, the beam window and spallation target are investigated depending on the requirements of the ADS. Furthermore a simplified safety case study and the contribution of the ADS to a HLW disposal concept are part of the feasibility study. The term of study will end in the second quarter of 2011. Final results will be published in the second half of 2011.

Preliminary results

The accelerator concept is based on a continuous wave (CW) proton LINAC, with a two-step compact cyclotron as back-up solution. Focused on a 10 mA and 600 MeV proton LINAC concept, the advantages of the two CEA CW LINACs (175 MHz and 350/700 MHz) are combined [6, 7]. Above 28 MeV the accelerator will be superconductive. The back-up solution is based on the PSI-concept for a two-step cyclotron facility, which will enable 10 MW DC beam power for 1 GeV protons [8]. Injection of the 1.2 MeV bunches into the 120 MeV cyclotron should be no problem. A challenge is the design of the extraction magnets with 1.3 T and 4 m bending radius.
For the neutron production the proton beam will be focused on a spallation target. The penetration length of the 600 MeV proton beam in tungsten is approx. 15 cm, but for an adequate illumination of the nuclear fuel a linear neutron source is essential. Different target designs will be investigated. The first design is a conical target with a length of 120 cm. First simulation results show, that a step shaped spallation target is inapplicable, because the energy deposition is too high for the structural stability of the target material. Therefore simulations with smooth shaped conical target were done (see Fig. 107).

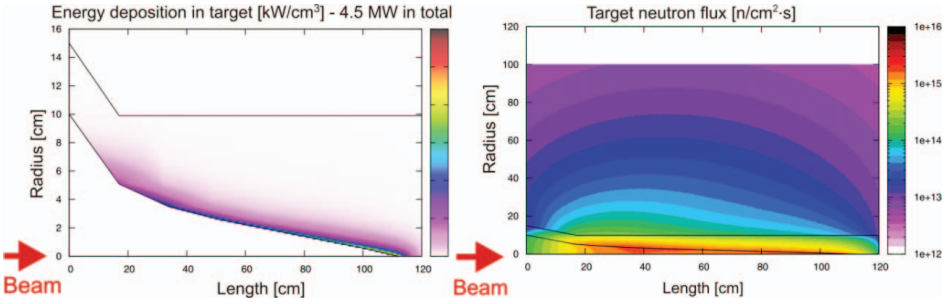

Fig. 107: Cross section of the spallation target. The left diagram shows the energy deposition of a 10 mA proton beam in the conical target. The right diagram shows the neutron flux around the conical target.

In Fig. 108 the temperature diagram of the flat shaped conical target cooled by Helium shows that the inner temperatures reach over 3.000 °C. These temperatures are in the range of the melting point of structural material tungsten. The preliminary result shows, that a conical

target is not coolable with gas. Further developments will investigate a segmented spallation target, which should be coolable.
The nuclear fuel in the startup phase will be a MOX-fuel with less than 20 wt% of Pu content. In the past facilities worked on the fabrication of fuel with less than 30 wt% Pu content (e.g. SNR-300 and Superphenix). A lot of expert knowledge is still available. Innovative ADS and fast spectrum nuclear fuel is in R&D. Till now the production of this kind of fuel is only possible in the laboratory. In the EUROTRANS project, part of the 6th EU-FP, a composite fuel (Pu, Am)O_{2-x} – ^{92}Mo (93 % enrichment) was chosen for a future European ADS demonstrator. Back-up fuel is a ceramic-metallic composite (Pu, Am)O_{2-x} – MgO (CerMet). This fuel will also be investigated in this feasibility study.

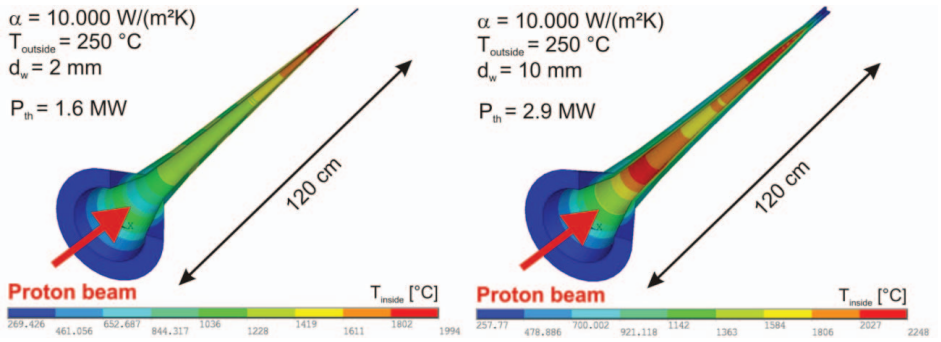

Fig. 108: Temperature diagram of the flat shaped conical target.

The AGATE reactor core consists of 10920 fuel pins with a length of 150 cm. For a maximum power of 100 MW_{th}, the maximum of the linear pin power is set to < 85 W/cm. In Fig. 109 the cross section of the reactor shows the fuel elements and the cladding of the spallation target. Detailed MCNP and MCNPX studies investigate the neutron flux and power density in the spallation target and reactor core. The neutron flux distribution in the core is also presented in Fig. 109. The first calculations were made with MOX fuel and show that more MA will be bred than burnt. The MOX composition is presented in Tab. 26. A positive transmutation effect should be achieved with optimized fuel composition like the EFIT-fuel (Pu-MA without U). First simulations with EFIT-fuel in the AGATE-core produced results, which agree with the results of Artioli et al [9].The AGATE main design parameters are presented in Tab. 27.

Tab. 26: MOX-Fuel with 20 wt.% Pu; U-Vector + Pu-Vector.

Element	U-235	U-238	Pu-238	Pu-239	Pu-240	Pu-241	Pu-242
Rel. content [%]	0.71	99.29	2.61	54	23.62	13.05	6.72

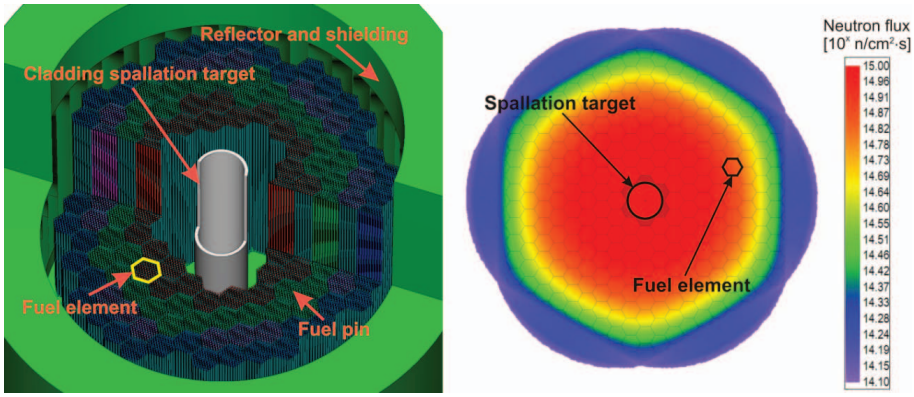

Fig. 109: The left picture shows the cross section of the reactor. The right picture is a top view of the reactor core. It shows the neutron flux distribution.

Tab. 27: Main design parameter of AGATE.

Parameter	Material/ Value
Coolant	He/ CO_2
Max. thermal power	100 MW
Maximum power of the accelerator	6 MW
Energy of the Protons	600 MeV
Current maximum	10 mA
Accelerator Mode	continuous wave (CW)
Spallation target form	conical or segmented plates
Spallation material	Tungsten
Nuclear fuel	MOX
Plutonium content – Start-up phase	≤ 20 wt%
Multiplication factor - k_{eff}	0.95 – 0.97
Cladding	HT-9
Gas pressure	6 MPa
Fuel assembly length	1500 mm

The reactor cooling was analyzed considering the neutronic calculations. Different parameter sets were calculated for the coolants CO_2 and He. The parameters for Helium are presented in Fig. 110. Detailed calculations with the core reference case (p = 6 MPa, w_{in} = 50 m/s) result in an inlet temperature of $T_{He,in}$ = 250 °C and an outlet temperature of $T_{He,out}$ = 405 °C. The cladding temperature reaches a maximum temperature of $T_{clad,max}$ = 530 °C, with a maximum fuel temperature of $T_{fuel,max}$ = 811 °C. A helium mass flow of 110 kg/s is necessary

to cool the reactor core under these conditions. Further considerations will investigate the heat transfer to a secondary circuit to use the reactor heat in a steam turbine.

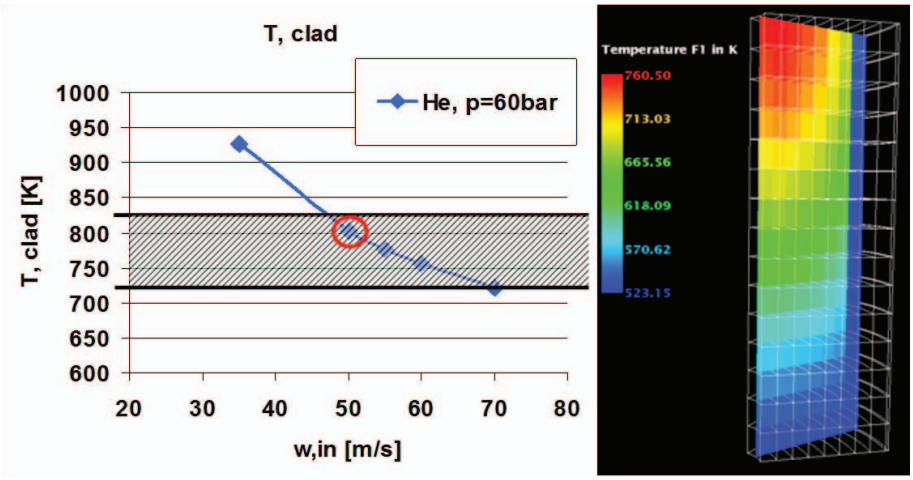

Fig. 110: Determination of possible cases for the reactor cooling. The right picture shows the He temperature [K] in 1/8th of the core geometry (thermohydraulic analysis).

Conclusions

The preliminary results of the feasibility study show the technical properties of gas-cooled ADS. The accelerator design is based on far developed concepts of CEA and PSI [6, 7, 8]. More effort is necessary for the research in the spallation target. Linear conical targets are not coolable with gas. The structural material is too much stressed by high temperatures. In the next step, a segmented spallation target based on well-designed tungsten plates will be investigated. Much effort is focused on the neutronic calculation for the AGATE reactor design. The first simulations were done with MOX-fuel (20 wt% of Pu content), which should be the fuel for the start-up phase of the ADS. Preliminary results show a negative transmutation trend of MA. Instead of MOX-fuel an advanced fuel, like the EFIT-fuel, is necessary for an acceptable transmutation rate. Simulations with EFIT-fuel in the AGATE core produce results, which agree with the results from the EFIT core design [9].

The ongoing feasibility study will focus on the simulation of the neutronic and thermohydraulic of the spallation target, beam window and reactor core. A simplified safety case study will also be performed, as well as the contribution of the ADS to a HLW disposal concept.

Acknowledgments

The authors would like to thank the Ministry of Innovation, Science and Research of the German State of North Rhine-Westphalia (MIWF) for its financing support.

References

[1] RED-IMPACT, Synthesis Report, ed. by W. von Lensa, R. Nabbi, M. Rossbach (2008), 178 pages, ISBN 978-389336-538-8

[2] A European Roadmap for Developing Accelerator Driven Systems (ADS) for Nuclear Waste Incineration, ENEA (2001), ISBN 88-8286-008-6
[3] Comparison of the transient behaviour of LBE-and gas-cooled experimental accelerator-driven systems, K. Mikityuk, P. Coddington, E. Bubelis, R. Chawla, Nuclear Engineering and Design (2006)
[4] Partitioning and transmutation Current developments – 2010, ed. by J. Blomgren, SKB, TR-10-35 (2010)
[5] PRELIMINARY DESIGN STUDY OF AN EXPERIMENTAL ACCCELERATOR DRIVEN SYSTEM OVERALL DESCRIPTION OF THE GAS-COOLED SYSTEM, B. Giraud, Framatome ANP SAS (2003)
[6] The Accelerator Prototype of the IFMIF/EVEDA Project, A. Mosnier et al, Proceedings IPAC 10, Kyoto, Japan (2010)
[7] European ADS and Its Challenge to Accelerators, J-L. Biarrote, A. C. Mueller, IPN Orsay, Beam Dynamics Newsletter 49, August 2006, p. 39-49
[8] Cyclotron Based High Intensity Proton Accelerators, J. Grillenberger, M. Seidel, PSI, Beam Dynamics Newsletter 49, August 2006, p. 61-72
[9] Minor actinide transmutation in ADS: the EFIT core design, C. Artioli et al, International Conference on the Physics of Reactors “Nuclear Power: A Sustainable Resource”, Interlaken, Switzerland (2008)

5.18. Monitoring Uranium Mining and Processing Sites: Some Findings from an Airborne Hyperspectral Survey of Uranium Mining Legacies under Rehabilitation

I. Niemeyer, C. Listner

Corresponding author: i.niemeyer@fz-juelich.de

Abstract

In preparation of the EnMAP mission, the German Remote Sensing Data Center (DLR/DFD) carried out an airborne hyperspectral campaign in summer 2009 using the HyMap Imaging Spectrometer. Our area of interest was located next to Zwickau/Saxony at the Wismut uranium mining legacies under rehabilitation. Simultaneously to image acquisition, we collected in-situ data in the investigation site: Surface reflectance using a field spectrometer, and soil and vegetation samples, which were analysed later on by mass spectrometry. The objective of our study was to assess the potential of hyperspectral imagery analysis for detecting directional or diffuse environmental contaminations due to uranium mining and processing. Though intended for environmental monitoring purposes, we expected the field study to also provide some implications on safeguards issues with regard to uranium mining and processing. In the given paper, we report on the acquisition of airborne and in-situ data, present methods used and investigations in the first project phase, and derive some preliminary conclusions from it.

Introduction

Hyperspectral sensors record the reflected radiation in several hundreds of very narrow contiguous or overlapping wavelength bands from visible to mid infrared. Using well-calibrated hyperspectral data allows to quantitatively estimate geophysical, geochemical and biochemical characteristics of the earth's surface. Hyperspectral imagery analysis could therefore provide information on surface activities connected to uranium ore drilling, mining and processing activities. By fusing the results of lower spatial resolution hyperspectral analysis results with high resolution imagery, both geometric and materials properties of surface objects can be extracted.

The only satellite-based hyperspectral instrument today, Hyperion, is flying onboard NASA's Earth Orbiter-1 (EO-1) spacecraft. Hyperion provides 220 spectral bands in the reflective solar wavelength region from 0.4 to 2.5 µm with contiguous spectral coverage and bandwidths of 10 nm at a scene size of 7.5 km by 100 km [1]. The spatial resolution of 30 m might be a limiting factor for using hyperspectral data in a number of safeguards-related purposes. Moreover, the Hyperion image data involves huge noise effects, i.e. the signal to noise ratio hinders the analysis. The latter, however, is expected to be improved by the Canadian Hyperspectral Environment and Resource Observer (HERO) mission [2] and the German Environmental Monitoring and Analysis Program (EnMap) [3].

Previous safeguards-related studies focused on the possibilities of extracting unique features of uranium mining and milling, and of verifying States' declarations, such as movement of material [4]. If these unique features exist, they could be used for identifying potential clandestine activities connected to uranium mining and processing. However, no specific "uranium signature" was found so far. In an earlier study, endmember spectra were extracted

from airborne SWIR Full Spectrum Imager (SFSI-2), acquired over the Canadian processing site Key Lake (Saskatchewan) [5]. The authors concluded that no uranium compounds were identified from the airborne data. Another study used airborne Probe-1 data acquired over the Canadian Pronto mine (Ontario) in order to distinguish uranium mine tailings from other types of mine tailings based on mineral absorption features [6]. Here, the authors finally stated that no spectral absorption feature could be associated with uranium mine tailings.
In preparation of the EnMAP mission, the German Remote Sensing Data Center (DLR/DFD) carried out an airborne hyperspectral campaign in summer 2009 (HyEurope 2009) [7] using the HyMap Imaging Spectrometer [8]. Our area of interest was located next to Zwickau/Saxony at the Wismut uranium mining legacies under rehabilitation. Simultaneously to image acquisition, we collected in-situ data in the investigation site. We measured the surface reflectance using the Analytical Spectral Devices Inc. (ASD) Fieldspec Pro spectrometer, and collected soil and vegetation samples, which were analysed later on by inductively coupled plasma mass spectrometry mass spectrometry (ICP-MS).
The objective of our study was to assess the potential of hyperspectral imagery analysis for detecting directional or diffuse environmental contaminations due to uranium mining and processing. The first project phase was intended to evaluate new hyperspectral data classifiers and change detection methods. The second project phase aims at integrating hyperspectral remote sensing and the in-situ measurements by applying traditional and new supervised hyperspectral classifiers. Though intended for environmental monitoring purposes, our study was supposed to give also some implications on monitoring uranium mining and processing sites from a nuclear safeguards perspective. The given paper reports on the acquisition of airborne and in-situ data, presents methods used and investigations in the first project phase, and derives some preliminary conclusions from it.

Area of Interest & Data

a) Investigation area

Our area of interest was located next to Zwickau/Saxony at the Wismut uranium mining legacies under rehabilitation. The Wismut Company was established in Saxony in 1947, initially run by the Soviet military, later in Soviet and then Soviet-German ownership. Wismut, exploiting the German uranium deposits for the Soviet nuclear program, produced a total of 231,000 tons of uranium during the four decades of its existence. This ranks Wismut as number three in world-wide uranium production after the US and Canada. Following German reunification, uranium mining was terminated in the end of 1990. Since mid 1991, Wismut GmbH has become a German Government-owned company operating in Saxony and Thuringia on decommissioning, cleanup, and rehabilitation of the former uranium mining and processing sites. [9]
We selected the Crossen site as one of the former processing facilities. Today, the location consists of the dismantled processing site (Fig. 111 a), the tailings dump (Fig. 111 b) and the tailings ponds Helmsdorf/Daenkritz I (Fig. 111 c).

b) HyMap™ Data

The HyMap™ hyperspectral scanner manufactured by Integrated Spectronics Pty Ltd. provides 128 bands across the reflective solar wavelength region of 0.45 to 2.5 µm with contiguous spectral coverage (except in the atmospheric water vapour bands) and bandwidths between 15 and 20 nm. The Hymap provides a signal to noise ratio (>500:1) and image quality that is setting the industry standard. [8]

During the HyEurope campaign, two images were acquired on August 20, 2009. The first scene was obtained in the afternoon (15:37 local time) with the best possible spatial resolution of 5 m (Fig. 111), the second was recorded half an hour later (15:52 local time) at a spatial resolution of 9.5 m. The images were atmospherically and geometrically corrected by DLR/DFD before delivering to us.

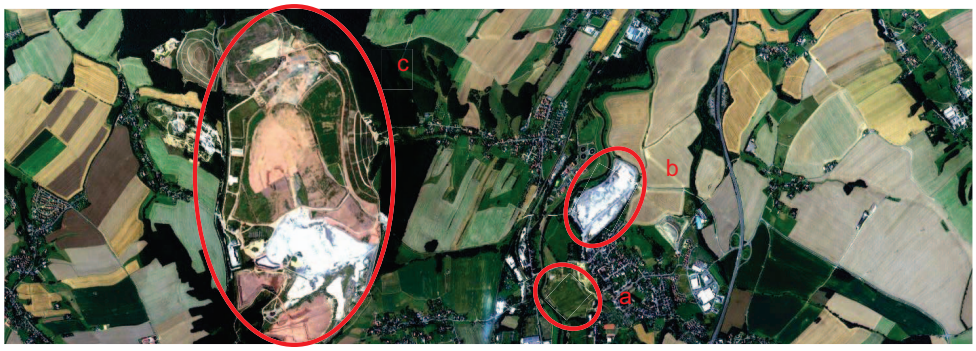

Fig. 111: Area of interest given by HyMAP on August 20, 2009: Wismut former processing site Crossen with the dismantled processing site (a), the tailings dump (b) and the tailings pond Helmsdorf/Daenkritz I (c). Flight time: 13:37 UTC; flight height: 2718 m; ground resolution: 5 m.

c) In-situ measurements

Simultaneously to image acquisition, we carried out a field campaign in order to

- measure the surface reflectance using the ASD Fieldspec Pro spectrometer, capable of recording reference spectra in 2151 bands in the 0.35 to 2.5 µm spectral range (Fig. 112);
- select soil and vegetation samples and subsequently analyze heavy metal concentrations in the samples by ICP-MS (Fig. 113);
- map the surface cartographically and measure GPS points.

In addition, we received environmental data from Wismut such as terrestrial surveying, climate and water quality data.

Fig. 112: Surface reflectance using the ASD Fieldspec Pro spectrometer. Left: Yellow stars indicate the locations of measurements. Right: Two spectra examples.

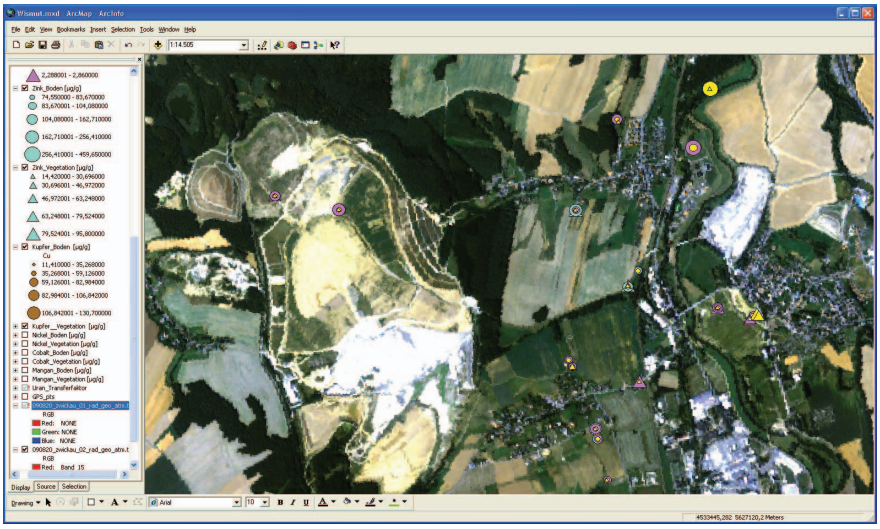

Fig. 113: Visualization of the vegetation and soil samples analysis by ICP-MS on Arsenic, Cadmium, Cobalt, Copper, Manganese, Nickel, Uranium, and Zinc.

Methodologies

a) Supervised Classification using Class-based Neural Networks

Hyperspectral images are characterized by their huge feature size due to the high number of narrow frequency bands. These bands provide a wealth of information regarding the physical nature of different objects in the scene. However, both high dimensionality and redundancy of the data makes it more difficult to use the data efficiently for classification. Several feature reduction techniques have been developed for this purpose [10]. Even after reducing the dimensionality, there are still a lot of features to be used in the classification. However, only a few features can be used to characterize a class and differentiate it from the other given classes. It is therefore advantageous to deal with the classes independently by considering only the best features related to each of the classes. These features distinguishing between the classes can be identified by using the sample distributions of the classes and separability measures such as the Bhattacharyya distance [11, 12] or the Jeffries-Matusita distance [13].
We used a new neural network architecture for classifying hyperspectral data based on the so called class-based feed forward networks (CBFFN) [14]. CBFFN is simply a feed forward neural network (FFN) for each class of interest where the inputs are the features uniquely characterizing that particular class. The architecture first tries to separate every class of interest from other classes using a suitable feature subspace, thus providing a better way to handle the complexity of the huge feature space available in hyperspectral images. In the second level, it uses another neural network to combine the output of the CBFFNs, which define the pattern of the classes, and generates a final decision. The architecture was originally developed for effectively dealing with huge object features spaces in object-based classification of spatial high-resolution optical imagery [13]. By considering the numerous bands of hyperspectral data as features and the image pixels as one-pixel-objects, the architecture was adapted to hyperspectral image classification [15]. The study demonstrated the usefulness of the CBFFN architecture for hyperspectral image processing using an effective non-linear classifier.

b) Change Detection by Multivariate Alteration Detection

The Multivariate Alteration Detection (MAD) transformation [16] is based on a classical statistical transformation referred to as canonical correlation analysis to enhance the change information in the difference images. The procedure is briefly described as follows: If multispectral images of a scene acquired at times t_1 and t_2 are represented by random vectors $\boldsymbol{X}$ and $\boldsymbol{Y}$, which are assumed to be multivariate normally distributed, the difference D between the two images is calculated by $D= \boldsymbol{a}^T\boldsymbol{X}- \boldsymbol{b}^T\boldsymbol{Y}$. Analogously to a principal component transformation, the vectors $\boldsymbol{a}$ and $\boldsymbol{b}$ are estimated subject to the condition that the variance of D is maximized and subject to the constraints that $\text{var}(\boldsymbol{a}^T\boldsymbol{X})= \text{var}(\boldsymbol{b}^T\boldsymbol{Y})=1$.

Determining the vectors $\boldsymbol{a}$ and $\boldsymbol{b}$ in this way is a standard statistical procedure which considers a generalized eigenvalue problem. For a given number of bands N, the procedure returns N eigenvalues, N pairs of eigenvectors and N orthogonal (uncorrelated) difference images, referred to as to the MAD components. The MAD components represent different categories of changes. Since relevant changes of man-made structures will generally be uncorrelated with seasonal vegetation changes or statistic image noise, they expectedly concentrate in different MAD components. If the components are sorted according to the increasing variance, higher order MAD components represent the small-scale changes whereas lower order components contain the overall or wide-area changes.

Experiments

Classification using CBFFN

CBFFN classification was applied to two subareas of interest, the dismantled processing site and the tailings dump (see Fig. 111 a/b) and the tailings pond Helmsdorf/Daenkritz I (see Fig. 111 c). Seven classes were defined for either subarea. For the first subarea, the classes of interest were agricultural area, built-up area, building, grassland, mine dump, forest and water. For the second subarea, we selected buildings, three different stadiums of increasing rehabilitation, grassland, forest and water.

No pre-processing steps were performed but only the statistical feature selection based on Jeffries-Matusita distance [12] was used to identify the features best distinguishing between classes. From the 128 hyperspectral HyMAP bands 28 bands (first subarea) and 29 bands (second subarea) respectively, the brightness and the maximum difference were selected as input for CBNN classification. The method therefore was able to reduce the dimensionality of the input dataset by 76%. Given the fact that the FFNs created for each class used only nine to 14 features, the dimensionality was even more decreased. The overall accuracy was estimated as 93 % (Fig. 114) and 94 % (Fig. 115).

Change Detection using MAD and Change Classification using CBFFN

Unfortunately, only one acquisition time was available for the area of interest. In order to assess the MAD technique for detecting temporal changes in our investigation area, we used a duplicate of the 5 m scene and edited manually simulated changes by copying and moving some images squares to other image positions. The original scene was considered as data recorded at time 1, the simulated image as data recorded at time 2. We assumed four generic land cover classes and considered a limited number of class transitions from time 1 to time 2 (Fig. 116 a).

Fig. 116b shows the results after applying both MAD for change detection and CBFFN for change classification. No-change areas and changes were identified correctly; however, the classification of changes involved some false alarms. We experimented with an increasing

number of training samples up to 19 as input for the supervised change classification. Besides CBFFN, also a Standard Nearest Neighbor (SNN) classifier was used for comparison. The best results were achieved applying CBFFN classification based on more than ten training samples (Fig. 117). Here, the overall classification accuracy amounted to values between 94 and 96 %.

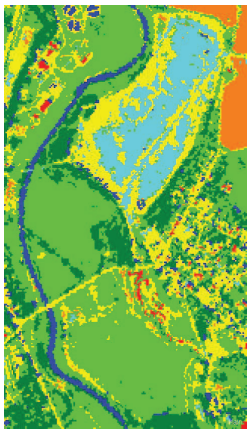

Class	Features used
Agricultural:	Max. Diff., 1, 2, 69, 70, 100, 101, 124, 125, Brightness
Built-up area:	Max. Diff., 14, 15, 16, 58, 69, 70, 71, 95, 96
Building:	Max. Diff., 3, 5, 15, 16, 21, 22, 69, 70, 124, 125
Grassland:	Max. Diff., 7, 8, 16, 49, 50, 58, 95, 125, Brightness
Mine dump:	Max. Diff., 1, 2, 3, 4, 5, 14, 15, 16, 91, 92, 93
Forest:	Max. Diff., 7, 8, 15, 16, 45, 46, 95, 96
Water:	Max. Diff., 1, 2, 69, 70, 100, 101, 124, 125

Fig. 114: Classification of the dismantled processing site and the tailings dump (see Fig. 111 a/b) using CBNN. The table on the right indicates the features used within classification.

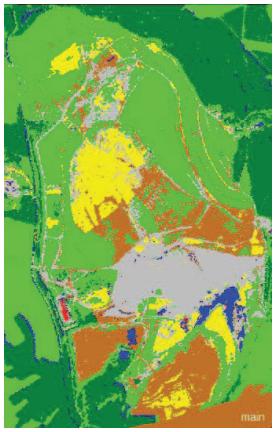

Class	Features used
Building:	Max.Diff., 1, 2, 4, 16, 95, 100, 103, 110, 114, 115
Stadium 1:	Max.Diff., 1, 2, 3, 15, 16, 69, 95, 99, 114,115
Stadium 2:	Max. Diff., 1, 2, 3, 7, 8, 11, 14, 42, 43
Stadium 3:	Max.Diff.,1, 2, 3, 6, 7, 8, 100, 101, 102, 114, 115, Brightness
Grassland:	1, 2, 3,4 , 6, 7, 8, 82, 82, 84, 102, 103, 104
Forest:	Max. Diff., 1, 2, 3, 4, 6, 7, 8, 10, 11, 15, 16, 95, 100
Water:	Max. Diff., 1, 2, 4, 16, 95, 100, 103, 110, 114, 115

Fig. 115: Classification of the tailings pond Helmsdorf/Daenkritz I (see Fig. 111 c) using CBNN. The table on the right indicates the features used within classification.

Conclusions and next steps

The preliminary results indicate that classification using class-based feed forward neural networks (CBFFN) is an alternative to traditional hyperspectral classifiers and may help to better identify uranium compounds. Change detection using the multivariate alteration

detection (MAD) transformation and change classification using CBFFN provides fast and reliable results on changes in bi-temporal hyperspectral datasets.
The second project phase currently continues on two issues. Firstly, the two resolutions (5 m and 9.5 m) will be analysed in an integrated way. Second, the in-situ measurements will also be integrated by applying new and traditional supervised classification, such as spectral unmixing by using the reference spectra from the ASD Field Spec Pro measurements. Also the results from the samples analysis and the data provided by Wismut will be considered. At the end, we aim to draw conclusions on directional or diffuse environmental contaminations induced by uranium mining and processing.

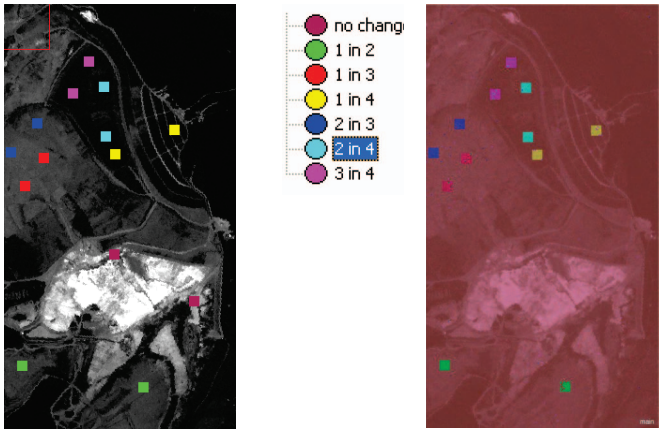

a) Simulated changes b) Calculated changes

Fig. 116: Change detection results for the tailings pond Helmsdorf/Daenkritz I (see Fig. 111 c). Simulated changes (a) and calculated changes using MAD (b).

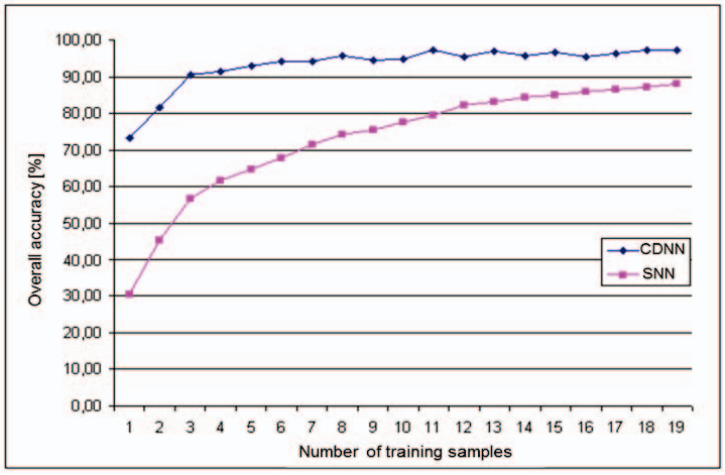

Fig. 117: Change detection results for the tailings pond Helmsdorf/Dänkritz I (see Fig. 111 c). Simulated changes (a) and calculated changes using MAD (b).

Acknowledgements

The work presented here was carried out as part of the “EnMAP Application Preparation”, funded by the Ministry of Economy and Technology (BMWi) and coordinated by the German Aerospace Center (DLR). The authors acknowledge in particular the support provided by M. Hillmann and Prof. C. Drebenstedt (TU Bergakademie Freiberg), Tim Buchholz (European Space Agency, ESA), Dr. C. Fischer und C. Ehrler (DLR), and WISMUT GmbH.

References

[1] H. J. Kramer, Observation of the Earth and Its Environment, Survey of Missions and Sensors, 4th edition, Springer, Berlin Heidelberg (2002).

[2] G. W. Jolly and M. Dettwiler, The Hyperspectral Environment and Resource Observer - A Canadian mission in support of sustainable development, Proc. 55th International Astronautical Congress of the International Astronautical Federation, the International Academy of Astronautics, and the International Institute of Space Law, Vancouver (2004).

[3] T. Stuffler, H. Kaufmann, S. Hofer, K.-P. Förster, G. Schreier, A. Müller, A. Eckardt, H. Bach, B. Penne, U. Benz, and R. Haydn, The EnMAP hyperspectral imager - An advanced optical payload for future applications in Earth observation programmes, Acta Astronautica, 61, 1-6, (2007) 115-120.

[4] C. L. Stork, H. A. Smartt, D. S. Blair, and J. L. Smith, Systematic Evaluation of Satellite Remote Sensing for Identifying Uranium Mines and Mills, Sandia Report, SAND2005-7791, Sandia National Laboratories, Albuquerque (2006).

[5] R. A. Neville, K. Staenz, J. Lévesque, C. Nadeau, Q. S. Truong, and G. A. Borstad, Uranium Mine Detection Using an Airborne Imaging Spectrometer, Proc. Fifth International Airborne Remote Sensing Conference, San Francisco, California (2001).

[6] J. Lévesque, R. A. Neville, K. Staenz, and Q. S. Truong, Preliminary Results on the Investigation of Hyperspectral Remote Sensing for the Identification of Uranium Mine Tailings, Proc. ISSSR'01, Québec City (2001).

[7] German Remote Sensing Data Centre, http://www.opairs.aero/hymap2009_en.html

[8] T. Cocks, R. Jenssen, A. Stewart, I. Wilson, and T. Shields, The HyMap Airborne Hyperspectral Sensor: The System, Calibration and Performance, Proc. 1st EARSeL Workshop on Imaging Spectroscopy, Zurich (1998).

[9] Wismut GmbH, http://www.wismut.de/index_english.htm

[10] S. B. Serpico, M. D’Inca, F. Melgani, and G. Moser, Comparison of feature reduction techniques for classification of hyperspectral remote sensing data, SPIE Proc. Vol. 4885, Image and Signal Processing for Remote Sensing VIII (2003) 347–358.

[11] Bhattacharyya, On a measure of divergence between two statistical populations defined by their probability distributions, Bull. Calcutta Math. Soc, 35, 99-109 (1943) 4.

[12] J. Hong and C. Lee, Separability measures for error estimation of two normally distributed classes, SPIE Proc. Vol. 3460, Applications of Digital Image Processing XXI (1998) 695–705

[13] S. Nussbaum and G. Menz, Object-based image analysis and treaty verification: New Approaches in Remote Sensing-Applied to Nuclear Facilities in Iran, Springer, Berlin Heidelberg (2008).

[14] P. R. Marpu, Geographic Object-based Image Analysis, Ph.D. Thesis, Freiberg University of Mining and Technology, Freiberg, Germany (2009).

[15] P. R. Marpu, P. Gamba, and I. Niemeyer, Hyperspectral Data Classification Using an Ensemble of Class-Dependent Neural Networks, Proc. IEEE 1st Workshop on Hyperspectral Image and Signal Processing: Evolution in Remote Sensing (WHISPERS), Grenoble (2009).

[16] A.A. Nielsen, The regularized iteratively reweighted MAD method for change detection in multi- and hyperspectral data, IEEE Transactions on Image Processing, Vol. 16, No. 2 (2007) 463-478.

5.19. Multiresolution segmentation adapted for object-based change detection

C. Listner, I. Niemeyer

Corresponding author: c.listner@fz-juelich.de

Abstract

In object-based change detection using specified object features as change measures, segmentation is the crucial step, especially when also shape changes are taken into consideration. The paper introduces a new segmentation approach for object-based change detection. The algorithm segments the first image using the multiresolution segmentation. Assigned to the second image, all segmentation merges are checked for consistency and removed if the check fails.

Introduction

Change detection has always been an important application for remote sensing data. It may be defined as the analysis of two or more images of the same area but acquired at different times in order to identify significant changes of or at the earth's surface. A huge number of data processing methods were proposed [1, 2, 3]: Methods analysing difference images, classification-based approaches and kernel-based methods such as principal component analysis or multivariate alteration detection, to name just a few examples. All these approaches have in common that they compare corresponding image pixels of different acquisition times.

However, due to the increased spatial resolution of remote imaging sensors, the aggregation of similar neighbouring pixels into homogeneous objects has become more and more popular. After the aggregation, also referred to as segmentation, the user might consider also shape, relations and texture of the image objects in the analysis. This paradigm is called object-based image analysis (OBIA) [4]. Change detection can also be carried out based on the image objects.

Earlier studies [5, 6] turned out that segmentation is the crucial step in object-based change detection. For image data taken over the same area at two different acquisition times, the image segmentation could be generally performed in three different ways:

a) On the basis of the bi-temporal data set, i.e. using a data stack consisting of both scenes;
b) based on the image data of one acquisition time; the generated object boundaries are then simply assigned to the image data of the second acquisition;
c) separately for the two times, i.e. the two data sets are segmented independently.

When using a segmentation as suggested in (a) or (b), the resulting image objects have the same geometric properties at the two times, i.e. time-invariant shape features. Change detection can only be applied to a limited number of time-variant object features, such as layer values, texture etc. Provided independent segmentation of the two scenes (c), also the image object geometry varies in time. In this case, all available object features could be used for object-based change detection. However, the issue of linking objects has not been solved satisfactorily yet. Moreover, region-growing segmentation algorithms provide different segmentation results in case of minor temporal image changes. In summary, each of the

three approaches has severe drawbacks concerning the use of shape features, segmentation robustness and quality, or the problem of linking corresponding objects of different acquisition times, see [5] for a more detailed discussion.
Therefore, we will present a new segmentation approach for object-based change detection. Given a bi-temporal dataset acquired over the same area, the adapted procedure aims to provide almost identical segments for image regions where no temporal changes occurred and different segments for temporally changed image regions.

Methods

The general idea of our work is to create segmentations of the two images I_1 and I_2, acquired at different times over the same area, that only differ in image regions where actual changes took place. For this purpose we adapted a region-growing segmentation algorithm called multiresolution segmentation [7], which is available in the eCognition software for object-based image analysis [8]. The multiresolution segmentation starts with pixels as initial segments and iteratively aggregates neighbouring segments to bigger segments according to predefined heterogeneity criteria.
However, object-based change detection requires a segmentation technique that similarly extracts objects that have not changed their shape and size between the two acquisition times. The multiresolution segmentation implemented in the eCognition software uses homogeneity criteria based on colour and shape, and a scale parameter in combination with local and global optimization techniques. Thus, applying the same segmentation parameters to both scenes does hardly produce similar objects in image regions with no or negligible changes, if other parts of the image have slightly changed.
In our procedure, the multiresolution segmentation is used to generate a segmentation of I_1. After that, the segmentation is also applied to I_2 and tested for its consistency. If a segment is found to be inconsistent with I_2, it will be split up. But let us start with describing the multiresolution segmentation in more detail, before introducing the adaption for change detection.
Multiresolution segmentation is a region-based approach. In this approach, segments can be considered as binary trees in which the leaf nodes correspond to single pixels and every merge step can be represented by a non-leaf node. According to this model, we will use the terms segment and node synonymously throughout this paper.
The multiresolution segmentation starts with an initial chessboard segmentation that identifies each pixel as an individual segment. Then, segments grow in multiple cycles. In each cycle a random seed S_1 of minimal tree depth is selected iteratively in order to check if one of its neighbours S_2 can be merged with S_1 to a new segment S_{new}. The degree of fitting is modelled by the measure of heterogeneity h that has to fulfil

$$h(S_{new}) < T, \qquad (1)$$

T being a given threshold. The aim is to minimize h in the neighbourhood of S_1 when being merged with S_2. Furthermore, S_1 has also to minimize h in the neighbourhood of S_2. Otherwise, S_2 is set to be the next seed. This strategy, called *local mutual best fitting* (see Fig. 118), results in a path of descending values for h leading to a local minimum. Hence, it is impossible to run into an infinite loop. Moreover, this strategy causes a regular growth of the segments. For specific formulas on the heterogeneity measure, see [9].

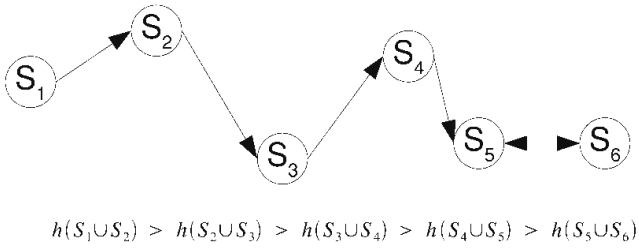

Fig. 118: Local mutual best fitting strategy.

If no local mutual best fitting neighbour has been found given seed S_1, it is marked as final. Final segments can no longer be merged with other segments until the end of a segmentation cycle or a merge of neighbouring segments. If all segments have been marked as final, the algorithm continues with the next cycle by resetting all segments from final. The algorithm ends if none of the present segments has been merged with another segment during a cycle.

In case a single image is being segmented, the information about the child segments has no further relevance after merging them. However, as we intend to test the segmentation of one acquisition time for consistency with an image of another acquisition time, the information on the segment history, i.e. the segment hierarchy, needs to be saved within the process. Depending on the applied consistency tests, also information on the neighbourhood existing at the time a segment was created could be necessary [9].

Following the insight into the multiresolution segmentation algorithm, we now focus on adapting this algorithm to the problem of segmenting two images of the same area acquired at different times. We therefore propose the following approach:

1. Segment image I_1 using the multiresolution segmentation algorithm.
2. Apply this segmentation to image I_2 and recalculate the heterogeneity of each segment based on the data of I_2.
3. Check every merge, i.e. every segment that consists of more than one pixel, for consistency by applying a test criterion. Not only the top-level segments, i.e. the nodes without parents, need to be examined but all nodes in each segment tree except for the leaf nodes.
4. Remove all inconsistent nodes using a segment removal strategy.
5. Re-run the multiresolution segmentation to obtain a final segmentation of the second image.

These steps present a general process which has to be specified in two aspects. First, how can segments of image I_1 be checked for consistency with image I_2 and second, how can inconsistent segments be removed?

With regard to the consistency tests we propose three different criteria. The first one, named *threshold test*, examines whether a given segment S fulfils the condition

$$h(S) < T_{check}. \qquad (2)$$

Otherwise the segment S is marked as inconsistent. The threshold test is the weakest test with respect to changes between the two images.

The second test, called *local best fitting test*, tries to repeat the merge procedure with the data of image I_2. Given an exemplary segment structure with parent segment S_3 and its children S_1 and S_2, the test assumes S_1 to be a seed and searches for locally best fitting

neighbours from the list of merge candidates that has been stored during the segmentation of image I_1. If the best fitting neighbour is S_2, the test is passed, otherwise it is failed. Besides, also the condition given in Equation 2 needs to be fulfilled. Obviously, this test is very sensitive even to small changes or noise in the imagery. In order to reduce the sensitivity of the test, a parameter $T_{checktolerance}$ is introduced. The idea of this additional parameter is that a merge may not be the locally best fitting one but could belong e.g. to the 10% best fitting ones. Therefore the test checks how many merge candidates perform better (n_{better}), equally well (n_{equal}) and worse (n_{worse}) than the segment that has been merged to the seed. If the condition

$$\frac{n_{better}}{n_{better}+n_{equal}+n_{worse}} < T_{checktolerance} \qquad (3)$$

holds, the consistency test is considered to be passed.

Finally, the third test is named *local mutual best fitting test*. It also tests if S_2 is the best fitting neighbour for seed S_1 in the list of merge candidates but checks additionally if S_1 is the best fitting neighbour for S_2. This test's principle is derived from the idea of local mutual best fitting presented before. Compared to the local best fitting test, this test is more sensitive; however, applying Equation 3 could also reduce the sensitivity of this test. In general, splitting-up segments could be avoided by increasing threshold T_{check}. Then, not all changes between I_1 and I_2 may result in changes of the segmentation.

After testing all given segments for consistency with the image I_2, those segments that did not pass the test have to be handled. We therefore introduce three strategies to remove these segments.

The first strategy is named *universal segment removal strategy*. The principal idea of this strategy is illustrated in Fig. 119: It searches for the top-level segment of an inconsistent segment and splits it into its elements. As a result, only pixel segments will remain. Obviously, this strategy affects the segmentation intensively and could therefore create changes in the final segmentation in areas where no actual changes can be observed.

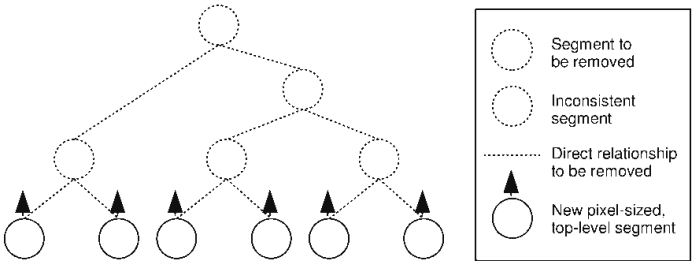

Fig. 119: Universal segment removal strategy.

The second strategy for removing inconsistent segments is the *global segment removal strategy*. Its basic principle, as illustrated in Fig. 120, is to remove the inconsistent segment and all its ancestors from the segment tree. During this process all remaining segments are considered to be new top-level segments. In this way, the impact on the segment tree is reduced. However, this strategy is very adaptive in creating changes only in parts of the segment tree in which changes can be detected and leaves the rest as it is.

The third and most complex segment removal algorithm is called *local segment removal strategy*. It is developed due to the fact that the global segment removal strategy affects parts of the segment tree which do not necessarily change between different acquisition times. Consider for example a big object in image I_1 which is segmented correctly. If only a small part of this object changes from one acquisition time to another, it may be a better to extract this small part instead of splitting up the whole object.

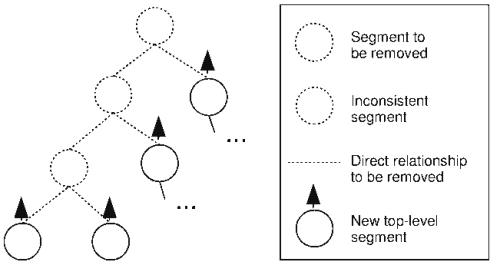

Fig. 120: Global segment removal strategy.

Therefore we propose an additional method for removing inconsistent segments: Assume *I* to be an inconsistent node. Then remove *I* and its parent *P* from the segment tree. Set *I*'s children C_1 and C_2 as top-level segments and put *I*'s sibling *S* as child of *I*'s grandparent *G*. This method is illustrated in Fig. 121. It has been turned out that the local segment removal strategy cannot be applied directly in all possible constellations. See [9] for a detailed discussion of this issue.

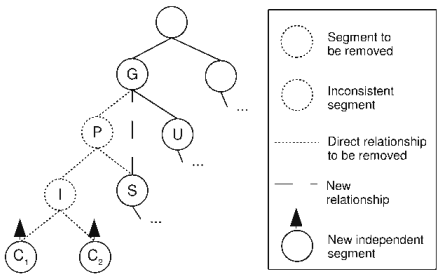

Fig. 121: Local segment removal strategy.

Experiments

The proposed methods were implemented using the C++ programming language including STL [10] and GDAL [11], and tested based on simulated data. The simulated data were produced by adding artificial changes to an aerial photography. In particular a polygon representing a house was copied and pasted to another position in the image. Furthermore, some Gaussian noise with $\mu = 0$ and $\sigma = 0.1$ was added. For reasons of visibility we will only show a part of this scene in this section.

Fig. 122 shows the results of the independent multiresolution segmentation of the images. The results indicate the main problem of multiresolution segmentation algorithm's stability as

it gives a difference in segmentation of 98%. This means that the shape of segments covering 98% of the image area has changed between the segmentations although just a small area has actually been altered. In practice, changes are not very big but they may have an impact on the change detection process when shape features are integrated. However, both segmentations represent the data very well.

Fig. 123 to Fig. 125 display the experimental results. From left to right, the figures give the segmentation of first image using multiresolution segmentation, the segmentation adapted to second image after consistency check and segment removal, and the final segmentation of the second image. Fig. 123 shows the segmentation results when applying the threshold test and the universal segment removal to the same imagery. The results differ very much from the independent segmentation of the second image given in Fig. 122, and the difference between the two image segmentations is only 9%. With regard to the centre of Fig. 123, this removal strategy has a huge impact on the structure of the segmentation. Again, the image data is well structured by the segmentation. Fig. 124 displays the segmentation results when applying the local mutual best fitting test combined with the global segment removal strategy. This approach leads to a segmentation difference of 13%. Although the combined strategies apparently provide a slightly worse result, their impact on the structure of the segmentation seems to be less significant in image areas without actual changes. Therefore, the method of global segment removal is better adapting to changes than the universal segment removal. Finally, the results of the local best fitting test in combination with the local segment removal strategy are given in Fig. 125. This approach leads to a segmentation difference of 13%, however, it seems to even better extract the area of change than the global segment removal strategy.

Fig. 122: Independent segmentation using multiresolution segmentation of two images covering the same area with simulated changes using parameters T = 75, w_s = 0.1 and w_{comp} = 0.5.

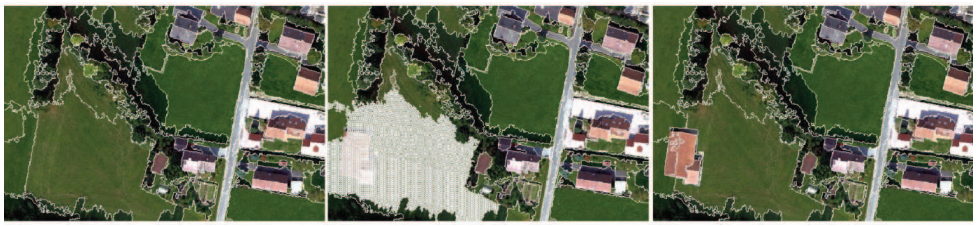

Fig. 123: Segmentation using threshold test and universal segment removal of two scenes with simulated changes and parameters T = 75, T_{check} = 75, w_s = 0.1 and w_{comp} = 0.5.

Fig. 124: Segmentation using local mutual best fitting test and global segment removal of two scenes with simulated changes using parameters T = 75, T_{check} = 75, $T_{checktolerance}$ = 0.5, w_s = 0.1 and w_{comp} = 0.5.

Fig. 125: Segmentation using local best fitting test and local segment removal of two scenes with simulated changes using parameters T = 75, T_{check} = 75, $T_{checktolerance}$ = 0.5, w_s = 0.1 and w_{comp} = 0.5.

Conclusion

We presented some new ideas for addressing the issue of segmenting remote sensing imagery for object-based change detection. An enhanced procedure based on multiresolution segmentation was presented, and it was shown that satisfying results for simulated data can be achieved.

Further developments are needed such as new consistency tests and segment removal strategies. Moreover, methods for enabling the user to easily select the segmentation parameters, e.g. by using training samples, would be helpful. Finally, the adapted multiresolution segmentation needs to be implemented as eCognition plugin for allowing its direct use in the proposed change detection workflow.

References

[1] A. Singh, Review Article Digital change detection techniques using remotely-sensed data, International Journal of Remote Sensing 10, 6 (1989) 989-1003.

[2] R. Radke, S. Andra, O. Al-Kofahi, Image change detection algorithms: a systematic survey, IEEE Transactions on Image Processing 14, 3 (2005) 294-307.

[3] M. J. Canty, Image Analysis, Classification, And Change Detection In Remote Sensing: With Algorithms For ENVI/IDL, Taylor & Francis Ltd, 2nd ed. (2009).

[4] T. Blaschke, S. Lang, and G. Hay (Eds.), Object-Based Image Analysis Spatial Concepts for Knowledge-Driven Remote Sensing Applications, Series: Lecture Notes in Geoinformation and Cartography, Springer, Berlin (2008).

[5] I. Niemeyer, P. R. Marpu, and S. Nussbaum, Change detection using object features, Blaschke, T., Lang, S. & Hay, G. (Eds.), Object-Based Image Analysis Spatial Concepts for Knowledge-Driven Remote Sensing Applications, Series: Lecture Notes in Geoinformation and Cartography, Springer, Berlin (2008) 185-201.

[6] I. Niemeyer, F. Bachmann, A. John, C. Listner, and P. R. Marpu, Object-based change detection and classification, Proc. SPIE Europe Remote Sensing 09, Vol. 7477A, Image and Signal Processing for Remote Sensing, Berlin (2009)

[7] M. Baatz and A. Schäpe, Multiresolution Segmentation: an optimization approach for high quality multi-scale image segmentation, J. Strobl., T. Blaschke, and M. Griesebener (Eds.), Angewandte Geographische Informationsverarbeitung XI. Beiträge zum AGIT-Symposium 1999, Salzburg (2000) 12-23.

[8] Definiens Imaging, Definiens eCognition Developer 8 User Guide, Munich (2009).

[9] C. Listner and I. Niemeyer, Multiresolution segmentation adapted for object-based change detection, Proc. SPIE Europe Remote Sensing 10, Vol. 7477A, Image and Signal Processing for Remote Sensing, Toulouse (2010).

[10] D. R. Musser and A. Saini, The STL Tutorial and Reference Guide: C++ Programming with the Standard Template Library, Addison Wesley Longman Publishing Co., Inc. Redwood City, CA (1995).

[11] GDAL Development Team, GDAL - Geospatial Data Abstraction Library, Version 1.6.0, Open Source, Geospatial Foundation (2010).

5.20. Nuclear Safeguards and Non-proliferation Issues in GMES

I. Niemeyer, C. Listner

Corresponding author: i.niemeyer@fz-juelich.de

Global Monitoring for Environment and Security (GMES)

GMES (Global Monitoring for Environment and Security) is a European Initiative aimed at establishing a European capacity for Earth Observation. [1] GMES is an EU-led initiative. Prototype and initial versions of the GMES services have been partly financed through the 7th Research and Development Framework Programme of the European Union. The European Space Agency is responsible for developments related to the observation infrastructure in the space component (i.e. Sentinel missions), while the European Environment Agency and Member States are in charge of the in situ component.
The users of GMES, in particular Policymakers and public authorities, will be provided with information through services supporting the systematic monitoring and forecasting the Earth's subsystems. Today, GMES services consist of five main services, namely on land monitoring, marine monitoring, atmosphere monitoring, emergency management, and security.
The land, marine and atmosphere monitoring services contribute directly to the monitoring of climate change and to the assessment of mitigation and adaptation policies. The two additional GMES services address emergency response (e.g. floods, fires, technical accidents, humanitarian aid) and security-related aspects (e.g. maritime surveillance, border control, non-proliferation).

GMES Security Service

The GMES services for security applications aim at supporting the related European Union policies in the priority areas of border surveillance, maritime surveillance and support to EU External Action. GMES has a strong potential to support EU External Action through the detection and monitoring of security threats effect (e.g. proliferation of weapons of massive destruction). It can also contribute towards improving crisis prevention, preparedness and response capacities.
The following projects have investigated the security domain over the past years:

- Global Monitoring for Security and Stability (GMOSS)
- Land and Sea Integrated Monitoring for European Security (LIMES)
- GMES Services for Management of Operations, Situation Awareness and Intelligence for regional Crises (G-MOSAIC)

Global Monitoring for Security and Stability (GMOSS)

GMOSS (Global Monitoring for Security and Stability) was a Network of Excellence (NoE) from March 2004 to February 2008 that aimed at integrating Europe’s civil security research [2]. Hence, rather than new developments, existing expertise in using Earth Observation data for civil security in Europe has been gathered and perspectives for future applications have been given. Monitoring of international treaties protecting against the proliferation of weapons of mass destruction was one of four applications. The work package on Treaty

Monitoring[3] cooperated intensively with each other throughout the GMOSS NoE period on the problems of verification of, particularly, two arms control treaties – the 1972 Nuclear Non-proliferation Treaty (NPT) and the 1996 Comprehensive Test Ban Treaty (CTBT). For four years, the group focused on the development and applications of space-based remote sensing techniques to the verification of the NPT and the CTBT. Their achievements have been documented in a number of individual or joint publications. There was also a very active participation in the Iran test case. The test case on the Iran investigated whether automated computer-based satellite imagery analysis could help to verify the Non-Proliferation Treaty (NPT): It was shown in the Iran test case that nuclear safeguards-relevant information can be (semi-) automatically extracted from EO data. (Semi-) automatic algorithms are essential for wide-area monitoring and facilitate the detailed detection and analysis of small-scale features of interest.

Land and Sea Integrated Monitoring for European Security (LIMES)

LIMES (Land and Sea Integrated Monitoring for European Security) continued from December 2007 to May 2010 with the topics of GMOSS, but gave more focus on development of image analysis and GIS technologies [3]. The 'Treaty Monitoring' work package[4] developed an integrated platform supporting the non-proliferation image analyst in in the task of collecting, managing and analysing satellite imagery - often in conjunction with data from other sources - and extracting non-proliferation relevant information. The platform incorporates three independent pillars each serving a particular purpose: a geographic information system, a Wiki system and a document repository. The main benefits of the platform are (i) integrating information from multiple sources and time-frames, including satellite imagery, site models, open source information, reports, etc.; (ii) improved information management using a GIS-based platform and (iii) enhanced methodologies for satellite image analysis. The platform components facilitate the analysis by highlighting changes and anomalies (Fig. 126 & Fig. 127), which are potentially safeguards-relevant and by providing quantitative measurements which are not readily available from the images. It improves the efficiency and effectiveness of the information assessment by providing all-source integration capabilities, which allow to easily access supporting collateral information (e.g. Open Source information) from an image analysis task, and vice versa (Fig. 128).
The platform was demonstrated in two user workshops to a number of interested stakeholders including DG-ENERGY, in charge of the implementation of the EURATOM treaty, and IAEA. The general feedback was that the project addressed important issues for the non-proliferation image analyst, regarding both supporting analysis tools and information integration. Clearly, none of the components can replace the analyst in interpreting the images from a non-proliferation point-of-view. However, they put a range of additional tools at his/her disposal, which can facilitate the analysis by highlighting changes potentially of interest and providing quantitative measurements which are not readily available from the images.

[3] Partner : Forschungszentrum Juelich, STE (DE), Kings College London (UK), TU Bergakademie Freiberg (DE), Technical University of Denmark (DK), Bundesanstalt für Geowissenschaften (DE), JRC Ispra (EC)

[4] Partner: JRC Ispra (EC), EU Satellite Center (EU), TU Bergakademie Freiberg/Forschungszentrum Juelich (DE), Joanneum Research (AT), CEA (FR)

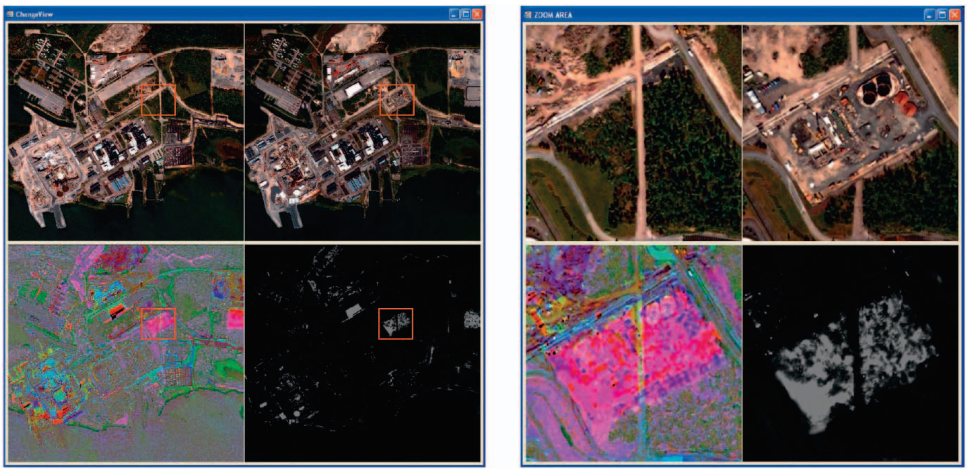

Fig. 126: Snapshot of the change visualisation tool. [4]

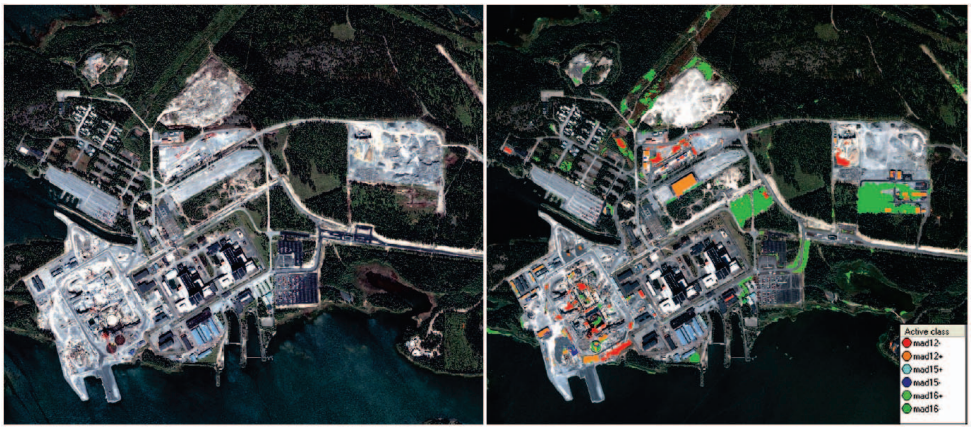

Fig. 127: Results of the object-based change detection for Olkiluoto between June 2005 (left) and July 2006 (right) based on 16 different object features and given by the 16 change components 12, 13 and 16 (right) calculated via multivariate alteration detection (MAD). [4]

GMES services for Management of Operations, Situation Awareness and Intelligence for regional Crises

G-MOSAIC (GMES services for Management of Operations, Situation Awareness and Intelligence for regional Crises) aims at providing pre-operational versions of GMES security services addressing border surveillance and support to EU External Action. Monitoring of treaties for non-proliferation is one of the service chains to be developed. The service developed by the non-proliferation work package[5] addresses the monitoring of nuclear

[5] Partner: INDRA (ES), Telespazio (IT), JRC Ispra (EC), EU Satellite Center (EU), TU Bergakademie Freiberg/ Forschungszentrum Juelich (DE), German Aerospace Center (DE)

facilities and other treaty related infrastructures. Main activities include regular assessment, identification and monitoring of nuclear capabilities and infrastructures, decommissioning sites. Other essential requirements such as weapons delivery systems and related defence infrastructures could also be covered later. The service includes the following service chains: Monitoring of nuclear decommissioning sites (MND) and continuous surveillance of nuclear facilities (SNF).

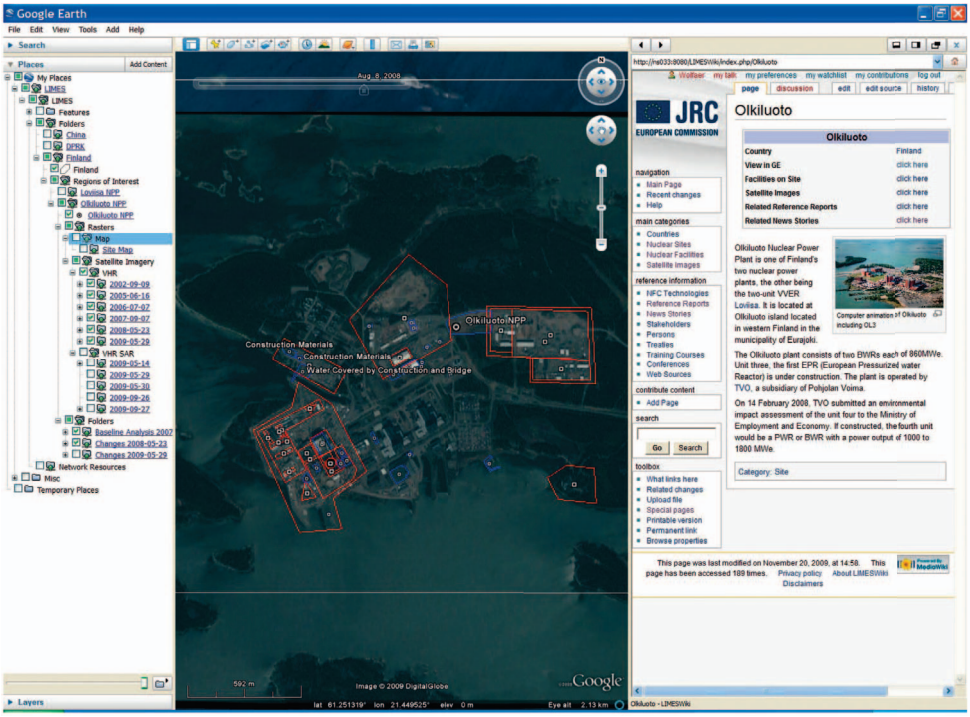

Fig. 128: Snapshot of geo-browser (GoogleEarth). The client application is visualising the spatial and non-spatial information served by the integration platform. [4]

References:

[1] Global Monitoring for Environment and Security (GMES), http://www.gmes.info.

[2] Global Monitoring for Security and Stability (GMOSS), http://gmoss.jrc.it/.

[3] Land and Sea Integrated Monitoring for European Security (LIMES), http://www.fp6-limes.eu/.

[4] J.G.M. Gonlçalves, K.H. Gutjahr, C. Listner, P. Loreaux, P.R. Marpu, I. Niemeyer, A. Patrono, A. Ussorio, E. Wolfart, Integrated Analysis of Satellite Imagery for Treaty Monitoring - The LIMES Experience. ESARDA Bulletin 43 (2009) 40-56.

[5] GMES services for Management of Operations, Situation Awareness and Intelligence for regional Crises (G-MOSAIC).

5.21. Use of TerraSAR-X Imagery for Geological Repositories Monitoring

I. Niemeyer[1], T. Engel[2]

[1] Institute of Energy and Climate Research – (IEK-6), Forschungszentrum Jülich GmbH

[2] Institute of Geotechnical Engineering and Mine Surveying, TU Clausthal

Corresponding author: i.niemeyer@fz-juelich.de

Abstract

The paper aims at investigating the potential of high-resolution SAR data for geological repositories monitoring as to the extraction of digital elevation models, 2D and 3D scene change detection. Using the ONKALO site as example, experiments for radargrammetry and interferometry will be presented and discussed.

Introduction

Olkiluoto Island in western Finland features the only spent nuclear fuel disposal site under construction today. The IAEA has been involved since the beginning of the underground construction in 2004, for instance by accompanying the inspections provided by the national authority STUK, and is currently developing a practical safeguards concept for the geological repository (W0LF) together with EURATOM, STUK and the operator POSIVA. The safeguards approach includes the use of monitoring techniques for observing pre-operational, operational and post-closure phase, and for implementing IAEA safeguards respectively. Among the satellite-based remote sensing techniques, synthetic aperture radar (SAR) imagery show some advantages compared to optical data for monitoring nuclear sites in northern climates. SAR sensors operate under almost all weather conditions and independently of the sunlight, i.e. time of the day. Such technical specifications are required both for continuous and for ad-hoc, timed surveillance tasks. With Cosmo-Skymed, TerraSAR-X and Radarsat-2, high-resolution SAR imagery with a spatial resolution up to 1 m and some technical innovations has recently become available. In practice, however, the operational value of SAR sensors for safeguards issues still has to be approved.

The joint Member State Support Program (MSSP) task entitled 'Use of Satellite Imagery Data for Geological Repositories' was initiated by the need to identify the remote sensing technologies and techniques that will best support the needs of safeguards in monitoring geological repositories. The objective of this joint program was to evaluate the potential effectiveness of various SAR satellite imagery technologies to detect undeclared activities for diverting spent fuel from a geological repository. The Canadian, German and Japanese Support Programs evaluated various approaches to processing SAR data. The paper analyses the performance of the high-resolution TerraSAR-X sensor and its potential for geological repositories monitoring in northern areas. In detail, a case study case on the Onkalo underground laboratory using TerraSAR-X imagery was conducted to investigate the application of interferometric processing and change detection techniques for extracting digital elevation models of site buildings, facilities and surrounding area, and for detecting 3D changes between different acquisition times.

The operational value of using SAR imagery strongly depends on the surface parameters (vegetation cover, topography etc.) of the area to be monitored and on the acquisition

parameters of the SAR system, such as the incidence angle [1,2]. That is why the investigation area proves to be challenging in two different aspects: First, the Olkiluoto Island is mainly covered by coniferous forest; second, the island's surface is rather flat with maximum 18 meters height above sea level. However, as W0LF is expected to get into operation in 2020 as the first geological repository worldwide, possibilities and limits of SAR imagery processing are to be studied for this particular area.

Site-specific Characteristics at Onkalo

In 2004, Finland began underground construction of the Onkalo (Underground Rock Characterisation Facility), planned to be later licensed as a part of the Geological Repository on the Olkiluoto Island adjacent to the Olkiluoto Nuclear Power Plant in western Finland. The Olkiluoto area is flat; the highest point of the Olkiluoto Island is 18 m above present sea level. The access tunnel to the Onkalo underground facility is located at one of the local rocky hills (near the borehole KR8, Fig. 129 left) at the elevation of 9 to 10 meters above the present sea level.

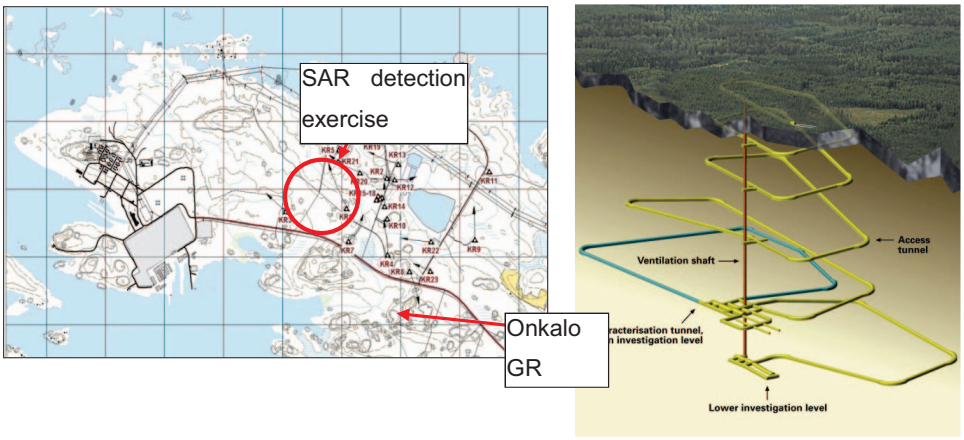

Fig. 129: Left: The location of the entrance to the underground research premises is located near the investigation borehole KR8 (marked with triangle symbols on the right) at the distance of 2 km from the nuclear power plant shown in the grey area on the left. [3]. Right: The underground rock characterisation premises to be excavated at Olkiluoto. The planned access tunnel on the left [4] is excavated during several phases of sub-contracts to the current fourth loop as shown on the right [5].

Investigations using TerraSAR-X imagery

TerraSAR-X, working with the X-band (9.65 Ghz), has been realized as Public Private Partnerships (PPP) between the German Aerospace Agency (DLR) and industry (EADS Astrium).

Depending on the acquisition mode, different swath widths and polarization modes are available. In the highest possible spatial resolution (High Resolution Spotlight Mode), TerraSAR-X offers single polarization (HH or VV) in 1.1 m and dual polarization (HH/VV) in 2.2 m resolution for a scene size of 10 km (cross) by 5 km (along) [6]. Two high-resolution spotlight images, acquired on May 23 and June 3, 2010 with the same parameters, were used for the study.

Tab. 28: Technical parameters of data used in the experiments and possible applications

Dataset	TSX-1a	TSX-1b	TSX-2	TSX-3	TSX-4
Acquisisiton date & time	2008-11-30 5:14 UTC	2008-11-30 5:14 UTC	2008-12-01 04:57 UTC	2009-06-27 5:14 UTC	2009-07-08 5:14 UTC
Orbit	93	93	108	93	93
Imaging mode[1]	HS	HS	HS	HS	HS
Resolution mode[2]	-	SE	SE	-	-
Spatial resolution [m]: **azimuth** **slant range** **ground range**	 1.10 1.18	 2.72 3.27	 1.52 1.80	 1.10 1.18	 1.10 1.18
Incidence angle [°]	22.14	22.14	42.02	22,16	22,16
Direction	Descending	Descending	Descending	Descending	Descending
Polarization mode	HH	HH	HH	HH	HH
Geometric projection[2]	SSC	MGD	MGD	SSC	SSC
Application[3]	InSAR, CCD	RG, nCCD,	RG, nCCD,	InSAR, CCD	InSAR, CCD

[1]) HS: High-resolution spotlight
[2]) SE: Spatially enhanced products
[3]) SSC: Single look slant range complex, MGD: Multi look ground range detected
[3]) RG: Radargrammetry, nCCD: Non-coherent change detection, CCD: coherent change detection, InSAR: Interferometry

QuickBird multispectral image, true colour, 07.09.2007 (Credit: DigitalGlobe)

TerraSAR-X, HH/VV, Stripmap mode, 21.10.2007 (Credit: Infoterra)

Fig. 130: Olkiluoto peninsula (Finland) in 2007, seen by QuickBird (left) and TerraSAR-X (right).

Extraction of a digital surface models from SAR imagery

Based on a TerraSAR-X spotlight stereo pair, acquired on November 31, 2008 with an incidence angle of 22.14° and a spatial resolution of 3.3 m (TSX-1b), and at December 1, 2008 with 42.02° and 1.8 m resolution (TSX-2), a DSM was extracted through radargrammetry [7,8].

The MGD products used in the study were already speckle-filtered. However, in order to investigate whether the speckle noise was sufficiently removed in the MGD processing, an additional filtering using different approaches was applied: Median, Gamma and Lee filtering were applied.
For geometric correction, internal Ground Control Points (GCPs) from the input data were used (as well as from an additional DEM derived from a topographic map (scale 1:25.000).
The best results were achieved when no filtering but additional GCPs were employed (Fig. 131). The values for the surface heights (i.e. including buildings, trees and other objects on the surface) amount around 20 m (green) and increase up to 40 m (yellow) and 60 m respectively for some outliers (red).

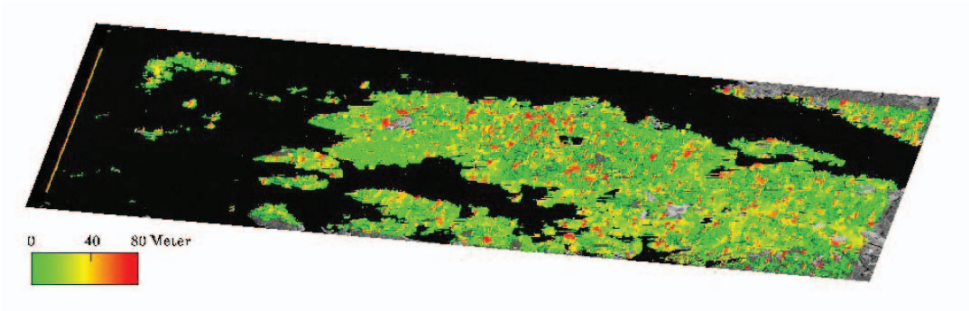

Fig. 131: DSM from Spotlight using external GCPs without filtering.

To assess the accuracy of the DSM, a DSM extracted from an IKONOS stereo pair was used as reference. The difference between the two DSMs indicates that the radargrammetric approach was not able to extract the buildings heights correctly and that the relatively high reactor buildings were not displayed in the SAR-based DSM. For further accuracy assessment, some points of known terrain heights were compared with the calculated surface heights. The height differences correspond approximately with the vegetation heights. The DSM, however, still shows many holes, possibly due to insufficient coherence where no heights could be calculated. The decorrelation from one day to the next is due to the different roughness of the vegetation cover during two acquisition times.

Interferometry

For interferometry [9,10], the interferometric pairs of TSX-1a and TSX3, TSX-3 and TSX-4, acquired on November 30, 2008, June 26, 2009 and July 8, 2009, were used as basis. The interferometric procedure was performed using the SARscape ® software.
Displayed in Fig. 132, the coherence calculated for both pairs was very poor (Tab. 29), in particular in water and vegetation areas. Only built-up areas without changes between the two acquisition times show stable backscatter values.

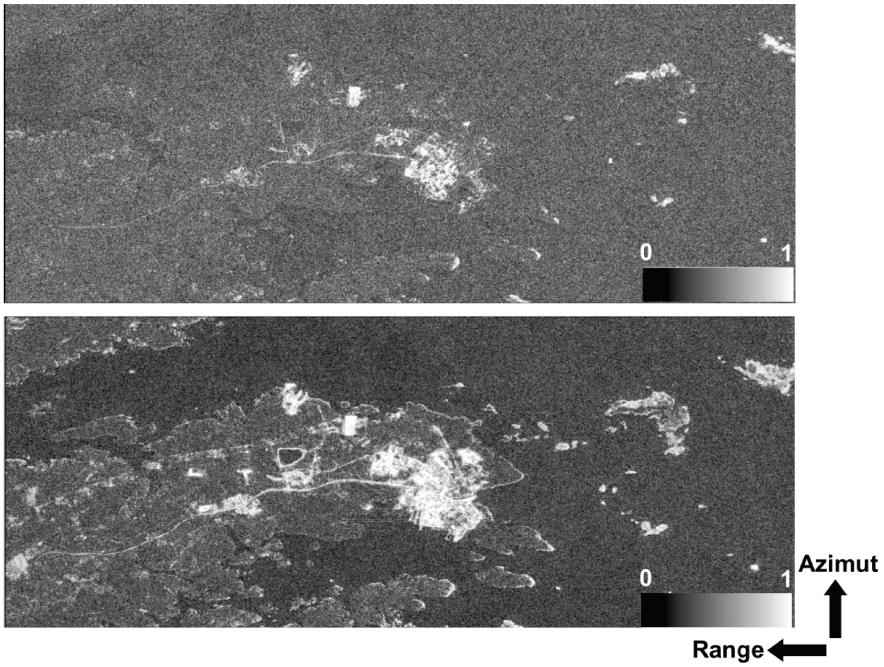

Fig. 132: Coherence of TSX-1a & TSX-3 (top) and TSX-3 & TSX-4 (bottom), Multilooking 3 (azimuth) x 1 (range).

Fig. 133 shows the interferogram for TSX-1a & TSX-3. Due to the low coherence a lot of noise is included. However, some topographical structures can be identified such as the reactor buildings of the nearby power plant (1), and waste dumps due to the construction activities for the third power reactor (2,3). The main construction area (4) is completely decorrelated.

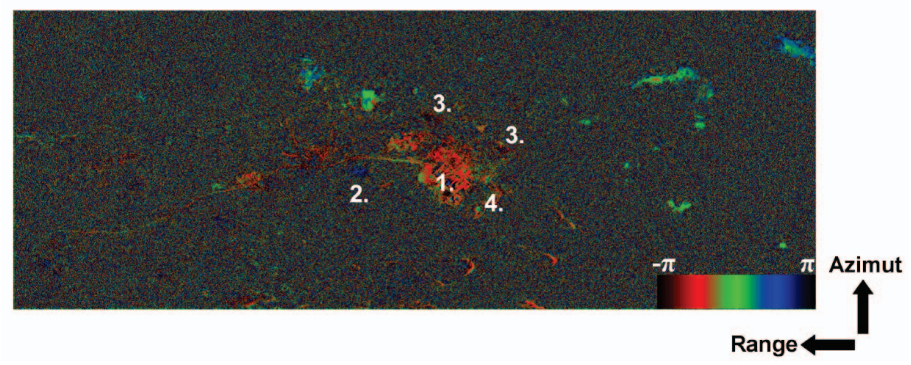

Fig. 133: Interferogram of Coherence of TSX-1a & TSX-3, Multilooking 3 (azimuth) x 1 (range). Time difference = 209 days, baseline = 112 m, 2π height accuracy = 29 m.

Fig. 134 contains the result for the ONKALO area. The interferogram (Fig. 134d) hardly shows any interference pattern due to the low coherence values (Fig. 134b) of the predominant vegetation cover. Also the height accuracy of the absolute phases is very inaccurate. Its range of values of 8π corresponds to a height difference of 100 m, which is very unlikely in this region.

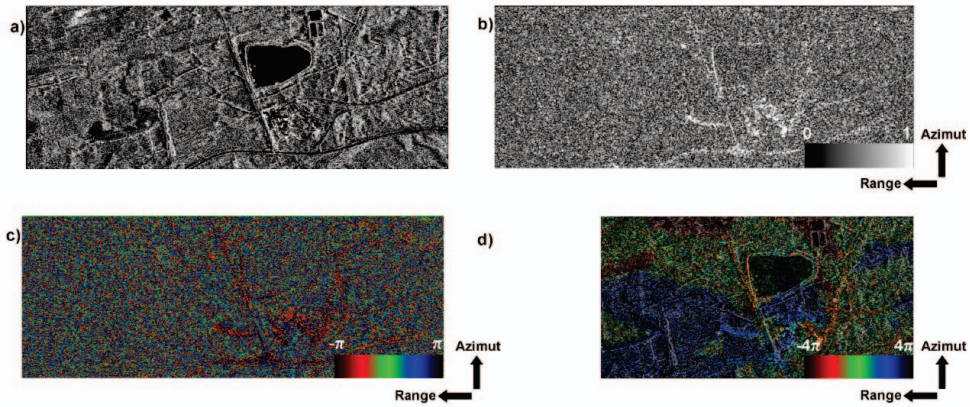

Fig. 134: Results for TSX-1a & TSX-3, Multilooking 3 (azimut) x 1 (range): a) amplitude, b) coherence, c) interferogram, d) absolute phase (overlayed by amplitude).

Differential interferometry was performed based on TSX-3 & TSX-4. Fig. 135 displays the results after removing the topographic phase. The differential interferogramm shows similar fringes compared to the interferogram in Fig. 133. The location of four boreholes was indicated as some interference patterns exist nearby.

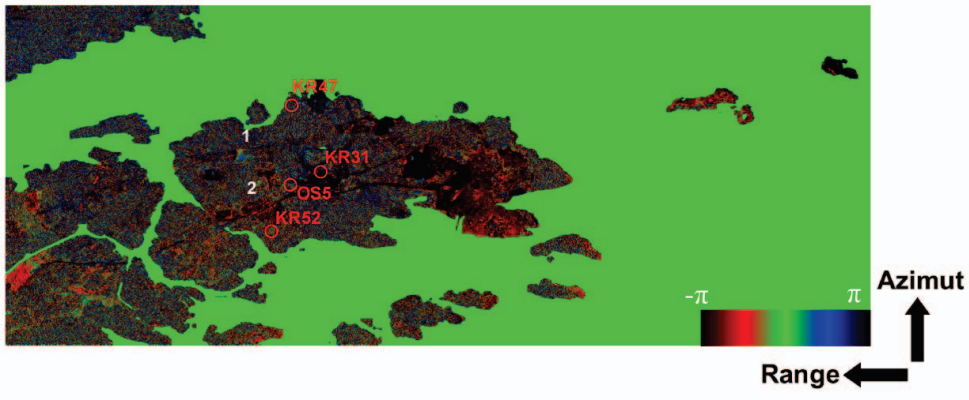

Fig. 135: Differential interferogram for TSX-3 & TSX-4, Multilooking 3 (azimut) x 1 (range).

Tab. 29: Coherence values for TSX-3 & TSX-4, total scene and extract shown in Fig. 132.

Coherence	min	max	mean	stdev
Scene	0.000	0.991	0.325	0.156
Extract (Fig. 132, top)	0.000	0.947	0.301	0.143

Conclusions and recommendations

The GerSP aimed to demonstrate the potential of the new generation, high-resolution TerraSAR-X imagery using two different SAR imagery analysis techniques for monitoring geological repositories in northern areas. The case of the Onkalo site was used to investigate the potential of radargrammetry, and InSAR [11,12].

The DSM extracted through radargrammetry did not yet provide satisfying results, but here might be some methodological options for improvements. In comparison to radargrammetry, InSAR was expected to provide DEMs with a much higher spatial resolution and precision. However, also the results from interferometry were disappointing so far.

In areas with low coherence values due to vegetation cover, surface changes or inappropriate acquisition geometries (temporal and geometric de-correlation), analysis techniques using the coherence between SAR scenes show only limited results or even fail. This applies to all coherence-based techniques for 3D information extraction and 2D/3D change detection, such as coherent change detection and interferometry. Probably methods such as Permanent Scatterer Interferometry (PSI) might provide improved results and should be evaluated for geological repositories monitoring.

Besides methodological improvements, technical innovations can enhance the application of SAR imagery analysis in terms of safeguards purposes, for instance the availability of single-pass or dual-pass interferometry without temporal de-correlation. In this regard, the TanDEM-X (TerraSAR-*X* add-on for Digital Elevation Measurement) mission, in June 2010, has promises. This mission includes a second, almost identical spacecraft that will fly together with TerraSAR-X in a closely controlled formation with typical altitude distances between 250 m and 500 m. This orbital formation will permit to minimise the temporal de-correlation between two SAR images over one area. Thus, the TanDEM-X is expected to provide more detailed DEMs and more accurate geometric information on surface deformations. TanDEM-X data should therefore be evaluated for geological repositories monitoring.

As for vegetated surfaces, the application of L-band data being able to penetrate the above ground biomass could be another solution. Today, only the PALSAR sensor onboard the ALOS satellite provides L-band data from space at 10 m spatial resolution. A comparison between X-, C- and L-band as to their suitability for geological repositories monitoring could give a deeper insight.

Acknowledgments

Financial support for this study was provided by the Ministry of Economy and Technology (BMWi) through the IAEA Safeguards Support Programme.

References

[1] A. Hein, Processing of SAR Data. Fundamentals, Signal Processing, Interferometry, Springer, Berlin Heidelberg (2004).

[2] H. Maître (ed.), Processing of Synthetic Aperture Radar Images; Digital Signal and Image Processing Series, ISTE/Wiley, London Hoboken (2008)
[3] Posiva Oy, Baseline conditions at Olkiluoto; Posiva Working Report 2003-02 (2003).
[4] Posiva Oy, Onkalo Underground Rock Characterisation Facility - Main Drawings Stage, Posiva Working Report 2003-26, (2003).
[5] Posiva Oy, ONKALO – Main Drawings in 2007, Posiva Working Report 2008-01 (2008).
[6] Cluster Applied Remote Sensing, TerraSAR-X Ground Segment, Basic Product Specification Document, German Aerospace Center (2008).
[7] F.W. Leberl, Radargrammetric Image Processing, Artech House, Norwood MA USA (1990).
[8] J.K. Kyaruzi, Quality assessment of DEM from radargrammetry data: quality assessment from the user perspective, Master Thesis ITC Enschede (2005).
[9] R. Hanssen, Radar Interferometry; Remote Sensing and Digital Image Processing Series, Vol. 2, Kluwer Academic Publishers, Dordrecht (2001).
[10] V.B.H. Ketelaar, Satellite Radar Interferometry. Subsidence Monitoring Techniques; Remote Sensing and Digital Image Processing Series, Vol 14, Springer, Berlin Heidelberg (2009).
[11] T. Engel, Anwendung der Radarinterferometrie bei der Safeguardsüberwachung geologischer Endlager für hochradioaktive Abfälle - am Beispiel des Standortes Olkiluoto, Finnland,. Unpublished Diploma Thesis, TU Bergakademie Freiberg (2010).
[12] I. Niemeyer, T. Engel, High-resolution SAR Satellite Imagery Analysis for Nuclear Safeguards Applications, Proc 31st Symposium on Safeguards and Nuclear Material Management, Vilnius (2009).

5.22. The NPT Review Conference 2010: Perspectives for International Safeguards

I. Niemeyer, B. Richter, G. Stein

Corresponding author: i.niemeyer@fz-juelich.de

Abstract

In Article VIII of the Treaty on the Non-Proliferation of Nuclear Weapons (NPT) a mechanism is embedded to review, at intervals of 5 years, the implementation of the Treaty. The 8th NPT Review Conference was held in May 2010 at the United Nations Headquarters in New York. As the majority of the Review Conferences, also the 2010 Conference ended with the adoption of a final document. The paper analyses and assesses the results of the NPT Review Conference with regard to international safeguards and gives perspectives for the further implementation of safeguards by the International Atomic Energy Agency.

Introduction

The 8th Review Conference of the Parties to the Treaty on the Non-Proliferation of Nuclear Weapons (NPT) ended with the adoption of the final document on May 28, 2010 [1]. This very fact could be called yet a success given the ongoing controversies between Nuclear Weapon States (NWS) and Non-Nuclear Weapon States (NNWS), among them in particular the non-aligned countries, the hot spot Middle East, the case Iran and other national issues.
The conference succeeded also compared to the previous conference of 2005, which failed to agree on any kind of decisions or recommendations how to further strengthen the NPT regime. In fact, only the agreements of 2000, the so-called “13 practical steps” [2] towards disarmament were confirmed, but without being implemented subsequently.
The initial status looked much better than in 2005, since U.S. President Obama announced his vision of a world free of nuclear weapons in 2009 [3] and concluded the new Strategic Arms Reduction Treaty (new START) with Russia [4]. Moreover, the U.S. clarified the security assurances not to use nuclear weapons against NNWS that are in full compliance with their NPT obligations and reduced the role of nuclear weapons in the Nuclear Posture Review [5]. Also the Nuclear Security Summit [6], hosted in April 2010 by the U.S., was expected to impact the outcome of the conference positively.
However, the final document is just a document. The actual state of the NPT regime in 2010 becomes more apparent by looking in detail into the review process, studying the numerous working papers, Parties’ statements and contributions to the discussions. Our paper aims at presenting a brief overview on these aspects with special emphasis on international safeguards, before discussing the final document that followed. Finally, we show some perspectives for the further implementation of safeguards performed by the International Atomic Energy Agency (IAEA).

The Review Process

172 of the 189 State Parties were present in order to evaluate the implementation of the NPT in the past five years and to agree on actions for further strengthening the non-proliferation regime. The conference started its first week on May 3 traditionally with the Parties’ Statements in the General Debate, followed by working meetings of the three Main Committees and their Subsidiary Bodies in the second and third week. It was decided by the

Preparatory Committee to allocate the following items to the Committees: Main Committee I reviewed the implementation of the Treaty with respect to disarmament and security assurances, the corresponding Subsidiary Body I focused on a disarmament action plan. Main Committee II dealt with safeguards, export control and Nuclear-Weapon Free Zones (NWFZ), its Subsidiary Body II concentrated on regional issues, such as the NWFZ Middle East and the 1995 Middle East Resolution. Main Committee III covered the peaceful use of nuclear energy, while Subsidiary Body III was responsible for other provisions of the Treaty, in particular the right to withdraw (Article X) and the review process itself. After this working phase, the fourth week was assigned to the preparation of the final document by the Drafting Committee and its adoption at the very last day.

The Review Statements & Discussions

General Debate

The General Debate was opened by Ban Ki-Moon, the Secretary General of the United Nations. He urged all NWS to realize the disarmament commitments and encouraged all Parties to strengthen the NPT regime, inter alia by ratifying the Additional Protocol (AP)[6], and to continue the efforts towards a NWFZ Middle East [8]. He also called on Iran "to comply fully with Security Council resolutions and (…) cooperate fully with the IAEA"[7]. To his opinion, "the onus is on Iran to clarify the doubts and concerns about its programme"[8]. He also encouraged the Democratic People's Republic of Korea (DPRK) "to return to the Six-Party Talks as soon as possible, without preconditions"[9].

As the second speaker, Yukiya Amano, Director General of the IAEA, requested all States to conclude and implement Comprehensive Safeguards Agreements (CSAs)[10] and to bring the AP into force [8]. The AP, he said, "is of vital importance for the Agency to be able to provide credible assurance not only that *declared* nuclear material is not being diverted from peaceful uses, but also that there are no *undeclared* nuclear material and activities in a State."[11] He mentioned the Agency's work on resolving important safeguards issues in three states: First DPRK, as it has refused safeguards implementation and with it safeguards conclusions since 2002, second Iran, where the IAEA "remains unable to confirm that all nuclear material is in peaceful activities"[12] and finally Syria, since it has not acted cooperatively on solving the Israeli attacks on alleged nuclear sites in their country.

The Debate was continued by 125 statements of States and Groups [10]. A detailed overview would go far beyond the scope of this paper; therefore we will try to reflect the opinions based on some selective statements.

---

[6] In May 1997, the IAEA Board of Governors approved the Model Additional Protocol to Safeguards Agreements (reproduced in INFCIRC/540(Corr.)). It aims at equiping the system with better tools to provide assurance about both declared and possible undeclared activities. Under the Model Additional Protocol, States are required to provide the Agency with an expanded declaration that contains information covering all aspects of their nuclear and nuclear fuel cycle activities. The States must also grant the Agency broader rights of access and enable it to use the most advanced technologies. [7], p. 6

[7] [8], p. 5

[8] [8], p. 6

[9] [8], p. 6

[10] The NPT makes it mandatory for all non-nuclear-weapon States (NNWS) parties to conclude comprehensive safeguards agreements with the IAEA, and thus allow for the application of safeguards to all of their source or special fissionable material. [7], p. 5

[11] [9], p. 4

[12] [9], p. 3

Iran, represented by President Ahmadinejad provoked in the beginning by accusing the NWS [10], in particular the USA, to cause insecurity and Israel, named the "Zionist regime"[13], to threaten the Middle East region by possessing nuclear weapons. Moreover, he blamed the US intelligence agencies and Israel to support "certain major terrorist networks"[14] and the USA that they have "never respected any of its commitments"[15] as to disarmament. However, his talk created a scandal only for short time, involving some headlines in the next day's newspapers, but was of little importance for the conference progress.

The group of the five established NWS (the so-called P5) declared their willingness and responsibility to undertake concrete and credible steps towards nuclear disarmament [12]. As the P5 called for the universality of the Comprehensive Test Ban Treaty (CTBT), also China and the USA agreed to sign and ratify the Treaty.

The 110 Non-Aligned Movement (NAM) State Parties to the NPT called as expected on a balance between NWS and NNWS and criticized the NWS for retaining and modernizing their nuclear arsenals [13]. They stated that "(t)he realization of the objective of a world free from nuclear weapons is the NAM State Parties' highest priority."[16] In this regard, the NAM demanded that a Nuclear Weapons Convention (NWC) should become an integral part of the disarmament plan to be adopted by the Conference. They highlighted the importance of the NWFZs in general, supported the Middle East NWFZ and recalled Israel to accede the NPT. Moreover, they underlined the "inalienable right of NPT State Parties to research, produce, and use nuclear technology for peaceful purposes without discrimination"[17] and the right to withdrawal according to Article X.

The European Union (EU), represented by their High Representative for Foreign Affairs and Security Policy, Catherine Ashton, called on making the conclusion of a CSA together with the AP the verification standard. She also demanded to bring the CTBT info force rapidly and to start the negotiations on the FMCT. [14]

b) Main Committee I & Subsidiary Body I

The discussions within Main Committee I and Subsidiary Body I on disarmament and security assurances were mainly, but not exclusively, characterized by the controversies between NWS and NAM, or individual States of these groups. The list of contentious issues implied [15]:

- Security doctrine, nuclear sharing (NATO States yes, NAM no);
- NWC, timeline for disarmament (NAM yes; NWS no, except for China);
- moratorium on the production of fissile materials for nuclear weapons, shut-down of sites for the production of weapons-grade fissile material, shut-down of nuclear test sites (NNWS and France yes, Russia and USA against the shut-down of test sites, China no to all);
- transparency of NWS (NNWS yes, NWS no with different nuances);
- reaction on non-compliance by Security Council (NWS yes, NAM no);
- constraining the development and qualitative improvement of nuclear weapons and ending the development of advanced new types of nuclear weapons (NNWS yes, NWS no);

[13] [11], p. 3
[14] [11], p. 6
[15] [11], p. 5
[16] [13], p. 1
[17] [13], p. 4

- unconditional security assurances for all NWS Parties (NAM and China yes; NWS no, expect for China);
- the universality of the Treaty including the naming of Israel together with India and Pakistan (NAM yes, USA no).

Only two matters were beyond dispute: the CTBT coming into force soon and the early start of the FMCT negotiations.

c) Main Committee II & Subsidiary Body II

In Main Committee II and Subsidiary Body II on safeguards, export control and NWFZ, the discussions focused on the following issues:

- Acceptance of CSA plus AP as verification standard (Western Parties yes, NAM no);
- effective export controls (Western Parties yes, NAM no);
- appreciation of the Zangger Committee and the Nuclear Suppliers Group (NSG) (Western Parties yes, NAM no);
- explicit nomination of Iran and DPRK as non-compliant States (Western Parties yes; NAM no on Iran);
- civil nuclear exports under the condition, that the receiving country accepts CSAs (NAM yes, USA no);
- practical steps for the preparation of a (N)WFZ Middle East (NAM yes, USA no).

c) Main Committee III & Subsidiary Body III

Main Committee III and the Subsidiary Body III covering the peaceful use of nuclear energy and other provisions of the Treaty mainly discussed two matters:

- Multilateral Nuclear Fuel Supply Guarantees and Spent Fuel Management (Western Parties and Russia yes, NAM no);
- increased sanctions and actions in case of Treaty withdrawal (Western Parties yes, NAM no);
- reform of the review process, suggested by Canada (NNWS no).

The Final Document

The final document [1] contains the review of the operation of the Treaty, reflected for the implementation of each Article, and conclusions and recommendations for follow-up actions in nuclear disarmament, non-proliferation, peaceful uses of nuclear energy, and as a fourth part, actions on the Middle East. The placement of this issue on a level with the three pillars of the Treaty reflects the vital importance the conference conceded to the implementation of the 1995 Resolution on the Middle East, the establishment of a NWFZ Middle East and the universality of the Treaty. The conference did not come to a consensus on the review part, which was thus characterized in a footnote as the president's view, but the conclusions and recommendations were fully agreed.

The final document names three of the usual suspects, India and Pakistan[18], DPRK[19], and also Israel[20]. With a strong support by the NAM states, the Iranian Delegation was successful in not being explicitly named in the final document. However, this result can be put into perspective by the fact that the UN Security Council (the five permanent member States and Germany) agreed on a draft resolution on Iran at their May 18 meeting, demanding that Iran

[18] [1], p. 16, item 107 & p. 18, item 114
[19] [1], p. 16, item 108 & p. 31, Other regional issues
[20] [1], p. 18, item 114 & p. 29, item 5

halt its uranium enrichment program and adheres to all International Atomic Energy Agency demands, including adoption of the AP [16]. Due to the draft resolution, also the Brazil-Turkey-Iran deal announced one day before remained without effect. On a trilateral May 17 meeting, Iran agreed to send 1200kg LEU to Turkey in exchange for a total of 120 kilograms of 20 percent enriched uranium [17].
The discussion of the outcome of the four areas mentioned above would again exceed the scope of the paper. Rather, we will focus on the safeguards aspects now.

Perspectives for the Further Implementation of International Safeguards

The conference reaffirmed in its review part that the IAEA is the competent authority responsible for verifying[21] and assuring compliance with their agreement and recognized that IAEA safeguards are a fundamental component of the nuclear non-proliferation regime[22]. This statement strengthened very much the future role of the IAEA and its safeguards activities in upcoming disarmament initiatives. On the other hand, the conference recalled that CSAs are a sufficient precondition for new supply arrangements on the transfer of material and equipment.[23] It was a very unfortunate result that the conference could not support CSAs and APs as the universal export standard and as the safeguards standard in principle.
In this context and in some way also as a contradiction, the conference reaffirmed that the implementation of CSAs should be designed to provide for verification by the IAEA for correctness and completeness of states' declarations, so that there is credible assurance of the non-diversion of nuclear material from declared activities and the absence of undeclared nuclear material and activities[24]. But later, the conference recognized that CSAs provide only a limited level of assurance regarding the absence of undeclared nuclear material and activities. Nevertheless, the conference noted that it is the sovereign decision of any state to conclude an AP[25], i.e. the AP is still a voluntary issue. This embarrassing result may be seen as diplomatic consensus compromise but could also base on the lack of information by many delegations on the structure of the AP. Unfortunately, the IAEA secretariat was not able to explain the AP sufficiently during the conference.
The conference was clearer and more straightforward in the assessment of the State-level approach believing that the development of the State-level approach for safeguards implementation and evaluation should have high importance. In connection with the implementation of State-level integrated safeguards approaches, the conference expected that this development should result in more comprehensive, flexible and effective safeguards.[26]
In the action part the conference called upon all states to assure that the IAEA has all political, technical and financial support to effectively meet its responsibilities to perform safeguards.[27] Through cooperation between member states and the IAEA the conference encouraged to further develop a robust, flexible, adaptive and cost-effective international technology base for advanced safeguards.[28] Regular assessment and evaluation of

[21] [1], p. 3, item 9
[22] [1], p. 3, item 11
[23] [1], p. 4, item 12
[24] [1], p. 4, item 13
[25] [1], p. 4, item 17
[26] [1], p. 5, item 20
[27] [1], p. 26, Action33
[28] [1], p. 26, Action 34

safeguards was also requested. Decisions adopted by the IAEA policy bodies aimed at further strengthening the effectiveness and improving the efficiency should be supported and implemented.[29]

In connection with fissile material the conference reaffirmed the urgent necessity for a FMCT which should be non-discriminatory, multilateral and internationally and effectively verifiable.[30] The NWS were encouraged to commit to declare as appropriate to the IAEA all fissile material no longer required for military purposes under IAEA verification.[31] The development of appropriate legally binding verification arrangements within the context of the IAEA should also be encouraged to ensure the irreversible removal of fissile material as no longer required for military purposes.[32]

The conference generally asked for wider application of safeguards to peaceful nuclear activities in NWS. Finally the conference expected that CSAs and APs should be universally applied once the complete elimination of nuclear weapons has been achieved.[33]

The final action plan of the conference assigned a strong role to the IAEA safeguards system in the disarmament process and the FMCT issue as well as in connection with efforts to reach Global Zero (i.e., to abolish all nuclear weapons). With this final goal the conference also accepted CSAs and AP as the universal standard for the peaceful use of nuclear energy in all states.

Conclusions

What were the main results and messages when considering not only the legal language but reading more between the lines and taking into account the diversity and complexity of the negotiations?

In general it can be said that the outcome of the conference was a success for the future introduction and use of peaceful nuclear energy. Only two delegations argued against the peaceful use of nuclear energy and noted concerns about environmental and health risks. A great number of delegations from the developing world expressed interest in implementing nuclear energy. In this context it is notable that the conference asked for full use of the nuclear fuel cycle including also HEU. The interest in nuclear energy was further reflected in the discussions of Article IV where strong safety and security standards were requested by the conference. Surprisingly, the discussion on Multilateral Nuclear Approaches (MNAs) attracted only little interest.

In the safeguards area the non-acceptance of the AP as universal standard was a step backward which can be solved in the future process of disarmament. Also, the weak withdrawal paragraph was not satisfactory. A very interesting and detailed discussion took place on the State-level approach which can be interpreted as the future standard for adaptable and flexible safeguards.

The IAEA together with their safeguards system was the winner, as the Agency is expected to play a leading role in the disarmament process and its verification.

---

[29] [1], p. 26, Action 32
[30] [1], p. 23, E.i.
[31] [1], p. 23, Action16
[32] [1], p. 24, Action 17
[33] [1], p. 25, Action 30

Acknowledgements

Financial support for this study was provided by the Ministry of Economy and Technology (BMWi) through the IAEA Safeguards Support Programme. I. Niemeyer and G. Stein attended the New York Review Conference from May 12 to 19, 2010 as Members of the German Delegation.

References[34]

[1] NPT/CONF.2010/50 (Vol. I), 2010 Review Conference of the Parties to the Treaty on the Non-Proliferation of Nuclear Weapons, Final Document, Volume I, Part I and Part II, New York, (2010) http://www.un.org/ga/search/view_doc.asp?symbol=NPT/CONF.2010/50%20%28VOL.I%29

[2] NPT/CONF.2000/28 (Vol. I), 2000 Review Conference of the Parties to the Treaty on the Non-Proliferation of Nuclear Weapons, Final Document, Volume I, Part I and Part II, New York, (2000) http://www.reachingcriticalwill.org/legal/npt/2000FD.pdf

[3] The White House, Remarks by President Obama, Prague (July 5, 2009) http://www.whitehouse.gov /the_press_office/ Remarks-By-President -Barack-Obama-In-Prague-As-Delivered/

[4] U.S. Department of State, New Strategic Arms Reduction Treaty (New Start) (2010) http://www.state.gov/t/vci/trty/126118.htm

[5] U.S. Department of Defense, Nuclear Posture Review (2010) http://www.defense.gov/npr/

[6] U.S. Department of State, Nuclear Security Summit (2010) http://fpc.state.gov/c35775.htm

[7] International Atomic Energy Agency, Non-Proliferation of Nuclear Weapons & Nuclear Security, IAEA Safeguards Agreements and Additional Protocols, Vienna (2005) http://www.iaea.org/Publications/Booklets/nuke.pdf

[8] UN Secretary General Ban-Ki Moon, Address to the 2010 Review Conference of the States Parties to the Treaty on the Non-Proliferation of Nuclear Weapons, United Nations, New York (May 3, 2010) http://www.reachingcriticalwill.org/legal/npt/revcon2010/statements/3May_UNSG.pdf

[9] IAEA Director General Yukiya Amano, Statement to the 2010 Review Conference of the States Parties to the Treaty on the Non-Proliferation of Nuclear Weapons (NPT), United Nations, New York (May 3, 2010) http://www.un.org/en/conf/npt/2010/statements/pdf/head_iaea_en.pdf

[10] United Nations, Conference statements and NGO presentations (2010) http://www.un.org/en/conf/npt/2010/statements/statements.shtml

[11] Statement by His Excellency Dr. Mahmoud Ahmadinejad, President of the Islamic Republic of Iran before the 2010 Review Conference of the States Parties to the Treaty on the Non-Proliferation of Nuclear Weapons (NPT), United Nations, New York (May 3, 2010) http://www.un.org/en/conf/npt/2010/statements/pdf/iran_en.pdf

[12] Statement by the People's Republic of China, France, the Russian Federation, the United Kingdom of Great Britain and Northern Ireland, and the United States of America to the 2010 Non-Proliferation Treaty Review Conference, United Nations, New York (May 5, 2010) http://www.un.org/en/conf/npt/2010/statements/pdf/russia5_en.pdf

[13] Statement by H.E. Dr. R. M. Marty M. Natalegawa, Minister for Foreign Affairs of the Republic of Indonesia on behalf of the NAM Stets Party to the Non-Proliferation of nuclear weapons Treaty (NPT) before The 2010 Review Conference of the Parties to the Non-Proliferation of nuclear weapons Treaty (May 3, 2010) http://www.un.org/en/conf/npt/2010/statements/pdf/nam_en.pdf

[14] Statement on behalf of the European Union by H.E. Ashton, High Representative of the European Union for Foreign Affairs and Security Policy at the General Debate of the 2010 Review Conference of the States Parties to the Treaty on the Non-Proliferation of Nuclear Weapons (NPT), United Nations, New York (May 3, 2010) http://www.un.org/en/conf/npt/2010/statements/pdf/eu_en.pdf

[15] H. Müller, Der nukleare Nichtverbreitungsvertrag nach der Überprüfung, HSFK-Report Nr. 3/2010 (2010) http://www.hsfk.de/fileadmin/downloads/report0310.pdf

[34] Internet links valid on July 11, 2010

[16] United Nations Security Council, Iran Resolution Elements (May 19,2010)
http://www.isisnucleariran.org/assets/pdf/UNSC_Iran_resolution_19May2010.pdf
[17] Press TV, Iran, Brazil, Turkey sign nuclear declaration (May 17,2010)
http://www.presstv.ir/detail.aspx?id=126735&sectionid=351020104

5.23. 2009-2010 annual report of PKS-WAA

Y. Aksyutina, E. Harren, F. Kreutz, S. Schneider, H. Tietze-Jaensch, M. Weidenfeld

Corresponding author: h.tietze@fz-juelich.de

The PKS-WAA team thoroughly evaluates the scientific and technical means of the radioactive waste conditioning and residue production processes and methods (so-called production process approval). The vitrification and waste conditioning plants are inspected at least twice a year to assure their performance to comply with the approved process specifications.

At the Sellafield site, UK, the process approval comprises the vitrification plant and, by now, the residue export facility for uploading CASTOR flasks for their transport to Germany. In La Hague, France, the vitrification of the high-level waste (HLW) has been completed while its transport back to Germany is still in progress. In addition complementary waste streams are subject of on-going process approval, e.g. the nuclear measurement station P2 of the metallic waste compaction plant (ACC) or the CSD-B waste stream of vitrified medium level effluents. PKS assess and evaluates the productions processes and reports its recommendations directly to BfS who is to decide and eventually grant their production approval.

The Karlsruhe vitrification plant VEK has become fully operational in Oct. 2009. The whole VEK campaign lasted until late 2010 and has produced the total of 140 high-level vitrified waste containers loaded into five CASTOR flasks, ready for transport to the interim storage facility ZLN near Greifswald. PKS has been inspecting the whole production campaign, had audited the responsible institutions and persons for production and quality assurance. Hitherto, PKS had evaluated all quality relevant production modifications and findings.

High-level waste nuclear inventory declarations of waste compounds from all the facilities conditioning German HLW have been checked and verified prior to loading and transport. All the accompanying product quality documentation has been checked and certified to comply with the acceptable product properties and process specifications to be viable for the German repository relevant regulatory requirements.

Dedicated R&D is conducted on numerical Monte Carlo methods and simulation programmes to help correctly interpreting the gamma- and neutron emission from highly compacted metallic waste residues. For instance, the effect of a varying concentration / activity and geometrical position of key nuclides in a heterogeneous material embedding are being addressed. The goal is to develop easy-to-use proof tools for examination and evaluation of disposal relevant nuclear properties of heterogeneous radioactive metallic waste compounds.

Individual experts of PKS-WAA participate in national and international advisory councils and consulting expert groups.

5.24. Development and Application of a Beowulf Cluster for Nuclear Simulation

S. Schneider, H. Tietze-Jaensch

Corresponding author: s.schneider@fz-juelich.de

Abstract

The computational power needed by most simulation tools for nuclear applications exceed the capabilities of desktop systems or small workstations. A large gap exists between the usage of workstations and the application of high performance computing (HPC). To close this gap and help the scientists to complete their resource demanding calculations in an adequate short time we developed and implemented a computational system designed with standard hardware for office use. In this paper we focus on the architectural issues and demonstrate the application to calculations for different aspects in nuclear science and technology.

Introduction

The name Beowulf cluster was first introduced by Thomas Sterling and Donald Becker in 1994. They developed at the NASA Goddard Space Flight Centre a network of workstations that could be used like a single computer [1]. During this time high performance computing was mainly limited only to a few research centres which could afford the dedicated super-computers like the NEC SX-4 [2]. These machines were built as massive parallel vector super-computers. Up to 64 CPUs, or even more, shared the same main memory. Therefore the name of this type of architecture was called shared-memory. Sterling and Becker thought of a different way using standard workstation for resource demanding calculations. The main idea of a Beowulf cluster is the usage of a network connecting all workstations for distributing the workload ideally uniformly between the nodes. Since each computer has its own memory space and a CPU from a workstation could not directly access the memory of a different computer. This cluster architecture was called distributed memory. In Fig. 136 the difference between these two architectures are shown.

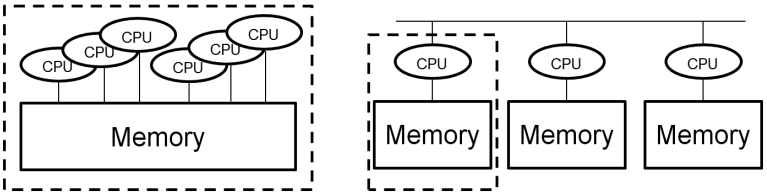

Fig. 136: (left) Shared-memory node (right) Distributed-memory system. The dashed lines represent one computer node.

Another term for Beowulf network-of-workstations is cluster computing. During the last two decades the number of cluster-based super-computers listed in the TOP 500 list increased constantly [3]. The TOP 500 list contains the 500 most powerful super-computers worldwide. In the TOP 500 from November 2010 the Jülich Center for Supercomputing was listed with two cluster-based systems on rank nine and 23.

For the application of simulation tools for nuclear science and engineering the HPC is a vital solution to minimize the computational time needed for the simulation. Unfortunately not all programs are capable to gain advantage of these highly parallel systems. Some of those programs base on code frameworks written over twenty years ago. So the code must be reengineered to run efficiently on these architectures. The main idea for the development of our cluster system was to use the cluster as a stepping stone between the workstation and the large scale HPC domain. Fig. 137 shows the application range of a Beowulf computational cluster.

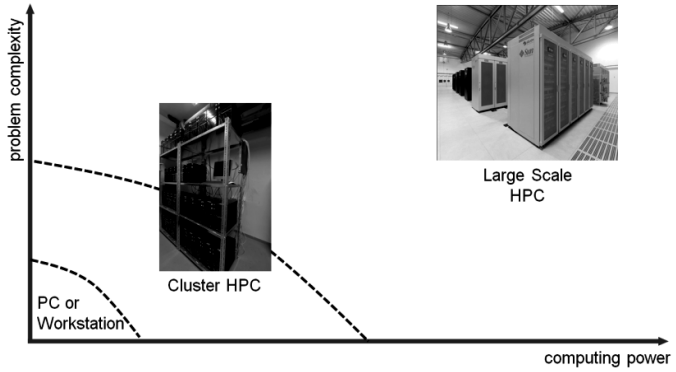

Fig. 137: The Cluster HPC is used to close the gap between the PC or workstation and the large scale HPC systems.

Logical Layers of the Compute Cluster

The cluster is divided in four different logical layers. Each layer depends on the functionality of the underlying layers. In the following sections explains the five different layers of the cluster. Fig. 138 shows the layer concept.

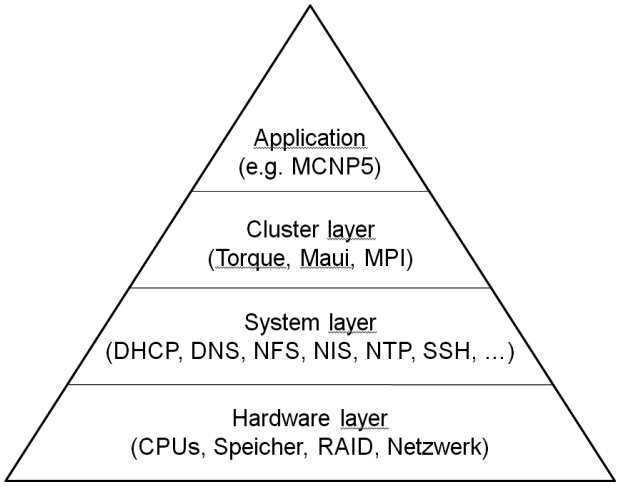

Fig. 138: The Cluster HPC is used to close the gap between the PC or workstation and the large scale HPC systems.

Hardware layer

The hardware layer is the most fundamental layer of the cluster. According to the Beowulf concept the cluster system at the IEK-6 was designed using standard consumer hardware for the compute nodes. Additional a second demand arises because the nodes should also be used as replacements for older office computers. Each compute node consists of a AMD Phenom II CPU with six cores per processor. The main memory of twelve GB RAM was chosen to obtain two GB memory useable per CPU core. Since most of the programs and data libraries are stored on the main node, the hard-drive of the compute nodes is limited to 250 GB. The main node consists of two Intel quad-core CPUs and 32 GB RAM. The system partition is installed on a mirrored hard drive subsystem to increase the fault tolerance in case of a hard drive failure. The programs, user home directories and data libraries remain on a RAID-5 subsystem. The interconnection between all the nodes is made of a gigabit Ethernet connection. Only the main node is connected with two bonded Ethernet ports to the network to increase the total bandwidth to the system. Additionally the main node, or also called head node, is protected with an uninterruptable power supply (UPS) to prevent an uncoordinated shutdown in case of a power cut. Since each CPU consists of six cores, the architecture of this cluster is therefore a hybrid between shared and distributed-memory. This specific type has to be taken in account for the deployment of the simulation software. The memory requirement can be reduced significantly if the hybrid architecture of the cluster is considered. For MCNP the workload is not distributed per core but per node. Since each node shares the same main memory, the total memory required for large scale Monte-Carlo calculations can be reduced by using MPI to distribute the workload on the different nodes and using a shared memory parallelization like OpenMP to start a thread on each CPU core.

System layer

The system layer contains the operation system and all the system services needed for the basic functionality of the cluster system. The Linux distribution Gentoo was used for the operation system. The philosophy of Gentoo is different compared to other Linux distributions. The programs are not shipped in a pre-compiled binary but instead are almost always compiled directly from the source code. This approach takes longer to install new software but in return the configuration of the software is more flexible than for other distributions. This unique behaviour of Gentoo Linux makes it a very reliable distribution for scientific computing. An important point for cluster computing is, that each compute node behaves in exactly the same way as all other machines, so it does not matter for the user on which nodes his computations are running. Therefore the head node provides a set of services for the compute nodes. One crucial point is that each node has access to the same programs and data libraries. The data file system as well as the user home directories are exported from the head node to the compute nodes using a network file system (NFS). Additionally other services are exported to the compute nodes as well, for instance the user privileges, current system time and others.

Cluster layer

All the system services described are needed to provide the minimum functionality of the cluster system. To use the cluster system as just one computer instead of a collection of independent computer systems additional cluster services are needed. The most important service is the “Message passing Interface” (MPI). It allows programs linked against the MPI

library to communicate with other CPUs even if they are not part of the same computer. MPI is nowadays the most commonly used basis for distributed computing.
In case that more than just a few people using the cluster system the management of the available resources can be quite difficult. To ease the administration the cluster layer also includes a cluster resource management system called Torque. Torque is an open-source fork of the commercial PBS cluster management software. It is also called batch-queuing-system. Each user must send his job accompanied with a list of resources he likes to get allocated to the Torque system. Torque calls a subsequent program called MAUI which schedules the job on a subset of nodes in the cluster depending on the resource demand. After the job was finished the results are copied back to the home directory of the user. The Torque system is also used to remain fairness between the users; in this case a single user can not block all computing resources for him alone.

Application layer

In the application layer resided all computational programs for the nuclear simulation or other resource demanding applications like crystallographic or quantum mechanical calculations. In the following sections we limit ourselves to neutronic simulation and burn-up calculations. Tab. 30 contains the installed software products and their application:

Tab. 30: Software installed on the IEK-6 cluster.

Name	Application
MCNP5 / X	Neutronic / Gamma Monte-Carlo, Criticality
TRIPOLI 4	Neutronic, Criticality
Geant4	Particle Transport
SCALE 6	Burn-up calculation and Criticality
BGMN	Crystallographic Software

Benchmarks and Examples

The main application of this cluster is the calculation of neutron and photon transport, criticality and burn-up calculation. The selected benchmarks in this section were used to define the parameters for the batch-queueing system and the upper limit of CPU resources per job. The performance of a parallel system is always limited by the amount of sequential code parts. These parts cannot be parallelized and therefore limit the execution of the program. The Amdahl law describes the scale up of a parallel program depending on its sequential part. The runtime of a program is defined as the sum of sequential and parallel code parts [3].

$$T(N) = \sigma + \frac{\pi}{N}$$

N is the number of CPUs used for the execution of the program. The scale up between the sequential case and a parallel execution is the ratio between the runtimes:

$$S = \frac{T(1)}{T(N)} = \frac{1}{(1-\pi) + \frac{\pi}{N}} \leq \frac{1}{(1-\pi)}$$

So in most applications the scale up is not linear with the amount of CPUs used for the calculation but is always limited by the sequential part. Many options in MCNP5 change the sequential part of the program. The first benchmark was the calculation of the photon flux outside a metal sphere. The fast neutron beam hits the sphere and causes (n,gamma) reactions. The emerging photons cross the outer shell of the sphere and are counted for the photon flux calculation.
The scale up of MCNP5 is shown in Fig. 139. The sequential part of the simulation restricts the scale up. The simulation was tested with different parameters to find an optimum value for the scale up to resource demand. For fixed source and criticality calculations the number of nodes is fixed to five computers to obtain 30 cores per job. This value is a compromise between performance and fairness between users. The cluster has 216 cores in total, so each MCNP5 job can allocate approx. 14 % of the total resources. The choice of the simulation parameters has also an effect on the performance of the MCNP job. Functionalities like the point-detector tally (F5), the pseudo deterministic transport (DXTRAN) or a criticality calculation, forces MCNP to use more saving and I/O operations. In these cases the performance of MCNP is degraded because of a high amount of sequential code parts.
To ease the parameter variation of a MCNP5 simulation, a software product called mcnp_pstudy was developed at the Los Alamos National Laboratory (LANL) [4]. The idea of the software was to search for keywords and replace them with a new value or a range of values. After the replacement of the keywords, the different simulation files are sent to a batch-queueing-system or executed locally on the workstation. This software was extended and adapted to the Torque/MAUI resource management.

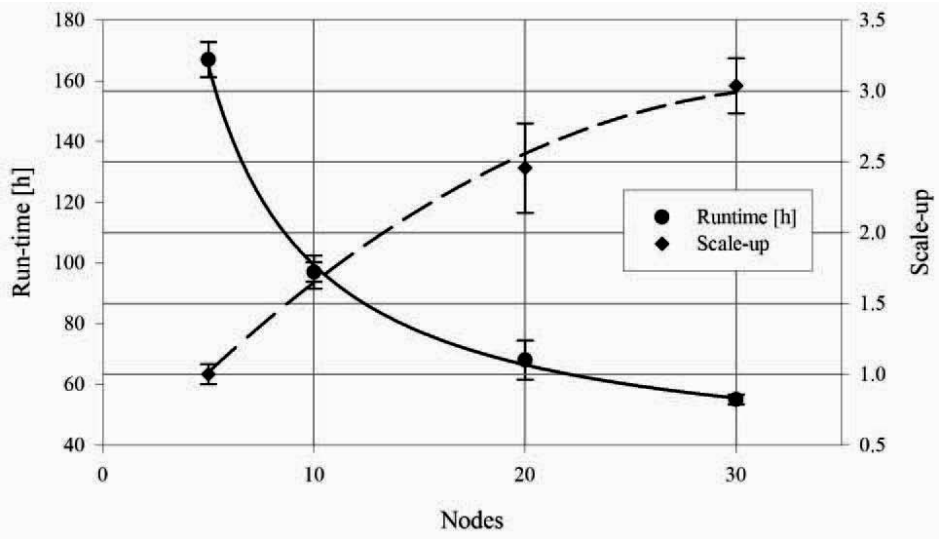

Fig. 139: Scale up of MCNP5 using a neutron-photon coupled problem.

As an example for the different functionalities of mcnp_pstudy we estimated the effect of different cross-section libraries to the criticality solution of a pure U-235 sphere. Each cross-section was calculated 30 times with different seed values for the random number generator.

```
C
c @@@ RNSEED = ( 2*int(rand(10000000))+1 )
c @@@ REN    = REPEAT 30
c @@@ XSFILE = 92235.42c 92235.49c 92235.50c 92235.61c 92235.66c
92235.70c
10 1 -18.74 -10 IMP:n=1
20 0             10 IMP:n=0

10 SO 8.741

MODE n
KSRC 0 0 0
KCODE 10000 1.0 50 250
M1 XSFILE -1.0
PRDMP 2j 1 1 0
RAND SEED=RNSEED
```

Fig. 140: Definition of a MCNP5 input file for the usage of pstudy.

In the upper part of the input file the keywords are initiated with a comment followed by a @@@ tag as shown in Fig. 140. RNSEED is a random number which is varied for each simulation file. REN is the number of repeats for each cross-section library. The XSFILE is a list of all cross-section files which are used for the estimation. So we have six cross-sections with 30 repeats and varying random seed values. This means that 180 different input files have to be written if mcnp_pstudy is not available. The pstudy script sends all the simulation files in a cluster queue. After completion of the jobs the results are combined to visualize the effect of the different cross-sections (Fig. 141).

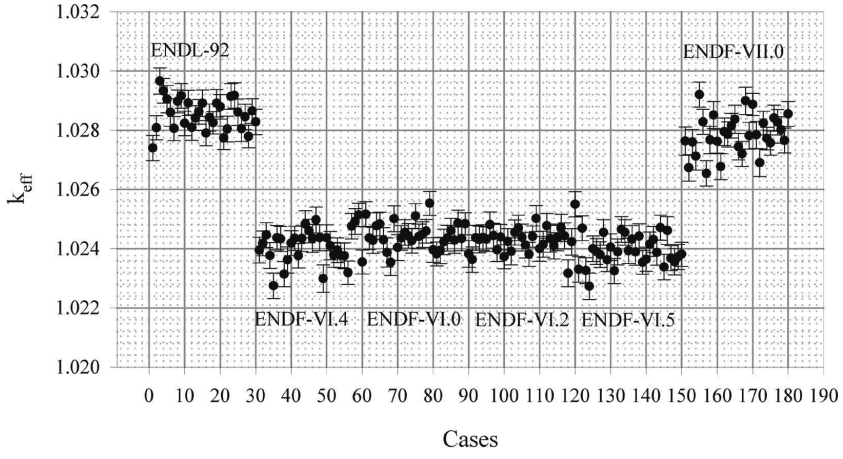

Fig. 141: Criticality solution for different cross-section libraries used.

The ENDF-B/V and ENDF-B/VI libraries yield a k_{eff} value around 1.024; the ENDL-92 and ENDF-VII.0 are 0.4% higher. So the evaluated fission cross-section has changed between the version VI and VII of the ENDF-B library. Tests like this one are often used to verify that the correct cross-sections are used.

Conclusion

The application of numerical simulations for nuclear science and engineering is a vital method to gain access to processes which could not observed directly. The computational demands of these tools are larger than the capabilities of workstations. The HPC cluster was developed and implemented to close the gap between the workstations and the large scale HPC systems. The cluster system is an important contribution for the institute to help the scientists getting there simulations done in a sufficient short amount of time.

References

[1] T. Sterling and D. Becker, ICPP95, (1995)
[2] S. J. Thomas et al., Parallel computing in regional weather modeling, 23(14), (1997).
[3] H. Bauke, S. Mertens, Cluster-Computing, Springer Verlag, (2006)
[4] F. Brown, Monte Carlo parameter studies and uncertainty analyses, LA-UR-04-0499, (2004).

5.25. 2009-2010 annual report of PKS-I

H.-J. Steinmetz, N. Gierke, H. Krumbach
Corresponding author: h.j.steinmetz@fz-juelich.de

Quality Control activities

The status as of December 2010 was a total of 37 quality control projects or orders mostly accounted to the public sector. Nevertheless since 2006 the activities of PKS-I are shifting and expanding more and more towards quality control of operation wastes from nuclear power plants (NPP).

The total value of the above projects exceeded 2 ½ Mio. Euro. This corresponded to a more than twofold increase compared to the annual budget in 2009.
Especially notable are new projects in 2010:

- Qualification of 139 waste containers containing evaporator concentrates produced by the NPP Gundremmingen (KGG). As a result of the successful progress of this project PKS-I will be commissioned with a major follow-up project in the years 2011 – 2013.
- Qualification of two large batches (3,400 and 1,485 radioactive waste drums) of the German Federal State of Lower Saxony or its former Collecting Facility. The project is scheduled for four years.
- Qualifications of processes and technologies for the backfilling of waste containers with concrete, as well as the FAKIR high-pressure press and the PETRA drying plant of the Gesellschaft für Nuklearservice (GNS).

Personnel resources (or staff resources)

Executing effectively the projects already commissioned for BfS in 2010 as well as the additional projects scheduled or expected for 2011 and later requires a significant growth in the personnel of PKS-I. It has been agreed with BfS to increase the numbers of experts in the next year by three with university qualifications.

R & D activities

The German Federal Ministry of Economics (BMWi) and ROSATOM requested for bi-national projects related to the decommissioning of nuclear facilities. In this context PKS-I has proposed a project on irradiated graphite which was successfully applied in 2010. Financial support for the three-years project has been granted by the German Federal Ministry for Education and Research (BMBF). The project coordinated by PKS-I includes a scientific cooperation with the Moscow Nuclear University MEPhI.

Conferences

In 2010 contributions were given in conferences in Germany (KTG Jahrestagung), USA (WM 2011) and Japan (ICEM ’10) as well as a MEPhI workshop in Russia.

5.26. Product control of waste products with new coating materials

H. Krumbach[1], H.-J. Steinmetz[1], R. Odoj[1], W. Wartenberg[2], H. Grunau[3]

[1] Institute of Energy and Climate Research – Nuclear Waste Management and Reactor Safety (IEK-6), Forschungszentrum Jülich GmbH, 52425 Jülich, Germany

[2] Company Nuclitec GmbH Braunschweig

[3] Company Eisenwerk Bassum m.b.H

Corresponding author: h.krumbach@fz-juelich.de

Abstract

The previously conditioned radioactive waste has to be suitable for a longer-term interim storage. They have to be treated in a way that they are chemically stable and that their integrity is guaranteed for a long time. That's why the waste product or the container is covered/ coated for special waste such as hygroscopic waste or waste that includes aluminium. The Product Control Group for radioactive waste (PKS) has to proof the suitability of the so-treated waste for the repository KONRAD on behalf of the Federal Office for Radiation Protection (BfS). This has to be done before the delivering. In this context the PKS also assesses the suitability of new coating materials for low radioactive waste products or containers and their correct technical application.

Objectives

By the time radioactive waste has to be conditioned and interim stored according to the final conditions requirements for disposal radioactive waste - „Anforderungen an endzulagernde radioaktive Abfälle – Schachtanlage Konrad“ [1] (Stand: Dezember 1995).
The waste products or waste packages must be chemically stable and technically in perfect condition until the date of the disposal. Regarding different wastes such as ash, concentrates (hygroscopic waste) or waste with aluminium, the integrity of the packaging shall be ensured by a special anti-corrosion coating. Before the application of such a coating their suitability has to be examined by experts and released by the Federal Office for Radiation Protection.
Because there is currently only a technical application for polyurethane coating it is also only part of the assessment by the product inspection for radioactive waste.

In the context of two research projects, the possibilities for the coating or backfill of waste products were inspected.
In this context the Institute of Materials Engineering at the University of Dortmund accomplishes long-term studies of polyurethane (PU) coated samples [2].
The second research project at the Institute for Energy Research 6 (IEF-6) of the Research Center Juelich, deals with the implementation of silicon plastics as coating or filling materials [3].
A major focus of those investigations was to ascertain the suitability of both materials in terms of corrosion-protection.
The using of silicon plastics as coating or backfill is mainly based on theoretical considerations and laboratory tests. These investigations show that silicon plastics can be used for the filling of containers with radioactive waste and are not suitable for the coating of radioactive waste products.

The Product Control Group has to conduct studies in order to assess the suitability of various coating materials. Those investigations proof, whether these new coating materials are in line with the disposal conditions requirements for radioactive waste „Anforderungen an endzulagernde radioaktive Abfälle - Schachtanlage Konrad [1] (Stand: Dezember 1995)".

Polyurethan coating

The coating with polyurethane is the most developed process in the industrial application.
A polyurethane coating is used as corrosion protection for the walls at the dock "Benser - Siel" in a long time test. There, the materials demonstrated the effectiveness as a corrosion protection for more than 20 years. The investigations by the Department of Materials Technology at the University of Dortmund also assess the suitability as a long-term corrosion protection.
In nuclear technology polyurethane was initially used as corrosion protection for KONRAD containers.
The coating of waste products can be used for corrosion protection as well and on the other hand; the material properties of polyurethane can be used as a further protective effect for the waste products.
The coating with polyurethane avoids the penetration of oxygen in hygroscopic waste other chemical reactions in the waste products can be blocked also. The basic property such as fire behaviour and thermal properties of polyurethane were examined in the approval of the coating material as a coating for disposal containers.
The PKS evaluation covers the technical suitability for coating material for waste products (water permeability, impact strength). Several techniques are used for the application of polyurethane. The common techniques for the coating of KONRAD – containers and barrels are spray proceedings (Fig. 142), while the coating of super compacted waste is made by cast proceedings (Fig. 143).

Fig. 142: Coating with Polyurethane

Fig. 143: Pellet in a cast form

Results

The PKS's own assessments concerning the acceptability for reposition of new coating materials have shown that the polyurethane coating of radioactive waste products is adequate.

Polysiloxane which has been investigated alternatively at the beginning is not suitable as a coating. Because this material is permeable to air it has only got a limited protective function.
The coating of radioactive waste products or containers with polyurethane can be used in cast proceeding as well as spraying procedures. For drums and containers the spray technique turned out to be advantageous. For super compacted waste (pellets) the cast proceeding has got considerable advantages.
The suitability of polyurethane as corrosion protection has been demonstrated by studies at the University of Dortmund and in practice by the coating of a port basin.
For reasons of economy the polyurethane coating is used only for problem waste.
The coating meets the demands of the final repository for radioactive waste “Schachtanlage KONRAD”.

References

[1] Peter Brennecke, Bundesamt für Strahlenschutz, Fachbereich Nukleare Entsorgung und Transport, Salzgitter: „Anforderungen an endzulagernde radioaktive Abfälle“ (Endlagerungsbedingungen, Stand: Dezember 1995) – Schachtanlage Konrad –, Dezember 1995, ET-IB-79

[2] Prof. Dr.-Ing. Friedrich-Wilhelm Bach, Lehrstuhl für Werkstofftechnologie, Fakultät Maschinenbau, Universität Dortmund: „Prüfbericht: Langzeituntersuchungen von PU - beschichteten Proben“, 2000

[3] Prof. Dr. R. Odoj, FZJ, Dr. S. Maischak, FZJ, W. Pfeifer, FZK, L Valencia, FZK, L. Schneider, A. Rohr and C. Herzog, Stoller Ingenieurtechnik: “Application of Polysiloxanes for the Treatment of Radioactive Waste to Guarantee Safe Long Term Storage”, Waste Management 2004 Symposium, Tucson, Arizona 2004

5.27. Challenges in Compliance with the Waste Acceptance Requirements for the KONRAD Mine

H. Krumbach, H.-J. Steinmetz

Corresponding author: h.krumbach@fz-juelich.de

Abstract

The licence for operating the KONRAD repository had initially been contested by opponents of disposal, but final court decision of 26 March 2007 established that the repository in the former iron ore mine KONRAD may be operated for the disposal of low- and intermediate-level radioactive waste from 2013. Preparations are currently being made in Germany for the delivery of waste packages to the KONRAD repository.
The demonstration of the suitability of the KONRAD mine as a repository proved particularly difficult with respect to legacy waste, for example, in the case of poor documentation of this legacy waste. The declaration of the radionuclides contained in that waste generally no longer fulfils the standards now required. Furthermore, it proved difficult to verify the assignment of the waste products created in the past to the waste product groups (WPGs) defined for KONRAD [2]. Another problem associated with the quality control of the legacy waste is the requirement that waste packages should be delivered to the KONRAD [2] repository in a depressurized state.
In order to fulfil this requirement, it must be ensured that there is little or no gas formation (e.g. due to the decomposition or fermentation of organic matter). Conditioned waste has already been cemented into the packages for disposal so that it is very difficult to provide sufficient proof that this requirement has been complied with.

Beginning in the 90s, radioactive waste was already conditioned in accordance with the draft KONRAD waste acceptance requirements published in 1990. A large volume of the waste produced at that time was packed into containers that were manufactured considering the 1990 requirements. However, the fulfilment of the KONRAD waste acceptance requirements has to be demonstrated prior to emplacement.

Finally, the declaration of substances of relevance for legislation relating to water [3] is a topic of current interest. This requirement must be fulfilled for both newly conditioned waste and also for legacy waste.

Objectives

On behalf of the Federal Office for Radiation Protection (BfS), the Quality Control Group for Radioactive Waste (PKS) has the task of monitoring compliance with the waste acceptance requirements [2] for the emplacement of radioactive waste in a repository. Problems frequently arise in demonstrating such proof with respect to the KONRAD requirements [2], especially in the case of legacy waste that has already been conditioned.
These problems arise in the field of repository documentation, in verifying the waste product, fulfilling basic requirements with respect to the container or identifying substances being hazardous to water – a requirement which has recently been included in the KONRAD waste

acceptance requirements [3]. In the meantime, practicable solutions have been found for most of the problems.

Documentation of waste packages

A special problem arises with the documentation of legacy waste that has already been conditioned with respect to verifying its suitability for disposal in KONRAD. The declaration of the radionuclides contained in the waste generally no longer fulfils the standards now required in the draft KONRAD waste acceptance requirements published in 1990. In the past usually only the total activity of a package, the dose rate and possibly also the mass were documented. Since 1990 activity limits for 108 nuclides must be complied with. The details of the declaration of an legacy waste package are far from adequate for present requirements. The data on radioactivity must be supplemented – a very time-consuming procedure.

Activity determination

The radioactivity in a waste package can be determined in a number of ways. For example, by determining nuclide vectors with the aid of which the activity inventory in the waste packages can be calculated from the dose rate and the mass. Another possibility is performing scanner measurements on waste drums and taking samples of the waste product to determine the alpha activity. In any case, the legacy waste must be re-qualified in a laborious procedure. The particular difficulty is collecting the documentation on conditioning compiled when the package was created. In documentation on legacy waste products, the conditioning sequence is frequently not described in sufficient detail or there may be a total lack of information on the raw waste.

This documentation, some of it incomplete, must be processed so that it is capable of being verified. There are also errors in the old documentation that have to be discovered and corrected. The experience gained by the quality control group (PKS) in developing methods for testing radioactive waste means that they are able to verify the plausibility of the assembled documentation. PKS has in particular made an intensive contribution to the development of scanners. Today, further development is being pursued at the Institute of Energy Research (Safety Research and Reactor Technology), IEK-6, of which PKS is part. In addition to scanner development, a tomograph has also been used for examining radioactive waste. A rarely used means of determining activity is destructive testing, for example of core samples, and PKS has also developed methods for this type of testing. However, efforts are made to ensure a plausible determination of activity by simple measuring methods thus enabling the documentation to be corrected.

Delivery in a depressurized state

Another problem arising with the quality control of the legacy waste is the requirement that waste packages should be delivered to the KONRAD repository [2] in a depressurized state.

In order to fulfil this requirement, it must be ensured that there is little or no gas formation (e.g. due to the decomposition or fermentation of organic matter). This can be verified relatively simply for newly produced packages or when loading KONRAD containers with waste products. However, already conditioned waste is also present in so-called lost concrete shielding (serving as a licensed package for the repository), which was cemented without depressurization measures (Fig. 144). For this waste it is very difficult to provide sufficient proof that this requirement has been complied with. On the basis of analogous considerations of the same type of waste that has not yet been cemented, it is possible to

perform calculations of pressure build-up in the cemented waste. However, due to the large number of factors involved in the calculation this is very difficult and cannot be successfully performed in every case.

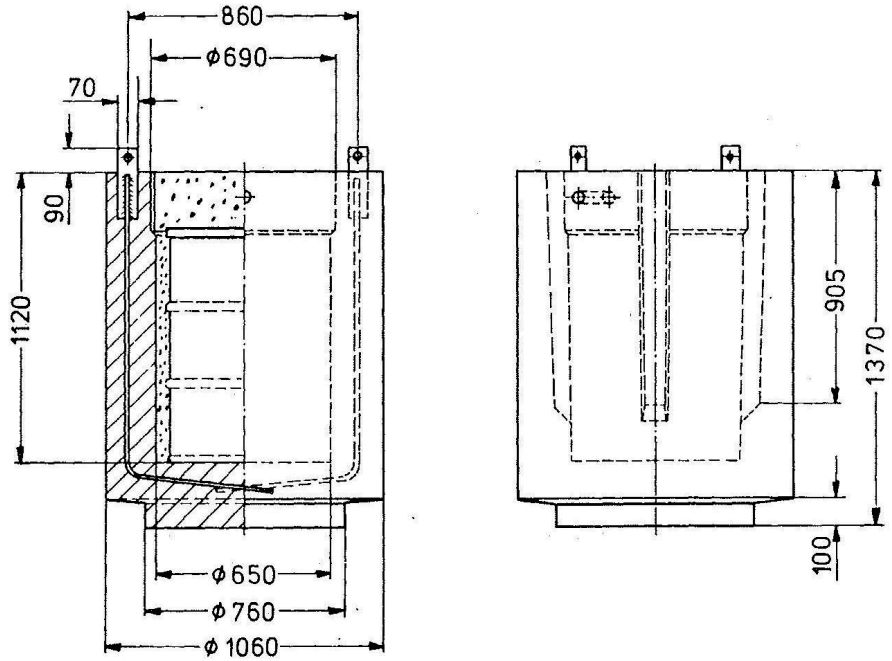

Fig. 144: Waste product cemented in lost concrete shielding without pressure relief

Packages which cannot be verified must be re-conditioned in a laborious process.

Substances relevant to water legislation

Finally, consideration should be given to a topic of current interest – the declaration of "substances of relevance with respect to water legislation'". This requirement, which has been taken over from legislation on conventional waste disposal sites, must be fulfilled for both newly conditioned waste and also for legacy waste. Fig. 145 shows an excerpt from the list of description and declaration thresholds for substances in accordance with List 1 of the Appendix to the Groundwater Directive [3].

Since a draft of the requirements to be fulfilled has only been available since October it is difficult to comment on the verification demanded. It does, however, seen apparent that in this case as well it will be more difficult to provide verification for packages that have already been produced than for those yet to be fabricated. As in the preparation of documentation described above, the main problem here will probably also is the quality of the old documents. In accordance with the draft of the repository conditions, no analysis of the waste product itself for verifying the substances of relevance for water legislation will be permitted. Verification will have to be provided by plausibility checks and analogous considerations. As with testing, application in practice will show how practicable this solution is.

Stoff	Beschreibungsschwellenwert		Deklarationsschwellenwert	
	Neuabfall	Altabfall	Neuabfall	Altabfall
Nr. 1 der Liste I				
Halogenierte Naphthaline	0,1	0,5	0,1	0,5
Halogenierte Phenole	0,1	0,5	0,1	0,5
Biphenyle	0,01	0,05	0,01	0,05
Hexachlorbenzol	0,01	0,05	0,01	0,05
γ-Hexachlorcyclohexan (Lindan)	0,1	0,5	0,1	0,5
Nr. 2 der Liste I				
Phosphorsäureester	1	5	1	5
Tributylphosphat	1	5	1	5
Dibutylphosphat	1	5	5	5
Hexamethylphosphorsäuretriamid	1	5	1	5
Nr. 4 der Liste I				
Na-Ethylendiamintetraessigsäure	0,1	0,5	0,1	0,5
Ethylendiamintetraessigsäure	0,3	1,5	0,3	1,5
Na-Nitrilotriessigsäure	1	5	1	5
Gold	1	5	25	25
Caesium	1	5	5	5
Lithium	1	5	1	5
Platin	1	5	—	—
Rubidium	1	5	5	5
Strontium	1	5	25	25
Nr. 5 der Liste I				
Quecksilber	1	5	1	5

Fig. 145: List of description and declaration thresholds [3]

Results

The fulfillment of the requirements for the repository KONRAD generates a challenge for a part of the legacy wastes. Because the requirements and enhancements of the repository conditions were late-specified, a part of the waste has to be treated again. This waste was conditioned in accordance to plans for the KONRAD repository.
However, today much more stringent requirements have to be met for packages to be emplaced in KONRAD. Nevertheless the repository condition allows possibilities, to fulfil the requirements.

References

[1] B.-R. Martens, Produktkontrolle radioaktiver Abfälle – Schachtanlage Konrad, Stand: Dezember 1995, Interner Arbeitsbericht, ET-IB-45-REV-3. –Germany-

[2] P. Brennecke, Anforderungen an endzulagernde radioaktive Abfälle (Endlagerungsbedingungen, Stand: Dezember 1995) – Schachtanlage Konrad – Interner Arbeitsbericht, BfS ET-IB-79. –Germany-

[3] Peter Brennecke, Karin Kugel, Stefan Steyer, Endlager Konrad – Vorgehensweise zur Umsetzung der wasserrechtlichen Nebenbestimmungen, 12 Oktober 2009, Entwurf, SE-IB-38/09-REV-1. –Germany-

6 Education and training activities

Education in nuclear safety research in particular with RWTH Aachen is supported by IEK-6. Dirk Bosbach holds the chair for the disposal of nuclear waste and Bruno Thomauske the chair for nuclear fuel cycle (Fig. 146). Further, a new accredited Master Curriculum "Nuclear Safety Engineering" was established at RWTH Aachen University in 2010. 13 students started this 2 years programme. A new practical course on nuclear measuring techniques in the radiochemistry laboratories of IEK-6 as well as the lecture "Introduction to Nuclear Chemistry" was launched in 2010 and has attracted almost 50 students from nuclear safety engineering, chemistry, computational engineering science and nuclear technology at RWTH Aachen. 14 PhD students are currently (May 2011) working on research projects related to the safe management of nuclear waste in Jülich. 6 PhD candidates had successfully defended their theses during the last 2 years, one with summa cum laude at RWTH Aachen University. Furthermore, 5 diploma and master theses were finished in 2009/10. IEK-6 is committed to support the education in nuclear / radio-chemistry in particular with respect to the safe management of nuclear waste in Aachen and beyond. IEK-6 also participates in the new graduate school Energy and Climate HITEC, which was founded in 2011 in Jülich.

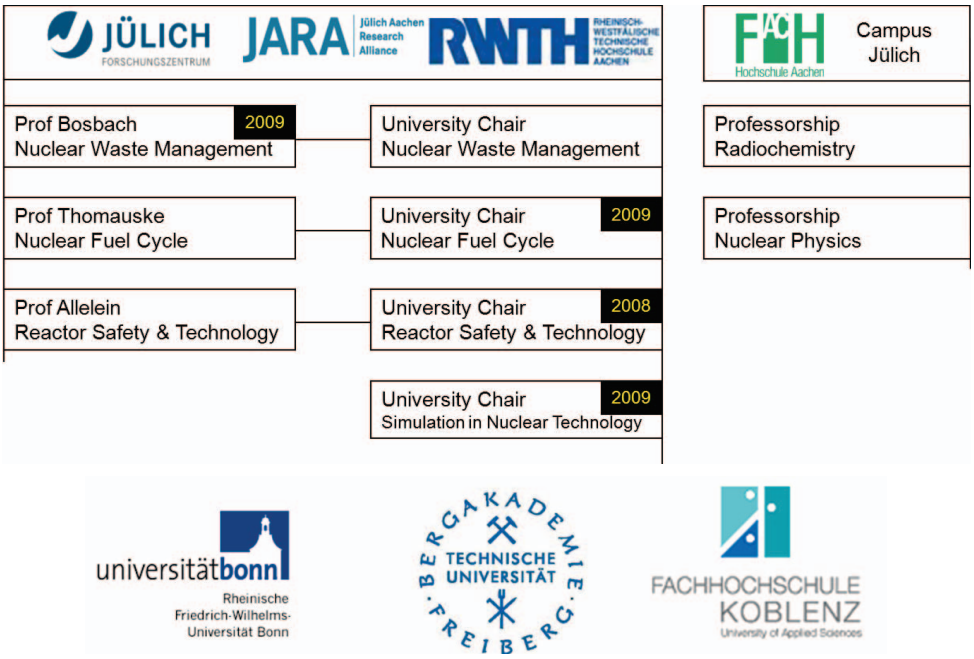

Fig. 146: Universities, where IEK-6 staff lecture.

6.1. Courses taught at universities by IEK-6 staff

Prof. Dr. D. Bosbach

RWTH Aachen University
Faculty of Georesources and Materials Engineering
Topic: Grundlagen der Kernchemie, Hours: 2 SWS, since WS 2010
Topic: Physikalisch-chemische Grundlagen für die Langzeitsicherheitsanalysen der Nuklearen Endlagerung, Hours: 2 SWS, WS 2009/2010
Topic: Kerntechnisches Messpraktikum, 1 week, since WS 2010

Prof. Dr. B. Thomauske

RWTH Aachen University
Faculty of Georesources and Materials Engineering
Topic: Endlagerung radioaktiver Abfälle und Sicherheitsanalysen, Hours: 2 SWS, WS 2009/2010
Topic: Nuklearer Brennstoffkreislauf I, Hours: 2 SWS, since WS 2010
Topic: Produkte und Märkte der Rohstoffindustrie, Hours: 2 SWS, since WS 2010
Topic: Rohstoffe und Energieversorgung, Hours: 2 SWS, since WS 2010

Dr. G. Modolo

Fachhochschule Aachen-Jülich, Fachbereich Chemie und Biotechnologie
European Master of Science in Nuclear Applications
Topic: Nuclear Fuel Cycle, Hours: 2 SWS

RWTH Aachen University
Faculty of Georesources and Materials Engineering
Topic: Brennstoffe, Wiederaufbereitung und Konditionierung, Hours: 2.5 SWS, since 2011
Topic: Sicherheit in der Wiederaufarbeitung, Hours: 3 SWS

Dr. I. Niemeyer

TU Bergakademie Freiberg
Faculty of Geosciences, Geoengineering and Mining

- SoSe 2009
  Topic: Geomonitoring, Hours: 4 SWS
  Topic: Remote Sensing I, Hours: 2 SWS
  Topic: Remote Sensing II / Digital Image Processing, Hours: 2 SWS
- SoSe 2010
  Topic: Geomonitoring, Hours: 2 SWS
  Topic: Digital Image Processing, Hours: 2 SWS

PD Dr. H. Schlenz

Universität Bonn
Faculty of Mathematics and Natural Sciences
Topics: Crystallography and Applied Mineralogy, Hours: 2 SWS

Dipl.-Ing. S. Schneider

Fachhochschule Koblenz
Fachbereich Mathematik & Technologie
Topic: Einführung in das objekt-orientierte Programmieren, Hours: 4 SWS

Dr. H. Tietze-Jaensch

Polytechnical University Warsaw
Faculty of Physics
Topic: Nuclear Energy & Reactor Safety, 15 h lecture
Topic: Introduction to Neutron Scattering, 6 h lecture

Prof. Dr. R. Nabbi

RWTH Aachen University
Faculty of Georesources and Materials Engineering
Topic: Grundlagen der Kern- und Strahlenphysik, Hours: 2 SWS, since WS 2010

Fachhochschule Aachen-Jülich
Topic: Reactor and neutron physics, WS 2009/2010; WS 2010/2011
Topic: Advanced reactor and neutron physics, SoSe 2010

6.2. Graduates

6.2.1 Diploma/Master Thesis

Cherault, N.: Development of an innovative SANEX process based on TODGA/Octanol; Chimie Paris Tech, Paris, Forschungszentrum Jülich, 2010; Masterarbeit, 2010

Esser, F.: Auslegung einer Neutronenabschirmung zwischen einer Cf-252-Neutronenquelle und einem Szintillationsdetektor mittels Monte-Carlo Simulation; Fachhochschule Aachen, Standort Jülich, Forschungszentrum Jülich, Diplomarbeit, 2010

Sobantka, A.P.: Synthese und Charakterisierung von mit Fe^{2+}, Co^{2+}, Ni^{2+} modifizierten Magnesium-Aluminium-Doppelhydroxidverbindungen, Fachhochschule Kaiserslautern, Standort Pirmasenz, Forschungszentrum Jülich, Diplomarbeit, 2009

Rose, J.: Bestimmung der Photopeak-Effizienz eines HPGe-Detektors im Energiebereich 0,05 - 10 MeV für die Prompt-Gamma-Neutronen-Aktivierungsanalyse; Fachhochschule Aachen, Standort Jülich, Forschungszentrum Jülich, 2009; Jülich, Diplomarbeit, 2010

Weidenfeld, M.: Herstellung von Uranbasierten Brennstoffpartikel nach dem Harzverfahren; Fachhochschule Aachen, Standort Jülich, Forschungszentrum Jülich, Diplomarbeit, 2010

6.2.2 Doctoral Thesis

Chiriki, S.: Disposal strategy of proton irradiated mercury from high power spallation sources, 124 Seiten, Schriften des Forschungszentrums Jülich; 67, Reihe Energie &

Umwelt / Energy & Environment 2010; ISBN 978-3-89336-632-3; Aachen, RWTH, Dissertation, 2010.

Florjan, M.W.: Dekontamination von Nukleargraphit durch thermische Behandlung; Forschungszentrum Jülich, Zentralbibliothek, 2010; Berichte des Forschungszentrums Jülich; 4322, JUEL-4322; Aachen, RWTH., Dissertation, 2010.

Hansen, B.: Synthese und Identifizierung von substituierten Mg-Al-Cl Doppelhydroxid-verbindungen mit Schwerpunkt IR-Spektroskopie, 205 Seiten; Schriften des Forschungszentrums Jülich; 107, Reihe Energie & Umwelt / Energy & Environment ISBN 978-3-89336-709-2, Aachen, RWTH, Dissertation, 2010.

Kettler, J.P.H.: Prompt-Gamma-Neutronen-Aktivierungs-Analyse zur zerstörungsfreien Charakterisierung radioaktiver Abfälle, 205 Seiten; Schriften des Forschungszentrums Jülich; 82, Reihe Energie & Umwelt / Energy & Environment ISBN 978-3-89336-665-1, Aachen, RWTH, Dissertation, 2010.

Schlögl, B.: Oxidationskinetik innovativer Kohlenstoffmaterialien hinsichtlich schwerer Lufteinbruchstörfälle in HTR's und Graphitentsorgung oder Aufarbeitung, 117 Seiten, Schriften des Forschungszentrums Jülich; 89, Reihe Energie & Umwelt / Energy & Environment 2010 ISBN 978-3-89336-676-7; Aachen, RWTH, Dissertation, 2010.

Sutanto, R.-P.: Das Verhalten der Urancarbide und -oxi-carbide in endlagerrelevanten aquatischen Phasen. Jülich, Forschungszentrum Jülich, Zentralbibliothek, 2009, Berichte des Forschungszentrums Jülich ; 4295, JUEL-4295, Aachen, RWTH, Dissertation, 2010.

6.3. Vocational training

Forschungszentrum Jülich offers different vocational training programs. The 3 years lasting education is supported by IEK-6 in nuclear / radio-chemistry. In 2009/10 four laboratory assistants were trained in the laboratories of IEK-6. Two of them already finished their education successfully and received a certificate of apprenticeship.

6.4. Further education and information events

IEK-6 is committed to support the education of young people including schoolchildren in nuclear safety research. Forschungszentrum Jülich participates in the nationwide **"Girls Day".** Girls from 5th to 13th class have the opportunity to become familiar with different professions such as chemist, physicist, or firewoman as well as the working conditions at laboratories, garages and offices. At IEK-6, the topic "No fear of radioactive materials" was presented. Basics about radioactivity in the environment and radioactive decay as well as different measuring techniques were explained. Measurements of different sample were carried out by the girls themselves to get a feeling for radioactivity (Fig. 147) and attract children's interest in science.

Fig. 147: Girls Day 2010 at IEK-6: Measurement of a uranium containing floor tile.

In terms of recruiting PhD students in the field of nuclear safety research, IEK-6 is represented at the **annual colloquia "Kernenergie hat Zukunft"** which is organized by the Deutsche Atomforum e.V.. The event is addressed to students of technical and scientific disciplines. They have the opportunity to get information at first hand from energy providers, research institutes, and technical inspection authorities on the manifold job-related perspectives in the field of nuclear energy. IEK-6 gave presentations (at events in Lünen, Speyer, and Hamburg) and had an information desk at the job exchange to introduce the research activities of the institute and to provide information about master, diploma, and PhD opportunities.

6.5. Institute Seminar

The IEK-6 organizes an institute seminar with internal talks and invited speakers, to present the recent research activities. Further information on www.fz-juelich.de/iek/iek-6.

6.5.1 Internal talks 2009

13.05.2009 **Bai, Y.:** Application of PGNAA for the Determination of Large Sample

13.05.2009 **Curtius, H.:** Übersicht über die Arbeiten zur Langzeitsicherheit

27.05.2009 **Klinkenberg, M:** Aufbereitung der sekundären Phasen

27.05.2009 **Kettler, J.:** Entwicklung eines innovativen Prüfverfahrens zur zerstörungsfreien Charakterisierung schwach- und mittelradioaktiver Abfallgebinde

10.06.2009 **Tietze-Jaensch, H.:** Was macht die PKS-WAA?

10.06.2009 **Modolo, G.:** Überblick über den Stand der Partitioning Arbeiten in Jülich

24.0620.09 **Sypula, M.:** Innovative process for actinide (III) separation

24.06.2009 **Rossbach, M.:** Qualitätskontrolle in der Spurenanalytik

27.07.2009 **Sobantka, A.:** Synthese und Charakterisierung von mit Fe^{2+}, Co^{2+}, Ni^{2+} modifizierten Magnesium-Aluminium-Doppelhydroxidverbindungen

28.10.2009 **Neumann, A.:** Aktuelle Promotionsergebnisse - Charakterisierung sekundärer endlagerrelevanter Phasen

04.11.2009 **Steinmetz, H.-J.:** Produktkontrolle radioaktiver Abfälle für das Endlager Konrad

04.11.2009 **Vulpius, D.:** Erste Ergebnisse zur Klärung der Bindungsverhältnisse von C-14 in bestrahlem Graphit

18.11.2009 **Daniels, H.:** Interne Gelierung von U(VI)-Systemen

18.11.2009 **Bukaemskiy, A.A.:** SiC ceramic as the promising matrix for the nuclear weste immobilisation

25.11.2009 **Wilden, A.:** Partitioning: Erste Ergebnisse im BMBF 2020 Vorhaben

25.11.2009 **Babelot, C.:** First results on the conditionning of actinides

17.11.2009 **Rose, J.:** Bestimmung der Photopeak-Effizienz eines HPGe-Detektors im Energiebereich 0,05-10 MeV für die Prompt-Gamma-Neutronen-Aktivierungsanalyse

09.12.2009 **Schneider, S.:** Gamma & Neutronen Emission von kompaktierten metallischen Abfällen (CSD-C)

09.12.2009 **Hansen, B.:** IR-Spektroskopie modifizierter LDH-Verbindungen

6.5.2 Internal talks 2010

18.01.2010 **Neumeier, S.:** Konditionierung von langlebigen Actiniden und Spaltprodukten in keramischen Materialien

05.02.2010 **Curtius, H., Krumbach, H., Mauerhofer, E., Modolo, G., Tietze-Jaensch, H., Vulpius, D.:** Stand und zukünftige Arbeiten in den unterschiedlichen Forschungs-/Servicebereichen

10.03.2010 **Weidenfeld, M.:** Herstellung von Uranbasierten Brennstoffpartikel nach dem Harzverfahren

09.06.2010 **Harren, E.:** Die Verlasungsanlange VEK und die Produktkontrolle ihrer HAW Glaskokillen

30.06.2010 **Listner, C.:** Automatisierte Analyse von Fernerkundungsdaten im Rahmen der Safeguardsüberwachung

30.06.2010 **Niemeyer, I.:** Hyperspektral- und Radarfernerkundung im Rahmen der Safeguardsüberwachung

06.07.2010 **Esser, F.:** Auslegung einer Neutronenabschirmung zwischen einer Cf-252-Neutronenquelle und einem Szintillationsdetektor mittels Monte-Carlo Simulation

14.07.2010 **Klinkenberg, M.:** Aufbereitung und Identifizierung sekundärer Phasen - Systeme UAl_x-Al und U_3Si_2-Al in Lauge 2

14.07.2010 **Wilden, A.:** Neue Ergebnisse zur Abtrennung langlebiger Radionuklide (Partitioning)

21.07.2010 **Babelot, C.:** Conditioning of Minor Actinides in Monazite-type Ceramics

21.07.2010 **Sypula, M.:** Development of an innovative SANEX process based on TODGA/Octanol

28.07.2010 **Daniels, H.:** Herstellung von keramischen Matrizes zur Actiniden-Transmutation - aktuelle Ergebnisse

28.07.2010 **Neumann, A.:** Quantifizierung sekundärer Phasen im System UAl_x-Al und U_3Si_2-Al in Lauge 2

27.10.2010 **Cherault, N.:** Development of an innovative SANEX process based on TODGA/Octanol

6.5.3 Invited talks 2009

30.04.2009 **Dr. K.-U. Ulrich:** Molecular Structure and Reactivity of Uranium Immobilizing Compounds
Washington University in St. Louis, USA

09.09.2009 **K. Rozov:** Synthesis, characterization and thermodynamics of hydrotalcite-like solid solution
Paul Scherrer Institut, Villingen, Switzerland

18.09.2009 **Dr. I. Niemeyer:** Internationale Kernmaterialüberwachung mit Hilfe von Geoinformationstechnologien
Technische Universität Freiberg, Germany

25.09.2009 **Prof. Dr. S.P. Mezyk:** Aqueous nitric acid radiation effects on solvent extraction process chemistry
Dep. of Chemistry, University at Long Beach, USA

25.09.2009 **Dr. B. J. Mincher:** Radiation chemistry at the back end of the fuel cycle
Idaho Nat. Laboratory, USA

01.10.2009 **Dr. Cédric Carasco:** Development and Application of Non-Destructive Methods for Nuclear Waste Characterization at CEA
CEA, France

20.10.2009 **Dr. M. Schlegel:** Lanthanide and uranium retention by clay minerals: a spectroscopic perspective?
CEA, France

25.11.2009 **Priv.-Doz. Dr. H. Schlenz:** Die Strukturanalyse amorpher Festkörper mittels Beugungsmethoden und Reverse-Monte-Carlo-Simulationen
Forschungszentrum Jülich, PTJ,Jülich, Germany

02.12.2009 **Prof. Jordi Bruno:** Status and future challenges of spent fuel stability in repository systems
CEO & Chairman of the Board AMPHOS21, Barcelona, Spain

08.12.2009 **Dr. H. Geiser:** Verbringung der radioaktiven Abfälle aus dem Betrieb und Rückbau von Kernkraftanlagen
GNS & WTI Jülich, Germany

15.12.2009 **Dr. Bernd Grambow:** Endlagerrelevante Eigenschaften radioaktiver Abfallprodukte von HTR und UNGG Reaktoren
SUBATECH Université des Nantes, France

18.12.2009 **Dr. Jürgen Krone:** Gemeinsame Arbeiten mit der GRS (BS) und BGR zum FuE-Vorhaben ISIBEL
DBE TECHNOLOGY GmbH, Peine, Germany

6.5.4 Invited talks 2010

08.01.2010 **Dr. Sascha Trumm:** Untersuchungen zur Komplexierung von Cm(III) und Eu(III) mit Partitioning-relevanten Liganden
KIT Karlsruhe, Germany

23.03.2010 **Dr. Thomas Krieger, Prof. Rudolf Avenhaus:** Quantitative Analyse von Unangekündigten Zwischeninspektionen im Rahmen der IAEO/EURATOM Kontrollen
Universität der Bundeswehr München, ITIS GmbH

24.03.2010 **Dr. Andreas Scheinost:** The Rossendorf Beamline at ESRF – A unique facility to perform X-ray absorption spectroscopy of radionuclides
Forschungszentrum Dresden/Rossendorf; Rossendorf Beamline, Grenoble, Switzerland

08.04.201 **Prof. Dr. Francis Livens:** Radiochemistry and Nuclear Research at the University of Manchester
University of Manchester, GB

26.05.2010 **Dr. Kastriot Spahiu:** The role of non uranium cations in the oxidative dissolution of high burn-up UO_2 fuel. Interfacial radiolytic processes in the hydrogen action on fuel dissolution
Chalmers University of Technology, Göteborg, Sweden

09.06.2010 **Dr. Nicole Erdmann**: Analytical Techniques for Nuclear Safeguards and Forensics
Nuclear Safeguards and Security, Institute for Transuranium Elements (ITU), Karlsruhe, Germany, Joint Research Center, European Commission

22.06.2010 **Prof. Dr. W. Depmeier:** Layered Hydrazinium Titanate LHT-9: A Convenient Approach to Radioactive Wate Treatment
Universität Kiel, Germany

22.06.2010 **Dr. E.V. Alekseev:** Actinide Borates: Synthesis, Structures, Properties and Possible Applications
Universität Kiel, Germany

24.06.2010 **Prof. Dr. Carlo Artioli:** Transmutation Performance of Advanced ADS-Concepts in Europe
University of Bologna, Italy; National Agency for New Technologies, Energy and Sustainable Economic Development (ENEA), Italy

18.08.2010 **Dr. Westmeier:** Neutronenproduktion bei Bestrahlung dicker Targets mit hochenergetischen Ionen
Kernchemie, FB Chemie, Philipps Universität, Marburg, Germany

21.09.2010 **Dr. N. Evans:** The Chemistry of UK Radioactive Waste Disposal
Department of Chemistry, Loughborough University, UK

09.11.2010 **Prof. Dr. Hamid Ait Abderrahim:** The European Transmutation Project MYRRAH (Potentials, Features, Implementation)
Vorstand SCK-CEN, Leiter des europäischen MYRRAH-Projekts

09.12.2010 **Dr. V.L. Vinograd:** Ab initio thermodynamics of non-isostructural solid solutions
Institute of Geosciences, University of Frankfurt, Germany

6.6. Visiting Scientists

Yunfei Bai

School of Nuclear Science Engineering; Shanghai Jiao Tong University
2008/2009 (2 years)

Marcin Brykała

Sol-Gel Laboratory, Department of Nuclear Methods of Material Engineering, Institute of Nuclear Chemistry and Technology, Warszawa, Poland
February 2010

Clemens Listner

TU Bergakademie Freiberg, Institute of Mine-Surveying and Geodesy
01.04.2010 to 31.05.2011

Ann Min Ho

KAIST - Korea Advanced Institute of Science and Technology, Daejeon, Südkorea
07.01.2010 – 31.03.2010

7 Awards

Dipl.-Ing. Henrik Daniels was awarded with the 2009 Buchpreis of the DECHEMA for his diploma thesis „Selektive Extraktion der dreiwertigen Actinoide durch N-Chelatkomplex-Bildner“. The prize was donated by the Max-Bucher-Forschungsstiftung.

Dr. Martina Klinkenberg was awarded with the 2009 Karl Jasmund Prize from the German Clay and Clay Mineral Group (DTTG). She received the prize for her PhD thesis "Einfluss des Mikrogefüges auf ausgewählte petrophysikalische Eigenschaften von Tongesteinen und Bentoniten“ (Federal Institute for Geosciences and Natural Resources (BGR), Hannover and University of Göttingen). The prize was presented on 26 August at the 5th Mid-European Clay Conference MECC 2010 in Budapest.

Dr. John Kettler was awarded in the first phase of the AC2 entrepreneurship competition for his business concept “isoTOP GmbH”, which supports industrial customers with an exclusive and innovative measuring system in 2010. This system is capable to identify chemo-toxic substances in sealed containers. In the final phase of the NUK Köln entrepreneurship competition he reached the top 13.

8 Selected R&D projects

8.1. EU projects

CARBOWASTE – Treatment and Disposal of Irradiated Graphite and Other Carbonaceous Waste, (02/2008 - 01/2012); Coordination: FZJ

G-MOSAIC - GMES services for Management of Operations, Situation Awareness and Intelligence for regional Crises; 01/2009 - 12/2011

LIMES - Land/Sea Integrated Monitoring for European Security; 12/2006 – 05/2010

ACSEPT - Actinide reCycling by SEParation and Transmutation, (03/2008 - 02/2012); Work package leader: Dr. G. Modolo, FZJ

SKIN Slow Processes in Close-to-Equilibrium Conditions for Radionuclides in Water/Solid Systems of Relevance to Nuclear Waste Management, (01/2011 – 12/2013); Work package leader: Prof. D. Bosbach, FZJ

8.2. More projects

Wechselwirkung mobilisierter Radionuklide mit sekundären Phasen in endlagerrelevanten Formationswässern (04/2007 - 03/2010)
Bundesministerium für Wirtschaft und Technologie (BMWi), Berlin/Deutschland

Grundlegende Untersuchungen zur Entwicklung und Optimierung von Prozessen zur Abtrennung langlebiger Radionuklide (Partitioning) – Energie 2020+ (07/2009 - 06/2012)
Bundesministerium für Wirtschaft und Technologie (BMWi), Berlin/Deutschland
Kooperation mit Universität Heidelberg/Deutschland; KIT, Karlsruhe/Deutschland; Universität Erlangen/Deutschland

Review of the long-term performance of potential Pu-wasteforms and radionuclide release from Pu-wasteforms under repository conditions (01/2010 - 04/2010)
NDA - Radioactive Waste Management Directorate, Oxfordshire/GB
Kooperation mit Brenk Systemplanung GmbH, Aachen/Deutschland

Neue Materialien für die nukleare Entsorgung (12/2009 – 12/2012)
Ministerium für Innovation, Wissenschaft, Forschung und Technik des Landes Nordrhein-Westfalen (MIWFT), Düsseldorf/Deutschland

VESPA - Verhalten langlebiger Spalt- und Aktivierungsprodukte im Nahfeld eines Endlagers und Möglichkeiten ihrer Rückhaltung (07/2010 – 06/2013)
Bundesministerium für Wirtschaft und Technologie (BMWi), Berlin/Deutschland

9 Committee work

Prof. Dr. D. Bosbach:

- Vertreter des Forschungszentrums Jülich im Kompetenzverbund Kerntechnik (2010).
- Director JARA Energy
- Mitglied des Beirates des Vorstands der Fachgruppe Radiochemie der GdCh
- NEA-TDB expert group

Prof. Dr. B. Thomauske:

- Kuratoriumsmitglied – Bundesanstalt für Geowissenschaften u. Rohstoffe
- Präsidiums- und Verwaltungsratsmitglied – Deutsches Atomforum
- Beiratsmitglied – VKTA Rossendorf
- Mitglied - Programmausschuss der Kerntechnischen Gesellschaft zur Jahrestagung Kerntechnik
- Vorsitzender Prüfungsausschuss Masterstudiengang „Nuclear Safety Engineering“

Dr. I. Niemeyer:

- European Safeguards Research and Development Association (ESARDA): Steering Committee,
- International Society for Photogrammetry and Remote Sensing (ISPRS): International Policy Advisory Committee (IPAC)

Dr. B. Richter:

- Institute of Nuclear Materials Management (INMM): Associate Editor
- European Safeguards Research and Development Assosiation (ESARDA): Editorial Commitee

Priv.-Doz. Dr. H. Schlenz:

- Co-Autor des Nationalen Entwicklungsplans Elektromobilität der Bundesregierung (2009).
- NEA-TDB expert group

Dr. H. Tietze-Jaensch:

- Entrap Steering Committee (European Network of Testing facilities for the quality checking of RAdioactive waste Packages)
- AK-HAW: BMBF Arbeitskreis für HAW Produkte
- Appointed member of the “Public Consultancy Board of the Polish National Programme for the Reduction of Emissions”

Dr. H.-J. Steinmetz:

- Appointed as a member of the International Program Committee (IPAC) of the largest international annual Waste Management Conference in Phoenix / Az. (USA).

K. Aymanns:

- Nominated as deputy representative of the German standardization (DIN) committee for waste water treatment in nuclear power plants.

10 Patents

E. Mauerhofer, J. Kettler, M. Steinbusch: „Verfahren zur Detektion von Sprengstoff in unterirdischen Objekten und Vorrichtung zur Durchführung“, DE 10 2008 063 735

E. Mauerhofer, J. Kettler: “Verfahren zur zerstörungsfreien Elementanalyse großvolumiger Proben und Vorrichtung zur Durchführung“, Deutsche Patentanmeldung 10 2010 031 844. Angemeldet am 27.10.2010.

Modolo G.; Odoj R.: Method of separating a trivalent americium from trivalent curium, US Patent 7,754,167 B2 erteilt Juli 13, 2010.

W. von Lensa, D. Vulpius, R. Nabbi, H.-J. Steinmetz, K. Baginski: "Verfahren zur Teildekontamination radioaktiver Abfälle", (Erfindungsmeldung: 12.07.2010)

11 Publications

The scientific and technical results of the work carried out at IEK-6 are published in relevant journals and presented to interested specialist audience at national and international conferences on the subject.

Tab. 31: Publications 2009/2010

Year		2009	2010
Publications	Peer-reviewed journals	20	8
	Books and journals	1	1
	Proceedings	8	17
	Diploma/Master theses	1	4
	PhD theses	2	2
Conferences	Presentations	10	17
	Poster	8	16

11.1. Highlights

Bai, Y.F., Mauerhofer, E., Wang, D.Z., Odoj: R.:

An improved method for the non-destructive characterization of radioactive waste by gamma scanning

Applied Radiation and Isotopes 67 (2009)1897–1903

A method to improve the reliability and accuracy of activity results in segmented gamma scanning of radioactive waste drums with non-uniform isotope and matrix distribution has been developed. The improved method which is based on numerical simulations of the measured angular dependent count rate distribution during drum rotation in segmented gamma scanning has been validated through the measurement of Cs-137 and Co-60 activities in 13 real radioactive waste drums with heterogeneous activity and matrix distributions. The results were compared to that obtained for the conventional method assuming homogeneous activity and matrix distributions.

Bukaemskiy A.A., Barrier D., Modolo G.:

Compressibility and sinterability of CeO_2-8YSZ powders synthesized by a wet chemical method

Journal of the European Ceramic Society, 29 (2009) 10, 1947 - 1954

The compressibility and sinterability of CeO2–8YSZ powders prepared by co-precipitation were investigated in detail. It was shown that the compressibility curves are characterized by three linear parts at low, middle and high pressures. The middle and high regions of the applied pressure, as least investigated, were studied in detail. The specific values of the compaction pressure (PY2) and density (ρY2) at the intersection point of the compressibility curves were determined for all investigated powders. It was shown that the compressibility curves for all investigated powders can be described by two straight lines by using special coordinates ρG/ρY2 and log(P/PY2). The sinterability curves of powders after drying and after calcination at 350 °C have a pronounced maximum. The optimum compaction pressures (P*) corresponding to the pressure at the maximal value of sintered density were determined for all investigated powders. It was shown that the region of optimal pressures is in the upper part of the middle-pressure region, whereas the P*/PY2 ratio varies between 0.7 and 0.9. The influence of the powder fractionation on the sinterability of the powders was also studied in detail as a function of the compaction pressure and calcination temperature.

Curtius H., Ufer K., Dardenne K.:

Preparation and characterization of Zr-IV-containing Mg-Al-Cl layered double hydroxide

Radiochimica Acta, 97 (2009), 423 - 428

In order to contribute to the long-term safety analysis of direct disposed research reactor fuel elements, the corrosion behaviour of these fuel-types in final repository relevant salt brines was determined. Due to the corrosion processes, radionuclides were mobilized first, but then trapped by the formed secondary phases. A Mg-Al layered double hydroxide (LDH) with chloride as interlayer anion was identified as one crystalline secondary phase component. The possibility to incorporate zirconium-IV into the lattice structure of the Mg-Al-Cl LDH was investigated by a co-precipitation process. The element zirconium was chosen because it has a low absorption cross section for neutrons, and is therefore used for nuclear energy applications, such as for cladding fuel elements. No zirconium release was detected, when the obtained LDH was treated with an ammonium carbonate solution. The molar stoichiometry with respect to Mg, Al and Zr remained stable and this is the first indication for the incorporation of zirconium. For further examination, the material was analysed by powder X-ray diffraction (XRD) combined with a Rietveld refinement. Due to a recursive calculation inside the Rietveld refinement, it was possible to derive structural parameters of the disordered LDH. Further on, the Mg-Al-Zr-LDH was analysed by EXAFS and the results did show that Zr is the central metal atom coordinated by 5 OH groups and by one chloride.

Hansen, B., Curtius, H., Odoj, R.:

Synthesis of a Mg-Cd-Al layered double hydroxide and sorption of selenium
Clays and Clay Minerals, Vol. 57, No. 3 (2009), 330 – 337.

Leaching experiments with metallic uranium-aluminum research-reactor fuel elements in repository-relevant $MgCl_2$-rich salt brine (brine 2) were performed. A Mg-Al layered double hydroxide (LDH) with chloride as the interlayer anion was identified as a crystalline secondary-phase component. In the present study, the incorporation of Cd into the structure of the Mg-Al-Cl LDH was investigated. Synthesis by a coprecipitation method was performed and the Mg-Cd-Al-Cl LDH obtained was characterized. The sorption behaviour of selenium on the LDH was investigated in water, clay pore-water (Mont-Terri-type), and brine 2. Using a LDH concentration of 10 g/L, the sorption kinetics were rapid and equilibrium was reached within 12 h. The sorption of selenium decreased with increasing amount of chloride anions in the solutions. The chloride anions acted as competing anions for the sorption of selenium. The effect of pH on selenium sorption was investigated and a large buffer capacity of the LDH was observed. For the range of selenium concentration used, linear sorption isotherms were obtained which obeyed the Freundlich and Dubinin-Radushkevich models. From these, the energies of selenium sorption were calculated to be in the range of ion-exchange processes.

Modolo G., Kluxen P., Geist A.:

Demonstration of the LUCA process for the separation of americium(III) from curium(III), californium(III), and lanthanides(III) in acidic solution using a synergistic mixture of bis(chlorophenyl)dithiophosphinic acid and tris(2-ethylhexyl)phosphate
Radiochimica Acta, 98 (2010) 4, 193 - 201

The LUCA process was developed at Forschungszentrum Jülich for the selective separation of Am(III) from an acidic solution containing the trivalent actinides Am(III), Cm(III), and Cf(III) as well as lanthanides. A mixture of 0.4 mol/L bis(chlorophenyl)dithiophosphinic acid and 0.15 mol/L tris(2-ethylhexyl)phosphate dissolved in 20% isooctane/80% tert-butyl benzene was used as the extractant. The process was carried out in centrifugal contactors using an optimized flowsheet involving 7 stages for extraction, 9 stages for scrubbing and 8 stages for back-extraction. Very encouraging results were obtained. A high feed decontamination factor was obtained for Am(III) (>1000), and recovery in the product after stripping was higher than 99.8%. The Am(III) product was contaminated with 0.47% Cm(III). More than 99.9% Cf(III), Eu(III) and >99.5% Cm(III) inventories were directed to the raffinate and the contamination with Am(III) (<0.08%) was low. The experimental results were in good agreement with the predictions of a computer code.

11.2. Publications 2009

11.2.1 Journal papers

Peer-reviewed journals

Bai, Y.F., **Mauerhofer, E.**, Wang, D.Z., **Odoj: R.**: An improved method for the non-destructive characterization of radioactive waste by gamma scanning, Applied Radiation and Isotopes 67 (2009)1897–1903

Bosbach, D.; Luckscheiter, B.; Brendebach, B.; Denecke, M.A.; Finck, N.: High level nuclear waste glass corrosion in synthetic clay pore solution and retention of actinides in secondary phases, Journal of Nuclear Materials, 385 (2) (2009) 2, 456 – 460

Bukaemskiy, A.A.; **Barrier, D.**; **Modolo, G.**: Thermal and Crystallization Behaviour of ThO_2-CeO_2 system, Journal of Alloys and Compounds, 485 (2009) 1/2, 783 – 788

Bukaemskiy, A.A.; **Barrier, D.**; **Modolo, G.**: Compressibility and sinterability of CeO2-8YSZ powders synthesized by a wet chemical method, Journal of the European Ceramic Society, 29 (2009) 10, 1947 – 1954

Bukaemskiy, A.A.; **Barrier, D.**; **Modolo, G.**: Thermal and Crystallization Behaviour of 8YSZ-CeO2 system, Journal of Alloys and Compounds, 472 (2009) 1/2, 286 – 293

Curtius, H.; Ufer, K.; Dardenne, K.: Preparation and characterization of Zr-IV-containing Mg-Al-Cl layered double hydroxide, Radiochimica Acta, 97 (2009), 423 – 428

Fermvik, A.; Ekberg, C.; Englund, S.; Foreman, M.R.S.J.; **Modolo, G.**; Retegan, T.; Skarnemark,G.: Influence of dose rate on the radiolytic stability of a BTBP solvent for actinide(III)/lanthanide(III) separation, Radiochimica Acta, 97 (2009), 319 – 324

Finck, N.; Schlegel, M.; **Bosbach, D.**: Sites of Lu(III) Sorbed to and Coprecipitated with Hectorite, Environmental Science and Technology, 43 (2009) 23, 8807 – 8812

Hansen, B., Curtius, H., Odoj, R.: Synthesis of a Mg-Cd-Al layered double hydroxide and sorption of selenium. Clays and Clay Minerals, Vol. 57, No. 3 (2009), 330 – 337.

Klinkenberg, M.; Kaufhold, S.; Dohrmann, R.; Siegesmund, S.: Abrasivity by bentonite dispersions, Applied Clay Science, 46 (2009) 1, 37 – 42

Lin, X.; Gerstenberg, H.; Lierse von Gostomski, Ch.; Henkelmann, R.; Türler, A.; **Rossbach, M.:** Determination of ko-values for the reactions 94Zr(n,y) 95Zr and 96Zr(n,y) 97Zr-97mNb by irradiation in highly thermalized neutron flux, Applied Radiation and Isotopes, 67 (2009) 12, 2092 – 2096

Magnusson, D.; Christiansen, B.; Glatz, J.-P.; Malmbeck, R.; **Modolo, G.**; Serrano-Purroy, D.; Sorel, C.: Towards an optimized flow-sheet for a SANEX demonstration process using centrifugal contactors, Radiochimica Acta, 97 (2009) 3, 155 – 159

Magnusson, D.; Christiansen, B.; Glatz, J.-P.; Malmbeck, R.; **Modolo, G.**; Serrano-Purroy, D.; Sorel, Chr.: Demonstration of a TODGA based Extraction Process for the Partitioning of Minor Actinides from a PUREX Raffinate - Part III: Centrifugal Contactor Run using Genuine Fuel Solution, Solvent Extraction and Ion Exchange, 27 (2009) 1, 26 – 35

Magnusson, D.; Chritiansen, B.; Foreman, M.R.S.; Geist, A.; Glatz, J.-P.; Malmbeck, R.; **Modolo, G.**; Serrano-Purroy, D.; Sorel, C.: Demonstration of a SANEX Process in Centrifugal Contactors using the CyMe4-BTBP Molecule on a Genuine Fuel Solution, Solvent Extraction and Ion Exchange, 27 (2009) 2, 97 – 106

Mincher, B.J.; **Modolo, G.**; Mezyk, St.P.: The Effects of Radiation Chemistry on Solvent Extraction 3: A Review of Actinide and Lanthanide Extraction, Solvent Extraction and Ion Exchange, 27 (2009) 5/6, 579 – 606

Mincher, B.J.; **Modolo, G.**; Mezyk, St.P.: Review Article: The Effects of Radiation Chemistry on Solvent Extraction: 1. Conditions in Acidic Solution and a Review of TBP Radiolysis, Solvent Extraction and Ion Exchange, 27 (2009) 1, 1 – 25

Mincher, B.J.; **Modolo, G.**; Mezyk, St.P.: Review Article: The Effects of Radiation Chemistry on Solvent Extraction: 2. A Review of Fission-Product Extraction, Solvent Extraction and Ion Exchange, 27 (2009) 3, 331 – 353

Rezniczek, A.; **Richter, B.**: Assessment of the Performance of Containment and Surveillance Equipment, Part I: Methodology, ESARDA-Bulletin, 41 (2009) June, 46 – 50

Rezniczek, A.; **Richter, B.**; Jussofie, A.: Assessment of the Performance of Containment and Surveillance Equipment, Part II: Trial Application, ESARDA-Bulletin, 41 (2009) June, 51 – 61

Richter, B.: The ESARDA Working Group on Containment and Surveillance, Activities in 2008 - Chairman's Report, ESARDA Bulletin, 41 (2009), 41-44

11.2.2 Proceedings/Books

Proceedings

Benay, G.; **Modolo, G**.; Robisson, A.C.; Grandjean, S.: Microspheres prepared by Internal Gelation for Actinide Co-Conversion - Influence of Organic Precursors in Initial Solution on Structure during Thermal Treatment, International Conference ATALANTE 2008 Nuclear Fuel Cycles for a Sustainable Future May 19-23 2008 Montpellier, France

Carrot, M.; Fox, D.; Maher, C.; **Modolo, G.**; McLachlan, F.; Sarsfield, M.; Taylor, R.; Woodhead,D.: Extraction and stripping of actinides in TBP and TODGA/TBP systems for advanced fuels processing, Proceedings of Global 2009, Paper 9033, Paris, France. - 6.-11.09.2009

Janssens, W.A.M.; Autrusson, B.; Boella, M.; Bril, L.-V.; Goncalves, J.G.M.; Janssens-Maenhout, G.G.A.; Martikka, E.; Mayer, K.; Peerani, P.; Rezniczek, A.; Richard, M.; **Richter, B.**; Sevini, F.; Stanley, W.T.; Stein, G.; Weh, R.: A Selection of Recent Achievements and Future Challenges in Safeguards R&D as Identified by the European Safeguards Research and Development Association, Proceedings of the INMM 50th Annual Meeting, Tuscon, 12.-16 Juli 2009, erschienen auf CD-ROM

Modolo, G.; Kluxen, P.; Geist, A.: Selective separation of americium(III) from curium(III), californium(III), and lanthanides(III) by the LUCA process, Proceedings of Global 2009, Paper 9193, Paris, France, 6-11.10.2009

Rezniczek, A.; **Richter, B.**; Jussofie, A.: Assessment of the Performance of Containment and Surveillance Equipment - Trial Application, Proceedings of the 31st ESARDA Annual Meeting, Vilnius, 26.-28.Mai 2009. - Erschienen auf CD-ROM

Stein, M.; Lange, S.; Möslinger, M.; Neumann, G.; Queirolo, A.; **Richter, B.**: Papier des ESARDA-Board and der WG-Chairs, Proceedings of the INMM 50th Annual Meeting, Tuscon, 12.-16. Juli 2009. - Erschienen auf CD-ROM

Stein, M.; Lange, S.; Möslinger, M.; Neumann, G.; Queirolo, A.; **Richter, B.**: The IAEA's Next Generation Surveillance System, System Testing - Phase IV Report, Prod. INMM 50th Annual Meeting, Tucson, 12.-16. Juli 2009. - Erschienen auf CD-ROM

Stein, M.; **Richter, B.**; Möslinger, M.; Queirolo, A.; Heppleston, M.; Neumann, G.; Lange, S.: The Next Generation Surveillance System - Development Project Overview, Proceedings of the 31st ESARDA Annual Meeting, Vilnius, 26.-28. Mai 2009. - Erschienen auf CD-ROM

Books

Jasani, B.; **Niemeyer, I.**; Nussbaum, S.; **Richter, B.;** Stein, G. (Hrsg.): International Safeguards and Satellite Imagery, Key Features of the Nuclear Fuel Cycle and Computer-Based Analysis, Springer, 2009, 9783540791317

11.2.3 Internal reports

Kreutz, F.: Bericht über die Prüfung der Daten und Unterlagen zu den COGEMA HAW-Glaskokillen der Beladung für den Transport VGO92, PKS-WAA-VG091 / 2009, Version: 1.0 vom 30.01.2009 Prüfberichte AREVA, Version: 1.0 vom 30.01.2009 Prüfberichte AREVA, Jülich, FZJ, Institut für Energieforschung-6, 2009

Kreutz, F.: Bericht über die Prüfung der Daten und Unterlagen zu den COGEMA HAW-Glaskokillen der Beladung für den Transport VGO92, PKS-WAA-VG092 / 2009, Version: 1.0 vom 05.11.2009 Prüfberichte AREVA, Version: 1.0 vom 05.11.2009, Jülich, FZJ, Institut für Energieforschung-6, 2009

Kreutz, F.: Bericht über die Prüfung der Daten und Unterlagen zu den COGEMA HAW-Glaskokillen der Beladung für den Transport VGO93, PKS-WAA-VG093 / 2009, Version: 1.0 vom 21.04.2009 Prüfberichte AREVA, Version: 1.0 vom 21.04.2009, Jülich, FZJ, Institut für Energieforschung-6, 2009

Kreutz, F.: Bericht über die Prüfung der Daten und Unterlagen zu den COGEMA HAW-Glaskokillen der Beladung für den Transport VGO94, PKS-WAA-VG094 / 2009, Version: 1.0 vom 05.11.2009 Prüfberichte AREVA, Version: 1.0 vom 05.11.2009, Jülich, FZJ, Institut für Energieforschung-6, 2009

Kreutz, F.: Bericht über die Prüfung der Daten und Unterlagen zu den COGEMA HAW-Glaskokillen der Beladung für den Transport VGO95, PKS-WAA-VG095 / 2009, Version: 1.0 vom 15.10.2009 Prüfberichte AREVA, Version: 1.0 vom 15.10.2009, Jülich, FZJ, Institut für Energieforschung-6, 2009

Kreutz, F.: Bericht über die Prüfung der Daten und Unterlagen zu den COGEMA HAW-Glaskokillen der Beladung für den Transport VGO96, PKS-WAA-VG096 / 2009, Version: 1.0 vom 31.08.2009 Prüfberichte AREVA, Version: 1.0 vom 31.08.2009, Jülich, FZJ, Institut für Energieforschung-6, 2009

Kreutz, F.: Bericht über die Prüfung der Daten und Unterlagen zu den COGEMA HAW-Glaskokillen der Beladung für den Transport VGO97, PKS-WAA-VG097 / 2009, Version: 1.0 vom 02.11.2009 Prüfberichte AREVA, Version: 1.0 vom 02.11.2009, Jülich, FZJ, Institut für Energieforschung-6, 2009

Kreutz, F.: Bericht über die Prüfung der Daten und Unterlagen zu den COGEMA HAW-Glaskokillen der Beladung für den Transport VGO97, PKS-WAA-VG097 / 2009, Version: 1.0 vom 10.12.2009, Prüfberichte AREVA

Modolo, G.: EU-Project ACSEPT (Contract No.: FP7-CP-2007-211267) WPASR n°1, WORKPACKAGE ACTIVITY SUMMARY REPORT, WP1.4 - Conversion, Reporting Period: 2008-03-01 - 2008-08-31

Modolo, G.: EU-Project ACSEPT (Contract No.: FP7-CP-2007-211267) WPASR n°1, WORKPACKAGE ACTIVITY SUMMARY REPORT, WP1.4 - Conversion, Reporting Period: 2008-09-01 - 2009-02-29

Modolo, G.: EU-Project ACSEPT (Contract No.: FP7-CP-2007-211267) WPASR n°1, WORKPACKAGE ACTIVITY SUMMARY REPORT, WP1.4 - Conversion, Reporting Period: 2009-03-01 - 2009-08-31

Modolo, G.; Benay, G.; Sypula, M.; Daniels, H.; Kluxen, P.; Schreinemachers, C.: EU-Project ACSEPT (Contract No.: FP7-CP-2007-211267) HYBAR n°1-Half-Yearly Beneficiary Activity Report, Reporting Period: 2008-03-01 - 2008-08-31

Modolo, G.; Benay, G.; Sypula, M.; Daniels, H.; Kluxen, P.; Schreinemachers, C.; Sadowski, F.: EU-Project ACSEPT (Contract No.: FP7-CP-2007-211267) HYBAR n°2-Half-Yearly Beneficiary Activity Report, Reporting Period: 2008-09-01 - 2009-02-29

Modolo, G.; Sypula, M.; Wilden, A.; Kluxen, P.; Schreinemachers, C.; Daniels, H.; Sadowski, F.: EU-Project ACSEPT (Contract No.: FP7-CP-2007-211267) HYBAR n°3-Half-Yearly Beneficiary Activity Report, Reporting Period: 2009-03-01 - 2009-08-31

Steinhardt, T.; Tietze-Jaensch, H.; Bosbach, D.: Auditierung von LR und Inspektion der Verglasungsanlage WVP Sellafield von Sellafield Ltd. durch die Produktkontrollstelle PKS am 11. und 12.03.2009, PKSING-ENG I/ 2009 - Rev. 1.3 vom 08.12.2009 Inspektionsberichte BNGS, 2009

Vulpius, D.: The Carbowaste Project, our further works, 2nd Steering Committee Meeting, April 21-22, 2009 Marcoule, France

Vulpius, D.: The Carbowaste Project, Work Package 3, - Progress Report, Carbowaste 2nd Working Group 3 and 4 Meeting, June 9-10, 2009, Madrid, Spain.

Vulpius, D.: Work Package 4, 2009, in: Carbowaste, 1st Periodic Report, European Commission, 29.05.2009

11.2.4 Poster

Bukaemskiy, A.A.; Modolo, G.; Bosbach, D.: Physical properties of ceramic in the CeO2-8YSZ and Nd203-8YSZ systems, CALPHAD XXXVIII, Prague: 15.05.2009 - 16.05.2009

Daniels, H.: Co-conversion of actinides into a ceramic phase, Evaluation of the programme nuclear safety research (POF II), Karlsruhe: 24.03.2009

Daniels, H.; Neumeier, S.; Modolo, G.; Odoj, R.: Sol-Gel Prozesse zur Herstellung keramischer Kernbrennstoffe, DKG Jahrestagung, Aachen: 03.03.2009

Hansen, B.; Curtius, H.; Odoj, R.: Preparation and characterization of a Fe(II)-containing Mg-Al-Cl layered double hydroxide, XIV International Clay Conference, Castellaneta Marina, Italy: 14.06.2009 - 20.06.2009

Klinkenberg, M.; Dohrmann, R.; Kaufhold, S.; Siegesmund, S.: Influence of carbonate microfabrics on the failure strength of Opalinus Clay and Callovo-Oxfordian Clay stones, XIV International Clay Conference, Castellaneta Marina, Italy: 14.06.2009 - 20.06.2009

Krumbach, H.; Steinmetz, H.-J.; Odoj, R.: Impacts of the Events on the 11th of September 2001 in the United States on Radiation Protection, the Nuclear Waste Management and the Nuclear Security in Germany, Waste Management Conference, Phoenix Arizona US: 01.03.2009 - 05.03.2009

Krumbach, H.; Steinmetz, H.-J.; Odoj, R.; Wartenberg, W.; Gronau, H.: Product Control of Waste Products with New Coating Materials, Waste Management Conference, Phoenix Arizona USA: 01.03.2009 - 05.03.2009

Neumeier, S.; Modolo, G.; Telle, R.; **Bosbach, D.**: Maßgeschneiderte Keramiken im Fokus nuklearer Entsorgungsstrategien, JARA-Energy-Poster Präsentation im Rahmen des Tages der Neugier, Jülich: 06.09.2009

11.2.5 Presentations

Conferences:

Daniels, H.; Benay, G.; Modolo, G.; Neumeier, S.; Odoj, R.: Uran-basierte Keramiken zur Actinoiden-Transmutation, DKG Jahrestagung, Aachen: 24.03.2009

Daniels, H.; Modolo, G.; Neumeier, S.; Bosbach, D.: Co-conversion of actinides into a ceramic phase, CHERNE Workshop 2009, Jülich: 08.06.2009

Kettler, J.; Mauerhofer, E.; Rossbach, M.; Bosbach, D.: An innovative method based on prompt-gamma-neutron-activation-analysis for non-destructive determination of toxic elements in radioactive waste drums, Winter Meeting of the American Nuclear Society, Washington DC, USA: 15.11.2009 - 19.11.2009

Klinkenberg, M.; Dohrmann, R.; Kaufhold, S.; Siegesmund, S.: Influence of clay microfabrics on the petrophysical properties of clays. 87. DMG-Tagung 2009, Hallesches Jahrbuch für Geowissenschaften, Band 31. - S. 128 Halle (Saale): 13.09.2009 - 16.09.2009

Modolo, G.; Kluxen, P.; Geist, A.: Selective separation of americium(III) from curium(III), californium(III), and lanthanides(III) by the LUCA process, Global 2009, Paris: 06.09.2009 - 11.09.2009

Neumann, A.; Curtius, H.; Odoj, R.: X-ray diffraction analysis of the corrosion products of research reactor fuel elements, Jahrestagung Kerntechnik, Dresden: 12.05.2009 - 14.05.2009

Neumeier, S.; Bukaemskiy, A.; Daniels, H.; Modolo, G.; Odoj, R.: Fixierung von Actinoiden und langlebigen Spaltprodukten in keramischen Materialen, DKG Jahrestagung, Aachen: 24.03.2009

Richter, B.; Rezniczek, A.; Jussofie, A.: Assessment of the Performance of Containment and Surveillance Equipment - Trial Application, 31st ESARDA Annual Meeting,Vilnius, Litauen: 26.05.2009 - 28.05.2009

Rossbach, M.: Ion beam analysis for cultural heritage research, International Topical Meeting on Nuclear Research Applications and Utilization of Accelerators, IAEA, Wien, Austria: 04.05.2009 - 08.05.2009

Vulpius, D.: The Carbowaste Project, Treatment and Purification of i-Graphite, 8th EPRI International Decommissioning and Radioactive Waste Workshop, Hamburg: 05.10.2009 - 08.10.2009

Invited Talks

Bosbach, D.: Der wissenschaftliche Stand der nuklearen Endlagerung, Projekt Leonardo der RWTH Aachen, Aachen: 03.12.2009

Bosbach, D.: Materialwissenschaftliche Aspekte der nuklearen Entsorgung, Kompetenzverbund Kerntechnik, Peine: 23.11.2009

Tietze-Jaensch, H.: Sichere Nukleare Entsorgung, Notwendigkeit und Möglichkeit, GeoScience Kolloquium der Freien Universität Berlin, 2.12.2009

Tietze-Jaensch, H.: Radioactive waste, management, transport & disposal, Nuclear Power Summit, Warsaw, 25-26 Nov 2009

Tietze-Jaensch, H.: Nuclear Energy for Poland, Managing safe & reliable energy supply, Faculty of Physics, TU Warsaw, 14 May 2009

Additional/Internal Talks

Bosbach, D.: Der wissenschaftliche Stand der nuklearen Endlagerung, Kolloquium Energie und Umwelt, Jülich: 22.09.2009

Daniels, H.; Benay, G.; Neumeier, S.; Sadowski, F.; Modolo, G.: Ceramic nuclear fuel via sol gel processes, ACSEPT First Annual Meeting, Madrid, Spain: 16.03.2009 - 20.03.2009

Modolo, G.: Co-conversion of actinides (EUROPART --> ACSEPT), ACSEPT Brainstorming meeting on co-conversion issues, Madrid, Spain: 16.03.2009 - 20.03.2009

Modolo, G.: Überblick über den Stand der Partitioning Arbeiten in Jülich, Institut für Anorganische Chemie Universität Karlsruhe (TH), Karlsruhe: 05.10.2009

Modolo, G.; Sypula, M.; Wilden, A.; Schreinemachers, C.: GANEX: FZJ Concepts & Progress, ACSEPT Second Half-Year Meeting, Bologna, Italy: 21.09.2009 - 23.09.2009

Sypula, M.; Daniels, H.; Kluxen, P.; Schreinemachers, C.; Sadowski, F.; Modolo, G.: Progress of work within WP2 and WP3, ACSEPT First Annual Meeting, Madrid, Spain: 16.03.2009 - 20.03.2009

Vulpius, D.: The Carbowaste Project, Work Package 4, Carbowaste, Progress Report, Carbowaste, 2nd Working Group 3 and 4 Meeting, Madrid, Spain: 09.06.2009 - 10.06.2009

11.3. Publications 2010

11.3.1 Journal papers

Peer-reviewed Journals

Iqbal, M.; Huskens, J.; Verboom, W.; **Sypula, M.; Modolo, G.**: Synthesis and Am/Eu extraction of novel TODGA derivates, Supramolecular Chemistry, 22 (2010) 11/12, 827 - 837

Kaufhold, S.; Dohrmann, R.; **Klinkenberg, M.:** Water uptake capacity of bentonites; Clays and Clay Minerals, 58 (2010) 1, 37- 43

Kaufhold, S.; Dohrmann, R.; **Klinkenberg, M.**; Siegesmund, S.; Ufer, K.: The N_2-BET specific surface area of bentonites; Journal of Colloid and Interface Science, 349 (2010) 1, 275 – 282

Lewis, F.W.; Harwood, L.M.; Hudson, M.J.; Drew, M.G.B.; **Modolo, G.**; **Sypula, M.**; Desreux, J.F.; Bouslimani, N.; Vidick, G.: Interaction of 6,6-bis(5,5,8,8-tetramethyl-5,6,7,8-tetrahydro-1,2,4-benzotriazin-3-yl)-2,2:6,2-terpyridine (CyMe4-BTTP) with some trivalent ions such as lanthanide(III) ions and americium(III), Dalton Transactions, 39 (2010), 5172 – 5182

Marpu, P.R.; Neubert, M.; Herold, H.; **Niemeyer, I.**: Enhanced evaluation of image segmentation results, Journal of Spatial Science, 55 (2010) 1, 55 – 68

Mincher, B.J., **Modolo, G.**, Mezyk, St.P.: Review: The Effects of Radiation Chemistry on Solvent Extraction 4: Separation of the Trivalent Actinides and Considerations for Radiation-Resistant Solvent Systems; Solvent Extraction and Ion Exchange, 28 (2010) 4, 415 – 436

Modolo, G., Kluxen, P., Geist, A.: Demonstration of the LUCA process for the separation of americium(III) from curium(III), californium(III), and lanthanides(III) in acidic solution using a synergistic mixture of bis(chlorophenyl)dithiophosphinic acid and tris(2-ethylhexyl)phosphate; Radiochimica Acta, 98 (2010) 4, 193 – 201

Niemeyer, I.; Richter, B.; Dürr, M.; Bosbach, D.: The New Safeguards R & D Structure in Germany - Coordinating the German Support Programme to the IAEA, ESARDA Bulletin 45 (2010), 8-9

11.3.2 Proceedings/Books

Proceedings

Babelot, C.; Neumeier, S.; Bukaemskiy, A.; Modolo, G.; Schlenz, H.; Bosbach, D.: Conditioning of Minor Actinides in Monazite-type Ceramics, First ACSEPT International Workshop, Lisboa, Portugal, 31.03.-02.04.2010

Brutscher, J.,; Birnbaum, A.; Keubler, J.; Jung, S.; Koestlbauer, M.; **Richter, B.**; Schwalbach, P.; von Zweidorf, A.: Concept and Development Status of the Digital Upgrade of the Mini Multi-channel Analyser, Proc. IAEA Symposium on International Safeguards, IAEA-CN-184/031

Button, P.; **Niemeyer, I.**; Okko, O.; Paquette, J.-P.; Parsons, G.; Tadono, T.; Use of SAR Satellite Imagery for Geological Repositories Monitoring, Proc. IAEA Symposium on International Safeguards, IAEA-CN-184/298

Concalves, J. G. M.; Funk, P.; **Richter, B.**: The ESARDA Working Group on Containment and Surveillance: Activities and Achievements, Proceedings IAEA Symposium 2010, Wien

Daniels,H.; Neumeier,S.; Modolo,G.: Synthesis of Uranium-based Microspheres for Transmutation of Minor Actinides, First ACSEPT International Workshop, Lisboa, Portugal, 31.03.-02.04.2010

Deptula, A.; Brykala, M.; Lada, W.; Olczak, T.; Wawszczak, D.; **Modolo, G.; Daniels, H.**; Chmielewski, A.G.: Synthesis of uranium dioxides by Complex Sol-Gel Processes (CSGP)\", Uranium 2010 - the future is U, Proceedings of the 3rd International Conference on Uranium, Volume II, 145-154 (2010) 3rd International Conference on Uranium, August 15-18, 2010, Saskatoon, Canada

Deptula, A.; Brykala, M.; Lada, W.; Olczak, T.; Wawszczak, D.; **Modolo, G.; Daniels, H.**; Chmielewski, A.G.: Synthesis of uranium oxides by Complex Sol-Gel-Process (CSGP), First ACSEPT International Workshop, Lisboa, Portugal, 31.03.-02.04.2010

Listner, C.; Niemeyer, I.: Multiresolution segmentation adapted for object-based change detection, Proceedings SPIE Remote Sensing, Toulouse, September 2010

Modolo, G.; Sypula, M.; Geist, C.; Hill, C.; Sorel, C.; Malmbeck, R.; Magnusson, D.; Foreman, M.R.St.J.: Development and demonstration of a new SANEX process for actinide(III)/lanthanide(III)separation using a mixture of CyMe4BTBP and TODGA as selective extractant; Proceedings of the 10th OECD/NEA Information Exchange Meeting on Actinide and Fission Product P&T, Mito, Japan, 6-10 October 2008, NEA No. 6420, OECD/NEA 2010. - S. 235 – 241

Niemeyer, I.: Supporting Non-Proliferation and Arms Control Treaties by Remote Sensing and Geoinformation Technologies, Proc. ISPRS Technical Commission VIII Symposium 2010, Kyoto, 09.-12.08.2010

Niemeyer, I.; Listner, C.; Buchholz, T.; Hillmann, M.: Monitoring Uranium Mining and Processing Sites: Some Findings From an Airborne Hyperspectral Survey of Uranium Mining Legacies Under Rehabilitation, Proceedings of the Institute of Nuclear Materials Management, 51st Annual Meeting July 11-15, 2010, Baltimore, MD USA

Niemeyer, I.; Richter, B.; Stein, G.: The NPT Review Conference 2010: Perspectives for International Safeguards, Proceedings of the Institute of Nuclear Materials Management, 51st Annual Meeting July 11-15, 2010, Baltimore, MD USA

Remagen, H.H.; **Niemeyer, I.; Richter, B.; Dürr, M.**; Rezniczek, A.; Stein, G.: International Safeguards in Germany - Status and Expectations, Proc. IAEA Symposium on International Safeguards, IAEA-CN-184/298

Schneider, S.; Tietze-Jaensch, H.; Bosbach, D.; Odoj, R.: Numerical Tools for the Evaluation of Super-Compacted Radwaste Residues, Supercomputing in Nuclear Application and Monte Carlo Conference (SNA-MC 2010), Tokyo, Japan: 15.10.2010 - 24.10.2010

Sypula, M.; Wilden, A.; Schreinemachers, C.; Modolo, G.: Separation of An(II) from PUREX raffinate as an innovative SANEX process based on a mixture of TODGA/TBP, First ACSEPT International Workshop, Lisboa, Portugal, 31.03.-02.04.2010

Wilden, A.; Sypula, M.; Schreinemachers, C.; Kluxen, P.; Modolo, G.: I-cycle SANEX process development studies performed at Forschungszentrum Jülich, First ACSEPT International Workshop, Lisboa, Portugal, 31.03.-02.04.2010

Wolfart, E.; Gonçalves, J.G.M.; Gutjahr, K.H.; **Listner, C.**; Loreaux, P.; Marpu, P.; **Niemeyer, I.**; Patrono, A.; Ussorio A.: GIS based Integration and Analysis of multiple source Information for Non-Proliferation Studies, Proc. IAEA Symposium on International Safeguards, IAEA-CN-184/231

Books:

Modolo, G.: Actinide(III)Recovery from High Active Waste Solutions Using Innovative Partitioning Processes, Washington D.C., American Chemical Society, 2010, ACS SYMPOSIUM SERIES 1046, Editors: Chien, M.W.; Mincher, B.J.

11.3.3 Internal reports

Curtius, H.; Kaiser, G.; Paparigas, Z.; Hansen, B.; Neumann, A.; Klinkenberg, M.; Müller, E.; Brücher, H.; Bosbach, D.: Wechselwirkung mobilisierter Radionuklide mit sekundären Phasen in endlagerrelevanten Formationswässern, Forschungszentrum Jülich, 2010, Berichte des Forschungszentrums Jülich, Jül-4333

Deissmann, G.; **Neumeier, S.; Modolo, G.; Bosbach, D.**: Review of the durability of potential plutonium waste forms under conditions relevant to geological disposal, Confidential report, June 2010

Harren, E.; Kreutz, F.; Tietze-Jaensch, H.: Bericht über Audit und Inspektion der VEK bei der WAK EntsorgungsGmbH, Karlsruhe durch die Produktkontrollstelle des Bundesamtes für Strahlenschutz 08.-09.02.2010, PKSINS/BER-WAK 2010-02-Rev. 20100810 Berichtszeitraum 26.10.2009 bis 07.02.2010 Inspektionsberichte WAK/VEK

Harren, E.; Kreutz, F.; Tietze-Jaensch, H.: Bericht über die Prüfung der Daten und Unterlagen zu den WAK-VEK-HAW-Glaskokillen der Beladung für den Transport CG-056, PKS-WAA-CG-056/2010-Rev. 20101215, 2010, Prüfberichte Beladung WAK/VEK

Harren, E.; Kreutz, F.; Tietze-Jaensch, H.: Bericht über die Prüfung der Daten und Unterlagen zu den WAK-VEK-HAW-Glaskokillen der Beladung für den Transport CG-058, PKS-WAA-CG-058/2010-Rev. 20100203, Prüfberichte Beladung WAK/VEK

Harren, E.; Kreutz, F.; Tietze-Jaensch, H.: Bericht über die Prüfung der Daten und Unterlagen zu den WAK-VEK-HAW-Glaskokillen der Beladung für den Transport CG-058, PKS-WAA-CG-058/2010-Rev. 20100908, Prüfberichte Beladung WAK/VEK

Harren, E.; Kreutz, F.; Tietze-Jaensch, H.: Bericht über die Prüfung der Daten und Unterlagen zu den WAK-VEK-HAW-Glaskokillen der Beladung für den Transport CG-059, PKS-WAA-CG-059/2010-Rev. 20100407, 2010, Prüfberichte Beladung WAK/VEK

Harren, E.; Kreutz, F.; Tietze-Jaensch, H.: Bericht über die Prüfung der Daten und Unterlagen zu den WAK-VEK-HAW-Glaskokillen der Beladung für den Transport CG-060, PKS-WAA-CG-060/2010-Rev. 20100810, Prüfberichte Beladung WAK/VEK

Harren, E.; Kreutz, F.; Tietze-Jaensch, H.: Bericht über die Prüfung der Daten und Unterlagen zu den WAK-VEK-HAW-Glaskokillen der Beladung für den Transport CG-060, PKS-WAA-CG-060/2010-Rev. 20100908, Prüfberichte Beladung WAK/VEK

Kreutz, F.; Tietze-Jaensch, H.; Bosbach, D.: Bericht über die Prüfung der Daten und Unterlagen zu den COGEMA HAW-Glaskokillen der Beladung für den Transport VG099, PKS-WAA-VG-099/2010, Version 1.0 vom 05.02.2010

Kreutz, F.; Tietze-Jaensch, H.; Bosbach, D.: Bericht über die Prüfung der Daten und Unterlagen zu den COGEMA HAW-Glaskokillen der Beladung für den Transport VG100, PKS-WAA-VG-100/2010, Version 1.0 vom 15.04.2010

Kreutz, F.; Tietze-Jaensch, H.; Bosbach, D.: Bericht über die Prüfung der Daten und Unterlagen zu den COGEMA HAW-Glaskokillen der Beladung für den Transport VG101, PKS-WAA-VG-101/2010, Version 1.0 vom 07.05.2010

Kreutz, F.; Tietze-Jaensch, H.; Bosbach, D.: Bericht über die Prüfung der Daten und Unterlagen zu den COGEMA HAW-Glaskokillen der Beladung für den Transport VG102, PKS-WAA-VG-102/2010, Version 1.0 vom 30.06.2010

Kreutz, F.; Tietze-Jaensch, H.; Bosbach, D.: Bericht über die Prüfung der Daten und Unterlagen zu den COGEMA HAW-Glaskokillen der Beladung für den Transport VG103, PKS-WAA-VG-103/2010, Version 1.0 vom 05.08.2010

Kreutz, F.; Tietze-Jaensch, H.; Bosbach, D.: Bericht über die Prüfung der Daten und Unterlagen zu den COGEMA HAW-Glaskokillen der Beladung für den Transport VG104, PKS-WAA-VG-104/2010, Version 1.0 vom 01.10.2010

Kreutz, F.; Tietze-Jaensch, H.; Bosbach, D.: Bericht über die Prüfung der Daten und Unterlagen zu den COGEMA HAW-Glaskokillen der Beladung für den Transport VG105, PKS-WAA-VG-105/2010, Version 1.0 vom 17.12.2010

Kreutz, F.; Tietze-Jaensch, H.; Bosbach, D.: Bericht über die Prüfung der Daten und Unterlagen zu den COGEMA HAW-Glaskokillen der Beladung für den Transport VG105 PKS-WAA-VG105/2010, Version 1.0 vom 17.12.2010 Prüfberichte AREVA

Modolo, G.: EU-Projekt ACSEPT, (Contract-No.:FP7-CP-2007-211267), WPASR No.5, WORK-PACKAGE ACTIVITY SUMMARY REPORT, WP1.4 - Conversion, Reporting Period: 01/03/2010-31/08/2010

Modolo, G.; Sypula, M.; Wilden, A.; Kluxen, P.; Schreinemachers, C.; Daniels, H.; Neumeier, S.; Weidenfeld, M.: EU-Project ACSEPT, (Contract-No: FP7-CP-2007-211267), HYBAR No. 4-Half Yearly Beneficiary Activity Report, Reporting Period: 01/08/2009- 31/03/2010

Stein, M.; Lange, S.; Möslinger, M.; Neumann, G.; Queirolo, A.; **Richter, B.**; Schwalbach, P.: The Next Generation Surveillance System, Development Project Overview, JOPAG/05.09-PRG-375

Wilden, A.; Modolo, G.: BMBF-Projekt "Verbundprojekt: Grundlegende Untersuchungen zur Entwicklung und Optimierung von Prozessen zur Abtrennung langlebiger Radionuklide

(Partitioning) - Stabilitätsuntersuchungen und Entwicklung von kontinuierlichen Prozessen", (Förderkennzeichen: 02NUK012E), 1. Halbjahresbericht, 11.02.2010, Berichtszeitraum: 01.07.2009-31.12.2009

Wilden, A.; Modolo, G.: BMBF-Projekt "Verbundprojekt: Grundlegende Untersuchungen zur Entwicklung und Optimierung von Prozessen zur Abtrennung langlebiger Radionuklide (Partitioning) - Stabilitätsuntersuchungen und Entwicklung von kontinuierlichen Prozessen", (Förderkennzeichen: 02NUK012E), 2. Halbjahresbericht, 27.07.2010, Berichtszeitraum: 01.01.2010-30.06.2010

11.3.4 Poster

Babelot, C.; Neumeier, S.; Bukaemskiy, A.; Modolo, G.; Schlenz, H.; Bosbach, D.: Conditioning of Minor Actinides in Monazite-type Ceramics, First ACSEPT International Workshop, Lisboa, Portugal: 31.03.2010 - 02.04.2010

Babelot, C.; Neumeier, S.; Bukaemskiy, G.; Modolo, G.; Bosbach, D.: Conditioning of Minor Actinides in Monazite-type Ceramics, CIMTEC 2010 Conference, Montecatini, Italy, 13.06.2010 - 18.06.2010

Biß, K.; Bongardt, K.; Bourrauel, P.; Cura, H.; Esser, F.; Greiner, W.; Hamzic, S.; **Kettler, J.;** Kolev, N.; **Maier, R**.; Mishustin, I.; **Modolo, G.; Nabbi, R.**; Nies, R.; Pshenichnov, I.; **Rossbach, M.; Shetty, N.; Thomauske, B.; Wank, A.; Wolters, J.:** Feasibility study of gas-cooled ADS, 11th Information Exchange Meeting on Actinide and Fission Product Partitioning and Transmutation, San Francisco, USA: 01.11.2010 - 05.11.2010

Brutscher, J.,; Birnbaum, A.; Keubler, J.; Jung, S.; Koestlbauer, M.; **Richter, B.**; Schwalbach, P.; von Zweidorf, A.: Concept and Development Status of the Digital Upgrade of the Mini Multi-channel Analyser, IAEA Symposium on International Safeguards, IAEA-CN-184/031

Button, P.; **Niemeyer, I.**; Okko, O.; Paquette, J.-P.; Parsons, G.; Tadono, T.; Use of SAR Satellite Imagery for Geological Repositories Monitoring, IAEA Symposium on International Safeguards, IAEA-CN-184/298

Curtius, H.; Kaiser, G.; Müller, E.; Bosbach, D.: Radionuclide Release from research reactor fuel, European Material Conference E-MRS Spring Meeting; Strassbourg: 07.06.2010 - 11.06.2010

Geist, A.; Müllich, U.; **Modolo, G.; Wilden, A.:** Selective aqueous complexation of actinides with hydrophilic BTP and BTBP: towards improve i-SANEX processes, 11th Information Exchange Meeting on Actinide and Fission Product Partitioning and Transmutation, San Francisco, USA: 01.11.2010 - 05.11.2010

Klinkenberg, M.; Curtius, H.; Neumann, A.; Bosbach, D.: Corrosion of research reactor fuel elements in Mont Terri clay pore water - treatment, preparation, and identification of secondary phases - Abstract, p. 483; 4th International Meeting: Clays in Natural & Engineered Barriers for Radioactive Waste Confinement; Nantes - Frankreich: 29.03.2010 - 01.04.2010

Klinkenberg, M.; Dohrmann, R.; Kaufhold, S.; Siegesmund, S.: Influence of Carbonate Microfabrics on the Failure Strength of Callovo-Oxfordian Clay Stones and Opalinus Clay.

Abstract, p. 769; 4th International Meeting: Clays in Natural & Engineered Barriers for Radioactive Waste Confinement; Nantes - Frankreich: 29.03.2010 - 01.04.2010

Krumbach, H.; Steinmetz, H.-J.: Challenges in Compliance with the Waste Acceptance Requirements for the KONRAD Mine; WM2010 Conference; Phoenix, AZ: 07.11.2010 - 11.11.2010

Modolo, G.; Bosbach, D.; Geist, A.; Malmbeck, R.: Recovery of Long-lived Minor Actinides from High Active Waste Solutions using Innovative Partitioning Processes, CIMTEC 2010 Conference, Montecatini, Italy: 13.06.2010 - 18.06.2010

Modolo, G.; Wilden, A.; Neumeier, S.; Babelot, C.; Daniels, H.; Sypula, M.; Bukaemskiy, A.; Schlenz, H.; Bosbach, D.: Neue Entsorgungsstrategien - Integraler Forschungsansatz, Studieninformationstag, RWTH Aachen, Aachen: 09.06.2010

Neumeier, S.; Bukaemskiy, A.; Modolo, G.; Bosbach, D.: Synthesis and Characterization of ZrO2 based Pyrochlore-type Ceramics for Nuclear Waste Conditioning, CIMTEC 2010 Conference, Montecatini, Italy: 13.06.2010 - 18.06.2010

Remagen, H.H.; **Niemeyer, I.; Richter, B.; Dürr, M.**; Rezniczek, A.; Stein, G.: International Safeguards in Germany - Status and Expectations, IAEA Symposium on International Safeguards, IAEA-CN-184/298

Schneider, S.; Tietze-Jaensch, H.; Bosbach, D.; Odoj, R.: Utilization of neutron emission spectra for nuclear inventory determination of super-compacted metallic radioactive waste residues and MC simulation for their evaluation and verification, Neutrons for Global Energy Solution (NGES 2010), Bonn: 27.09.2010 - 29.09.2010

Wolfart, E.; Gonçalves, J.G.M.; Gutjahr, K.H.; **Listner, C.**; Loreaux, P.; Marpu, P.; **Niemeyer, I.**; Patrono, A.; Ussorio A.: GIS based Integration and Analysis of multiple source Information for Non-Proliferation Studies, IAEA Symposium on International Safeguards, IAEA-CN-184/231

11.3.5 Presentations

Conferences:

Daniels, H.; Neumeier, S.; Bukaemskiy, A.A.; Modolo, G.: Co-Conversion of actinides into an uranium-matrix, CIMTEC 2010 Conference, Montecatini, Italy: 13.06.2010 - 18.06.2010

Daniels, H.; Neumeier, S.; Modolo, G.: Synthesis of Uranium-based microspheres for Transmutation of Minor Actinides, First ACSEPT International Workshop, Lisboa, Portugal: 31.03.2010 - 02.04.2010

Haart, L.G.J. de; **Neumann, A.**; Menzler, N. H.: Is chronium poisoning of LSM cathodes avoidable? SOFC-XII Symposium, 219th ECS Meeting, Montreal, Kanada: 01.05.2011 - 06.05.2011

Klinkenberg, M.; Dohrmann, R.; Kaufhold, S.; Siegesmund, S.: Influence of clay microfabrics on petrophysical properties of clay stones and bentonites, 5th Mid-European Clay Conference MECC, Budapest, Hungary 25.08.2010 - 29.08.2010

Listner, C.; Niemeyer, I.: Multiresolution Segmentation Adapted for Object-based Change detection, SPIE Europe Remote Sensing 2010, Toulouse, 20.-23.09.2010

Modolo, G.; Bosbach, D.; Geist, A.; Malmbeck, R.: Recovery of Long-lived Minor Actinides from High Active Waste Solutions using Innovative Partitioning Processes, CIMTEC 2010 Conference, Montecatini, Italy: 13.06.2010 - 18.06.2010

Modolo, G.; Geist, A.; Malmbeck, R.: Separation of AM(III)from Cm(III) and Ln(III)using aromatic dithiophosphinic acid 239th, ASC National Meeting, San Francisco: 22.03.2010 - 22.03.2010

Niemeyer, I.: Supporting Non-Proliferation and Arms Control Treaties by Remote Sensing and Geoinformation Technologies, ISPRS Technical Commission VIII Symposium 2010, Kyoto, 09.-12.08.2010

Niemeyer, I.: SAR and Hyperspectral Satellite Imagery Analysis for Safeguards Purposes, 32nd ESARDA Annual Meeting, Luxemburg, 03.-06.05.2010

Niemeyer, I.: Use of SAR Satellite Imagery for Geological Repositories Monitoring, Application of Safeguards to Geological Repositories (ASTOR) Meeting, Ispra, 08./09.11.2010

Niemeyer, I.; Listner, C.; Buchholz, T.; Hillmann, M.: Monitoring Uranium Mining and Processing Sites: Some Findings from an Airborne Hyperspectral Survey of Uranium Mining Legacies under Rehabilitation, INMM 51st Annual Meeting, Baltimore, 11.-15.07.2010

Niemeyer, I.; Listner, C.; Buchholz, T.; Hillmann, M.; Fischer, C.; Ehrler, C.; Drebenstedt, C.: Entwicklung von Analyseverfahren zum Monitoring bergbaubedingter Umweltauswirkungen mittels der Hyper¬spektralfernerkundung, 11. Geokinematischer Tag, Freiberg, 06./07.05.2010

Niemeyer, I.; Richter, B.; Stein, G.: The NPT Review Conference 2010: Perspectives for International Safeguards, INMM 51st Annual Meeting, Baltimore, 11.-15.07.2010

Schneider, S.; Tietze-Jaensch, H.; Bosbach, D.; Odoj, R.: Numerical Tools for the Evaluation of Super-Compacted Radwaste Residues, Supercomputing in Nuclear Application and Monte Carlo Conference (SNA-MC 2010), Tokyo, Japan: 15.10.2010 - 24.10.2010

Sypula, M.; Wilden, A.; Schreinemachers, C.; Modolo, G.: Separation of An(III)from PUREX raffinate as an innovative SANEX process based on a mixture of TODGA/TBP, First ACSEPT International Workshop, Lisboa, Portugal: 31.03.2010 - 02.04.2010

Wilden, A.; Sypula, M.; Modolo, G.; Geist, A.: One-cycle SANEX process development studies and lab-scale demonstrations, 11th Information Exchange Meeting on Actinide and Fission Product Partitioning and Transmutation, San Francisco, USA: 01.11.2010 - 05.11.2010

Wilden, A.; Sypula, M.; Schreinemachers, C.; Kluxen, P.; Modolo, G.: 1-cycle SANEX process development studies performed at Forschungszentrum Jülich, First ACSEPT International Workshop, Lisboa, Portugal: 31.03.2010 - 02.04.2010

Invited Talks

Curtius, H.: Wechselwirkungen mobilisierter Radionuklide mit sekundären Phasen, 21. Arbeitsskreissitzung Entsorgung von Forschungsreaktoren, Mainz: 10.11.2010

Schneider, S.; Tietze-Jaensch, H.; Bosbach, D.; Odoj, R.: Neutron and gamma emission measurements for the evaluation of supercompacted radioactive waste residues, 11th Int. Seminar of Neutron Scattering, Poznan: 12.05.2010 - 17.05.2010

Tietze-Jaensch, H.: German National Energy Concept and Efficiency Programme, Int. Energy Efficiency Forum, Warsaw, Poland: 27.10.2010 - 29.10.2010

Tietze-Jaensch, H.: Lessons to be learnt from ASSE, Int. Seminar on Nuclear Power for Poland, Warsaw, Poland: 02.04.2010 - 05.04.2010

Additional Talks

Curtius, H.: Radionuclide Release from Research Reactor Spent Fuel, Spent Fuel Workshop, 3.-5.11.2010, Barcelona

Tietze-Jaensch, H.: Sichere Nukleare Entsorgung, Notwendigkeit und Möglichkeit, GeoScience Kolloquium der Freien Universität Berlin, Berlin: 02.12.2010

12 How to reach us

Postal Address

Forschungszentrum Jülich
Institut für Energie und Klimaforschung (IEK-6)
Nukleare Entsorgung
52425 Jülich

By car

Coming from Cologne (Köln) take the A 4 motorway (Cologne – Aachen), leave the motorway at the Düren exit, and then turn right towards Jülich (B 56). After about 10 km, turn off to the right onto the L 253, and follow the signs for "Forschungszentrum".
Coming from Aachen take the A 44 motorway (Aachen – Düsseldorf) and leave the motorway at the Jülich-West exit. At the first roundabout turn left towards Jülich, and at the second roundabout turn right towards Düren (B 56). After about 5 km, turn left onto the L 253 and follow the signs to "Forschungszentrum".
Coming from Düsseldorf Airport take the A 52 motorway (towards Düsseldorf/Mönchengladbach), followed by the A 57 (towards Cologne). Turn off at Neuss-West, and continue on the A 46 until you reach the crossroads "Kreuz Wanlo". Take the A 61 (towards Koblenz/Aachen) until you reach "Dreieck Jackerath" where you should take the A 44 (towards Aachen). Continue as described in "Coming from Düsseldorf".

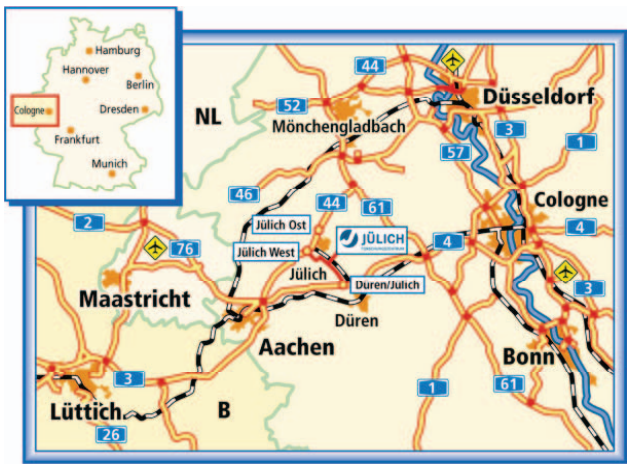

Fig. 148: Euregio Rheinland map

Coming from Düsseldorf on the A44 motorway (Düsseldorf – Aachen) you have two options:
1. (Shorter route but more traffic) turn right at the Jülich-Ost exit onto the B 55n, which you should follow for approx. 500 m before turning right towards Jülich. After 200 m, before the

radio masts, turn left and continue until you reach the "Merscher Höhe" roundabout. Turn left here, drive past the Solar Campus belonging to the University of Applied Sciences and continue straight along Brunnenstrasse. Cross the Römerstrasse junction, continue straight ahead onto Wiesenstrasse and then after the roundabout and the caravan dealers, turn left towards "Forschungszentrum" (signposted).
2. (Longer but quicker route) drive until you reach the "Jülich-West" exit. At the first roundabout turn left towards Jülich, and at the second roundabout turn right towards Düren (B 56). After about 5 km, turn left onto the L 253 and follow the signs to "Forschungszentrum".

Navigation systems

In your navigation system, enter your destination as "Wilhelm-Johnen-Strasse". From there, it is only a few hundred metres to the main entrance – simply follow the signs. The Research Centre itself is not part of the network of public roads and is therefore not recognised by navigation systems.

By train from Cologne Bonn Airport

From the railway station at the airport, take the S13 to Cologne main train station (Hauptbahnhof) and then continue with the regional express to Düren, or go to Köln-Ehrenfeld by regional express and then take the S12 to Düren. Continue from Düren as described in "By train".

By train from Düsseldorf International Airport

From the railway station at the airport, travel to Cologne main train station and then continue on to Düren. Some trains go directly to Düren whereas other connections involve a change at Cologne main train station. Continue from Düren as described in "By train".

Fig. 149: Forschungszentrum Jülich

By train:

Take the train from Aachen or Cologne to the train station in Düren. From here, take the local train ("Rurtalbahn" [RTB]) for Jülich and get out at the "Forschungszentrum" stop. To make sure that the train stops at "Forschungszentrum" you should press the request stop button (Haltewunsch) in good time after the "Selgersdorf" stop. Bus number 11 leaves from this stop for the Research Centre (for bus timetables, see "Aachen - Jülich bus connections"). If you walk, it will take you approximately 20 minutes to reach the Research Centre's main entrance.

By bus:

Aachen - Jülich bus connection

The SB11 bus line connects the Research Centre to the local public transport system. Commuters from Aachen travelling to the Research Centre have 19 options every day of reaching their destination and 18 in the other direction to get back to Aachen.

Institute:

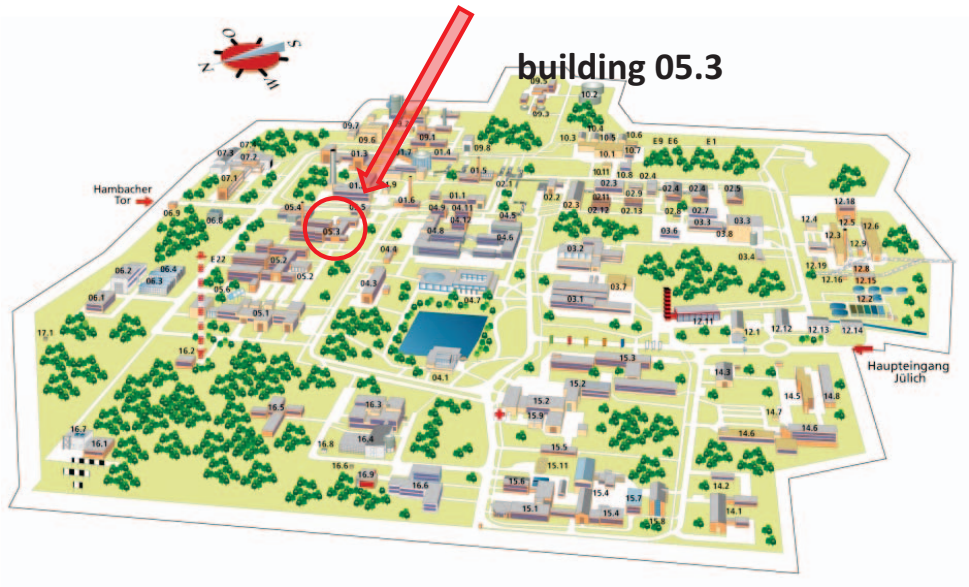

Fig. 150: Map showing the Institute, Helmholtz-Ring H18, building no. 05.3.

1. **Einsatz von multispektralen Satellitenbilddaten in der Wasserhaushalts- und Stoffstrommodellierung – dargestellt am Beispiel des Rureinzugsgebietes**
   von C. Montzka (2008), XX, 238 Seiten
   ISBN: 978-3-89336-508-1

2. **Ozone Production in the Atmosphere Simulation Chamber SAPHIR**
   by C. A. Richter (2008), XIV, 147 pages
   ISBN: 978-3-89336-513-5

3. **Entwicklung neuer Schutz- und Kontaktierungsschichten für Hochtemperatur-Brennstoffzellen**
   von T. Kiefer (2008), 138 Seiten
   ISBN: 978-3-89336-514-2

4. **Optimierung der Reflektivität keramischer Wärmedämmschichten aus Yttrium-teilstabilisiertem Zirkoniumdioxid für den Einsatz auf metallischen Komponenten in Gasturbinen**
   von A. Stuke (2008), X, 201 Seiten
   ISBN: 978-3-89336-515-9

5. **Lichtstreuende Oberflächen, Schichten und Schichtsysteme zur Verbesserung der Lichteinkopplung in Silizium-Dünnschichtsolarzellen**
   von M. Berginski (2008), XV, 171 Seiten
   ISBN: 978-3-89336-516-6

6. **Politikszenarien für den Klimaschutz IV – Szenarien bis 2030**
   hrsg.von P. Markewitz, F. Chr. Matthes (2008), 376 Seiten
   ISBN 978-3-89336-518-0

7. **Untersuchungen zum Verschmutzungsverhalten rheinischer Braunkohlen in Kohledampferzeugern**
   von A. Schlüter (2008), 164 Seiten
   ISBN 978-3-89336-524-1

8. **Inorganic Microporous Membranes for Gas Separation in Fossil Fuel Power Plants**
   by G. van der Donk (2008), VI, 120 pages
   ISBN: 978-3-89336-525-8

9. **Sinterung von Zirkoniumdioxid-Elektrolyten im Mehrlagenverbund der oxidkeramischen Brennstoffzelle (SOFC)**
   von R. Mücke (2008), VI, 165 Seiten
   ISBN: 978-3-89336-529-6

10. **Safety Considerations on Liquid Hydrogen**
    by K. Verfondern (2008), VIII, 167 pages
    ISBN: 978-3-89336-530-2

11. **Kerosinreformierung für Luftfahrtanwendungen**
von R. C. Samsun (2008), VII, 218 Seiten
ISBN: 978-3-89336-531-9

12. **Der 4. Deutsche Wasserstoff Congress 2008 – Tagungsband**
hrsg. von D. Stolten, B. Emonts, Th. Grube (2008), 269 Seiten
ISBN: 978-3-89336-533-3

13. **Organic matter in Late Devonian sediments as an indicator for environmental changes**
by M. Kloppisch (2008), XII, 188 pages
ISBN: 978-3-89336-534-0

14. **Entschwefelung von Mitteldestillaten für die Anwendung in mobilen Brennstoffzellen-Systemen**
von J. Latz (2008), XII, 215 Seiten
ISBN: 978-3-89336-535-7

15. **RED-IMPACT**
Impact of Partitioning, Transmutation and Waste Reduction Technologies on the Final Nuclear Waste Disposal
SYNTHESIS REPORT
ed. by W. von Lensa, R. Nabbi, M. Rossbach (2008), 178 pages
ISBN 978-3-89336-538-8

16. **Ferritic Steel Interconnectors and their Interactions with Ni Base Anodes in Solid Oxide Fuel Cells (SOFC)**
by J. H. Froitzheim (2008), 169 pages
ISBN: 978-3-89336-540-1

17. **Integrated Modelling of Nutrients in Selected River Basins of Turkey**
Results of a bilateral German-Turkish Research Project
project coord. M. Karpuzcu, F. Wendland (2008), XVI, 183 pages
ISBN: 978-3-89336-541-8

18. **Isotopengeochemische Studien zur klimatischen Ausprägung der Jüngeren Dryas in terrestrischen Archiven Eurasiens**
von J. Parplies (2008), XI, 155 Seiten, Anh.
ISBN: 978-3-89336-542-5

19. **Untersuchungen zur Klimavariabilität auf dem Tibetischen Plateau - Ein Beitrag auf der Basis stabiler Kohlenstoff- und Sauerstoffisotope in Jahrringen von Bäumen waldgrenznaher Standorte**
von J. Griessinger (2008), XIII, 172 Seiten
ISBN: 978-3-89336-544-9

20. **Neutron-Irradiation + Helium Hardening & Embrittlement Modeling of 9%Cr-Steels in an Engineering Perspective (HELENA)**
by R. Chaouadi (2008), VIII, 139 pages
ISBN: 978-3-89336-545-6

21. **in Bearbeitung**

22. **Verbundvorhaben APAWAGS (AOEV und Wassergenerierung) – Teilprojekt: Brennstoffreformierung – Schlussbericht**
von R. Peters, R. C. Samsun, J. Pasel, Z. Porš, D. Stolten (2008), VI, 106 Seiten
ISBN: 978-3-89336-547-0

23. **FREEVAL**
Evaluation of a Fire Radiative Power Product derived from Meteosat 8/9 and Identification of Operational User Needs
Final Report
project coord. M. Schultz, M. Wooster (2008), 139 pages
ISBN: 978-3-89336-549-4

24. **Untersuchungen zum Alkaliverhalten unter Oxycoal-Bedingungen**
von C. Weber (2008), VII, 143, XII Seiten
ISBN: 978-3-89336-551-7

25. **Grundlegende Untersuchungen zur Freisetzung von Spurstoffen, Heißgaschemie, Korrosionsbeständigkeit keramischer Werkstoffe und Alkalirückhaltung in der Druckkohlenstaubfeuerung**
von M. Müller (2008), 207 Seiten
ISBN: 978-3-89336-552-4

26. **Analytik von ozoninduzierten phenolischen Sekundärmetaboliten in *Nicotiana tabacum* L. cv Bel W3 mittels LC-MS**
von I. Koch (2008), III, V, 153 Seiten
ISBN 978-3-89336-553-1

27. **IEF-3 Report 2009. Grundlagenforschung für die Anwendung**
(2009), ca. 230 Seiten
ISBN: 978-3-89336-554-8

28. **Influence of Composition and Processing in the Oxidation Behavior of MCrAlY-Coatings for TBC Applications**
by J. Toscano (2009), 168 pages
ISBN: 978-3-89336-556-2

29. **Modellgestützte Analyse signifikanter Phosphorbelastungen in hessischen Oberflächengewässern aus diffusen und punktuellen Quellen**
von B. Tetzlaff (2009), 149 Seiten
ISBN: 978-3-89336-557-9

30. **Nickelreaktivlot / Oxidkeramik – Fügungen als elektrisch isolierende Dichtungskonzepte für Hochtemperatur-Brennstoffzellen-Stacks**
von S. Zügner (2009), 136 Seiten
ISBN: 978-3-89336-558-6

31. **Langzeitbeobachtung der Dosisbelastung der Bevölkerung in radioaktiv kontaminierten Gebieten Weißrusslands – Korma-Studie**
von H. Dederichs, J. Pillath, B. Heuel-Fabianek, P. Hill, R. Lennartz (2009), Getr. Pag.
ISBN: 978-3-89336-532-3

32. **Herstellung von Hochtemperatur-Brennstoffzellen über physikalische Gasphasenabscheidung**
von N. Jordán Escalona (2009), 148 Seiten
ISBN: 978-3-89336-532-3

33. **Real-time Digital Control of Plasma Position and Shape on the TEXTOR Tokamak**
by M. Mitri (2009), IV, 128 pages
ISBN: 978-3-89336-567-8

34. **Freisetzung und Einbindung von Alkalimetallverbindungen in kohlebefeuerten Kombikraftwerken**
von M. Müller (2009), 155 Seiten
ISBN: 978-3-89336-568-5

35. **Kosten von Brennstoffzellensystemen auf Massenbasis in Abhängigkeit von der Absatzmenge**
von J. Werhahn (2009), 242 Seiten
ISBN: 978-3-89336-569-2

36. **Einfluss von Reoxidationszyklen auf die Betriebsfestigkeit von anodengestützten Festoxid-Brennstoffzellen**
von M. Ettler (2009), 138 Seiten
ISBN: 978-3-89336-570-8

37. **Großflächige Plasmaabscheidung von mikrokristallinem Silizium für mikromorphe Dünnschichtsolarmodule**
von T. Kilper (2009), XVII, 154 Seiten
ISBN: 978-3-89336-572-2

38. **Generalized detailed balance theory of solar cells**
by T. Kirchartz (2009), IV, 198 pages
ISBN: 978-3-89336-573-9

39. **The Influence of the Dynamic Ergodic Divertor on the Radial Electric Field at the Tokamak TEXTOR**
von J. W. Coenen (2009), xii, 122, XXVI pages
ISBN: 978-3-89336-574-6

40. **Sicherheitstechnik im Wandel Nuklearer Systeme**
von K. Nünighoff (2009), viii, 215 Seiten
ISBN: 978-3-89336-578-4

41. **Pulvermetallurgie hochporöser NiTi-Legierungen für Implanat- und Dämpfungsanwendungen**
von M. Köhl (2009), XVII, 199 Seiten
ISBN: 978-3-89336-580-7

42. **Einfluss der Bondcoatzusammensetzung und Herstellungsparameter auf die Lebensdauer von Wärmedämmschichten bei zyklischer Temperaturbelastung**
von M. Subanovic (2009), 188, VI Seiten
ISBN: 978-3-89336-582-1

43. **Oxygen Permeation and Thermo-Chemical Stability of Oxygen Permeation Membrane Materials for the Oxyfuel Process**
by A. J. Ellett (2009), 176 pages
ISBN: 978-3-89336-581-4

44. **Korrosion von polykristallinem Aluminiumoxid (PCA) durch Metalljodidschmelzen sowie deren Benetzungseigenschaften**
von S. C. Fischer (2009), 148 Seiten
ISBN: 978-3-89336-584-5

45. **IEF-3 Report 2009. Basic Research for Applications**
(2009), 217 Seiten
ISBN: 978-3-89336-585-2

46. **Verbundvorhaben ELBASYS (Elektrische Basissysteme in einem CFK-Rumpf) - Teilprojekt: Brennstoffzellenabgase zur Tankinertisierung - Schlussbericht**
von R. Peters, J. Latz, J. Pasel, R. C. Samsun, D. Stolten
(2009), xi, 202 Seiten
ISBN: 978-3-89336-587-6

47. **Aging of ^{14}C-labeled Atrazine Residues in Soil: Location, Characterization and Biological Accessibility**
by N. D. Jablonowski (2009), IX, 104 pages
ISBN: 978-3-89336-588-3

48. **Entwicklung eines energetischen Sanierungsmodells für den europäischen Wohngebäudesektor unter dem Aspekt der Erstellung von Szenarien für Energie- und CO_2 - Einsparpotenziale bis 2030**
von P. Hansen (2009), XXII, 281 Seiten
ISBN: 978-3-89336-590-6

49. **Reduktion der Chromfreisetzung aus metallischen Interkonnektoren für Hochtemperaturbrennstofzellen durch Schutzschichtsysteme**
von R. Trebbels (2009), iii, 135 Seiten
ISBN: 978-3-89336-591-3

50. **Bruchmechanische Untersuchung von Metall / Keramik-Verbundsystemen für die Anwendung in der Hochtemperaturbrennstoffzelle**
von B. Kuhn (2009), 118 Seiten
ISBN: 978-3-89336-592-0

51. **Wasserstoff-Emissionen und ihre Auswirkungen auf den arktischen Ozonverlust**
Risikoanalyse einer globalen Wasserstoffwirtschaft
von T. Feck (2009), 180 Seiten
ISBN: 978-3-89336-593-7

52. **Development of a new Online Method for Compound Specific Measurements of Organic Aerosols**
by T. Hohaus (2009), 156 pages
ISBN: 978-3-89336-596-8

53. **Entwicklung einer FPGA basierten Ansteuerungselektronik für Justageeinheiten im Michelson Interferometer**
von H. Nöldgen (2009), 121 Seiten
ISBN: 978-3-89336-599-9

54. **Observation – and model – based study of the extratropical UT/LS**
by A. Kunz (2010), xii, 120, xii pages
ISBN: 978-3-89336-603-3

55. **Herstellung polykristalliner Szintillatoren für die Positronen-Emissions-Tomographie (PET)**
von S. K. Karim (2010), VIII, 154 Seiten
ISBN: 978-3-89336-610-1

56. **Kombination eines Gebäudekondensators mit H2-Rekombinatorelementen in Leichwasserreaktoren**
von S. Kelm (2010), vii, 119 Seiten
ISBN: 978-3-89336-611-8

57. **Plant Leaf Motion Estimation Using A 5D Affine Optical Flow Model**
by T. Schuchert (2010), X, 143 pages
ISBN: 978-3-89336-613-2

58. **Tracer-tracer relations as a tool for research on polar ozone loss**
by R. Müller (2010), 116 pages
ISBN: 978-3-89336-614-9

59. **Sorption of polycyclic aromatic hydrocarbon (PAH) to Yangtze River sediments and their components**
by J. Zhang (2010), X, 109 pages
ISBN: 978-3-89336-616-3

60. **Weltweite Innovationen bei der Entwicklung von CCS-Technologien und Möglichkeiten der Nutzung und des Recyclings von CO_2**
Studie im Auftrag des BMWi
von W. Kuckshinrichs et al. (2010), X, 139 Seiten
ISBN: 978-3-89336-617-0

61. **Herstellung und Charakterisierung von sauerstoffionenleitenden Dünnschichtmembranstrukturen**
von M. Betz (2010), XII, 112 Seiten
ISBN: 978-3-89336-618-7

62. **Politikszenarien für den Klimaschutz V – auf dem Weg zum Strukturwandel, Treibhausgas-Emissionsszenarien bis zum Jahr 2030**
hrsg. von P. Hansen, F. Chr. Matthes (2010), 276 Seiten
ISBN: 978-3-89336-619-4

63. **Charakterisierung Biogener Sekundärer Organischer Aerosole mit Statistischen Methoden**
von C. Spindler (2010), iv, 163 Seiten
ISBN: 978-3-89336-622-4

64. **Stabile Algorithmen für die Magnetotomographie an Brennstoffzellen**
von M. Wannert (2010), ix, 119 Seiten
ISBN: 978-3-89336-623-1

65. **Sauerstofftransport und Degradationsverhalten von Hochtemperaturmembranen für CO2-freie Kraftwerke**
von D. Schlehuber (2010), VII, 139 Seiten
ISBN: 978-3-89336-630-9

66. **Entwicklung und Herstellung von foliengegossenen, anodengestützten Festoxidbrennstoffzellen**
von W. Schafbauer (2010), VI, 164 Seiten
ISBN: 978-3-89336-631-6

67. **Disposal strategy of proton irradiated mercury from high power spallation sources**
by S. Chiriki (2010), xiv, 124 pages
ISBN: 978-3-89336-632-3

68. **Oxides with polyatomic anions considered as new electrolyte materials for solid oxide fuel cells (SOFCs)**
by O. H. Bin Hassan (2010), vii, 121 pages
ISBN: 978-3-89336-633-0

69. **Von der Komponente zum Stack: Entwicklung und Auslegung von HT-PEFC-Stacks der 5 kW-Klasse**
von A. Bendzulla (2010), IX, 203 Seiten
ISBN: 978-3-89336-634-7

70. **Satellitengestützte Schwerewellenmessungen in der Atmosphäre und Perspektiven einer zukünftigen ESA Mission (PREMIER)**
von S. Höfer (2010), 81 Seiten
ISBN: 978-3-89336-637-8

71. **Untersuchungen der Verhältnisse stabiler Kohlenstoffisotope in atmosphärisch relevanten VOC in Simulations- und Feldexperimenten**
von H. Spahn (2010), IV, 210 Seiten
ISBN: 978-3-89336-638-5

72. **Entwicklung und Charakterisierung eines metallischen Substrats für nanostrukturierte keramische Gastrennmembranen**
von K. Brands (2010), vii, 137 Seiten
ISBN: 978-3-89336-640-8

73. **Hybridisierung und Regelung eines mobilen Direktmethanol-Brennstoffzellen-Systems**
von J. Chr. Wilhelm (2010), 220 Seiten
ISBN: 978-3-89336-642-2

74. **Charakterisierung perowskitischer Hochtemperaturmembranen zur Sauerstoffbereitstellung für fossil gefeuerte Kraftwerksprozesse**
von S.A. Möbius (2010) III, 208 Seiten
ISBN: 978-3-89336-643-9

75. **Characterization of natural porous media by NMR and MRI techniques: High and low magnetic field studies for estimation of hydraulic properties**
by L.-R. Stingaciu (2010), 96 pages
ISBN: 978-3-89336-645-3

76. **Hydrological Characterization of a Forest Soil Using Electrical Resistivity Tomography**
by Chr. Oberdörster (2010), XXI, 151 pages
ISBN: 978-3-89336-647-7

77. **Ableitung von atomarem Sauerstoff und Wasserstoff aus Satellitendaten und deren Abhängigkeit vom solaren Zyklus**
von C. Lehmann (2010), 127 Seiten
ISBN: 978-3-89336-649-1

78. **18th World Hydrogen Energy Conference 2010 – WHEC2010 Proceedings**
Speeches and Plenary Talks
ed. by D. Stolten, B. Emonts (2010)
ISBN: 978-3-89336-658-3

78-1. **18th World Hydrogen Energy Conference 2010 – WHEC2010 Proceedings**
Parallel Sessions Book 1:
Fuel Cell Basics / Fuel Infrastructures
ed. by D. Stolten, T. Grube (2010), ca. 460 pages
ISBN: 978-3-89336-651-4

78-2. **18th World Hydrogen Energy Conference 2010 – WHEC2010 Proceedings**
Parallel Sessions Book 2:
Hydrogen Production Technologies – Part 1
ed. by D. Stolten, T. Grube (2010), ca. 400 pages
ISBN: 978-3-89336-652-1

78-3. **18th World Hydrogen Energy Conference 2010 – WHEC2010 Proceedings**
Parallel Sessions Book 3:
Hydrogen Production Technologies – Part 2
ed. by D. Stolten, T. Grube (2010), ca. 640 pages
ISBN: 978-3-89336-653-8

78-4. **18th World Hydrogen Energy Conference 2010 – WHEC2010 Proceedings**
Parallel Sessions Book 4:
Storage Systems / Policy Perspectives, Initiatives and Cooperations
ed. by D. Stolten, T. Grube (2010), ca. 500 pages
ISBN: 978-3-89336-654-5

78-5. **18th World Hydrogen Energy Conference 2010 – WHEC2010 Proceedings**
Parallel Sessions Book 5:
Stategic Analysis / Safety Issues / Existing and Emerging Markets
ed. by D. Stolten, T. Grube (2010), ca. 530 pages
ISBN: 978-3-89336-655-2

78-6. **18th World Hydrogen Energy Conference 2010 – WHEC2010 Proceedings**
Parallel Sessions Book 6:
Stationary Applications / Transportation Applications
ed. by D. Stolten, T. Grube (2010), ca. 330 pages
ISBN: 978-3-89336-656-9

78 Set (complete book series)

18th World Hydrogen Energy Conference 2010 – WHEC2010 Proceedings
ed. by D. Stolten, T. Grube, B. Emonts (2010)
ISBN: 978-3-89336-657-6

79. **Ultrafast voltex core dynamics investigated by finite-element micromagnetic simulations**
by S. Gliga (2010), vi, 144 pages
ISBN: 978-3-89336-660-6

80. **Herstellung und Charakterisierung von keramik- und metallgestützten Membranschichten für die CO_2-Abtrennung in fossilen Kraftwerken**
von F. Hauler (2010), XVIII, 178 Seiten
ISBN: 978-3-89336-662-0

81. **Experiments and numerical studies on transport of sulfadiazine in soil columns**
by M. Unold (2010), xvi, 115 pages
ISBN: 978-3-89336-663-7

82. **Prompt-Gamma-Neutronen-Aktivierungs-Analyse zur zerstörungsfreien Charakterisierung radioaktiver Abfälle**
von J.P.H. Kettler (2010), iv, 205 Seiten
ISBN: 978-3-89336-665-1

83. **Transportparameter dünner geträgerter Kathodenschichten der oxidkeramischen Brennstoffzelle**
von C. Wedershoven (2010), vi, 137 Seiten
ISBN: 978-3-89336-666-8

84. **Charakterisierung der Quellverteilung von Feinstaub und Stickoxiden in ländlichem und städtischem Gebiet**
von S. Urban (2010), vi, 211 Seiten
ISBN: 978-3-89336-669-9

85. **Optics of Nanostructured Thin-Film Silicon Solar Cells**
by C. Haase (2010), 150 pages
ISBN: 978-3-89336-671-2

86. **Entwicklung einer Isolationsschicht für einen Leichtbau-SOFC-Stack**
von R. Berhane (2010), X, 162 Seiten
ISBN: 978-3-89336-672-9

87. **Hydrogen recycling and transport in the helical divertor of TEXTOR**
by M. Clever (2010), x, 172 pages
ISBN: 978-3-89336-673-6

88. **Räumlich differenzierte Quantifizierung der N- und P-Einträge in Grundwasser und Oberflächengewässer in Nordrhein-Westfalen unter besonderer Berücksichtigung diffuser landwirtschaftlicher Quellen**
von F. Wendland et. al. (2010), xii, 216 Seiten
ISBN: 978-3-89336-674-3

89. **Oxidationskinetik innovativer Kohlenstoffmaterialien hinsichtlich schwerer Lufteinbruchstörfälle in HTR´s und Graphitentsorgung oder Aufarbeitung**
von B. Schlögl (2010), ix, 117 Seiten
ISBN: 978-3-89336-676-7

90. **Chemische Heißgasreinigung bei Biomassenvergasungsprozessen**
von M. Stemmler (2010), xv, 196 Seiten
ISBN: 978-3-89336-678-1

91. **Untersuchung und Optimierung der Serienverschaltung von Silizium-Dünnschicht-Solarmodulen**
von S. Haas (2010), ii, 202 Seiten
ISBN: 978-3-89336-680-4

92. **Non-invasive monitoring of water and solute fluxes in a cropped soil**
by S. Garré (2010), xxiv, 133 pages
ISBN: 978-3-89336-681-1

93. **Improved hydrogen sorption kinetics in wet ball milled Mg hydrides**
by L. Meng (2011), II, 119 pages
ISBN: 978-3-89336-687-3

94. **Materials for Advanced Power Engineering 2010**
ed. by J. Lecomte-Beckers, Q. Contrepois, T. Beck and B. Kuhn (2010), 1327 pages
ISBN: 978-3-89336-685-9

95. **2D cross-hole MMR – Survey design and sensitivity analysis for cross-hole applications of the magnetometric resistivity**
by D. Fielitz (2011), xvi, 123 pages
ISBN: 978-3-89336-689-7

96. **Untersuchungen zur Oberflächenspannung von Kohleschlacken unter Vergasungsbedingungen**
von T. Melchior (2011), xvii, 270 Seiten
ISBN: 978-3-89336-690-3

97. **Secondary Organic Aerosols: Chemical Aging, Hygroscopicity, and Cloud Droplet Activation**
by A. Buchholz (2011), xiv, 134 pages
ISBN: 978-3-89336-691-0

98. **Chrom-bezogene Degradation von Festoxid-Brennstoffzellen**
von A. Neumann (2011), xvi, 218 Seiten
ISBN: 978-3-89336-692-7

99. **Amorphous and microcrystalline silicon applied in very thin tandem solar cells**
by S. Schicho (2011), XII, 190 pages
ISBN: 978-3-89336-693-4

100. **Sol-gel and nano-suspension electrolyte layers for high performance solid oxide fuel cells**
by F. Han (2011), iv, 131 pages
ISBN: 978-3-89336-694-1

101. **Impact of different vertical transport representations on simulating processes in the tropical tropopause layer (TTL)**
by F. Plöger (2011), vi, 104 pages
ISBN: 978-3-89336-695-8

102. **Untersuchung optischer Nanostrukturen für die Photovoltaik mit Nahfeldmikroskopie**
von T. Beckers (2011), xiii, 128 Seiten
ISBN: 978-3-89336-696-5

103. **Impact of contamination on hydrogenated amorphous silicon thin films & solar cells**
by J. Wördenweber (2011), XIV, 138 pages
ISBN: 978-3-89336-697-2

104. **Water and Organic Nitrate Detection in an AMS: Laboratory Characterization and Application to Ambient Measurements**
by A. Mensah (2011), XI, 111 pages
ISBN: 978-3-89336-698-9

105. **Entwicklung eines neuen Konzepts zur Steuerung der thermischen Ausdehnung von glaskeramischen Verbundwerkstoffen mit angepasster Fließfähigkeit am Beispiel der Hochtemperatur-Brennstoffzelle**
von E. Wanko (2011), xi, 134 Seiten
ISBN: 978-3-89336-705-4

106. **Tomographic reconstruction of atmospheric volumes from infrared limb-imager measurements**
by J. Ungermann (2011), xiv, 153 pages
ISBN: 978-3-89336-708-5

107. **Synthese und Identifizierung von substituierten Mg-Al-Cl Doppelhydroxidverbindungen mit Schwerpunkt IR-Spektroskopie**
von B. Hansen (2011), XII, 121 Seiten
ISBN: 978-3-89336-709-2

108. **Analysis of spatial soil moisture dynamics using wireless sensor networks**
by U. Rosenbaum (2011), xxii, 120 pages
ISBN: 978-3-89336-710-8

109. **Optimierung von APS-ZrO2-Wärmedämmschichten durch Variation der Kriechfestigkeit und der Grenzflächenrauhigkeit**
von M. E. Schweda (2011), 168 Seiten
ISBN: 978-3-89336-711-5

110. **Sorption of a branched nonylphenol isomer and perfluorooctanoic acid on geosorbents and carbon nanotubes**
by C. Li (2011), X, 102 pages
ISBN: 978-3-89336-716-0

111. **Electron Transport in the Plasma Edge with Rotating Resonant Magnetic Perturbations at the TEXTOR Tokamak**
by H. Stoschus (2011), iv, 113 pages
ISBN: 978-3-89336-718-4

112. **Diffusion and Flow Investigations in Natural Porous Media by Nuclear Magnetic Resonance**
by N. Spindler (2011), viii, 144 pages
ISBN: 978-3-89336-719-1

113. **Entwicklung und Erprobung des Hygrometer for Atmospheric Investigations**
von T. Klostermann (2011), IV, 118 Seiten
ISBN: 978-3-89336-723-8

114. **Application of functional gene arrays for monitoring influences of plant/seasons on bacterial functions and community structures in constructed wetlands (Bitterfeld, Germany)**
by J. Ning (2011), xiv, 157 pages
ISBN: 978-3-89336-724-5

115. **Wasseraustrag aus den Kathodenkanälen von Direkt-Methanol-Brennstoffzellen**
von A. Schröder (2011), VII, 228 Seiten
ISBN: 978-3-89336-727-6

116. **CITYZEN Climate Impact Studies**
ed. by M. Schultz (2011), 45 pages
ISBN: 978-3-89336-729-0

117. **Software Tools zum interoperablen Austausch und zur Visualisierung von Geodatensätzen über das Internet**
von M. Schultz, M. Decker, S. Lührs (2011), iv, 156 Seiten
ISBN: 978-3-89336-730-6

118. **Optimierung eines Leichtbaudesigns für ein SOFC-Brennstoffzellenstack**
von T. Nguyen-Xuan (2011), III, 154 Seiten
ISBN: 978-3-89336-732-0

119. **Institute of Energy and Climate Research IEK-6:**
Nuclear Waste Management & Reactor Safety Report 2009/2010
Material Science for Nuclear Waste Management
ed. by M. Klinkenberg, S. Neumeier, D. Bosbach (2011), 240 pages
ISBN: 978-3-89336-735-1

Institute of Energy and Climate Research
IEK-6: Nuclear Waste Management & Reactor Safety

Due to the use of nuclear energy about 17.000 t (27.000 m^3) of high level waste and about 300.000 m^3 of low- and intermediated level waste will have accumulated in Germany until 2022. Research in the Institute of Energy and Climate Research (IEK-6), Nuclear Waste Management and Reactor Safety devision focuses on fundamental and applied aspects of the safe management of nuclear waste – in particular the nuclear aspects. In principle, our research in Forschungszentrum Jülich is looking at the material science/solid state aspects of nuclear waste management. It is organized in several research areas:

The **long-term safety of nuclear waste disposal** is a key issue when it comes to the final disposal of high level nuclear waste in a deep geological formation. We are contributing to the scientific basis for the safety case of a nuclear waste repository in Germany. In Jülich we are focusing on a fundamental understanding of near field processes within a waste repository system. The main research topics are spent fuel corrosion and the retention of radionuclides by secondary phases. In addition, **innovative waste management strategies** are investigated to facilitate a qualified decision on the best strategy for Germany. New ceramic waste forms for disposal in a deep geological formation are studied as well as the partitioning of long-lived actinides. These research areas are supported by our **structure research group**, which is using experimental and computational approaches to examine actinide containing compounds.

Complementary to these basic science oriented activities, IEK-6 also works on rather applied aspects. The development of non-destructive methods for the **characterisation of nuclear waste** packages has a long tradition in Jülich. Current activities focus on improving the segmented gamma scanning technique and the prompt gamma neutron activation analysis. Furthermore, the **waste treatment group** is developing concepts for the safe management of nuclear graphite.

Within the **product quality control group (PKS)** 16 scientists and engineers are currently working on the qualification of radioactive waste on behalf of the Federal Office for Radiation Protection (BfS). The **nuclear safeguards** group is coordinating the joint safeguards R&D programme between IAEA and BMWi.

Research and development activities are integrated into national and international research programms and cooperations. They represent a substantial part of the Helmholtz Research programme „Nuclear Safety Research“.

Material science for nuclear waste management is the research subject of IEK-6, Nuclear Waste Management part.

Energie & Umwelt / Energy & Environment
Band / Volume 119
ISBN 978-3-89336-735-1

JÜLICH
FORSCHUNGSZENTRUM